

AD-A230 033

DTIC FILE COPY

3

The National Center for Physical Acoustics

DTIC
SELECTED
DEC 24 1990
S D &

DISTRIBUTION STATEMENT A
Approved for public release
Distribution Unlimited



*The
University of Mississippi*

AN EXPERIMENTAL INVESTIGATION OF
ACOUSTIC CAVITATION IN GASEOUS LIQUIDS

BY

DARIO FELIPE GAITAN

B.S., University of Southwestern Louisiana, 1984

National Center for Physical Acoustics
University, MS 38677

September 1990

Technical Report
prepared for:

Office of Naval Research
Physics Division
Contract # N00014-90-J-4021

NCPA.LC.02.90

DISTRIBUTION STATEMENT A

Approved for public release
Distribution Unlimited

DTIC
ELECTE
DEC 24 1990
S D D



Accession For	
NTIS CRA&I	<input checked="" type="checkbox"/>
DTIC TAB	<input type="checkbox"/>
Unannounced	<input type="checkbox"/>
Justification	
By	
Distribution	
Availability Codes	
Dist	Avail and/or Special
A-1	

90 12 21 010

Unclassified

SECURITY CLASSIFICATION OF THIS PAGE

REPORT DOCUMENTATION PAGE

Form Approved
OMB No. 0704-0188

1a. REPORT SECURITY CLASSIFICATION Unclassified			1b. RESTRICTIVE MARKINGS		
2a. SECURITY CLASSIFICATION AUTHORITY			3. DISTRIBUTION/AVAILABILITY OF REPORT Approved for public release Distribution unlimited		
2b. DECLASSIFICATION/DOWNGRADING SCHEDULE					
4. PERFORMING ORGANIZATION REPORT NUMBER(S) NCPA.LC.02.90			5. MONITORING ORGANIZATION REPORT NUMBER(*)		
6a. NAME OF PERFORMING ORGANIZATION National Center for Physical Acoustics		6b. OFFICE SYMBOL (If applicable) LC		7a. NAME OF MONITORING ORGANIZATION Office of Naval Research	
6c. ADDRESS (City, State, and ZIP Code) Coliseum Drive University, MS 38677		7b. ADDRESS (City, State, and ZIP Code) Department of the Navy Arlington, VA 22217			
8a. NAME OF FUNDING/SPONSORING ORGANIZATION		8b. OFFICE SYMBOL (If applicable)		9. PROCUREMENT INSTRUMENT IDENTIFICATION NUMBER N00014-90-J-4021	
8c. ADDRESS (City, State, and ZIP Code)		10. SOURCE OF FUNDING NUMBERS			
		PROGRAM ELEMENT NO.		PROJECT NO.	TASK NO.
					WORK UNIT ACCESSION NO.
11. TITLE (Include Security Classification) An experimental investigation of acoustic cavitation in gaseous liquids.					
12. PERSONAL AUTHOR(S) Gaitan, D. Felipe; Crum, Lawrence A.					
13a. TYPE OF REPORT Technical		13b. TIME COVERED FROM 90-1-1 TO 90-12-31		14. DATE OF REPORT (Year, Month, Day) 1990, November 8	
				15. PAGE COUNT 207	
16. SUPPLEMENTARY NOTATION					
17. COSATI CODES			18. SUBJECT TERMS (Continue on reverse if necessary and identify by block number)		
FIELD	GROUP	SUB-GROUP			
19. ABSTRACT (Continue on reverse if necessary and identify by block number) High amplitude radial pulsations of a single bubble in several glycerine and water mixtures were observed in an acoustic stationary wave system at acoustic pressure amplitudes on the order of 150 kPa at 21-25 kHz. Sonoluminescence, a phenomenon generally attributed to the high temperatures generated during the collapse of cavitation bubbles, was observed as short light pulses occurring once every acoustic period. These emissions could be seen to originate at the geometric center of the bubble when observed through a microscope. It was observed that the light emissions occurred simultaneously with the bubble collapse. Using a laser scattering technique, experimental radius-time curves were obtained which confirmed the absence of surface waves which are expected at pressure amplitudes above 100 kPa. From these radius-time curves, measurements of the pulsation amplitude, the timing of the major bubble collapse, and the number of rebounds were made and compared with several theories. The implications of this research on the current understanding of cavitation were discussed.					
20. DISTRIBUTION/AVAILABILITY OF ABSTRACT <input type="checkbox"/> UNCLASSIFIED/UNLIMITED <input checked="" type="checkbox"/> SAME AS RPT. <input type="checkbox"/> DTIC USERS			21. ABSTRACT SECURITY CLASSIFICATION Unclassified		
22a. NAME OF RESPONSIBLE INDIVIDUAL Lawrence A. Crum			22b. TELEPHONE (Include Area Code) (601) 232-5905		22c. OFFICE SYMBOL LC

Abstract

AN EXPERIMENTAL INVESTIGATION OF ACOUSTIC CAVITATION IN GASEOUS LIQUIDS

GAITAN, DARIO FELIPE. B. S. , University of Southwestern Louisiana, 1984. Ph. D. , University of Mississippi, 1990. Dissertation directed by Dr. Lawrence A. Crum.

High amplitude radial pulsations of a single gas bubble in several glycerine and water mixtures have been observed in an acoustic stationary wave system at acoustic pressure amplitudes as high as 1.5 bars. Using a laser scattering technique, radius-time curves have been obtained experimentally which confirm the absence of surface waves. Measurements of the pulsation amplitude, the timing of the major bubble collapse, and the number of rebounds have been made and compared with the theory. From these data, calculations of the internal gas temperature and pressure during the collapse have been performed. Values of at least 2,000 K and 2,000 bars have been obtained using a sophisticated model of spherically symmetric bubble dynamics. Simultaneously, sonoluminescence (SL), a phenomenon discovered in 1933 and attributed today to the high temperatures and pressures generated during the collapse of the bubbles, were observed as short light pulses occurring once every acoustic period. The light emissions can be seen to originate at the geometric center of the bubble when observed through a microscope. Also, the simultaneity of the light emissions and the collapse of the bubble has been confirmed with the aid of a photomultiplier tube. This is the first recorded observation of SL generated by a single bubble. Comparisons of the measured quantities have been made to those predicted by several models. In addition, the implications of this research on the current understanding of cavitation related phenomena such as rectified diffusion, surface wave excitation and sonoluminescence are discussed. Future experiments are suggested .

ACKNOWLEDGEMENTS

I would like to acknowledge my appreciation to the following individuals and organizations for their contributions to this dissertation and their support during my graduate education:

To Dr. Lawrence Crum for his personal and professional advice, critical comments, and patience in directing this dissertation.

To Dr. Andrea Prosperetti for his scientific expertise and valuable suggestions during the course of this project.

To Dr. Ron Roy for technical advice and continuous encouragement in the pursuit of my career.

To Dr. Charles Church for sharing his knowledge and physical insights during many helpful discussions and for his valuable help in calculating the data in Chapter III (rectified diffusion thresholds).

To Milena Gaitan, Sandra Smith, Nancy Roy, and Janice Mills for their help in preparing this manuscript, especially to Sandra Smith for her friendship and support during the last five years.

To former members of the cavitation group at NCPA, Glynn Holt, Steve Horsburgh and Brian Fowlkes, for many enlightening discussions, technical support and their companionship. I am especially grateful to Glynn Holt and Steve Horsburgh for letting me use their theoretical calculations on Mie scattering (Chapter II) and surface instabilities threshold (Chapter III), respectively.

To the National Center for Physical Acoustics and the University of Mississippi for their support of this work and to the other members of my dissertation committee, Dr. Robert Hickling, Dr. Mack Breazeale, Dr. James Reidy, and Dr. Charles Hussey, as well as to Dr. Roy Arnold, Glynn Holt, and Ali Kolaini for their useful scientific and editorial comments.

Finally, to my parents, Dario and Luz, for their moral and financial support during my educational career and to my wife, Milena, for her encouragement, help and great patience during the writing of this dissertation.

Table of Contents

LIST OF TABLES.....	viii
LIST OF FIGURES.....	ix
Chapter	
I. INTRODUCTION.....	1
A. Statement of the Problem.....	1
B. Historical Perspective.....	2
1. Models of Sonoluminescence.....	2
2. The Phase of Sonoluminescence.....	10
3. Sonoluminescence as a Probe of Acoustic Cavitation.....	17
4. Acoustic Cavitation and Bubble Dynamics.....	21
C. Recapitulation and General Overview of the Dissertation.....	24
II. APPARATUS AND EXPERIMENTAL PROCEDURE.....	27
A. Introduction.....	27
B. Acoustic Levitation Apparatus.....	28
1. Levitation Cells.....	28
2. Rise-time Measuring Apparatus.....	33
3. Hydrophones.....	35
C. Calibration of Acoustic Levitation Apparatus.....	39
1. Absolute Sound Field Pressure.....	39
2. Phase of the Sound Field Pressure.....	46

D. Light Scattering Experiment.....	47
1. Apparatus.....	47
2. Calibration.....	48
a. Absolute Bubble Radius.....	48
b. Phase of Radial Bubble Pulsations.....	59
3. Procedure	61
E. Sonoluminescence Detection Experiment.....	63
1. Apparatus.....	63
2. Calibration.....	67
3. Procedure	68
a. Phase of Sonoluminescence vs Bubble Motion	68
b. Phase of Sonoluminescence vs Sound Field.....	68
III. THEORY.....	71
A. Introduction.....	71
B. Radial Bubble Motion.....	72
1. Theoretical Formulations.....	72
2. Basic Concepts of Radial Bubble Motion	82
3. Limitations of the Theoretical Formulations	95
C. Surface Instabilities	104
D. Rectified Diffusion.....	109
IV. RESULTS AND DISCUSSION	114
A. Introduction.....	114

B. Light Scattering Experiments	123
1. Comparison between Theories and Experiment:	
Prosperetti's Theory	123
a. Radius-time curves	123
b. Pulsation Amplitude.....	128
c. Phase of Collapse	136
d. Number of Radial Minima	142
e. Comparison with the Polytropic Theory and Flynn's Theory	150
2. Theoretical Values of Temperature, Pressure and Relative Density	161
3. Phase of Sonoluminescence vs Bubble Motion.....	172
C. Time-to-Amplitude Converter System:	
Sonoluminescence vs Sound Field.....	174
1. Single Bubble Cavitation Field.....	174
2. Multi-bubble Cavitation Fields	181
V. SUMMARY, CONCLUSIONS AND TOPICS FOR FUTURE STUDY..	185
A. Summary of the dissertation	185
B. Conclusions	186
C. Topics for Future Study	187
REFERENCES	189
APPENDIX A	198

List of Tables

Table no.	Description
1	The phase of SL Predicted by the different models..... 11
2	Summary of measurements of the phase of sonoluminescence... 14
3	Summary of measured relative densities, temperatures and pressures inside cavitation bubbles..... 18
4	Summary of predictions of R_0 obtained from Prosperetti's formulation. 149
5	Summary of predictions of R_0 obtained from Flynn's formulation..... 157
6	Summary of predictions of R_0 obtained from the polytropic formulation..... 158
7	Summary of maximum theoretical temperatures inside 20-25 μm bubbles for the range of p_A used during the experiments..... 166
8	Summary of maximum theoretical pressures inside 20-25 μm bubbles for the range of p_A used during the experiments..... 166
9	Summary of maximum theoretical relative densities inside 20-25 μm bubbles for the range of p_A used during the experiments..... 166

List of Figures

Figure no.	Description	
1	Schematic drawing of cylindrical acoustic levitation cell with bubble.....	30
2	Schematic drawing of rectangular acoustic levitation cell with bubble.....	31
3	Schematic diagram of rise-time measurement apparatus.....	34
4	Schematic drawing of needle hydrophone (NDL1).....	36
5	Plot of the side pill transducer response vs the depth of the needle hydrophone.....	38
6	Plot of the needle hydrophone response vs the side pill transducer.....	38
7	Pressure profile of cylindrical levitation cell as a function of depth in GLY42 at $f=23.6$ kHz.	41
8	Schematic diagram of experimental apparatus used to record the light intensity scattered by the bubble as a function of time.	49
9	Theoretical scattered intensity of the parallel polarized component S_2 as a function of scattering angle (0 is forward) for $ka=661$. This corresponds to a radius	

	of 38.6 μm with respect to the Ar-I 488.0 nm line.....	53
10	Theoretical scattered intensity of the parallel component S2 as a function of equilibrium radius at 66 degrees.....	54
11	Theoretical scattered intensity of the parallel component S2 as a function of equilibrium radius at 70 degrees.....	55
12	Theoretical scattered intensity of the parallel component S2 as a function of equilibrium radius at 80 degrees.....	56
13	Measured scattered light intensity vs equilibrium bubble radius for 42% glycerine. The solid line corresponds to a 2 nd degree polynomial fit.	58
14	Theoretical phase of bubble radius minimum for 42% glycerine at 0.1, 0.2 and 0.3 bars and $f=23.6$ kHz used in the phase calibration of the light-scattering apparatus.....	60
15	Schematic diagram of experimental apparatus used to measure the phase of sonoluminescence relative to the sound field.....	64
16	Schematic diagram of circuit used to measure the phase of sonoluminescence relative to the sound field.	66
17	Theoretical bubble-response curves calculated using Prosperetti's formulation for water at $p_A=0.1-0.5$ bars, $f=21.0$ kHz.....	83
18	Theoretical radius-time curve calculated using the polytropic formulation for water at $p_A=0.8$ bars, $R_0/R_{res}=0.7$, $f=21.0$ kHz.....	85

19	Theoretical radius-time curve calculated using the polytropic formulation for water at $p_A=0.8$ bars, $R_o/R_{res}=0.39$, $f=21.0$ kHz.	86
20	Theoretical radius-time curve calculated using Prosperetti's formulation for water at $p_A=1.2$ bars, $R_o/R_{res}=0.14$, $f=21.0$ kHz.	88
21	Theoretical internal temperature-time curve calculated using Prosperetti's formulation for the same conditions used in figure 20.	89
22	Theoretical internal pressure-time curve calculated using Prosperetti's formulation for the same conditions used in figure 20.	91
23	Theoretical bubble-response curve calculated using Prosperetti's formulation for water at $p_A=1.2$ bars, $f=21.0$ kHz.	92
24	Theoretical phase-of-collapse curve calculated using Prosperetti's formulation for the same conditions used in figure 23.	94
25	Theoretical internal temperature curve calculated using Prosperetti's formulation for the same conditions used in figure 23.	96
26	Theoretical internal pressure curve calculated using Prosperetti's formulation for the same conditions used in figure 23.	97
27	Theoretical liquid pressure vs. liquid temperature at the	

	interface during one acoustic period for GLY42, $R_o \approx 20 \mu\text{m}$, $p_A = 1.5$ bars and $f = 23.6$ kHz. These data were calculated using Flynn's formulation.....	101
28	Pressure-amplitude threshold curve for the excitation of surface waves calculated by Horsburgh (1990) at $f = 22.2$ kHz for air bubbles in water.....	107
29	Pressure-amplitude threshold curve for bubble growth by rectified diffusion calculated by Church (1990) at $f = 21.0$ kHz in air-saturated water.....	111
30	Simultaneous oscilloscope traces of sonoluminescence (top) and acoustic pressure (bottom) for water at $f = 21.0$ kHz ($T = 47.6 \mu\text{m}$).....	115
31	Depiction of cavitation streamers in the cylindrical levitation cell.....	117
32	Graphic representation of the range of pressure in which radial stability was observed in water-glycerine mixtures at $f = 21\text{-}25$ kHz.....	121
33	Experimental radius-time curve obtained with the light- scattering apparatus in 21% glycerine at $p_A = 1.22$ bars and $f = 22.3$ kHz.....	124
34	Theoretical calculation of the steady state solution of the bubble radius for the experimental conditions described in Fig. 33 and $R_o \approx 20 \mu\text{m}$ using Prosperetti's formulation.	126
35	Measured and theoretical pulsation amplitude (R_{max}^i) vs	

	acoustic pressure amplitude in water using Prosperetti's formulation at $f=21.0$ kHz.....	129
36	Measured and theoretical pulsation amplitude (R_{max}^i) vs acoustic pressure amplitude in GLY21 using Prosperetti's formulation at $f=22.3$ kHz.....	130
37	Measured and theoretical pulsation amplitude (R_{max}^i) vs acoustic pressure amplitude in GLY35 using Prosperetti's formulation at $f=23.0$ kHz.....	131
38	Measured and theoretical pulsation amplitude (R_{max}^i) vs acoustic pressure amplitude in GLY42 using Prosperetti's formulation at $f=23.6$ kHz.....	132
39	Measured and theoretical pulsation amplitude (R_{max}^i) vs acoustic pressure amplitude in GLY60 using Prosperetti's formulation at $f=24.8$ kHz.....	133
40	Measured and theoretical phase of bubble collapse (ϕ_c) vs acoustic pressure amplitude in water using Prosperetti's formulation at $f=21.0$ kHz.....	137
41	Measured and theoretical phase of bubble collapse (ϕ_c) vs acoustic pressure amplitude in GLY21 using Prosperetti's formulation at $f=23.3$ kHz.....	138
42	Measured and theoretical phase of bubble collapse (ϕ_c) vs acoustic pressure amplitude in GLY35 using Prosperetti's formulation at $f=23.0$ kHz.....	139
43	Measured and theoretical phase of bubble collapse (ϕ_c) vs	

	acoustic pressure amplitude in GLY42 using Prosperetti's formulation at $f=23.6$ kHz.....	140
44	Measured and theoretical phase of bubble collapse (ϕ_c) vs acoustic pressure amplitude in GLY60 using Prosperetti's formulation at $f=24.8$ kHz.....	141
45	Measured and theoretical number of minima (M^i) vs acoustic pressure amplitude in water using Prosperetti's formulation at $f=21.0$ kHz.....	143
46	Measured and theoretical number of minima (M^i) vs acoustic pressure amplitude in GLY21 using Prosperetti's formulations at $f=22.3$ kHz.....	144
47	Measured and theoretical number of minima (M^i) vs acoustic pressure amplitude in GLY35 using Prosperetti's formulation at $f=23.0$ kHz.....	145
48	Measured and theoretical number of minima (M^i) vs acoustic pressure amplitude in GLY42 using Prosperetti's formulation at $f=23.6$ kHz.....	146
49	Measured and theoretical number of minima (M^i) vs acoustic pressure amplitude in GLY60 using Prosperetti's formulation at $f=24.8$ kHz.....	147
50	Measured and theoretical pulsation amplitude (R^i_{max}) vs acoustic pressure amplitude in water using all three formulations at $f=21.0$ kHz.	151
51	Measured and theoretical pulsation amplitude (R^i_{max}) vs	

	acoustic pressure amplitude in GLY42 using all three formulations at $f=23.6$ kHz.	152
52	Measured and theoretical phase of bubble collapse (ϕ_c) vs acoustic pressure amplitude in water using all three formulations at $f=21.0$ kHz.	153
53	Measured and theoretical phase of bubble collapse (ϕ_c) vs acoustic pressure amplitude in GLY42 using all three formulations at $f=23.6$ kHz.	154
54	Measured and theoretical number of minima (M') vs acoustic pressure amplitude in water using all three formulations at $f=21.0$ kHz.	155
55	Measured and theoretical number of minima (M') vs acoustic pressure amplitude in GLY42 using all three formulations at $f=23.6$ kHz.	156
56	Theoretical maximum gas temperature reached during the bubble collapse in water for $R_o=15$ and 20 microns at $f=21.0$ kHz.	162
57	Theoretical maximum gas temperature reached during the bubble collapse in GLY42 for $R_o=15$ and 20 microns at $f=23.6$ kHz.	163
58	Theoretical maximum gas pressure reached during the bubble collapse in water for $R_o=15$ and 20 microns at $f=21.0$ kHz.	164
59	Theoretical maximum gas pressure reached during the	

	bubble collapse in GLY42 for $R_0=15$ and 20 microns at $f=23.6$ kHz.....	165
60	Simultaneous plots of the bubble radius (bottom) representing the bubble radius and sonoluminescence (top) in GLY21 at $p_A=1.2$ bars at $f=22.3$ kHz.	173
61	Phase of sonoluminescence emitted by a single bubble as a function of time. It was measured in water at $p_A \approx 1.1$ bars and $f=21.0$ kHz using the time-to-amplitude converter (TAC) system.....	175
62	Phase of sonoluminescence emitted by a single bubble as a function of time. It was measured in water at $p_A \approx 1.2$ bars and $f=21.0$ kHz using the time-to-amplitude converter (TAC) system during a transition (see text).....	177
63	Phase of sonoluminescence emitted by a single bubble as a function of time. It was measured in water at $p_A \approx 1.3$ bars and $f=21.0$ kHz using the time-to-amplitude converter (TAC) system during bubble breakup and disappearance.....	180
64	Phase of sonoluminescence emitted by a multibubble cavitation field as a function of time. It was measured in water at $p_A \approx 1.3$ bars and $f=21.0$ kHz using the time-to- amplitude converter (TAC) system.	182
65	Phase of sonoluminescence emitted by a multi-bubble cavitation field as a function of time. It was measured in	

	water at $p_A \approx 1.3$ bars and $f = 21.0$ kHz using the time-to-amplitude converter (TAC) system.	184
A1	Calibration chart and specifications for B&K hydrophone type 8103.	199
A2	Measured scattered light intensity vs equilibrium bubble radius for water at $f = 21.0$ kHz. The solid line corresponds to a 2 nd degree polynomial fit.	200
A3	Measured scattered light intensity vs equilibrium bubble radius for 35% glycerine mixture at $f = 23.0$ kHz. The solid line corresponds to a 2 nd degree polynomial fit.	201
A4	Measured scattered light intensity vs equilibrium bubble radius for 42% glycerine mixture at $f = 23.6$ kHz. The solid line corresponds to a 2 nd degree polynomial fit.	202
A5	Measured scattered light intensity vs equilibrium bubble radius for 60% glycerine mixture at $f = 24.8$ kHz. The solid line corresponds to a 2 nd degree polynomial fit.	203
A6	Experimental radius-time curve obtained with the light-scattering apparatus in water glycerine at $p_A = 1.22$ bars and $f = 21.0$ kHz.	204
A7	Experimental radius-time curve obtained with the light-scattering apparatus in 35% glycerine at $p_A = 1.37$ bars and $f = 23.0$ kHz.	205
A8	Experimental radius-time curve obtained with the light-	

	scattering apparatus in 42% glycerine at $p_A=1.50$ bars and $f=23.6$ kHz.....	206
A9	Experimental radius-time curve obtained with the light- scattering apparatus in 60% glycerine at $p_A=1.27$ bars and $f=24.8$ kHz.....	207

Chapter I

Introduction

I. A. Statement of the Problem

The subject of this dissertation is the dynamics of bubbles in acoustic cavitation fields of moderate intensities. For the purpose of this study, acoustic cavitation may be defined as the formation and pulsation of vapor or gas cavities or bubbles in a liquid through the negative pressure half cycle of a sound field. A particularly interesting phenomenon associated with the violent pulsations of gas bubbles is a weak emission of light called sonoluminescence. This light emission has been attributed to the high temperatures generated during the rapid compression of the bubbles, brought about by the action of the sound field. Despite the extensive amount of research done on both acoustic cavitation and sonoluminescence, many important questions relating to the nature and dynamics of these phenomena remain unanswered. Attesting to this uncertainty is the multiplicity of existing models describing the mechanisms of light production as well as the number of conflicting views and observations of cavitation-related phenomena found in the literature.

The motivation behind this research was to answer questions such as: What is the motion of the light-emitting cavities involved in sonoluminescence? How applicable are the present theories of single, spherical bubble dynamics in describing these cavities? What are the physical conditions attained in the

interior of the bubbles during the collapse ? Is it possible to detect sonoluminescence from a single pulsating bubble ? Answers to these questions have been pursued for over 50 years and, needless to say, complete answers to all of them have not been found here. In the process of seeking those answers, however, some experimental observations were made which have clarified some of the past and present research in this field. It is my hope that some of these observations will point to new directions that future researchers may follow.

I. B. Historical Perspective

Cavitation was first predicted by Leonhard Euler in 1754 when he suggested that, if the velocity in a liquid was high enough, negative pressures could be generated and the liquid might "break". This "breaking" was given the name "cavitation" in 1895 by R.E. Froude, an English naval architect, to describe the appearance of voids and clouds of bubbles around propellers rotating at high speeds. Since then, the term "cavitation" has been used to describe the appearance of voids or bubbles when liquids are sufficiently stressed.

The first theoretical treatment of cavitation was made by Lord Rayleigh in 1917. In it, he derived an equation to describe the motion of a vapor-filled cavity in a liquid. In this cavity, called a Rayleigh cavity, the internal pressure was less than the ambient pressure, and they both remained constant. By its definition, this cavity could not be in equilibrium with the surrounding liquid and began to collapse immediately. Although very simplistic, this model has been used successfully to represent cavities formed by rotating propellers and, more

generally, by hydrodynamic cavitation. No further improvements to Rayleigh's theory were made until more than 30 years later, with the introduction of acoustic cavitation.

The first systematic study of acoustic cavitation was published by Blake in 1949. In it, Blake describes the formation of bubbles in the focal region of a parabolic projector where sound waves were made to converge. According to Blake, bubbles in the cavitation region moved erratically and, if the amplitude were high enough, they emitted a hissing noise. This hissing, he postulated, was generated by cavities collapsing under the action of the sound field. These cavities were used to explain a particularly interesting effect of acoustic cavitation that had been observed 15 years before. When ultrasound of sufficiently high intensity was passed through a liquid saturated with gas, a weak emission of light was observed. This effect was called sonoluminescence, i.e., light "produced" by sound.

I. B. 1. Models of Sonoluminescence

First observed by Marinesco *et al.* in 1933, sonoluminescence (SL) was discovered when photographic plates became exposed when submerged in an insonified liquid. It was not until 1947, however, that Paounoff *et al.* showed that the exposure of the plates occurred at the pressure antinodes of the standing wave field. The first attempt to explain this phenomenon was made by Zimakov in 1934. After studying SL from various aqueous solutions, he concluded that the emission was caused by an electric discharge between vapor cavities and the glass wall of

the container. Frenzel and Schultes (1935), after noticing that light was not emitted from degassed water, concluded that the emission was caused by friction between cavitating bubbles and water. Chamber (1936) studied SL from 36 different liquids at an insonation frequency of 10 kHz and was the first to observe light emission from nonaqueous solutions. He also established an inverse relationship between SL intensity and the ambient liquid temperature. Based on his observations, he postulated the first formal model of SL known as The Triboluminescent Model. This model suggested that SL was generated by the sudden destruction of the quasi-crystalline structure of the liquid, a process similar to the one observed when many crystals are crushed. Since the breaking of the structure occurred during the cavity formation, this model predicted the light emission to occur during the expansion phase of the acoustic cycle.

A year later, Levshin and Rzhevkin (1937) concluded that SL originated in the gas phase (and not in the liquid) after observing that potassium iodide and pyrogallol, a quencher of photoluminescence in the liquid, did not quench sonoluminescence, whereas CO₂, a gas quencher, did. They also proposed that SL was caused by an electric discharge resulting from the liquid rupture which excites the vapor filling the cavities, producing sonoluminescence. This theory was further developed by Harvey (1939), who suggested that these electric charges were balloelectric in nature; i.e., they were produced by an increase in the surface charge of fluids. Harvey's model, known as The Balloelectric Model, draws an analogy with the mechanism through which water droplets in a gas become charged, as occurs in rain and waterfalls. By suggesting the inverse phenomenon, i.e., charged bubbles in a liquid, Harvey postulated that an electric

field exists in the surrounding liquid which increases as the bubbles are compressed until a discharge occurs, giving rise to a weak emission. This model, therefore, predicted the light to be emitted during the compression phase of the sound field.

Another model, also based on the existence of electric charges on the walls of cavities, was that of Frenkel (1940) called The Microdischarge Model. It postulated that statistical variations of the charge distribution on the lens-shaped cavity formed by the rupture of the liquid created regions of opposite charge on the cavity wall. As the cavity expanded, it became spherical causing the electric field within it to strengthen until a discharge occurred during the expansive phase of the sound field.

In 1949, Weyl and Marboe proposed that the light was emitted by the radiative recombination of ions created as the quasi-crystalline structure of the liquid was destroyed at the newly created surface of an expanding bubble. This model was called The Mechanochemical Model of sonoluminescence.

Several criticisms have been made to these early models, mainly due to the observed lack of sensitivity of the light emission to the electrical conductivity of the liquid, which would be expected to affect the electric charge formation. In fact, SL is often enhanced by the addition of electrolytes (Negishi, 1961) and is particularly strong in mercury (Kuttruff, 1950). Also, these models suggest that cavitation arises from molecular ruptures whereas, at moderate acoustic intensities, cavitation is known to occur from the growth of stabilized gaseous nuclei (Atchley *et al.*, 1984).

Despite the strong evidence against models of SL based on electrical discharges, new models are still being introduced. In 1974, Degrois and Baldo proposed the "new electrical hypothesis" in which charge on gas bubbles arises from the neutralization of anions on the bubble surface by gas molecules adsorbed on the inside of the gas-liquid interface. The electrical field is generated as the gas molecules become polarized due to their asymmetric surroundings. As the bubble collapses, the charge density increases until it exceeds a critical value, at which point a discharge of electrons occurs from the inside of the interface into the liquid. This model has been called The Anion Discharge Model. A thorough review of this hypothesis has been given by Sehgal and Verral (1982), in which they show how this model disagrees with the experimental data.

More recently, Margulis (1984) has proposed a new electric charge model in order to explain some experimental facts such as the observation of electric pulses in an insonated liquid (Gimenez, 1982), SL flashes during the expansion phase of the sound field (Golubnichii *et al.*, 1970) and sonoluminescence and sonochemical reactions in low frequency acoustic fields (Margulis, 1982, 1983). These facts, however, have only been observed by a few investigators and constitute a very small percentage of all the available data on sonoluminescence. Margulis' model is based on the accumulation of charge on a small neck of a "fragmentation bubble" which is still attached to the parent bubble. Fragmentation bubbles are caused by spherical instabilities of the pulsating bubbles. The transfer of charge is effected through the liquid stream passing around the bubble neck at high speeds.

After almost 20 years of investigation, it became clear to researchers that gas bubbles played a significant role in cavitation and the generation of

sonoluminescence. Thus, a practical model for the motion of these bubbles was necessary to further advance the understanding of cavitation-related phenomena. To this end, Noltingk and Neppiras (1950) developed the first theory of acoustic cavitation. The theory used Rayleigh's equation as a starting point, adding to it a term for an internal pressure due to the gas inside the bubble, a variable pressure term applicable to acoustic fields as well as the effect of surface tension. They obtained an ordinary differential equation describing the radial motion of a gas bubble in terms of the pressure amplitude and frequency of the sound field as well as the equilibrium radius of the bubble. Their contribution became the first significant improvement to the theory since Rayleigh's seminal paper in 1917.

Based on their theory, Noltingk and Neppiras introduced The Hot Spot Model of sonoluminescence. This model is based on the adiabatic heating of the cavity contents. They proposed that, during cavitation, a gaseous nucleus grows slowly and isothermally by the action of the sound field, until reaching a maximum radius, R_{max} . At this point, the bubble collapses rapidly, causing the gas inside to heat up to incandescent temperatures. The maximum temperature reached inside the bubble is given by

$$T_{ad} = T_{\infty} \left(\frac{R_{max}}{R_{min}} \right)^{3(\gamma-1)}, \quad (1.1)$$

where T_{∞} is the ambient temperature, R_{min} the minimum bubble radius at the end of the collapse and γ the ratio of the specific heat capacities. The gas is then assumed to radiate like a blackbody.

After integrating the differential equation for the bubble motion for several sets of parameters, Noltingk and Neppiras found that conditions for cavitation (high pressures and temperatures both inside and outside the bubble) would only occur for nuclei less than resonance size (defined later in Chapter III). They also concluded that cavitation was restricted not only to a finite range of insonification frequencies and nucleus equilibrium sizes, but also to a fixed range of ambient and acoustic pressure amplitudes. Their theory was very successful in explaining many of the observations of SL such as the decrease in SL intensity as the frequency and ambient pressure were increased as well as the increase in SL intensity as the acoustic pressure amplitude was increased. It also explained the dependency of SL intensity on the type of gas dissolved in the liquid. Gases with larger values of γ (monatomic gases) were predicted to emit more light due to the higher temperatures reached in the interior, as can be seen from equation 1.1 and confirmed by experimental observations. The theory also showed that lower internal pressures were obtained with monatomic gases than with polyatomic gases (air and CO_2 , for example), indicating that SL was primarily the result of high temperatures rather than high pressures.

The Hot Spot model, however, failed to explain the observed difference in SL intensity among the inert gases, in which the gases with larger atomic weight generated more light. As originally postulated, the Hot Spot model did not consider the heat flow to the surroundings during the short collapse time of the cavity. In order to explain the experimental evidence, Hickling (1963) was the first to quantify this effect by considering a model of a spherical cavity containing a thermally conducting ideal gas in an incompressible liquid. Although having the

same value of γ , the heavier gases were less thermally conducting due to their smaller molecular velocities. Using this model, he successfully explained the SL intensity data for several gases.

A variation of the Hot Spot model was proposed by Jarman (1960), in which shock waves in the gas undergoing multiple reflections at the bubble wall were responsible for the light emissions. The luminescence emitted by this mechanism is thermal in origin, with small contributions due to Bremsstrahlung and recombination of ions. This model is very similar in principle to the model proposed by Noltingk and Neppiras. In addition, the conditions necessary for the formation of shock waves are not often realized, as will be shown in Chapter III.

Numerous experiments with ultrasound using different liquids and gases had provided evidence that chemical reactions occurred during cavitation and, especially, during light emission. Spectral studies of sonoluminescence in aqueous solutions of electrolytes (Gunther, 1957b) had indicated the emission of lines and bands characteristic of metal radicals superimposed on a background continuum which suggested that other sources of radiation were present in addition to the blackbody. To Griffing (1950, 1952), these observations suggested that SL was in fact a chemiluminescence. She then proposed The Chemiluminescent Model in which the high temperatures generated inside the collapsing cavity gave rise to oxidizing agents such as H_2O_2 through thermal dissociation which then dissolved in the surrounding liquid causing further reactions, some of a chemiluminescent character.

The ideas introduced by the Hot Spot and Chemiluminescent models are considered today the accepted explanation of the phenomenon of

sonoluminescence. These ideas have been further confirmed during the course of this investigation.

In 1957, Gunther (1957b) observed for the first time that SL was emitted as short flashes of light, lasting 1/10th to 1/50th of an acoustic period. If enough SL were being produced, i.e., if the acoustic intensity were sufficiently high, the flashes were seen to occur periodically, with the same frequency as that of the sound field. Several measurements of the phase of the light emission relative to the sound field have been made since its discovery. When these measurements failed to provide consistent results, researchers attempted to measure the phase of SL with respect to the bubble motion, some with relative success. Brief descriptions of these measurements are given in the next Section.

I. B. 2. The Phase of Sonoluminescence

During the late 1950's and early 1960's, several experiments were performed in an attempt to determine the relationship between the phase of SL emission and the phase of the sound field. The motivation behind these experiments was to discriminate among the different models based on the opposite predictions on the phase of the SL emission, some of which have been summarized in Table 1. As shown in this Table, the Triboluminescence, Microdischarge and Mechanochemical models all predict the light to be emitted during bubble growth. Although it was not known then, the phase of SL relative to the sound field is dependent on the experimental conditions such as the insonation frequency, the initial bubble radii and the liquid parameters. Nevertheless, the phase of SL can

be used to calculate a range of equilibrium radii of the bubbles emitting light in a particular experimental arrangement, assuming a constant acoustic pressure amplitude, as will be shown later. This fact was first used by Macleay and Holroyd (1961) in their experiment.

Table 1. The phase of SL predicted by the different models.

Sonoluminescence Model	O SL during bubble <i>growth</i> • SL during bubble <i>collapse</i>
Triboluminescence	O
Balloelectric	•
Microdischarge	O
Mechanochemical	O
Anion Discharge	•
Hot-spot	•
Chemiluminescence	•

The first attempt to measure the phase of SL relative to the sound field was made by Gunther *et al.* (1957a). They were the first to use a FMT to examine SL emissions from a standing wave field at 30 kHz. Using a cathode ray oscilloscope, they noted that SL was emitted from the pressure antinodes and that it occurred near the end of the compression phase i.e., 360° measured from the negative-going part of the sound cycle. A year later, in 1958, Wagner used a similar experimental arrangement and found, unlike Gunther *et al.* (1957a), that SL was emitted close to the sound pressure minimum (90°) in Kr-saturated water. The duration of the emission was found to depend on the ambient pressure p_{∞} , the acoustic pressure amplitude p_A and the solution temperature, but it was usually less than one tenth of an acoustic period. This disagreement prompted other researchers to

investigate the issue of the phase of SL further. Using a cylindrical transducer driven at 16.5 kHz to produce an axial pressure antinode in a stationary wave system, Jarman (1959) found that SL was emitted close to the sound pressure minimum (90°) in non-volatile liquids like water, in agreement with Wagner (1958). In volatile liquids, he found that SL was emitted near the sound pressure maximum (270°). To further complicate the picture, Golubnichii *et al.* (1970) found that emission occurred close to the beginning of the compression phase (180°), its exact location depending on the solvent.

It was not until 1961 that researchers began to use theoretical calculations of bubble motion to predict the properties of cavitation fields. An interesting experiment was performed by Macleay and Holroyd (1961), in which they used the theory of Noltingk and Neppiras (1950) to predict the phase of SL (i.e., bubble collapse) for a range of initial bubble radii. In addition, by assuming that the SL intensity was proportional to $R_{min}^2 T_{max}^4$ (where R_{min} and T_{max} are the bubble radius and the temperature respectively during SL emission) and that bubbles of all sizes were present in the liquid, they were able to deduce an SL intensity distribution as a function of the phase of SL emission. This distribution ranged from 180 to 350 degrees with a well defined peak around 270 degrees. When compared with the experimental data, agreement was surprisingly good. According to their calculations, the peak at 270° corresponded to a bubble radius of about 2 microns at 400 kHz and 1.8 bars of pressure amplitude.

It is now known that the phase of bubble collapse depends on several parameters such as the driving frequency, pressure amplitude and equilibrium bubble radius. Also, as noted by Jarman and Taylor (1970), the most likely cause of

this widespread disagreement was the use of poorly characterized hydrophones and of electronics which introduced unknown phase shifts. After calibrating all their electronics properly, Jarman and Taylor (1970) performed what were then the most careful measurements of the phase of SL. Using a cylindrical piezoelectric transducer driven at 14.4 kHz, they found that most SL flashes occurred around 360°. Using the theory of Noltingk and Neppiras, they calculated the phase to correspond to bubbles of resonance size of 220 microns. In addition, they reported results at 23 kHz with the phase of most SL flashes occurring around 290°. They also found secondary flashes usually occurring a short time after the main flash which they attributed to bubble rebounds.

The results of these experiments, as reported by the different authors, have been summarized in Table 2. The phase of SL is measured from the negative-going part of the sound cycle and R_0 is the equilibrium radius corresponding to the measured phase of SL reported by the authors. In most cases, the pressure amplitude was not known or not reported, which in part explains the large discrepancies among the different results. This also makes it impossible to explain these discrepancies in light of the new, more accurate bubble dynamics models.

Interestingly, the results of Macleay *et al.* are the most consistent with the results of the present study despite the different experimental arrangement. However, as pointed out by Jarman and Taylor (1970), the high frequency used in their experiments provided a poor resolution of phase. Further comparisons will be made in Chapter IV.

Table 2. Summary of measurements of the phase of sonoluminescence.

Experiment	Insonation frequency (kHz)	Pressure Amplitude (bars)	Host Liquid	Phase of SL (degrees)	Bubble Radius, R_0 (μm)
Gunther <i>et al.</i> (1957a)	30	--	H ₂ O	360	
Wagner (1958)	30	--	H ₂ O	90	
Macleay <i>et al.</i> (1961)	400	1.8-2.8	H ₂ O	270	0.3-3
Jarman <i>et al.</i> (1970)	14.4	2.2	H ₂ O	360	220
" "	23.3	--	H ₂ O	90	
Gaitan (1990)	21	1.1-1.3	H ₂ O	190-210	15-20
"	21-25	1.1-1.5	H ₂ O/GLY	200-250	15-20

In view of the inability to obtain a unique value of the phase of SL, researchers opted to study how SL varied with the bubble volume rather than with the acoustic pressure. The first attempt was made by Meyer and Kuttruff in 1959 who produced cavitation bubbles in ethylene glycol on the end of a nickel rod driven magnetostrictively at 25 kHz. By illuminating the bubbles with a flash tube triggered by the time-delayed SL flashes, they visually determined that the SL flashes occurred during the bubble volume minima. Because the bubbles were generated on the face of the transducer, i.e., near a solid boundary, they were most likely collapsing asymmetrically. Although the phase of these bubbles may differ from that of free, symmetrically collapsing bubbles, the experiment did provide strong evidence that SL and the bubble collapse occurred simultaneously.

In 1960 another investigator, Negishi, made the first and only attempt reported in the literature to obtain an experimental radius-time curve of

acoustically driven cavitation bubbles using a dark-field illumination technique to record the volume of the cavitation zone as a function of time. In his experiment, he projected the image of the cavitation bubbles produced by a 28 kHz ferrite transducer onto a screen, allowing some of the light to pass through a small hole and strike a PMT. Although the light recorded by the PMT was not linearly related to the volume of the cavitation bubbles, it was proportional to it. After turning the light source off, he then recorded the SL emission during cavitation. With this apparatus, Negishi (1960,1961) was able to determine the phases of the radial maxima and minima and, plotting these simultaneously with the PMT output, he demonstrated that the SL flashes coincided with the minimum bubble cloud volume. Recent studies have shown, however, that bubble clouds behave in a collective manner and their motion is, therefore, different from that of a single bubble.

Other techniques have been designed to investigate collapsing bubbles, although the bubbles were not acoustically driven. Two of these techniques utilized laser and spark-induced cavitation which allowed the position of the bubble to be predicted, as opposed to acoustic cavitation where cavitation events occurred essentially at random locations in the liquid. In both of these techniques a local portion of the liquid is heated to high temperatures very rapidly, creating a vapor cavity instantaneously. As the cavity expands, the vapor cools quickly allowing the liquid to collapse in the manner of a Rayleigh cavity (see chapter III). In addition to recording radius as a function of time, researchers have detected sonoluminescence flashes emitted during the collapse. In 1971, Buzukov and Teslenko, using a light scattering technique similar to Negishi's, obtained the

radius-time curve of a collapsing cavity produced by a single pulse from a ruby laser. When it was focused on a point in a liquid, a pulsating bubble was created from which a short flash of light was emitted in coincidence with the minimum bubble radius during the first compression of the bubble. Simultaneously with the bubble collapse, they also detected acoustic emissions in the form of shock waves.

A second experiment was performed by Benkovskii *et al.* in 1974 using spark-induced cavitation. In this case, cavities were produced in two different experiments by rapidly melting a thin tungsten wire underwater and by an electric spark produced between two electrodes immersed in a test liquid. According to Walton *et al.* (1984), Benkovskii (1974) obtained results similar to those of laser-induced cavitation using a pulse of 100 kV and $5 \cdot 10^{-8}$ sec duration applied to point-electrodes 1 mm apart. In addition to the first flash, SL flashes occurred during the second and even third collapse. Furthermore, Golubnichii *et al.* (1979) claimed that with spark-induced cavitation the SL flash does not coincide with the minimum volume of the bubble. A discrepancy of 12 μ sec was reported in water but only 1-2 μ sec in glycerine and ethylene glycol. More recently, researchers have been able to photograph laser-induced cavities with high speed cameras using conventional and holographic photography. Frame rates as high as 300,000/sec have been achieved by Lauterborn *et al.* (1986) in his study of laser-induced cavity collapse, and much has been learned from their observations.

I. B. 3. Sonoluminescence as a Probe of Acoustic Cavitation

Most of the previous studies of SL have focused on the determination of its mechanism. Unfortunately, little effort had been made, until recently, to use this phenomenon to study the physical conditions attained during cavitation. Since SL is generated by cavitation, information on the properties of the interior of the cavitation bubble during collapse can be extracted from SL, assuming that the light is emitted during the collapse. A few measurements of temperature and pressure were made by researchers, however, using the characteristics of the emitted light. Parameters such as wavelength of maximum emission and bandwidth at half the maximum intensity (FWHM) have been measured in order to determine the density (relative to the equilibrium conditions) of the emitting species. Since one of the results of the present study has been a determination of the minimum temperature and pressure inside a cavitation bubble necessary to generate SL, a review of previous measurements will be given next. It should be noted, however, that the spread of the emitted light spectrum on which some of these measurements are based may be due to the inhomogeneity of the cavitation field, as pointed out by Sehgal *et al.* (1979, 1980). Cavitation is a dynamic process, and the temperature and pressure fields inside the bubbles fluctuate within a large range of values as the bubbles expand and collapse. SL may be emitted at slightly different stages of the bubble motion, in which case the physical conditions would be different at the time of the light emission. The inhomogeneity of the cavitation field during which these measurements were made also implies that

bubbles of different sizes would be present, reflecting a variety a physical conditions.

Previous measurements of relative densities, temperatures and pressures of the gas during cavitation have been summarized in Table 3. In this Section, the experiments and the results are described briefly. A full discussion of the results will not be given until Chapter IV.

Table 3. Summary of measured relative densities, temperatures and pressures inside cavitation bubbles.

Reference	Temperature (Kelvin)	Pressure (bars)	Relative Density	R_0/R_{min}
Taylor <i>et al.</i> (1970) ($f=16$ kHz, Argon)	10,000 ^a	2,000 ^b	~60 ^c	3.9 ^d
Golubnichii <i>et al.</i> (1979) (spark-induced)	9,000 ^b	19,000 ^b	~600 ^c	30 ^c
Sehgal <i>et al.</i> (1979) ($f=459$ kHz, Argon)	2450 ^a	310 ^b	~40 ^c	3.4 ^d
Sehgal <i>et al.</i> (1980) ($f=459$ kHz) NO-	1350 ^c	---	---	5.9 ^a
($f=459$ kHz) NO ₂ -	860 ^c	---	---	9.7 ^a
Suslick <i>et al.</i> (1986b,1990) ($f=20$ kHz, Argon)	5200 ^c	500 ^b	---	---

^aBlackbody spectrum measurement. ^bCalculated using ideal gas Law. ^cMeasured (bold)

^dCalculated from the relative density. ^eCalculated using Young's (1976) equation.

The first column contains the references as well as the insonation frequency and dissolved gas used in the experiments. Note that lower temperatures are expected for higher insonation frequencies because the resonance size of the

bubbles is smaller, allowing more heat to escape into the liquid. The dissolved gas is important when using the specific heat ratio (γ) to calculate the temperatures ($\gamma=5/3=1.67$ for monatomic gases, and $7/5=1.4$ for diatomic gases). Values in bold type indicate experimental values, as opposed to values calculated based on different assumptions, as indicated by the footnotes.

Taylor and Jarman (1970) measured relative densities (with respect to equilibrium conditions) of about 60 in various argon-saturated aqueous solutions at an insonation frequency of 16 kHz. These measurements were based on the FWHM of the sodium D line. Assuming a temperature of 10,000 K - based on blackbody spectral measurements - they deduced pressures of 2,000 bars from the ideal gas Law. The determination of temperature by fitting the SL spectra to that of blackbody radiation is now believed to be incorrect due to the chemiluminescent rather than incandescent nature of the radiation, as Taylor and Jarman (1970) have pointed out. Furthermore, even an adiabatic collapse would result in temperatures of only $\sim 5,000$ K for a relative density of 60, and $\gamma=5/3$.

Golubnichii *et al.* (1979) measured the collapse ratio (R_m/R_{min} , where R_m is the maximum radius attained by the vapor cavity) of spark-induced cavitation bubbles using the shadowing technique. They obtained values of about 30 which corresponded to adiabatic temperatures of 9,000 K assuming that the vapor has cooled to room temperature when $R=R_m$. They also measured the maximum absolute density reached during the collapse by introducing NaCl into the liquid (a water-glycerine mixture) and measuring the pressure broadening of the sodium D lines. This gave $n=1.5 \cdot 10^{28} \text{ m}^{-3}$, from which they calculated a maximum pressure of 19,000 bars using the ideal gas law.

More extensive investigations were made by Sehgal *et al.* at frequencies of 459 kHz. They made independent measurements of the relative density (Sehgal *et al.* 1979) and of the temperature (Sehgal *et al.* 1980). The density measurement, like Taylor's, was made by measuring the line shifts and FWHM of potassium resonance peaks emitted by insonated aqueous solutions of alkali and halide salts saturated with argon. They obtained a value of the relative density (with respect to the density of the medium at STP) of about 40. This corresponds to a collapse ratio (R_o/R_{min}) of 3.4, where R_o and R_{min} are the initial and minimum bubble radius reached during the collapse, respectively. Using an equation derived by Young (1976) which compensates for thermal diffusion, they calculated the internal temperature to be 2450 K and, from the ideal gas law, they calculated internal pressures of 310 bars.

The measurement of temperature by Sehgal *et al.* (1980) was based on the relative distribution of SL intensities from NO- and NO₂- saturated aqueous solutions. In their experiment, intracavity temperatures of 1350 ± 50 K and 860 ± 100 K for NO and NO₂, respectively were obtained. Collapse ratios were calculated using Young's (1976) equation to be 5.9 and 9.7 respectively at an acoustic pressure amplitudes of 6.2 bars.

A recent, more precise measurement of the temperature inside cavitation bubbles has been made by Suslick *et al.* (1986a,b) using a comparative rate thermometry technique in alkane solutions of metal carbonyls. The technique consisted of measuring the reaction rates of the metal carbonyls as a function of their concentration inside the cavitation bubbles. The change in concentration was effected by increasing the bulk temperature of the solutions which increased

the vapor pressure of the metal carbonyls. The overall vapor pressure of the solutions was kept constant by using appropriate solvent mixtures. These solutions were irradiated with a collimated 20 kHz beam from an amplifying horn. Suslick *et al.* reported a maximum temperature of 5200 ± 650 K reached in the gas phase. In addition, by extrapolating their results, they found a nonzero value of the reaction rates corresponding to zero metal carbonyl concentration. Based on this finding, they concluded that a reaction zone existed in the liquid phase with an effective temperature of ~ 1900 K. The pressure amplitude used in their experiment is not specified except for a total acoustic intensity at the horn's surface of 24 W/cm^2 . For comparison, assuming plane waves in water, this intensity corresponds to about 8 bars.

L B. 4. Acoustic Cavitation and Bubble Dynamics

Cavitation has generally been classified in two types: "Transient" and "stable" (gaseous) cavitation. This classification traces its origin back when the first visual observations of cavitation activity were made (Blake, 1949; Willard, 1953), and was introduced in order to describe these observations. Transient cavitation was used to describe events that lasted only fractions of a second, usually occurring at high pressure amplitudes. These events were attributed to vapor or gas bubbles which expanded to large sizes during the negative part of the pressure cycle, after which they began to collapse. Because of the large radius attained during the expansion, their collapse was very rapid and violent, often resulting in the destruction of the bubbles. Flynn (1964) attempted to define these terms more precisely. According

to him, a transient cavity is "that which, on contraction, from some maximum size, its initial motion approximates that of a Rayleigh cavity..." whereas a stable cavity "oscillates nonlinearly about its equilibrium radius.". Flynn (1975b) further refined this definition of transient and stable cavities in terms of the equations of bubble dynamics. He defined two functions: an inertial function, IF, and a pressure function, PF, which represent the inertial and pressure forces controlling the bubble motion and which are functions of time, R_o and p_A . For transient cavities, IF is much larger than PF and therefore the motion is inertia controlled whereas the opposite is true for stable cavities. Flynn then defined a transient cavitation (dynamical) threshold in terms of the expansion ratio, R_{max}/R_o , i.e., the dynamics of bubbles pulsating with R_{max}/R_o above this threshold are controlled by IF, whereas bubbles below this threshold are controlled by PF.

After an extensive investigation of the thermal behavior of pulsating bubbles, Flynn also introduced an expansion-ratio threshold for the occurrence of thermal phenomena during cavitation (e.g. sonoluminescence). This threshold was based on the fact that small bubbles tend to dissipate the internal heat generated during collapse (isothermal motion), whereas large bubbles behave more adiabatically, generating high temperatures in their interior. From his calculations, Flynn concluded that small bubbles ($< 5 \mu\text{m}$) reach the dynamical (transient cavitation) threshold before exhibiting sonoluminescence. Large bubbles ($> 5 \mu\text{m}$), on the other hand, are able to generate high internal temperatures and therefore, exhibit sonoluminescence before becoming a transient. It should be noted here that becoming "transient" does not necessarily mean that the cavity is not stable. However, inertia-dominated cavities tend to collapse very rapidly, promoting

surface instabilities which often cause breakup. Therefore, when the dynamical threshold is greatly exceeded, cavities are, in general, not expected to survive for more than a few of cycles. Flynn's model of cavitation bubbles will be used to explain some of the observations made in this study. It will be shown that observations of the thresholds for sonoluminescence and transient bubble motion agree with this model.

As mentioned previously, several descriptions of the behavior of bubbles in ultrasonically-induced cavitation fields were made during the early years of cavitation research (Blake, 1949; Willard, 1953; Neppiras *et al.*, 1969). Neppiras (1980), in his thorough review of acoustic cavitation, describes several types of cyclic cavitation processes. These observations are presented in this Section as an introduction to the study of long-term periodic behavior of the phase of the light emitted by cavitation bubbles. It should be noted that Neppiras did not cite any references when describing these observations and it was, therefore, not possible to obtain the original works. Some of these observations are:

- i. The gaseous cavitation cycle occurs when a bubble is made to grow by rectified diffusion (see Chapter III), eventually reaching the transient cavitation threshold (Flynn, 1964). Then, the bubble immediately expands, implodes and disintegrates. The residual fragments may be either too small and dissolve completely or start growing again by coalescence and rectified diffusion. This process repeats itself, although not very regularly, since the bubbles are variable in size. It can be observed in high-speed photography of cavitation in gassy liquids by examining successive frames.

ii. The degassing cycle consists of bubbles growing, as in the case of the gaseous cavitation cycle, by rectified diffusion in such a way that the conditions for complete collapse never occur. Eventually the bubble will become large enough to float to the surface, gradually causing the solution to become undersaturated. This degassing can only occur within a restricted range of R_0 and p_A and, according to Neppiras (1980), its rate can be maximized by choosing appropriate treatment conditions related to the bubble-size distribution.

iii. The resonance bubble cycle with emission of microbubbles. At sufficiently high frequencies, bubbles reach their resonance size before separating out under gravity. Bubbles of resonance size are highly likely to develop instabilities, exciting surface modes of vibration. The strong surface vibrations are parametrically excited at half the driving frequency and are strongly coupled to the radial pulsations. In an intense field, the surface waves may grow to large amplitudes and "throw off" microbubbles from the crests. This can occur very rapidly, the parent bubble apparently exploding, which may explain the "disappearing bubbles" reported by Nyborg and Hughes (1967). These microbubbles are usually all equal in size, with radii near $\lambda_s/4$ where λ_s is the wavelength of the surface oscillation (Neppiras, 1980).

I. C. Recapitulation and General Overview of the Dissertation

The Hot Spot and Chemiluminescent models of the mechanism of light production during cavitation (known as sonoluminescence) can explain the majority of the experimental evidence. In addition, previous studies of acoustic

cavitation have provided many qualitative and semi-quantitative observations. In particular, fairly convincing data exist which demonstrate the temporal coincidence of the sonoluminescence emission and the collapse of bubbles. Previous studies of cavitation, however, were limited to a general (statistical average) description of the bubble field due to the inability to specify the bubble-size distribution at any particular point in space or time. In a cavitation field, these cavities or "nuclei" are constantly changing. For this reason, the correlation of the light emission with the motion of a single bubble has not been possible. The only correlation that has been made is between the collective motion of the bubble field and the light emission (SL). In addition, several observations of cyclic cavitation processes indicate that cavitation bubbles may break up and coalesce in a periodic manner. This dissertation is mostly a collection of experiments using single- and multiple-bubble cavitation fields designed to advance our understanding of acoustic cavitation and sonoluminescence.

The information contained in this dissertation has been organized in the following manner. Chapter II contains a detailed description of the apparatus and the experimental procedures used to acquire the data, including the calibration methods.

Chapter III describes briefly the different mathematical models used to describe the motion of acoustically driven bubbles. Three formulations of radial pulsations of bubbles are presented: Keller-Miksis' (1980) with the polytropic approximation, Prosperetti's (1986) and Flynn's (1975a) formulations. Some basic concepts of nonlinear bubble dynamics are introduced which are necessary to

understand the results of the experiments. In addition, brief descriptions of the equations describing shape oscillations of bubbles as well as the phenomenon of rectified diffusion are presented.

In Chapter IV, the results of the different experiments are presented and discussed including the observations of the stabilization process for a single bubble. Rather than following the chronological order of the experiments, data from the single-bubble experiments are presented first to make the interpretation of the multi-bubble experimental results easier. Single-bubble data include the radius-time curves and the phase of SL emission. Then, a study of the phase of SL in multi-bubble cavitation fields is presented.

Finally, a summary of the dissertation, the conclusions drawn from the experiments and some topics for future study are given in Chapter V.

Chapter II

Apparatus and Experimental Procedure

II. A. Introduction

In this Chapter, the experimental method used to study cavitation bubbles is described. The experiment is divided in two parts: 1) the measurement of the radius-time curve of a single cavitation bubble was obtained and 2) the measurement of the phase of the sonoluminescence (SL) emitted by single- and multi-bubble cavitation relative to the phase of the pressure field as well as relative to the bubble motion.

In both experiments, a levitation cell was used to excite a stationary wave sound field in several glycerine/water mixtures. Using this apparatus, single- and multibubble cavitation was generated at pressure amplitudes in the range $1.0 < p_A < 1.5$ bars. Several parameters associated with cavitation were measured including the radial bubble pulsation amplitude, the phase of the bubble collapse, and the number of rebounds at a fixed pressure amplitude, p_A . In addition, the phase of SL was monitored for long periods of time in order to study the behavior of bubbles in cavitation fields.

In the first part of the experiment, a single bubble was levitated at a fixed position in the levitation cell, while pulsating radially at large amplitudes. Light from an Ar-Ion laser was scattered off the bubble and detected with a photodiode. The amplitude of the scattered light, modulated by the large radial pulsations, was

converted to radius via an experimental transfer curve in which the bubble radius was related to the scattered intensity. By this method, experimental radius-time (R-t) curves of bubbles pulsating periodically (i.e., in a steady state) were obtained. The radial pulsation amplitude, the timing of the bubble collapse, and the number of rebounds were measured from the R-t curves.

In the second part of the experiment, SL from a single bubble was detected with a photomultiplier tube in a light-tight enclosure. Then, by using an intermediate reference, the emission of SL was correlated in time with the first part of the experiment in order to obtain the phase of SL emission relative to the bubble motion. It was determined that SL was emitted during the collapse of the bubble. Finally, the phase of SL relative to the sound field in single- and multibubble cavitation was monitored for long periods of time (thousands of acoustic cycles) in order to study the behavior of bubbles in cavitation fields. This phase was measured with a time-to-amplitude converter and an analog-to-digital data acquisition system based on a microcomputer.

II. B. Acoustic Levitation Apparatus

1. Levitation Cells

The basic apparatus used in the experiments consists of two levitation cells, one cylindrical and one rectangular, and their driving and controlling electronics. This Section describes these components in some detail.

A levitation cell is a container filled with liquid in which a stationary acoustic wave is excited. The radiation force (Crum, 1970) exerted on the gas bubble by the

stationary wave is used to counteract the hydrostatic or buoyant force, enabling the bubble to remain suspended in the liquid indefinitely, effectively removed from all boundaries. The cylindrical cell, shown in Fig. 1, is made from two 7.5 cm (3.0 in) O.D. concentric piezoelectric cylindrical transducers joined together by a glass cylinder of approximately equal dimensions. These cylindrical transducers were poled to be driven primarily in the thickness mode. A thin Plexiglass disc was glued to the bottom of the cell, providing a nearly free boundary at the frequencies used in all the experiments. All the components were glued with a silicon-base gel to ensure a water-tight enclosure while keeping all elements mechanically decoupled. A pill-shaped transducer (0.5 cm dia. x 0.3 cm thick) was attached to the outside of the glass in order to monitor the pressure amplitude and the phase of the acoustic field in the cell.

In addition to the cylindrical cell, a rectangular levitation cell like the one shown in Fig. 2 was built in order to photograph and observe the levitated bubbles more clearly. These cells were constructed from one piece rectangular Pyrex containers (Vitro Dynamics) 4.5 x 4.5, 5.1 x 5.1 and 6.0 x 6.0 cm² cross section and 12.0 cm long with the top end open. A piezoelectric cylindrical transducer 5 cm in diameter was glued to the bottom of each container with extra-rigid epoxy (Torr Seal®) to provide good mechanical coupling. As with the cylindrical cell, a side pill transducer was attached to a side wall in order to provide a non-invasive way to monitor the acoustic pressure in the liquid. Although this type of cell was not as stable in frequency and amplitude as the cylindrical type, it provided flat optical surfaces through which gas bubbles could be observed with excellent clarity.

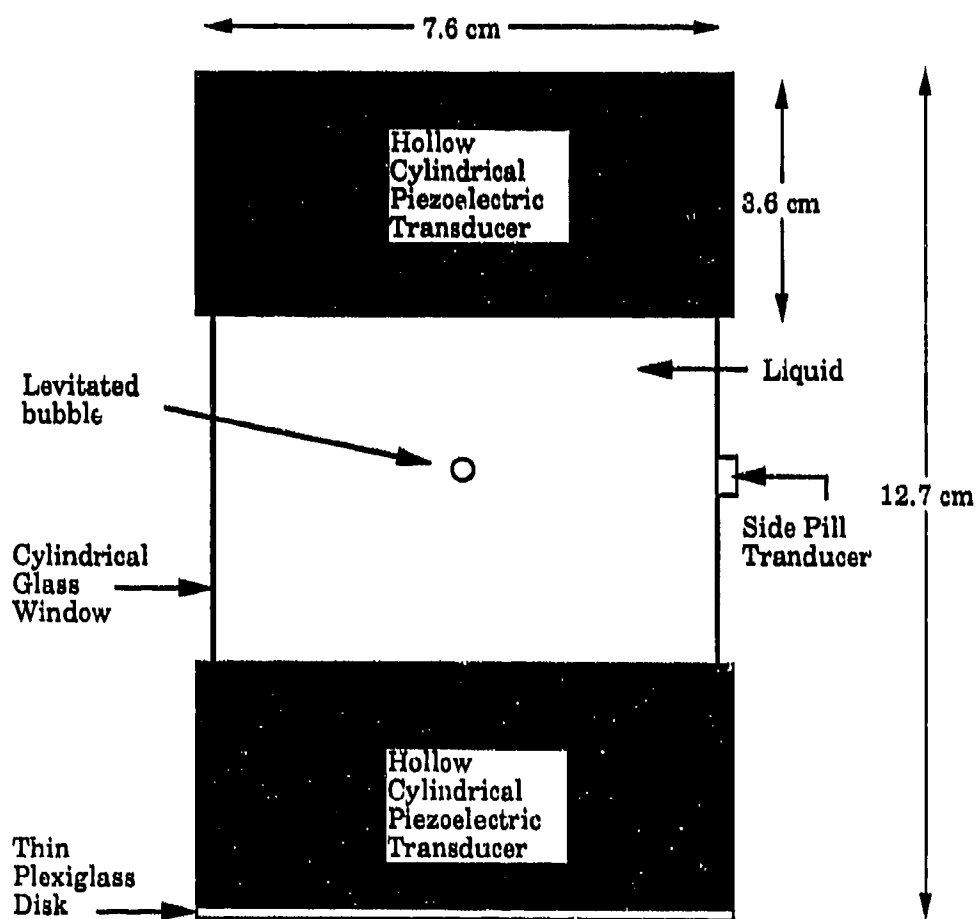


Figure 1. Schematic drawing of cylindrical acoustic levitation cell with bubble.

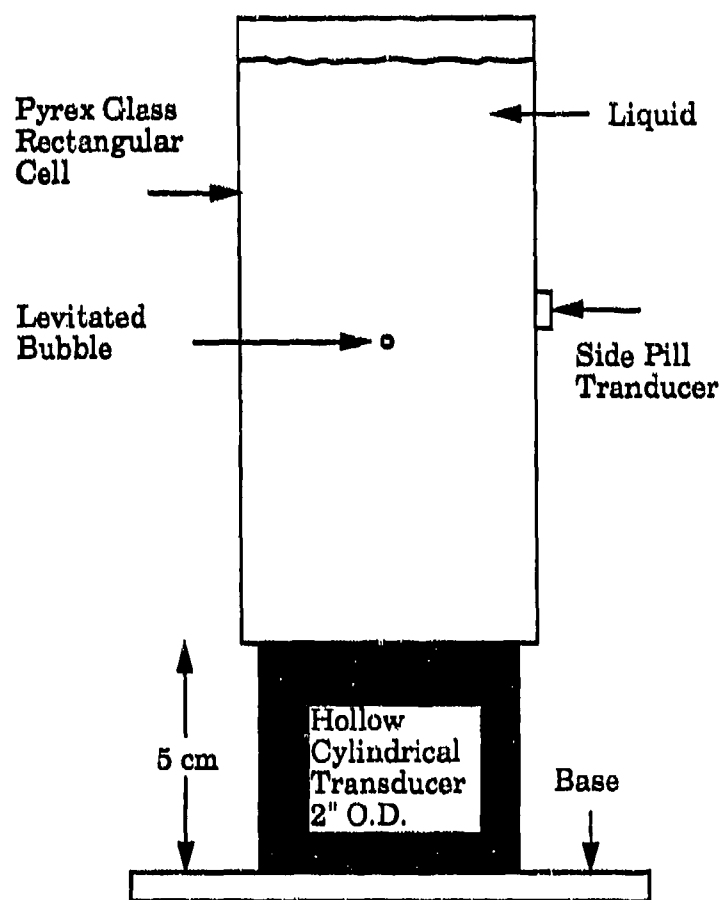


Figure 2. Schematic of rectangular acoustic levitation cell.

For each experiment, the cell in use was filled with one of five different water/glycerine mixtures and driven by a 75 watt Krohn-Hite amplifier (model 7500) connected to the cell by an impedance matching coil with an inductance of approximately 4 mH. The amplifier was operated by a Hewlett-Packard 3312A function generator which was controlled by an Isaac II process control and data acquisition system. When driven at resonance, the levitation cells were capable of generating up to 4 atmospheres of peak pressure amplitude at the antinodes. The cell was always driven at resonance during the experiments, usually between 20 to 25 kHz, depending on the mixture used. The particular stationary wave excited was determined by the driving frequency. In all of the experiments (using the cylindrical cell), a (r, θ, z) mode of $(1, 0, 1)$ was used. The $\theta = 0$ means the wave is symmetric about the cylindrical axis, while $r = z = 1$ means a single antinode exists in the \hat{r} and \hat{z} directions. In reality, however, an additional pressure maximum was present near the top and bottom of the cell due to the less-than-ideal-pressure-release boundaries. This, however, did not pose any experimental problems, and all calibrations were done using the measured profiles rather than the theoretical ones. The cell in use was mounted on a two degree of freedom translation stage, providing 0.000393 cm (0.001") resolution and 2.5 cm (1") travel in the x and z direction with the use of manual micrometer drives. This arrangement allowed the positioning of the bubble anywhere in the plane perpendicular to the Ar-I laser, described in Section D of this chapter. The entire apparatus, including the necessary optics with the exception of the laser, was mounted on a 45 x 36 cm (1.5' x 3') optical table.

In order to keep the side pill transducer calibrated, the system had to be maintained to within 2 hertz of resonance. In addition, some of the experiments required changes in pressure amplitude to be made quickly, accurately and repetitively. For this purpose, the amplitude and frequency of the function generator were controlled via the amplitude modulation (AM) and voltage controlled oscillator (VCO) analog inputs. An Apple IIe computer with an Isaac II data acquisition and control system was used which enabled the operator to control the system from a terminal keyboard. This data acquisition system also served to provide a continuous reading of the acoustic pressure amplitude during the experiments. This was done by reading the RMS voltage from a Fluke 8600A digital multimeter to which the pill transducer was connected. This voltage was read via a GPIB interface by the Apple IIe computer, converted to units of pressure and displayed on the CRT screen. Because the system had to be recalibrated often, this feature provided an immediate value of the pressure in order to efficiently check the system between calibrations.

II. B. 2. Rise-time Measuring Apparatus

One of the methods used to determine the equilibrium size of the bubbles was a rise-time technique described in the pressure calibration Section. This technique required measuring the terminal rise velocity of the bubble when the sound field was turned off. Thus, the time needed for the bubbles to rise through a known distance was measured and recorded. The apparatus used to accomplish this will be described in the next paragraph.

Because the bubble sizes used were as small as $10\text{ }\mu\text{m}$, travel distances as small as $100\text{ }\mu\text{m}$ or less had to be measured. Thus, a calibrated Gaertner filar micrometer microscope model M110A was used. The rise-time was measured with a digital timer which was activated by the same push-button switch used to turn the sound field on and off. A schematic diagram of this circuit is shown in Fig. 3. This circuit worked as follows: when the switch was pressed, the counter was started and the sound field was turned off, allowing the bubble to rise freely. When the bubble had risen through a predetermined distance, the switch was released, turning the counter off and the sound field back on and bringing the bubble back into the center of the cell. This apparatus was used in several of the experiments described in this chapter when bubble sizes had to be measured.

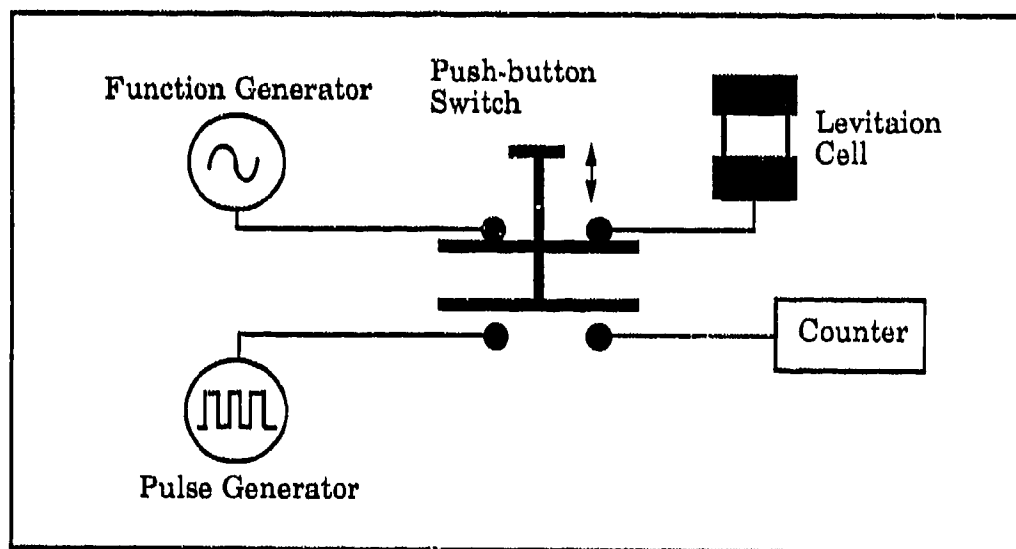


Figure 3. Schematic diagram of risetime measurement apparatus.

When the Pyrex rectangular cell was used, the bubble radius was also measured with the filar micrometer microscope directly. The filar micrometer used with a 20X magnification had a resolution of approximately $\pm 5 \mu\text{m}$. This method provided an estimate of the bubble radius which allowed us to check on the rise-time results if thermal currents were suspected to be present.

II. B. 3. Hydrophones

In order to calibrate the side pill transducers, two techniques were employed which utilized two different hydrophones. Because these hydrophones could not be used at pressures amplitudes above 0.5 bars without the risk of cavitation damage, the pill transducers had to be calibrated at relatively low amplitudes. Extrapolated values were then used during the experiments. This Section will describe these hydrophones in more detail.

The first and most often used device was a needle shaped hydrophone built by the author which will be referred to as NDL1. A cross section of this device is shown in Fig. 4. Due to its small dimensions, it affected the sound field in the cell very little as can be seen in Fig. 5. This figure is a plot of the side pill response *vs* the depth of the hydrophone in the cell measured in cm from the bottom of the cell. This hydrophone was built using a small cylindrical piezoelectric transducer mounted on two concentric steel needles which provided a rigid support. The center needle was connected to the inside pole while the outside needle was connected to the outside pole of the transducer. This geometry provided good electrical shielding as well as ease of construction, although it was possible that

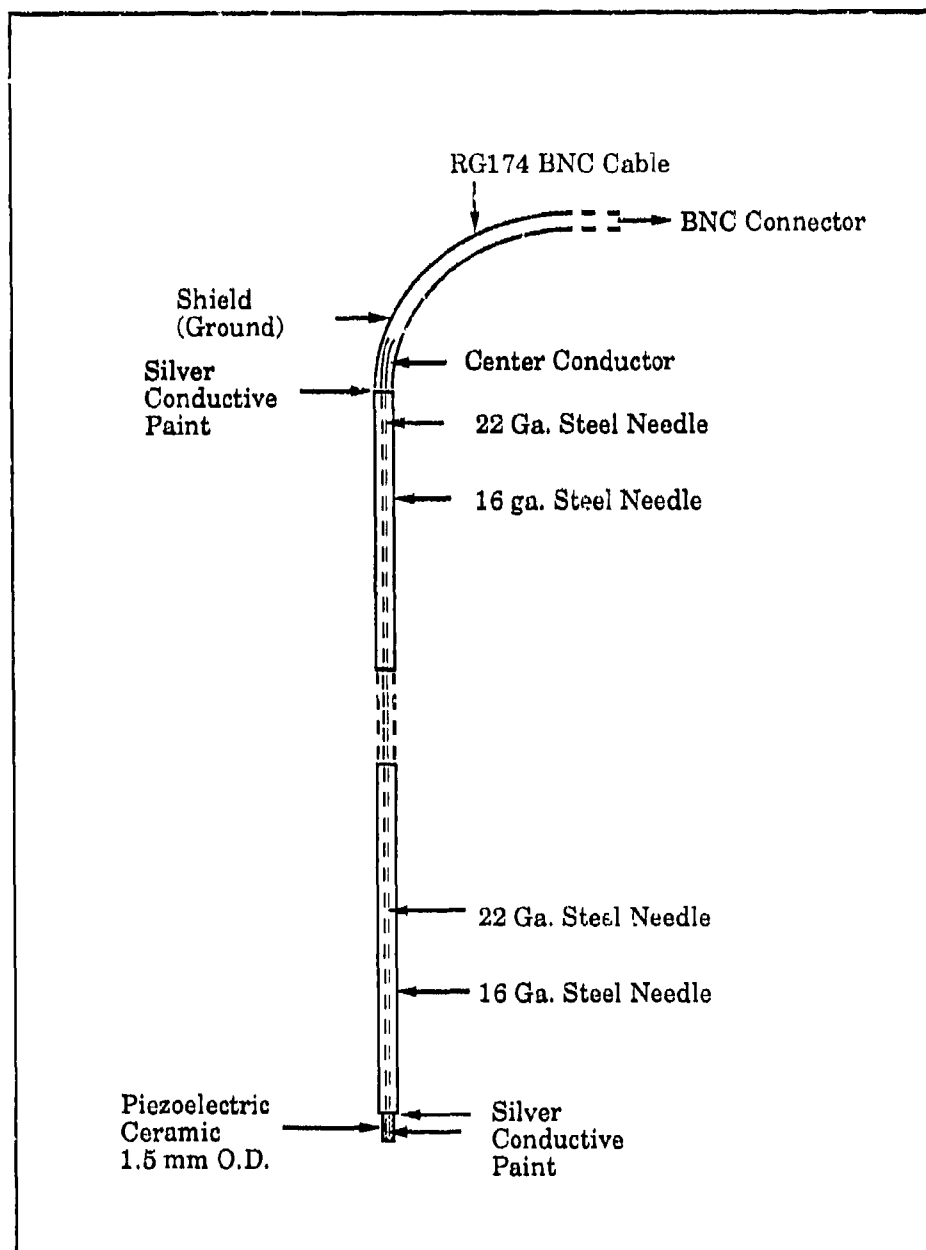


Figure 4. Schematic drawing of needle hydrophone (NDL1)

some of the acoustic energy could be coupled to the sensitive element through the needles. This coupling was verified to have no significant effect on the linearity of the hydrophone, as can be seen in Fig. 6, where the hydrophone response has been plotted vs the pill transducer response. The linearity of the pill transducer as a function of the voltage to the driving cylindrical transducers was also verified.

The active element is a piezoelectric transducer 2 mm in length and 1.5 mm O.D. Its estimated resonance frequency was in the MHz range providing a flat response in the frequency range of interest, i.e. 20-25 kHz. Silver conductive paint was used to provide electrical coupling between the steel needles and the PZT element. This sensitive element was left unprotected in order to increase the sensitivity of the hydrophone. At the other end, the center lead of an RG174 coaxial cable was connected to the inside needle and the shield lead to the outside needle, using conductive paint to provide good electrical contact. After drying, the connection was covered with Torr Seal[®] epoxy resin, providing rigidity to the joint in order to avoid breaking the electrical contact from repeated bending.

The second hydrophone used for calibration was a B&K model 8103 factory-calibrated hydrophone. Because of its large size it could only be used in much larger containers, as described in the next Section. The response of this hydrophone was flat up to 20 kHz according to the specifications (see Fig. A1 in Appendix A). It was used in conjunction with a model B&K 2635 charge amplifier.

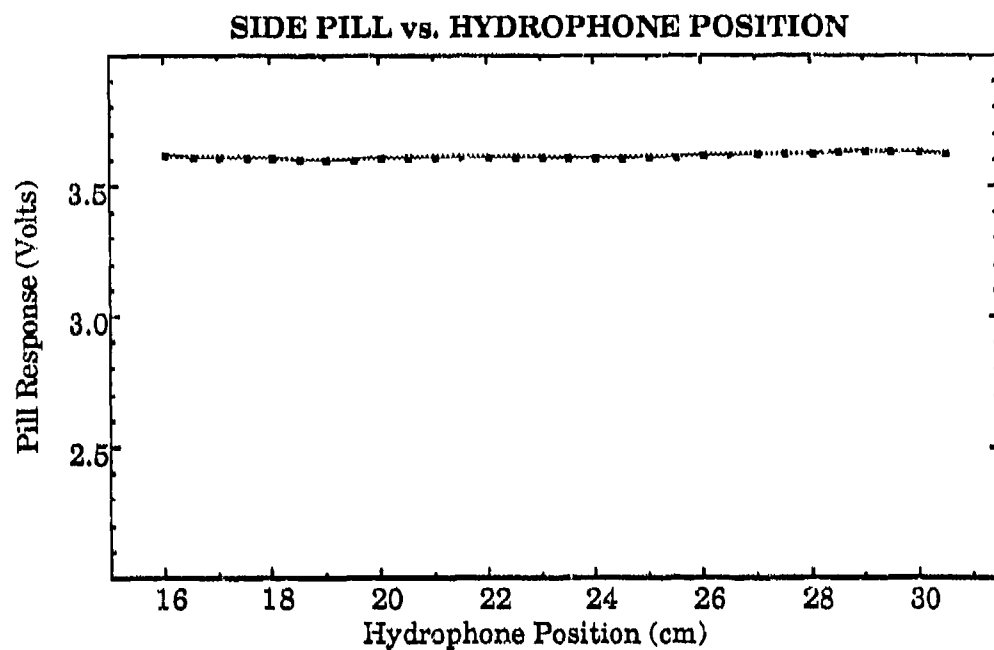


Fig. 5. Plot of side pill transducer response vs. the depth of the needle hydrophone.

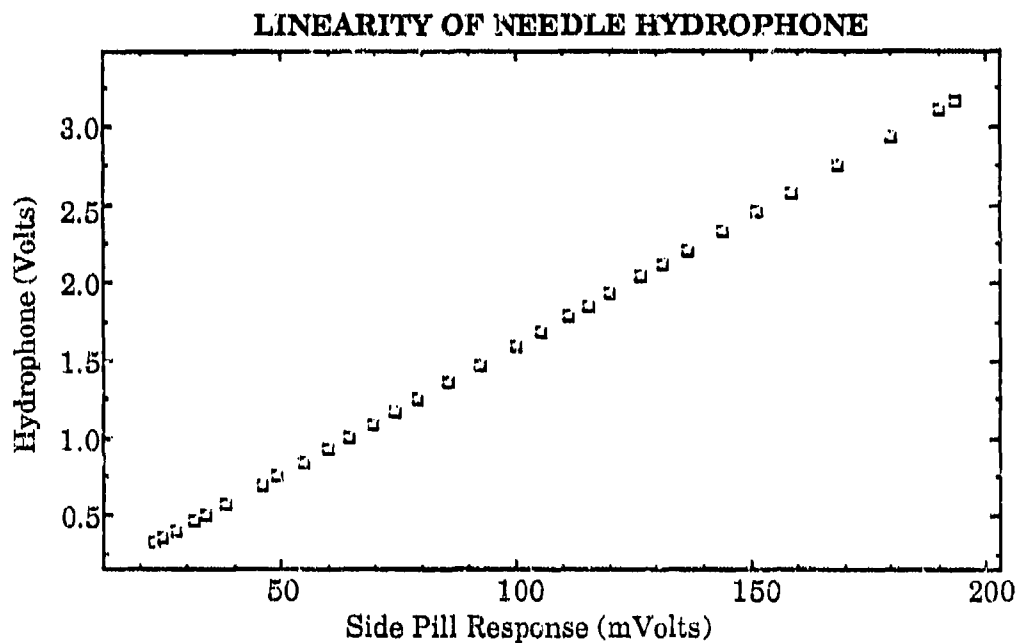


Fig. 6. Plot of needle hydrophone response vs. side pill transducer.

II. C. Calibration of Acoustic Levitation Apparatus

1. Absolute Sound Field Pressure

Two different methods for determining the absolute acoustic pressure in the levitation cells were used. One method gave a direct calibration of the pill transducer. However, the response of the pill was dependent on the liquid used and a more reliable reference was therefore required. For this purpose, the needle hydrophone NDL1 was used. The second method consisted of calibrating the needle hydrophone directly using a commercially available calibrated reference (B&K 8103). Thus, the purpose of this procedure was to obtain a calibration constant for the needle hydrophone (NDL1) which was then used for all the experiments by calibrating the pill transducer separately for each liquid mixture. In all instances, the output of the side pill transducer was used to record the acoustic pressure amplitude after being calibrated at the beginning of each experiment. The methods used to calibrate NDL1 will be described in this Section.

Method A: Levitation Technique. This technique was first suggested by Gould (1968), and it consists of measuring the equilibrium radius and position above the antinode of a bubble levitated at a given pressure amplitude. Using the fact that at equilibrium the buoyancy and radiation pressure forces on a levitated bubble are equal in magnitude and opposite in direction, a linear approximation for the pressure amplitude in terms of the bubble radius and its vertical position z relative to the pressure node in the sound field can be derived. This expression is given by (Crum, 1970)

$$p\lambda = \frac{2\rho_l g \lambda_s p_\infty \left(1 - \frac{\omega^2}{\omega_b^2}\right)}{\pi \sin\left(\frac{4\pi z}{\lambda_s}\right)}, \quad (2.1)$$

where ρ_l is the liquid density, g is the acceleration of gravity, λ_s is the wavelength of the stationary sound field along the cylindrical axis, p_∞ is the pressure at infinity (ambient pressure), ω is the driving angular frequency and ω_b is the linear resonance frequency of the bubble which is a function of its radius. A linearized expression for the radial response of the bubble to the applied sound field has been used to derive this equation.

The position of the levitated bubble with respect to the stationary wave pressure antinode was determined by measuring the acoustic pressure profile at the cell's vertical axis. Such a profile is shown in Fig. 7 for 42% by weight water/glycerine mixture at 22.6 kHz measured by the needle hydrophone. The accuracy of this profile is critical in order to obtain good calibration results, and it was one of the main reasons for building the hydrophone. The profile was obtained by immersing the hydrophone in the liquid until the sensitive element was close to the antinode. Once there, the micrometer of the vertical translation stage was used to move the cell up and down until the region of interest was mapped. The wavelength λ_s of the stationary sound field was also obtained from these data.

During the calibration, the levitated bubble was observed through the Gaertner microscope. The fixed horizontal cross hair was chosen as the reference point. When the bubble and the cross hairs were seen to coincide, the position was

PRESSURE PROFILE OF LEVITATION CELL

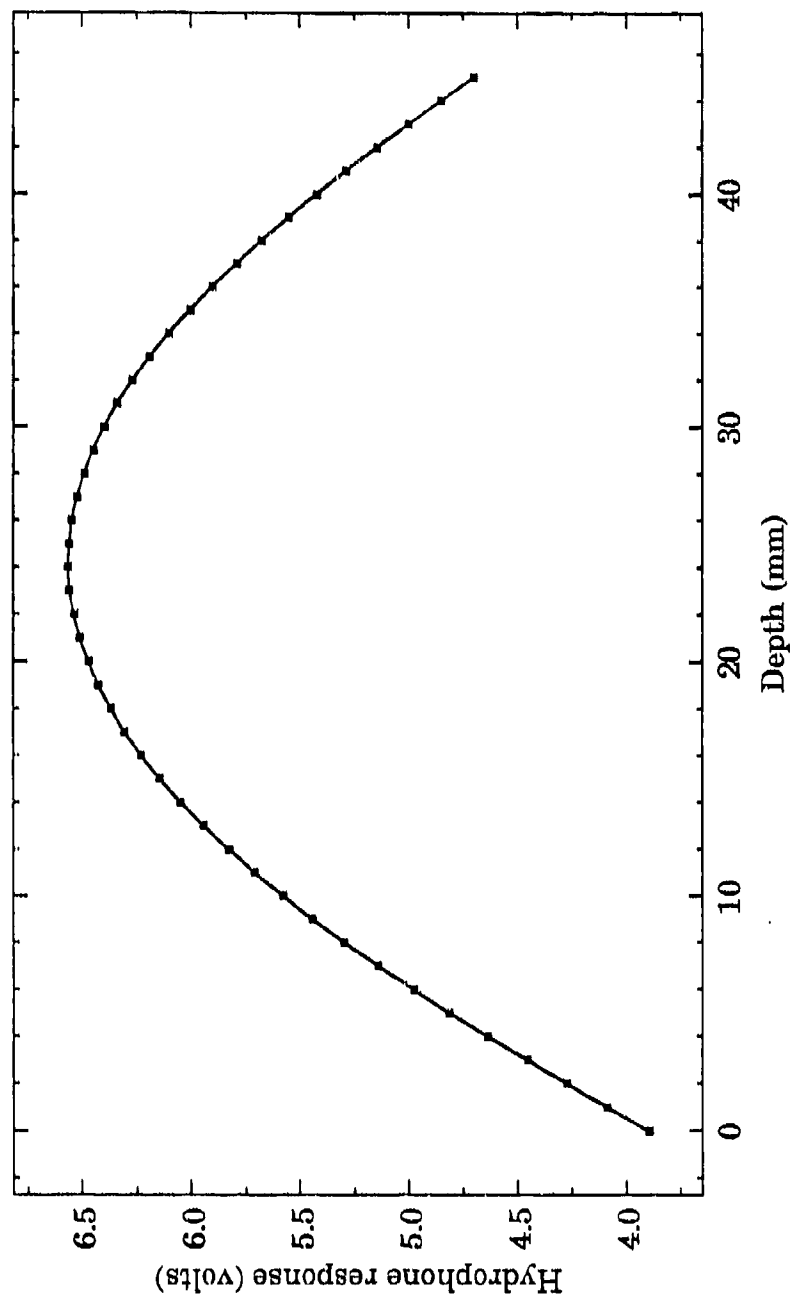


Figure 7. Pressure profile of cylindrical levitation cell as a function of depth.

recorded from the micrometer reading. If the bubble changed its position, the cell was moved until the bubble and the cross hairs were aligned again, and the new position was recorded. The position had to be determined within a few seconds of the rise-time measurement before the bubble had changed in size significantly.

The equilibrium radius of the levitated bubble was determined by measuring its terminal rise velocity when the sound field was turned off. Using the apparatus described in Section II.B.2, the procedure was as follows: the levitated bubble was positioned at the top mark as seen through the Gaertner microscope. When the switch was pressed, the sound field was turned off, starting the counter and allowing the bubble to float upwards. The bubble could be seen through the microscope to move downwards since the image is inverted. When it reached the bottom mark the switch was released, turning the sound field back on and stopping the counter. The terminal velocity of the levitated bubble could then be calculated from the time interval and distance travelled.

The expression for the equilibrium radius can be derived as follows: when terminal velocity is reached i.e., the acceleration is equal to zero, the buoyant force and the viscous drag force on the bubble are equal in magnitude and opposite in direction i.e.,

$$F_B = -F_D$$

or

$$\frac{4}{3}\pi R^3 \rho g = \frac{1}{2}\pi C_D \rho u^2 R^2, \quad (2.2)$$

where R is the bubble radius, u is the terminal rise velocity, and C_D is the drag coefficient given by

$$C_D = \frac{24 \chi}{R_e} = \frac{12\mu \chi}{R\rho u}, \quad (2.3)$$

where R_e is the Reynolds number and χ is an empirical correction factor commonly expressed in terms of the Reynolds number.

For smaller bubbles (less than 40 μm in radius), in which case $\chi = 1$, the drag law for a rigid sphere (Stokes's law) can be used. For larger bubbles, more accurate expressions must be used to account for the deformation of the bubble such as the Langmuir-Blodgett or Schiller-Nauman empirical drag laws. The expression for the radius in terms of the terminal rise velocity is given by

$$R = \frac{9}{2} \frac{\mu u \chi}{\rho g}. \quad (2.4)$$

The correction factor χ , according to Schiller and Nauman, is given by

$$\chi = 1 + 0.15R_e^{0.687}, \quad (2.5)$$

and according to Langmuir and Blodgett by

$$\chi = 1 + 0.197R_e^{0.63} + 2.6 \times 10^{-4} R_e^{1.38}. \quad (2.6)$$

Recently, Crum *et al.* (1984) have found discrepancies between the theory and experiment of the bubble response when it is driven near its harmonics, i.e., integer multiples of the bubble's resonance frequency. Since equation (2.1) was derived using a linearized expression for the bubble response, Crum's observations give this method of calibration a certain degree of unreliability. In order to eliminate this uncertainty, a restriction on the size of the bubbles used during the calibration was imposed. This modification was suggested by Prosperetti (1990). Assuming small pulsation amplitudes, it can be shown that bubbles below about 40 μm pulsate with an amplitude which is independent of their size. The dependence of the pressure amplitude at the antinode, p_A , on the bubble radius is implicit in the term $(\omega/\omega_0)^2$ in equation (2.1). If the bubble is small, however, this term is very small and can be ignored, making the expression independent of the bubble radius. It was verified experimentally that the position in the cell of bubbles between 20 and 40 μm was indeed independent of the radius. Bubbles below 20 μm , however, did not behave predictably, possibly due to the presence of foreign material which is known to accumulate at the gas-liquid interface or to thermal currents which could easily affect the rise-time measurements of small bubbles. Thus, several bubbles between 20 μm and 40 μm were used to perform the calibration. This method gave a much smaller standard deviation (over the repeated measurements), as expected, and was therefore considered more reliable. Since bubbles are small, we can use Stokes's law (Eq. 2.3 with $\chi = 1$) to approximate the viscous drag. Using this approximation, and the ratio $(\omega/\omega_0)^2 \approx 0$, the expression for the pressure amplitude simplifies to

$$p\lambda \approx \frac{2 \rho_l g \lambda_z p_m}{\pi \sin\left(\frac{4\pi z}{\lambda_z}\right)}, \quad (2.7)$$

which is a function of the position z only. The calibration was made by levitating a number of bubbles (one at a time) at a range of pressure amplitudes and recording their positions. The corresponding pressures were obtained using equation (2.7) with λ_z obtained from the pressure profile for GLY42. The statistical mean and the standard deviation were calculated. Since it was not possible to introduce the needle hydrophone (NDL1) in the cell while the bubbles were levitated, this calibration was made with the pill transducer. NDL1 was then calibrated in the same liquid with no bubbles present.

Method B: Substitution Method. In this method, a factory-calibrated B&K 8103 hydrophone was used to calibrate NDL1. It consisted of inserting both the B&K and NDL1 hydrophones at the same time and side by side in a RF shielded 10 gallon fish tank filled with water. A stationary acoustic wave was set up in the tank by a 7.6 cm (3") O.D. cylindrical piezoelectric transducer attached to the glass bottom. The transducer was glued to the tank with silicon gel, and it was driven at around 21 kHz, the exact frequency depending on the water level. This method will be discussed in the next paragraph.

In order to ensure that the two hydrophones were sensing the same pressure, they were positioned near an antinode and their voltage output maximized. If the sensitive element of NDL1 was within 2 mm of the acoustic center of the B&K hydrophone (see Appendix Fig. A.1), then the calibration was performed. Several

antinodes were used during this calibration, and the results averaged with equal weights.

These two calibration methods were made in order to account for any systematic errors inherent to any particular method. The sensitivity of the needle hydrophone was measured by method A to be 19.9 ± 0.6 and by method B to be 19.6 ± 0.8 volts/bar. The final calibration constant was determined statistically, giving the result of each method an equal weight. Its value was calculated to be 19.8 ± 0.7 volts/bar corresponding to a standard deviation of about 4%. This value was used to recalibrate the pill transducer for each experiment. As expected, the calibration constant for the pill transducer changed for different liquid mixtures and/or liquid levels. It was thus necessary to recalibrate it often.

II. C. 2. Phase of the Sound Field Pressure

The phase of the pill transducer relative to the acoustic pressure was determined by direct comparison with the needle (NDL1) hydrophone positioned at the pressure antinode. Because the resonance frequency of the sensitive element of NDL1 was in the MHz range, it could be assumed that it responded in phase with the 20-25 kHz sound field. There still remained an uncertainty of 180° in the phase due to the unknown polarity of the PZT element. This uncertainty was resolved in two ways: 1) By applying a static pressure to the sensitive element and observing the polarity of the voltage output, and 2) By direct comparison with the phase calibrated B&K hydrophone.

The phase of the pill was measured using the two zero-crossing circuits described in Section II.F. A schematic diagram of one of these circuits can be seen as part of the circuit shown in Fig. 16. Each of these circuits produced periodic narrow pulses at the zero crossing of each signal. These pulses were then displayed on the digital oscilloscope and the phase difference measured and recorded. The procedure was repeated several times during each experiment since the phase of the pill transducer relative to the acoustic pressure was found to depend strongly on the driving frequency and liquid level. It was found, however, that as long as the system was kept at resonance, the phase of the pill remained constant to within 2-3 degrees even if the water level changed slightly. For this reason, the frequency control system was designed such that the frequency could be specified with a precision of ± 1 Hz.

II. D. Light Scattering Experiment

1. Apparatus

In order to record the radius of the bubble as a function of time, linearly polarized light from a laser was scattered from the bubble. The scattered light intensity is modulated by the bubble pulsations and, if measured at the appropriate angle, this intensity can be converted to an absolute bubble radius. This technique was developed by Hansen (1984) to size air bubbles under similar conditions and has been used to record small amplitude radial and nonradial bubble oscillations by Holt (1988) and Horsburgh (1990). A more detailed description of this technique and of the apparatus can be found in these references.

A schematic diagram of the apparatus is shown in Fig. 8, the shaded blocks indicating the support equipment. The light source used was a 3-watt water-cooled Lexel model 95 argon-ion laser operated in the TEM₀₀ mode. An optical rotating polarizer was placed in front of the laser which provided a 1200:1 linear polarization ratio. The laser was used at 0.8 watt power at a wavelength of 488 nm. This power setting was determined empirically by using the maximum power possible before the energy absorbed by the bubble was large enough to affect its motion. The scattered light was detected by an Oriel 7182-1 photovoltaic silicon photodiode with integral preamplifier. This photodiode had a detection area of 100 mm² and a 488 nm laser line transmission filter in order to reduce background noise. The output of this diode was connected to both a DC voltmeter which provided information on the temporal average radius of the bubble and a Stanford Research Systems model SR560 low-noise preamplifier in order to further increase the signal-to-noise ratio. The amplifier was set to a gain of 40 dB and was connected to an AC-coupled LeCroy 9400 digital oscilloscope which recorded the scattered light intensity of the pulsating bubble as a function time. A National Instruments GPIB interface was used to transfer the data from the oscilloscope to a Macintosh II computer for analysis and graphical output.

II. D. 2. Calibration

a. Absolute Bubble Radius

The technique used to calibrate the output of the photodetectors was first developed by Hansen (1984) and later refined by Holt (1988) and Horsburgh (1990)

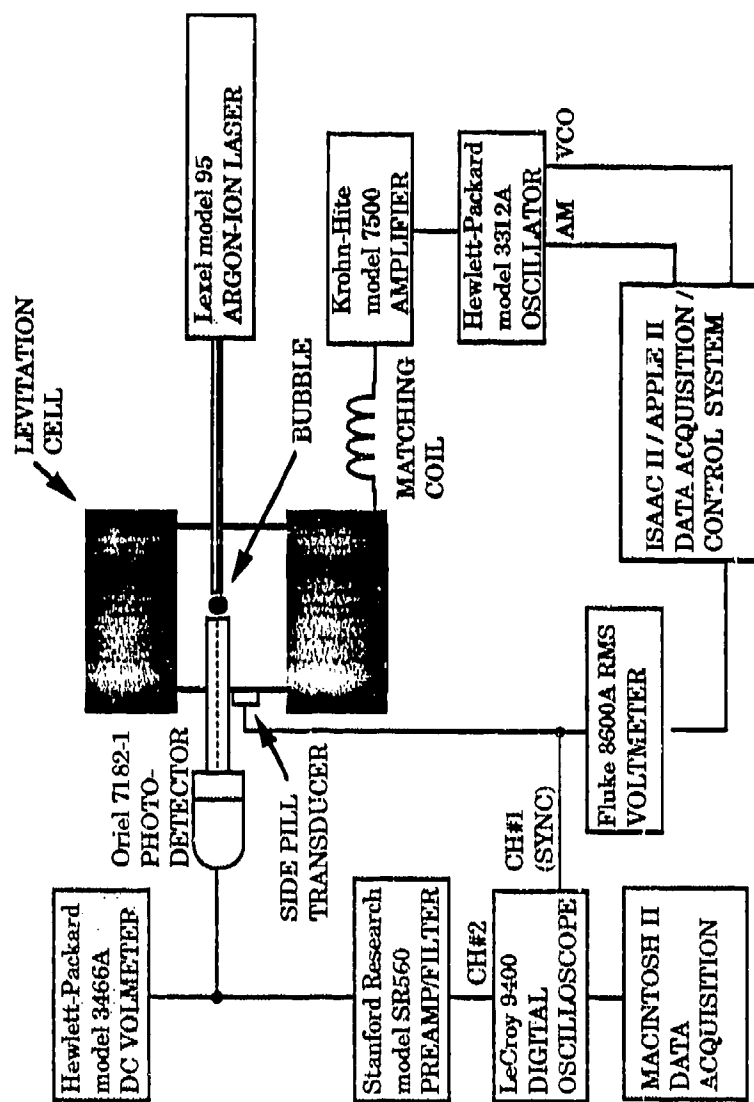


Figure 8. Schematic diagram of experimental apparatus used to record the scattered light intensity as a function of time.

for experiments similar to those described in this work. Using Mie scattering theory, Hansen (1984) showed that at certain scattering angles a monotonic relation exists between the light intensity and the bubble radius. Thus, before the calibration procedure is described, let us first introduce this relation.

The theory describing the scattering of electromagnetic radiation from dielectric spheres was developed by Gustav Mie in 1908. A complete treatment of it can be found in Kerker's (1969) excellent book on the subject, and his notation will be used here. The following are the results applicable to the component of the scattered intensity in the far field and parallel to the scattering plane (defined by the incident and scattered directions) for an incident wave of unit intensity:

$$I = \frac{\lambda^2}{4\pi^2 r^2} |S|^2 \cos^2 \phi, \quad (2.8)$$

where r is the distance from the center of the bubble, ϕ is the azimuthal angle, and λ is the wave length of the light in the liquid. The scattering amplitude S is given by

$$S = \sum_{n=1}^{\infty} \frac{2n+1}{n(n+1)} [a_n \tau_n(\cos \theta) + b_n \pi_n(\cos \theta)], \quad (2.9)$$

where θ is the scattering angle, and forward scattering corresponds to $\theta = 0$. The angular functions are given by

$$\pi_n(\cos \theta) = \frac{P_n^{(1)}(\cos \theta)}{\sin \theta}, \quad (2.10)$$

$$\tau_n(\cos\theta) = \frac{dP_n^{(1)}(\cos\theta)}{d\theta}, \quad (2.11)$$

where the $P_n^{(1)}(\cos\theta)$ are the associated Legendre functions. The coefficients a_n and b_n are found from

$$a_n = \frac{\psi_n(\alpha)\psi'_n(\beta) - m\psi_n(\beta)\psi'_n(\alpha)}{\delta_n(\alpha)\psi'_n(\beta) - m\psi_n(\beta)\delta'_n(\alpha)}, \quad (2.12)$$

$$b_n = \frac{m\psi_n(\alpha)\psi'_n(\beta) - \psi_n(\beta)\psi'_n(\alpha)}{m\delta_n(\alpha)\psi'_n(\beta) - \psi_n(\beta)\delta'_n(\alpha)}, \quad (2.13)$$

where $m = k_1/k_2 = m_1/m_2$ is the relative index of refraction. Subscript 1 refers to the bubble interior, while subscript 2 refers to the surrounding liquid, k is the wave number, m is the index of refraction, $\alpha = 2\pi m_2 R/\lambda_0$ is the size parameter, λ_0 is the wavelength of the incident light in vacuum, $\beta = \alpha m$, and primes denote differentiation with respect to argument. The functions

$$\Psi_n(\alpha) = \alpha j_n(\alpha), \quad (2.14)$$

$$\delta_n(\alpha) = \alpha h_n^{(2)}(\alpha), \quad (2.15)$$

are the Ricatti-Bessel functions with $j_n(\alpha)$ and $h_n^{(2)}(\alpha)$ the ordinary spherical Bessel functions of the first and third kind respectively. For convenience, we define the relative intensity as

$$I_{rel} = \frac{4\pi^2 r^2 I}{\lambda^2} = |S|^2 \cos^2\phi. \quad (2.16)$$

For the purpose of illustration, parameters relevant to an air bubble in water will be chosen, with the incident wavelength being 488 nm. Fig. 9 is a plot of $\log_{10} I_{rel}$ vs θ for 0 to 180 degrees for a size parameter α equal to 661, corresponding to a bubble of radius 38 μm . Looking at this graph, we want to determine what the optimal angle is which would make the intensity a monotonic function of the radius. If possible, θ should be less than 90° since the intensity drops considerably for angles greater than 75° . Fig. 10 is a plot of I_{rel} as a function of radius for $\theta = 66^\circ$. As can be seen, the coarse structure due to the interference of the reflected and refracted rays make this angle an undesirable one. Fig. 11 shows the same calculation for an angle $\theta = 70^\circ$. Although the coarse structure is less pronounced, I_{rel} is still not a single valued function of the radius. The theoretical relative intensity for a scattering angle $\theta = 80^\circ$ from the forward direction is shown in Fig. 12 demonstrating the ideal type of radial dependency. The fine structure disappears when the intensity is calculated using a finite solid angle as would be the case during the experiment. Because this angle gives the greatest intensity with a smoothly increasing function of the bubble radius, it was used for all the experiments. This is the same result obtained by Holt (1988) and Horsburgh (1990) who had previously demonstrated the validity of Mie theory for this type of experiment. The calculations shown in Figs. 9-12 were made by Holt using a modified version of a program developed by Wiscombe (1980).

In order to determine the instantaneous bubble radius from the scattered light intensity, an intensity-radius transfer curve was obtained. For this purpose, bubbles of different sizes were levitated and the scattered light intensity recorded.

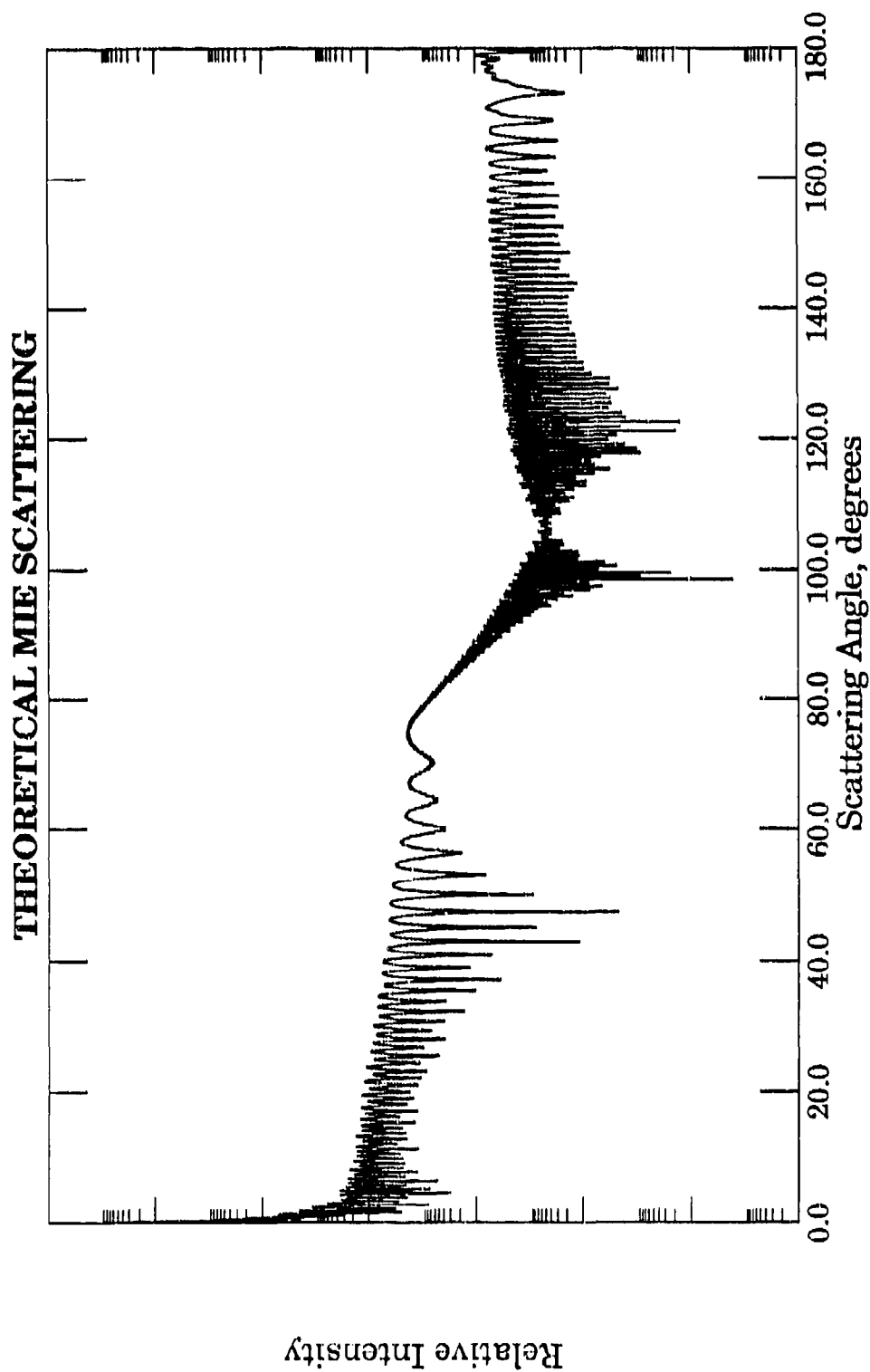


Figure 9. Theoretical scattered intensity of the parallel polarized component S2 as a function of scattering angle (0 is forward) for $ka=661$. This corresponds to a radius of $38.6 \mu\text{m}$ with respect to the Ar-I 488.0 nm line.

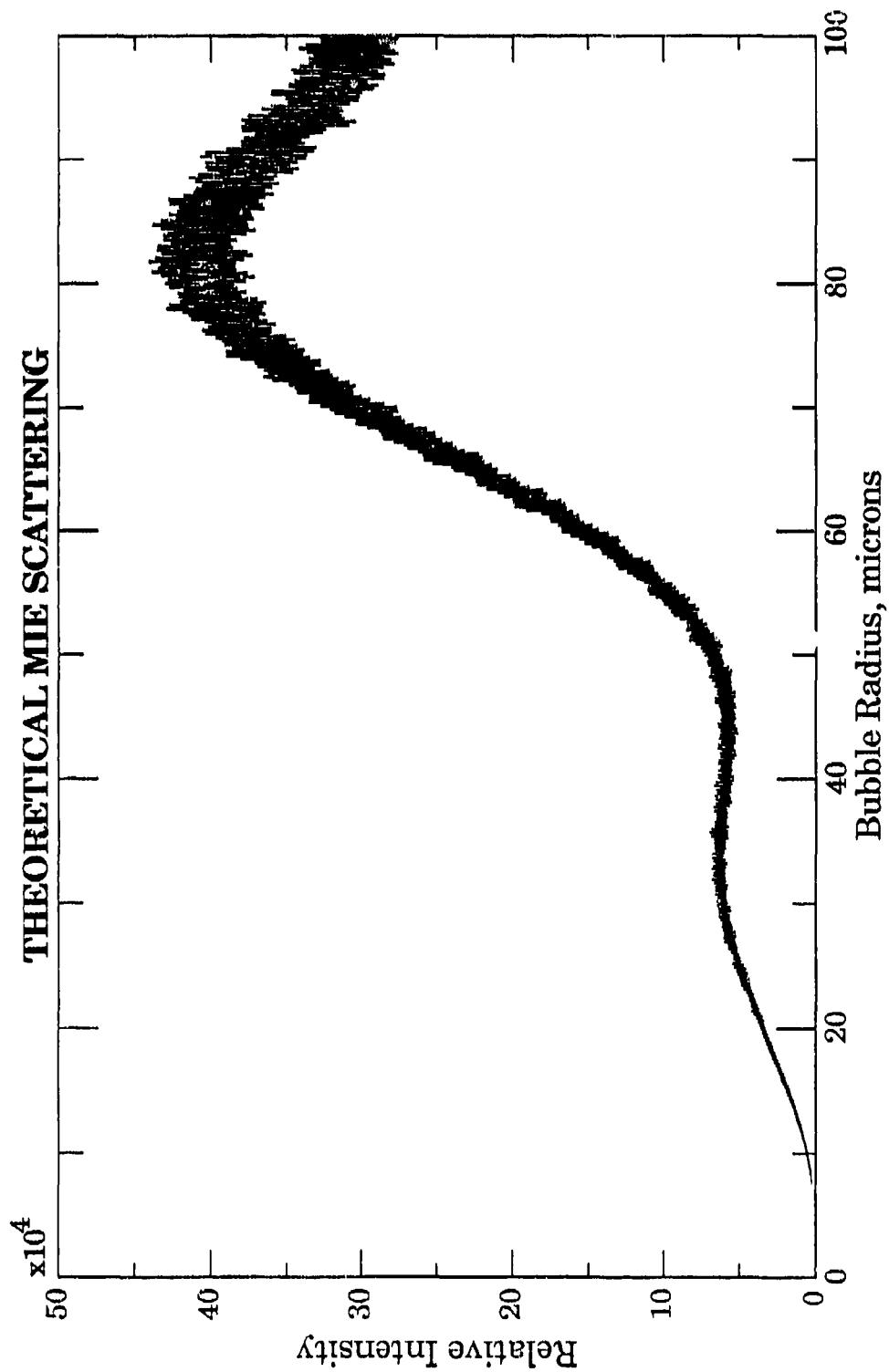


Figure 10. Theoretical scattered intensity of the parallel component S2 as a function of equilibrium radius at 66 degrees.

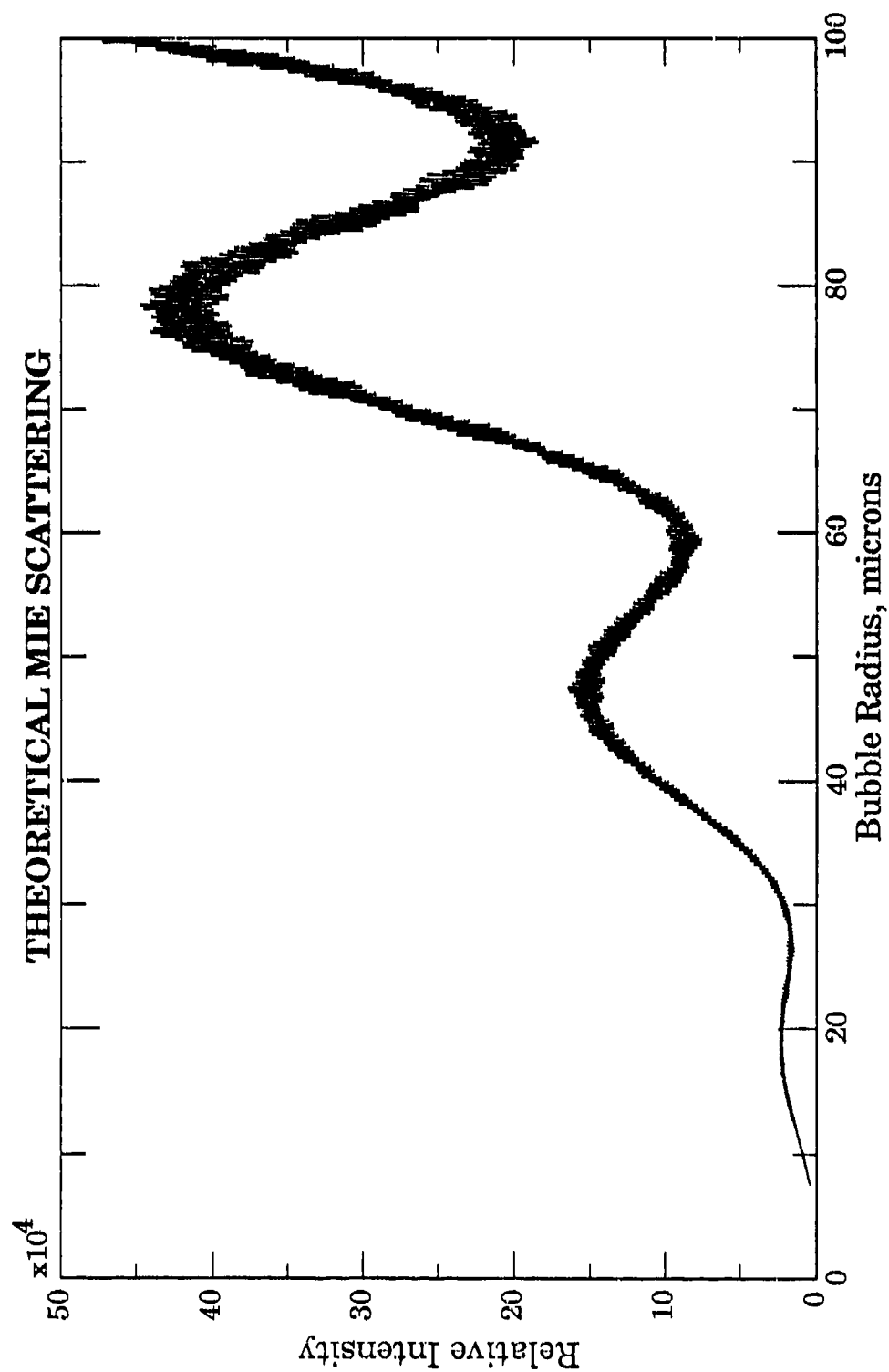


Figure 11. Theoretical scattered intensity of the parallel component S₂ as a function of equilibrium radius at 70 degrees.

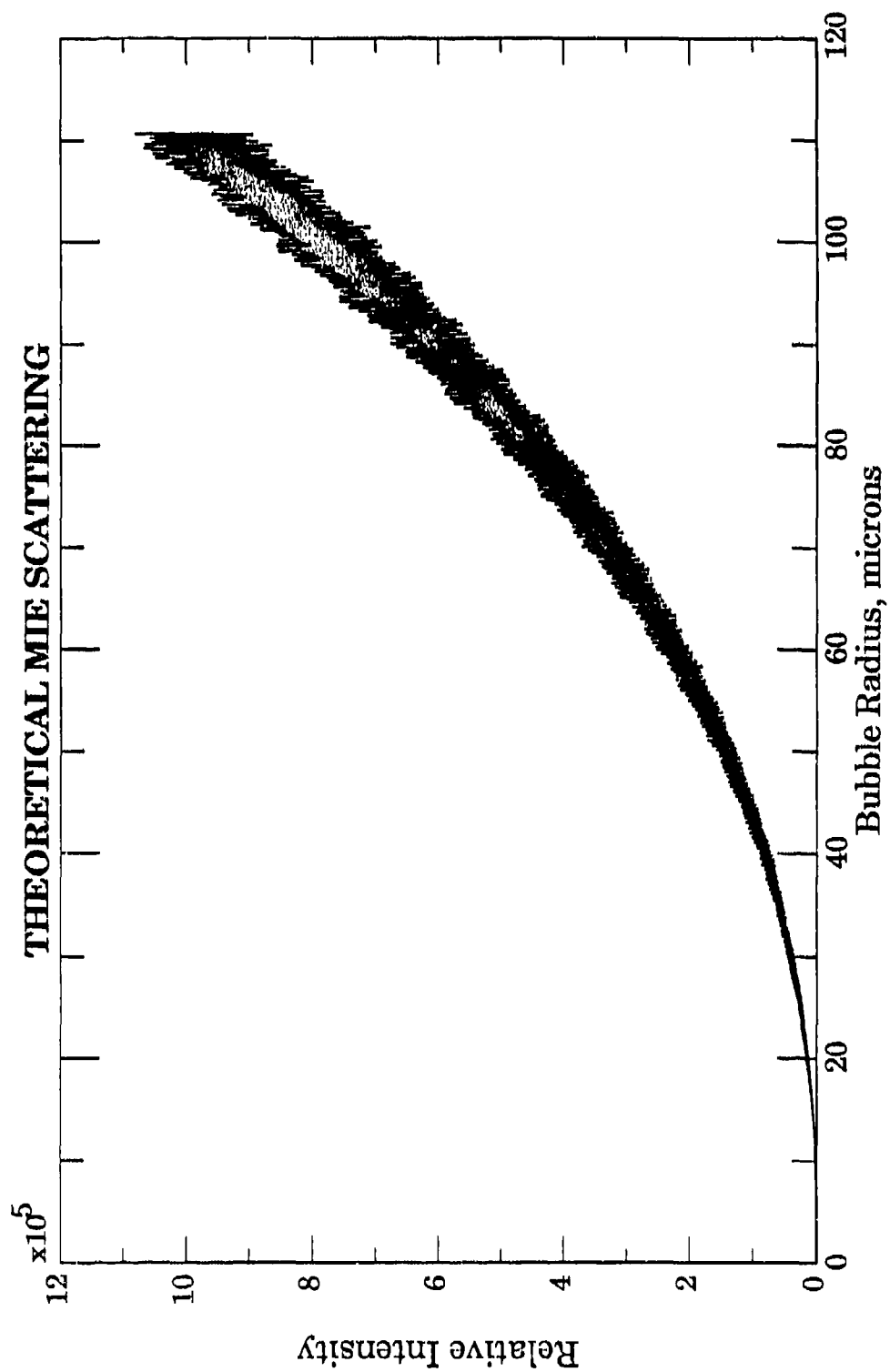


Figure 12. Theoretical scattered intensity of the parallel component S2 as a function of equilibrium radius at 80 degrees.

The size of the bubbles was determined by the rise-time method described previously using the appropriate drag law. The experimental Mie scattering intensity for bubbles between 20 and 80 microns for 42% glycerine mixture is shown in Fig. 13. The solid line is a 3rd degree polynomial fit to the data. Curves for Water, 21%, 35% and 60% glycerine can be found in Appendix A, Figs. A2-A5. These curves were used to convert scattered intensity to bubble radius.

It should be noted that the Mie scattering calibration data were taken without the preamplifier in order to avoid internal DC offsets from introducing calibration errors. During the experiment, the intensity-time data were taken with the preamplifier set to a fixed gain and AC-coupled to the oscilloscope. In order to obtain radius from intensity, the gain of the preamplifier had to be considered first. The correct DC offset was then added such that the average of the intensity minima of each trace was equal to the background intensity. This background level was obtained from the intensity-radius calibration curves for each mixture. Generally, the background intensity corresponded to a bubble radius between 10 and 20 μm depending on the mixture. Since bubbles are certain to collapse to values of the radius less than 10 μm , it can then be assumed that the minimum light intensity detected by the apparatus is that of the background. The determination of the background level from these curves constituted the largest source of error. The other source of error was the finite width of the laser beam. Since the bubble was not perfectly stationary, it was possible that it could have moved outside the beam while the data were being taken. An error analysis procedure estimated the total uncertainty to be $\pm 5 \mu\text{m}$.

EXPERIMENTAL MIE SCATTERING FOR 42% GLYCERINE

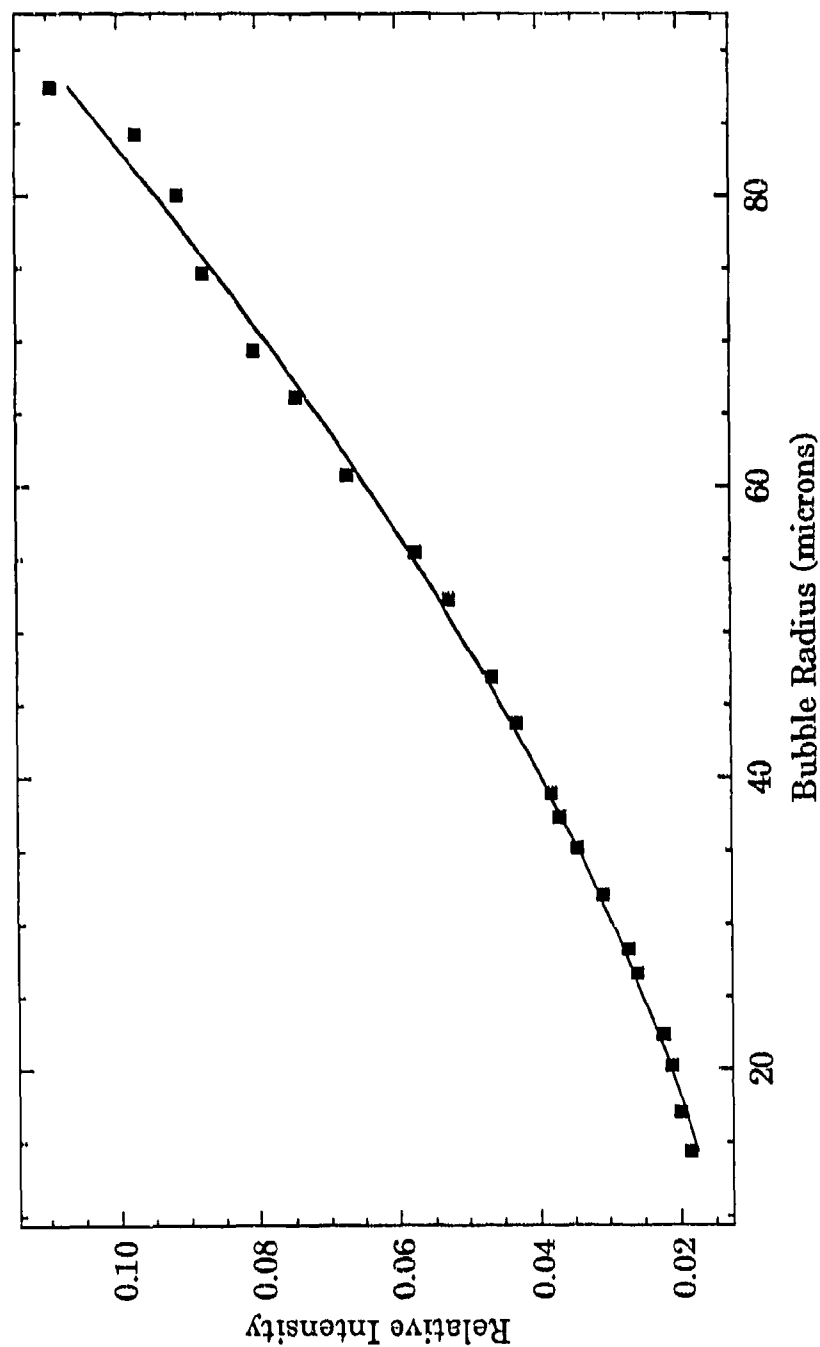


Figure 13. Measured scattered light intensity vs equilibrium bubble radius for 42% glycerine.
The solid line corresponds to a 2nd degree polynomial fit.

II. D. 2. b. Phase of Radial Bubble Pulsations

The phase of the bubble pulsations was measured relative to the calibrated side pill transducer. For the light scattering experiment, a more direct method than the one described in Section II.C.2 was devised to calibrate the pill. This calibration was made relative to the oscillations of a levitated bubble driven at a low pressure amplitude and far from its resonance frequency. As illustrated in Fig. 14, the theoretical phase of the radial minimum in the region $0.6R_0 \leq R \leq 0.75R_0$ is not only flat but fairly independent of the pressure amplitude. Since this region corresponds to bubbles away from their harmonic resonances, this phase corresponds to the only radial minimum occurring each cycle of the driving pressure. This phase was also found to be independent of the formulation used to calculate it. Thus, by knowing the phase of the bubble pulsations relative to the sound field, the phase of the pill transducer could also be determined. Bubbles in this size range were levitated and the simultaneous oscilloscope traces of both the pill transducer output and scattered light intensity were stored in the computer. The two traces were displayed on the MacII CRT screen using Passage II plotting software. The time difference between minima was measured from which the phase difference was calculated. The estimated total error of the calibration procedure was ± 5 degrees. This error was mostly due the uncertainty of the bubble sizes used in the calibration procedure.

PHASE of RADIUS MINIMA for 42% GLYCERINE

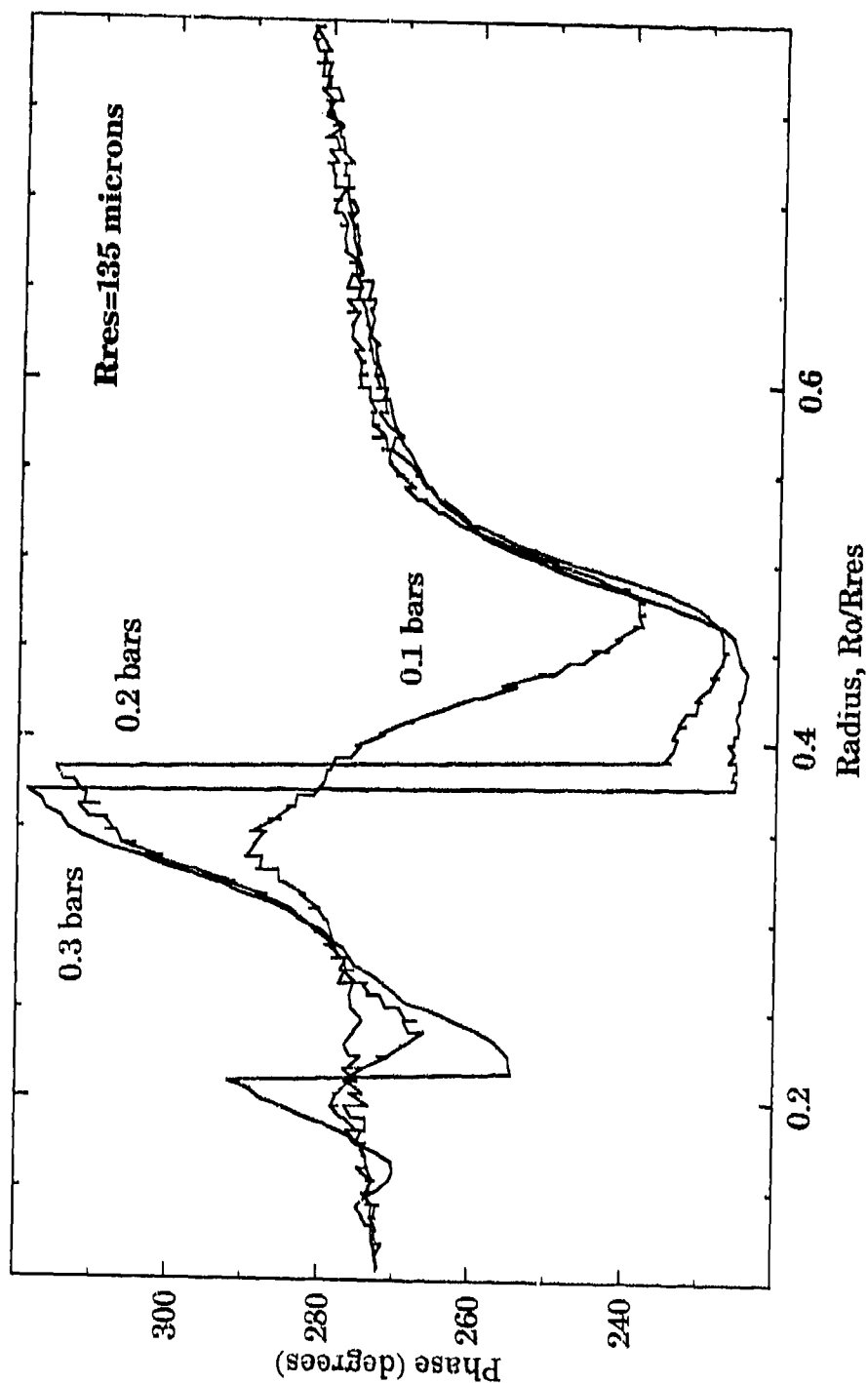


Figure 14. Theoretical phase of bubble radius minimum of the steady state solution for 42% glycerine at 0.1, 0.2 and 0.3 bars and $f=23.6$ kHz used in the phase calibration of the light-scattering apparatus.

II. D. 3. Procedure

The light scattering apparatus described in the previous Section was used to obtain the radius *vs* time curves for radial pulsations of bubbles. Five different glycerine/water mixtures were used in this experiment in order to obtain data for liquids with several different values of the liquid density, viscosity, surface tension and speed of sound. These mixtures were pure water, GLY21, GLY35, GLY42 and GLY60, where the two digits represent the percent by weight of glycerine. The solutions were prepared from 99.5% pure glycerine and water filtered down to 0.2 μm in particle size. In order to lower the gas content, the mixtures were periodically vacuum-filtered through a 5 μm Teflon filter. This procedure also served to remove impurities after the liquid had been used for some time.

The procedure was relatively straightforward, once the bubble was stabilized in the radial mode. After positioning the bubble in the center of the beam, simultaneous traces of the pill transducer output and scattered light intensity were stored in the oscilloscope and transferred to the computer for permanent storage. The process was repeated for each mixture as the pressure amplitude, p_A , was increased using the same bubble whenever possible. At the higher pressures, the bubble often exhibited vertical oscillations, with a frequency around 1 Hz or higher. If the amplitude of these oscillations was large enough so that part of the time the bubble was off the center of the beam, several traces were recorded but only the ones with the largest scattered intensities were transferred to the computer. It was assumed that the largest values were obtained while the bubble was in the center of the beam. Each trace corresponded to about 0.2 msec of

real time. In addition, if the signal-to-noise ratio was too small, as was the case for the lowest values of the pressure amplitude, time averages over 100 traces were performed by the LeCroy oscilloscope before transferring the data to the computer. Because the scattered intensity was periodic over several minutes, no information was lost in the time-averaging procedure.

All the light intensity traces were converted to radius using the transfer curves for each liquid mixture. The pulsation amplitude (R_{max}), the phase of collapse (ϕ_c) and the number of radial minima (M) of the oscillations were obtained from these traces. These quantities will be defined more precisely in Chapter III. The value of the equilibrium radius of the bubble (R_0) was obtained by the rise-time method, although thermal and acoustic pressure currents in the liquid made this measurement difficult and imprecise. From these measurements, however, it was determined that the bubble sizes were less than 20 μm for all of the liquid mixtures. Mie scattering techniques also were imprecise because of the very low signal-to-noise ratio at these bubble sizes.

The gas concentration during these measurements was somewhat below saturation. Since no dependence of the bubble pulsations on the gas concentration was expected, no attempt was made to control this parameter extensively. During the single bubble experiments, however, a certain amount of under-saturation was required in order to suppress cavitation which generated copious streaming and disturbed the stably pulsating bubble. The higher concentration glycerine solutions required less under-saturation, since air does not readily dissolve in glycerine and it is thus naturally "degassed".

II. E. Sonoluminescence Detection Experiment

1. Apparatus

When the pressure amplitude in the levitation cell was high enough to produce sonoluminescence from cavitation, it was desired to measure the onset as well as the phase of the light emission relative to the sound field. This Section describes the apparatus used to acquire these data.

Because of the low intensity of the light emissions, an eight cubic foot light-tight box was built which allowed the use of a photomultiplier tube (PMT) to detect them. Bulkhead BNC connectors on both side walls were used in order to bring all the necessary electrical signals in and out of the box. During the experiment, the front cover was tightly secured with 4 sets of removable 1/4 inch nut and bolt combinations. A rubber gasket around the edge was used to provide a tight fit between the cover and the box. A model R585/C617 PMT/preamplifier combination made by Hamamatsu for single photon counting applications was used to detect the light emissions. The dark current and gain specifications of this system were 1 count/sec and 10^5 respectively while the rise and fall times were 15 nanoseconds each. This system provided a high signal-to-noise ratio as well as a time resolution on the order of 1/500th of an acoustic period ($< 1^\circ$) necessary to measure the phase of sonoluminescence accurately. Fig. 15 shows the schematic diagram of this apparatus, the shaded blocks indicating the support equipment.

The phase of SL flashes was measured relative to a reference signal. This signal consisted of a series of fast electronic pulses generated with a fixed phase relative to, and the same frequency as, the sound field. By measuring the time

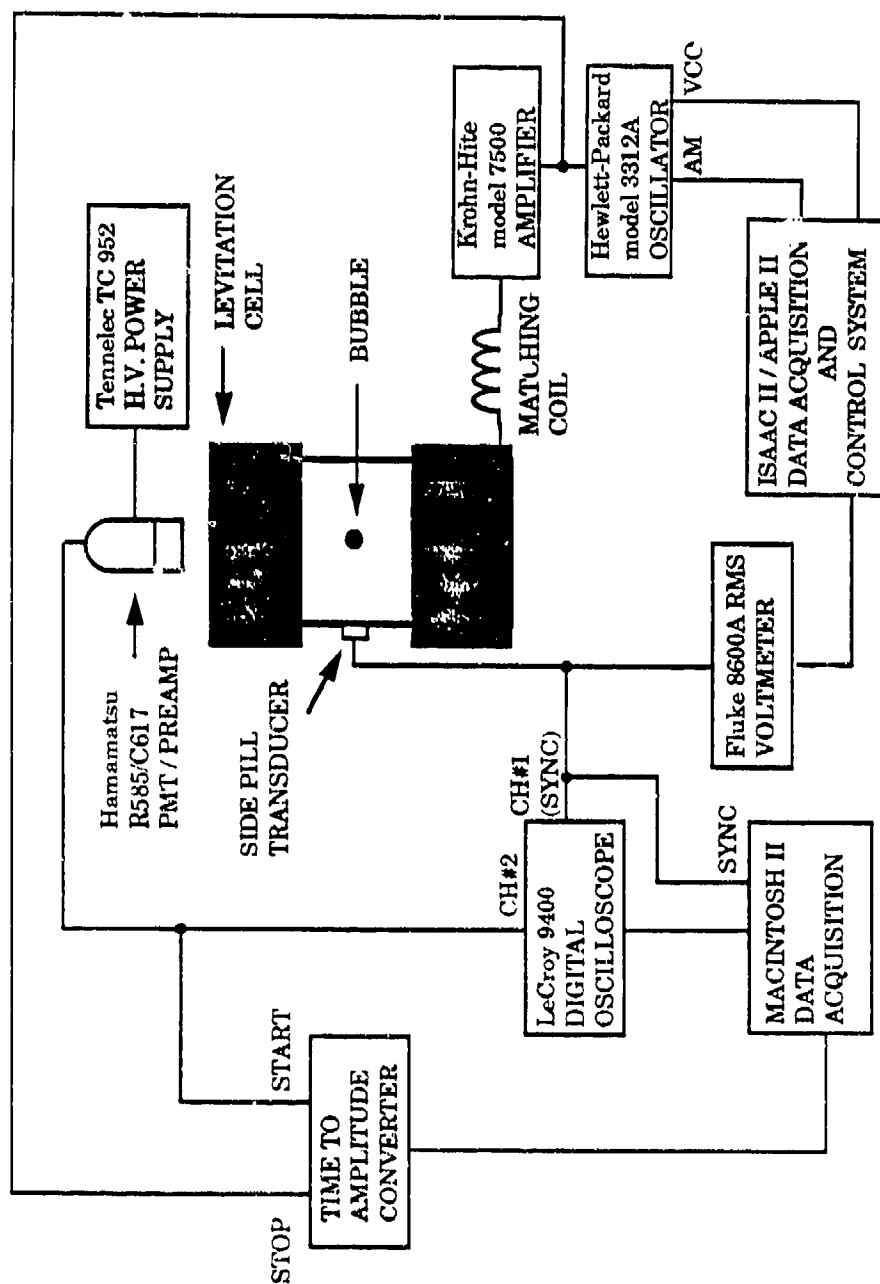


Figure 15. Schematic diagram of experimental apparatus used to measure the phase of sonoluminescence relative to the acoustic pressure.

interval between these pulses and SL events, the phase of SL was determined. A schematic diagram of the circuit used to measure this phase is shown in Fig. 16. One of the functions of this circuit was to generate NIM* -type pulses (-0.5 V peak amplitude and 100 nanoseconds long) at the negative-slope zero-crossing of the periodic, sinusoidally varying signal generated by the side pill transducer. The phase of this signal was usually different from that of the sound field and therefore required calibration (see Section II.C.2). The pulses were generated by the zero-crossing detector circuit shown in the upper left region of Fig. 16. The output of this circuit (\bar{Q} on the 4047 chip) was connected to the STOP input of the time-to-amplitude converter (TAC) module. The pulses generated by the PMT when a sonoluminescence event occurred were connected to the input of an Ortec constant fraction discriminator in order to convert them to NIM-type pulses. A variable time delay was then inserted to these pulses with a delay generator unit before being connected to the START input of the TAC module. The purpose of the time delay was to maximize the amplitude of the TAC output pulses and, therefore, the precision of the data acquisition system. The amplitude of the output pulses generated by the TAC were proportional to the time interval between START and STOP pulses. This apparatus was designed to facilitate the measurement of the phase of thousands of sonoluminescence events. To minimize the amount of dead time in the TAC circuit, the reference signal was used as the stop pulse. The reference pulses occurred every acoustic cycle at a fixed phase, while sonoluminescence events usually happened sporadically. If a

* NIM=nuclear instrumentation module.

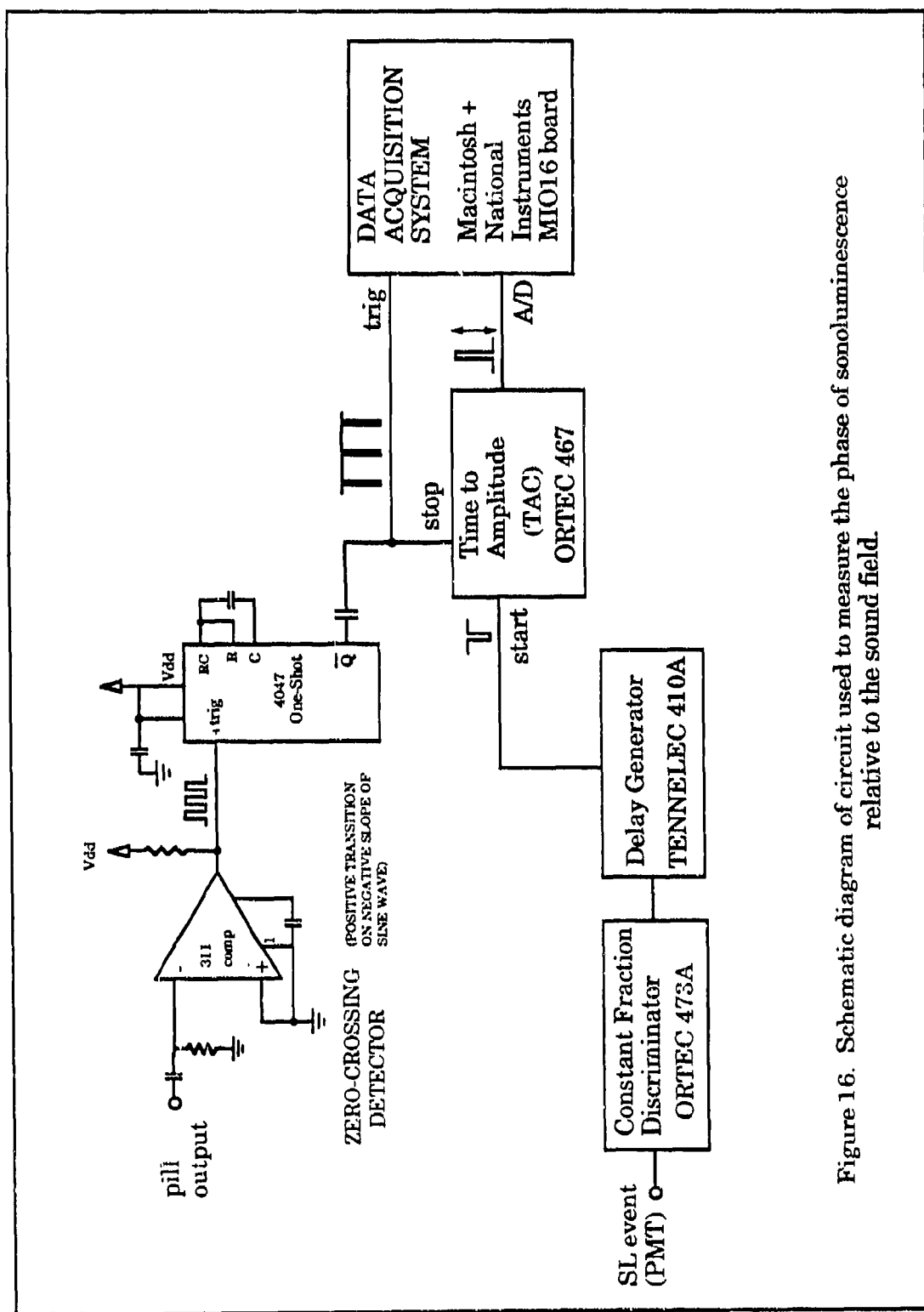


Figure 16. Schematic diagram of circuit used to measure the phase of sonoluminescence relative to the sound field.

stop pulse occurred without a previous valid start pulse, the stop pulse was ignored by the TAC. Thus, only stop (reference) pulses which occurred after a start pulse (sonoluminescence event) within the given time interval generated an output pulse. All other situations were effectively ignored and generated no output.

The amplitude of the output pulses was measured by a multipurpose I/O board made by National Instruments (MIO16) with a maximum sampling rate of 100 kHz. The host computer was a MAC II using the Labview® software. The precision of the data acquisition system was 12 bits which corresponded to a precision of $\Delta\phi_c = \pm 0.1$ degrees of the phase if measured under noiseless conditions. Typical noise levels were ± 1 degree. This system was able to sample the phase for thousands of consecutive cycles. Since the data were acquired with a DMA (direct memory access) board, the maximum number of data points that could be taken consecutively was determined by the amount of memory in the MacII computer. Typically, each set of data consisted of 1000 acoustic cycles, equivalent to about 50 msec. However, data sets as long 20,000 acoustic cycles were possible if needed, corresponding to about 1 sec of real time.

In order to obtain information on the frequency of sonoluminescence events, data conversions on the analog-to-digital convertor (ADC) board were triggered every cycle. Thus, if in a given acoustic cycle no sonoluminescence events occurred, or if they occurred outside the maximum time window set in the TAC module, an analog voltage value of zero was read by the computer. Otherwise, the amplitude of the pulse carrying the phase information was read. The data were displayed on a CRT screen before being stored permanently.

II. E. 2. Calibration

The calibration of this apparatus was done as follows. First, the front panel reading of the delay generator module was calibrated using a digital oscilloscope to measure the true time delay. The resulting second degree polynomial fit was then incorporated into the conversion routine written in Labview®. Next, two pulses separated in time by a variable interval were input into the TAC module using the calibrated delay generator. Similarly, a second degree polynomial fit was obtained relating the pulse amplitude and the time interval and incorporated into the conversion routine. After this, the only other calibration factor needed was the phase shift of the side pill transducer relative to the sound field. This factor was obtained as explained in Section C.2 of this Chapter.

II. E. 3. Procedure

a. Phase of Sonoluminescence *vs* Bubble Motion

Using the light scattering apparatus and the photomultiplier (PMT) SL detection system, the phase of SL was measured relative to the instantaneous radius of the bubble. This is the most direct way of determining the point during the bubble motion in which the SL flash is emitted. Since both the photomultiplier tube (PMT) and the laser could not be on simultaneously, an intermediate phase reference had to be used. The procedure was as follows: After positioning a pulsating bubble in the center of the laser beam, an instantaneous intensity-time

the computer. The laser and the room lights were then turned off and the PMT turned on with a black cloth wrapped around it and the levitation cell. Similarly, simultaneous traces of the PMT output and the pill transducer output were stored in the computer. All traces were obtained very quickly to ensure that all parameters remained constant. The intensity-time and SL traces could then be compared directly after verifying that the two pill output traces were in phase.

II. E. 3. b. Phase of Sonoluminescence *vs* Sound Field

The phase of SL was measured for different values of the liquid density, viscosity, surface tension and speed of sound. The time-to-amplitude converter (TAC) system provided a very efficient method of recording the phase of SL for thousands of cycles at a time or even in real time if desired. The general procedure was as follows: After filling the cell with the desired glycerine mixture, an amplitude and phase calibration of the pill transducer was made using the procedure described in Section II.C. A bubble was then introduced into the liquid and made to sonoluminesce at the desired pressure amplitude. After the light-tight box was closed, the phase of SL was measured for different pressure amplitudes using the TAC system and stored in the computer for later analysis. The system was checked periodically and kept at resonance in order to maintain the calibration.

Measurements were also made of the phase of SL during streamer activity when the cavitation field was composed of many bubbles sonoluminescing

simultaneously. The purpose of this experiment was to study the behavior of bubbles during intense cavitation activity.

Chapter III

Theory of Bubble Dynamics

III. A. Introduction

In this Chapter, the mathematical formulations used to describe the motion of a single bubble in a spatially uniform acoustic field are presented. This field is assumed to vary sinusoidally in time. During the calculations, three different formulations will be used, the results of which will be compared to the measurements. These formulations are the Keller-Miksis (1980) radial equation with a linear polytropic exponent approximation, the Keller-Miksis radial equation with Prosperetti's (1986) exact formulation for the internal pressure, and Flynn's (1975) formulation, which also includes thermal effects inside the bubble. These formulations will be referred to as polytropic, Prosperetti's, and Flynn's formulations respectively. Because of the large pressure amplitudes, p_A , used in the calculations, only formulations that included correction terms for the compressibility of the liquid were considered. In addition, Section B.2 introduces some basic concepts of bubble dynamics which will be needed to understand the results of the experiments. In Section B.3 the assumptions made in the derivation and the limits of the formulations will be discussed. In particular, the extent to which these limits are exceeded in the present calculations will be considered.

Two other effects are important when treating acoustically driven bubbles: surface waves and rectified diffusion. Surface instabilities, also known as surface

waves or shape oscillations, can occur when the acceleration of the interface exceeds a certain value. This type of instability usually results in the breakup of the bubbles at these amplitudes. Similarly, rectified diffusion, a mechanism by which bubbles can grow in an acoustic field, exhibits a threshold behavior. The pressure amplitudes above which surface waves are excited is called the surface wave threshold, and that above which growth by rectified diffusion is positive is called the rectified diffusion threshold. Brief presentations of the mathematical theories used to describe these two phenomena are presented in Sections C and D, respectively.

III. B. Radial Bubble Motion

1. Theoretical Formulations

The first attempt to describe mathematically the collapse of an empty spherical cavity in a previously undisturbed liquid was made by Rayleigh in 1917. His work was motivated by the increasing concern over the rapid deterioration of ship propellers. This deterioration was caused by what is now known as hydrodynamic cavitation. Rayleigh's equation can be obtained by equating the power at infinity and the time rate of change of the kinetic energy in an incompressible liquid (Commander, 1985) and it can be expressed as

$$R\ddot{R} + \frac{3}{2}\dot{R}^2 = -\frac{p_{\infty}}{\rho_l}, \quad (3.1)$$

where p_{∞} is the pressure at infinity (in this case, the ambient pressure), ρ_l is the liquid density, R the radius of the cavity and dots indicate time derivatives. In his seminal paper, Rayleigh found an explicit expression for the bubble wall velocity U as a function of R :

$$U^2 = \frac{2}{3} p_{\infty} \left(\frac{R_0^3}{R^3} - 1 \right), \quad (3.2)$$

where R_0 is the initial radius. As simple as these equations are, they constitute the basis for all subsequent work on bubble dynamics.

It was not until 30 years later that any significant improvements were made to Rayleigh's equation. The first of these was made by Plesset (1949) in which he added the variable pressure term (appropriate for acoustic cavitation) and surface tension term. This equation, together with a viscous damping term added by Poritsky (1952) is known today as the Rayleigh-Plesset equation, and is given by

$$R\ddot{R} + \frac{3}{2}\dot{R}^2 = \frac{1}{\rho_l} \left[p_g(t) - p_{\infty}(t) - \frac{2\sigma}{R} - \frac{4\mu\dot{R}}{R} \right], \quad (3.3)$$

where p_g is the gas pressure in the interior of the bubble, p_{∞} is the driving pressure (including ambient pressure), and μ is the shear viscosity of the liquid. This is probably the best known equation describing the spherical motion of a gas bubble in a liquid. Despite the fact that it assumes an incompressible liquid, it is still used extensively. However, because the velocity of the interface can easily reach values comparable to the speed of sound in the liquid, it is necessary to include at

least first order compressibility terms in this equation, in order to account properly for the energy stored in the liquid. Following the procedure used by Keller & Miksis (1980), Prosperetti (1984) has obtained the following equation:

$$\left(1 - \frac{\dot{R}}{c}\right) R \ddot{R} + \frac{3}{2} \dot{R}^2 \left(1 - \frac{\dot{R}}{3c}\right) = \left(1 + \frac{\dot{R}}{c}\right) \frac{1}{\rho_l} \left[p_B(R, t) - p_A\left(t + \frac{R}{c}\right) \right] + \frac{R}{\rho_l c} \frac{dp_B(R, t)}{dt}, \quad (3.4)$$

where c is the speed of sound in the liquid, $p_B(R, t)$ is the pressure on the liquid side of the bubble interface, and $p_A(t + R/c)$ is the time-delayed driving pressure. $p_B(R, t)$ can be expressed in terms of the internal pressure by the condition on the normal stress across the boundary

$$p_B(R, t) = p_\mu(R, t) - \frac{2\sigma}{R} - 4\mu \frac{\dot{R}}{R}. \quad (3.5)$$

The relationship between the internal pressure and the bubble radius is determined mainly by the thermodynamic properties of the gas. Although this relation can be assumed to be isothermal or adiabatic under some circumstances, a polytropic relation has often been used (Noltingk and Neppiras, 1950; Flynn, 1964; Prosperetti, 1974; Lauterborn, 1976; Keller and Miksis, 1980) of the form

$$p_\mu = p_o \left(\frac{R_o}{R} \right)^{3\kappa}, \quad (3.6)$$

where κ is the polytropic exponent, and p_o is the internal pressure of the bubble at equilibrium, defined by

$$p_o = p_{\infty} + \frac{2\sigma}{R_o}. \quad (3.7)$$

The value of κ varies between 1 and γ , for isothermal and adiabatic motion respectively, γ being the ratio of the specific heat capacities C_p/C_v , where the subscripts p and v indicate that the pressure and volume are kept constant. This exponent is calculated according to Prosperetti (1984). In this study, the Keller-Miksis radial equation (3.4) with a polytropic approximation is used as an example of a first order compressible radial equation using a constant speed of sound.

The procedure used to obtain equation (3.4) requires the elimination of higher order terms. It is thus expected that several similar equations exist as derived by different authors. Another commonly used formulation is that of Gilmore (1952). Although no calculations will be made with this model, it is considered by many scientists to be a principal formulation of bubble dynamics. It is therefore included here for a sense of completeness.

In his formulation, Gilmore considers the enthalpy h of the liquid a fundamental quantity. In addition, the quantity $r(h + u^2/2)$ is postulated to propagate with a velocity $c + u$ where u is the particle velocity, as first suggested by Kirkwood and Bethe (1942) (see Rozenberg, 1971 for a detailed derivation). The resulting equation is known as Gilmore's equation and is given by

$$\left(1 - \frac{\dot{R}}{c}\right)R\ddot{R} + \frac{3}{2}\dot{R}^2\left(1 - \frac{\dot{R}}{3c}\right) = \left(1 + \frac{\dot{R}}{c}\right)H + \frac{R}{c}\frac{dH}{dt}\left(1 - \frac{\dot{R}}{c}\right), \quad (3.8)$$

where H is the free enthalpy at the bubble wall, which for water is usually given by

$$H = \frac{n}{n-1} \frac{(B+1)^{\frac{1}{n}}}{\rho_l} \left[(p_B(R,t) + B)^{\frac{n-1}{n}} - (p_{\infty}(t) + B)^{\frac{n-1}{n}} \right], \quad (3.9)$$

where the constant B has been measured to be 3000 bars, $n = 7$ and the time dependent speed of sound is given by

$$c = \left(c_{\infty}^2 + (n-1)H \right)^{\frac{1}{2}}, \quad (3.10)$$

where c_{∞} is the speed of sound at infinity. Assuming adiabatic motion, the pressure at the boundary $p_B(R)$, as in the previous formulation, is equal to

$$p_B(R,t) = \left(p_{\infty} + \frac{2\sigma}{R} \right) \left(\frac{R_0}{R} \right)^{3\gamma} - \frac{2\sigma}{R} - \frac{4\mu\dot{R}}{R}. \quad (3.11)$$

Despite the very different approaches, Gilmore's equation nearly equals equation (3.4) if the substitution

$$H = \frac{(p_B - p_{\infty})}{\rho_{\infty}}, \quad (3.12)$$

is made and the speed of sound is kept constant.

Although the polytropic approximation has been generally thought to be a fairly accurate model, an experimental study by Crum and Prosperetti (1984) has shown large discrepancies between theory and experiment for oscillations near the harmonics of the resonance frequency of the bubble. Since compressibility and viscous effects are expected to be small at these amplitudes, these results suggest that thermodynamics play a more important role in the motion of the bubble than

originally expected. For this reason, a more accurate expression for the internal pressure has been obtained by Prosperetti *et al.* (1986). In their formulation, several approximations have been made. Some of them are: a uniform pressure field inside the bubble, the temperature in the surrounding liquid remains unchanged and an ideal gas is assumed. Of course, these approximations place severe limitations on the model, especially when the pulsations are large and the wall velocities reach values comparable to the speed of sound. Despite its limitations, theoretical values of the internal temperature and pressure with a degree of accuracy comparable only to Flynn's (1975) will be obtained with this formulation. The following is a brief outline of Prosperetti's model starting with the conservation equations for the interior of the bubble.

The momentum equation with spherical symmetry can be written as

$$\frac{du}{dt} = -\frac{1}{\rho_l} \frac{\partial p}{\partial r}, \quad (3.13)$$

Assuming spatially uniform pressure, the momentum equation reduces to

$$p = p(t). \quad (3.14)$$

The conservation of mass equation can be expressed as

$$\frac{d\rho}{dt} + \rho_l \vec{\nabla} \cdot \vec{u} = 0, \quad (3.15)$$

where

$$\frac{d}{dt} = \frac{\partial}{\partial t} + u \frac{\partial}{\partial r},$$

is called the convective derivative, and $\vec{u} = u \hat{r}$ is the velocity vector in the radial direction \hat{r} . The conservation of energy equation, ignoring the viscous heating term, can be written as

$$\rho C_p \frac{dT}{dt} + \frac{T}{\rho_l} \left(\frac{\partial \rho_l}{\partial T} \right)_p \frac{dp}{dt} = \vec{\nabla} \cdot (K \vec{\nabla} T), \quad (3.16)$$

where T is the temperature, C_p is the specific heat at constant pressure, and K is the thermal conductivity of the gas. In order to obtain the velocity field in terms of the temperature, we multiply the conservation of mass equation (3.15) by $C_p T$ and add it to energy equation (3.16) to obtain

$$C_p \frac{d}{dt} (\rho_l T) + \frac{T}{\rho_l} \left(\frac{\partial \rho_l}{\partial T} \right)_p \frac{dp}{dt} + C_p \rho_l T \vec{\nabla} \cdot \vec{u} = \vec{\nabla} \cdot (K \vec{\nabla} T). \quad (3.17)$$

From the ideal gas laws with constant specific heats, we can express

$$C_p \rho_l T = \frac{\gamma p}{\gamma - 1} \quad \text{and} \quad \left(\frac{T}{\rho_l} \right) \left(\frac{\partial \rho_l}{\partial T} \right)_p = -1. \quad (3.18)$$

Inserting equation (3.18), (3.17) becomes

$$\frac{\dot{p}}{\gamma p} + \vec{\nabla} \cdot \left(\vec{u} - \frac{(\gamma - 1)}{\gamma p} K \vec{\nabla} T \right) = 0. \quad (3.19)$$

Due to the spherical symmetry assumption, this equation can be integrated directly to obtain

$$u = \frac{1}{\gamma p} \left((\gamma - 1) K \frac{\partial T}{\partial r} - \frac{1}{3} r \dot{p} \right). \quad (3.20)$$

Using the boundary condition

$$u(r = R, t) = \dot{R}, \quad (3.21)$$

equation (3.20) can be used to obtain a differential equation for \dot{p} by evaluating it at $r = R$:

$$\dot{p} = \frac{3}{R} \left((\gamma - 1) K \frac{\partial T}{\partial r} \Big|_R - \gamma p \dot{R} \right), \quad (3.22)$$

which can be solved simultaneously with the radial equation (3.4) once the gradient of the temperature field at the boundary is found. For this we use the energy equation (3.16) which can be now written as

$$\frac{\gamma}{\gamma - 1} \frac{p}{T} \left(\frac{\partial T}{\partial t} + u \frac{\partial T}{\partial r} \right) - \dot{p} = \vec{\nabla} \cdot (K \vec{\nabla} T). \quad (3.23)$$

The only difficulty in solving this partial differential equation is the temperature dependence of the thermal conductivity K . One way to solve this difficulty is by the transformation

$$\tau = \int_{T_-}^T K(\theta) d\theta, \quad (3.24)$$

where T_∞ is the ambient temperature. In addition, it is convenient to have a fixed rather than a moving boundary condition. Therefore, a new variable is introduced

$$y = \frac{r}{R(t)}. \quad (3.25)$$

Using (3.20), (3.24) and (3.25), the energy equation (3.23) becomes

$$\frac{\partial \tau}{\partial t} + \frac{(\gamma-1)}{\gamma p R^2} \left(\frac{\partial \tau}{\partial y} - \frac{\partial \tau}{\partial y} \Big|_{y=1} \right) \frac{\partial \tau}{\partial y} - D\dot{p} = \frac{D}{R^2} \nabla^2 \tau, \quad (3.26)$$

where the Laplacian operator ∇^2 is now with respect to the variable y , and

$$D(p, T) = \frac{K(T)}{C_p \rho_i(p, T)} = \frac{\gamma-1}{\gamma} \frac{K(T) T}{p}, \quad (3.27)$$

is the appropriate form of the thermal diffusivity for an ideal gas. The boundary condition for the vector τ is

$$\tau(y=1, t) = 0. \quad (3.28)$$

This condition postulates the continuity of the temperature field across the bubble wall.

The third formulation used to compare to the experimental results is Flynn's (1975) in which the thermodynamics of the bubble interior are included. Just as in Prosperetti's formulation, Flynn assumes that the pressure inside the bubble is uniform. A major improvement relative to Prosperetti's formulation, however, is

that the energy equation in the liquid surrounding the bubble is included. Preliminary tests indicated that, for the pressure amplitudes considered here, the temperature in a thin shell of liquid around the bubble is increased significantly during the radial minima. In this respect, this model should provide additional information on the thermodynamics of bubble motion.

Unfortunately, the derivation of Flynn's formulation is rather involved. For this reason, only the radial equation is written here, using Prosperetti's nomenclature, as follows:

$$\left(1 - \frac{\dot{R}}{c}\right) R \ddot{R} + \frac{3}{2} \dot{R}^2 \left(1 - \frac{\dot{R}}{3c}\right) = \left(1 + \frac{\dot{R}}{c}\right) \frac{1}{\rho_l} [p_B(R, t) - p_A(t)] + \frac{R}{\rho_l c} \left(1 - \frac{\dot{R}}{c}\right) \frac{dp_B(R, t)}{dt}. \quad (3.29)$$

The major difference between this equation and the Keller-Miksis equation is the factor $(1 - \dot{R}/c)$ multiplying the time derivative of the pressure just outside the bubble, dp_B/dt . Comparing the results of Flynn's and Prosperetti's formulations, it appears that this extra compressibility term makes a significant contribution when the bubble wall velocities, U , are high, reducing the strength of the collapse (Church, 1990b). A more detailed comparison will be given in Chapter IV. For the details of Flynn's formulation, the interested reader is referred to the cited literature.

These three formulations are solved numerically. The first two, polytropic and Prosperetti's, are solved using an IMSL (IMSL, 1987) integration routine. This routine employs Gear's (1971) "backward differentiation" technique. A spectral solution scheme developed by Kamath and Prosperetti (1989) is used to

solve for the vector τ in equation (3.26). Flynn's (1975) set of equations are solved using an improved Euler method routine written by Church (1990c). Five DEC MicroVaxes in a cluster configuration are used to perform the computations.

III.B. 2. Basic Concepts of Radial Bubble Motion

The purpose of this Section is to present some general characteristics of the motion of a single gas bubble driven sinusoidally. Unless otherwise stated, the examples plotted in this Section were calculated with the polytropic formulation, which required the least amount of computational time. The other formulations give qualitatively similar results.

In Fig. 17, several examples of bubble response curves, as predicted by Prosperetti's formulation for water at $f=21$ kHz, have been plotted. Here, the maximum radius (R_{max}) during one period of the driving (acoustic) frequency after the solution has reached steady state is plotted as a function of the equilibrium radius (R_o) for several values of the pressure amplitude, p_A , as indicated by the numbers labeling each curve. Since the steady state solution has a period equal to that of the driving frequency, R_{max} is single valued. The resonance radius of an air bubble in water driven at 21 kHz, for example, is 150 microns. Linear behavior usually requires that the pulsation amplitude be less than 10% of the equilibrium radius. For $p_A=0.1$ bars, the maximum response occurs when the normalized radius (R_o/R_{res}) is nearly equal to 1, where the resonance radius is defined as the radius of a bubble whose linear resonance frequency is equal to the driving frequency. Other peaks can be seen at or near $R_o/R_{res}=1/2, 1/3, 1/4 \dots$ etc, each

BUBBLE RESPONSE CURVES for WATER

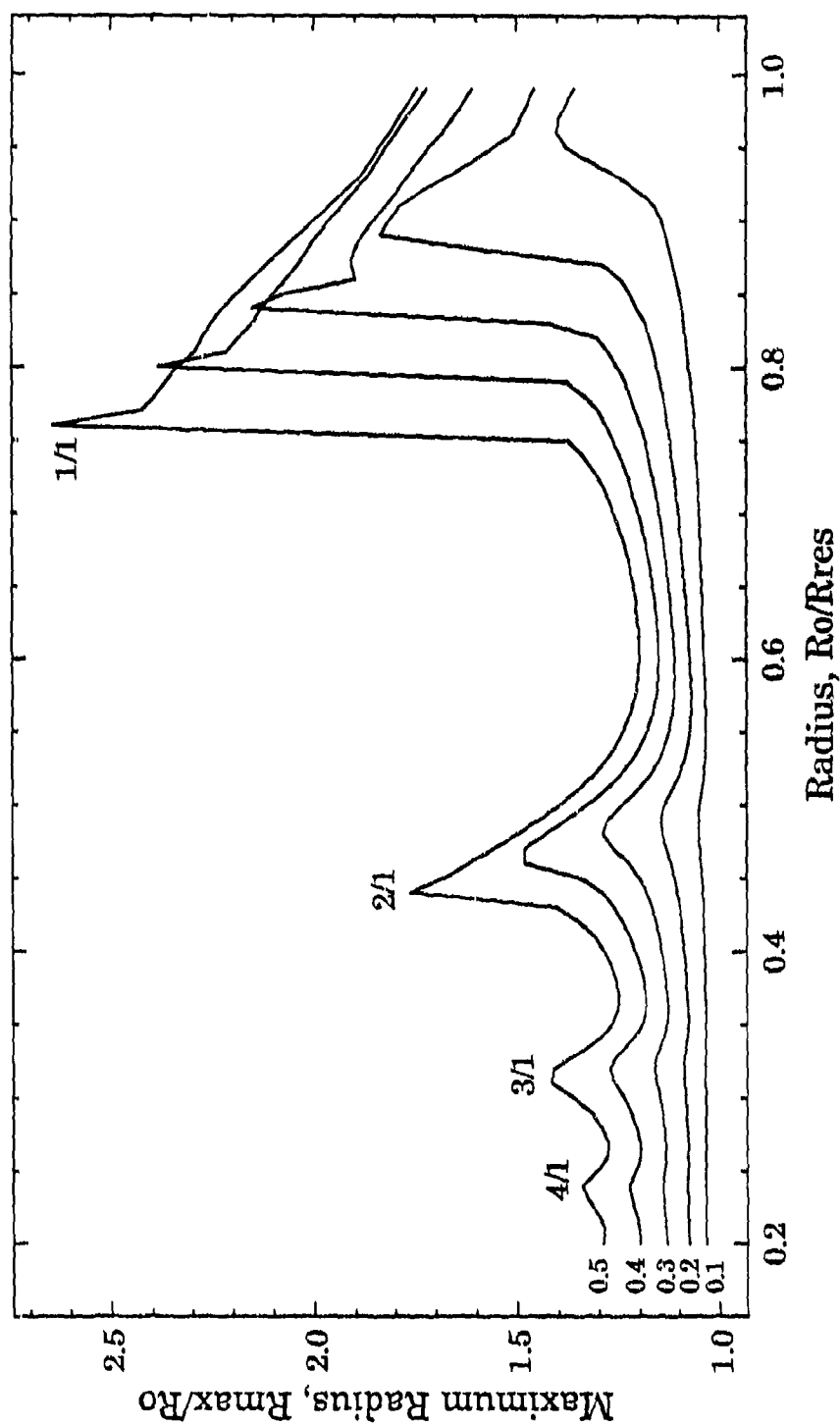


Figure 17. Theoretical bubble response curves calculated using Prosperetti's formulation for water at $p_A=0.1-0.5$ bars, $f=21.0$ kHz.

lower in amplitude than the previous one. They are known as the harmonics of the resonance response. These peaks, shown in Fig. 17, have been labeled with an expression n/m , called the order of the resonance according to the notation introduced by Lauterborn (1976). In this notation, n and m can be defined as follows: If T_R is the period of the bubble motion, T_f the period of free bubble oscillations and T the period of the driving frequency, then for a given steady state solution we can express $T_R = mT$ and $T_R = nT_f$. The case when $m=1$ and $n=2, 3, \dots$ has already been mentioned and are the well known harmonics, whereas the resonances when $n=1$ and $m=2, 3, \dots$ are called subharmonics. In this study, we will encounter both harmonic and subharmonic bubble motion. The resonances when $n=2, 3, \dots$ and $m=2, 3, \dots$ are called ultraharmonics. However, since they were never observed in the range of parameters used here, they will not be discussed any further. Thus, the motion of bubbles near the $n=1$ peaks can be characterized by the number of minima occurring in one acoustic period, T , after the solution has reached steady state. For example, bubbles of radii R_o/R_{res} near the $1/1$ peak exhibit 1 radial minimum and bubbles near the $2/1$ peak exhibit 2 radial minima, and so on. Examples of radial pulsations of bubbles near the $1/1$ and $2/1$ peaks are shown in Figs. 18 and 19, respectively. Since T_f is proportional to the bubble radius, R_o , it is now clear that the number of minima occurring in one acoustic period gives some indication of the size of the bubble, with the smaller bubbles having the larger number of minima.

An often observed characteristic of resonance curves of nonlinear oscillations is the shifting of the resonance peaks as the driving amplitude is increased. This effect can also be observed in Fig. 17 for bubble pulsations and is due to the

RADIUS-TIME CURVE FOR WATER

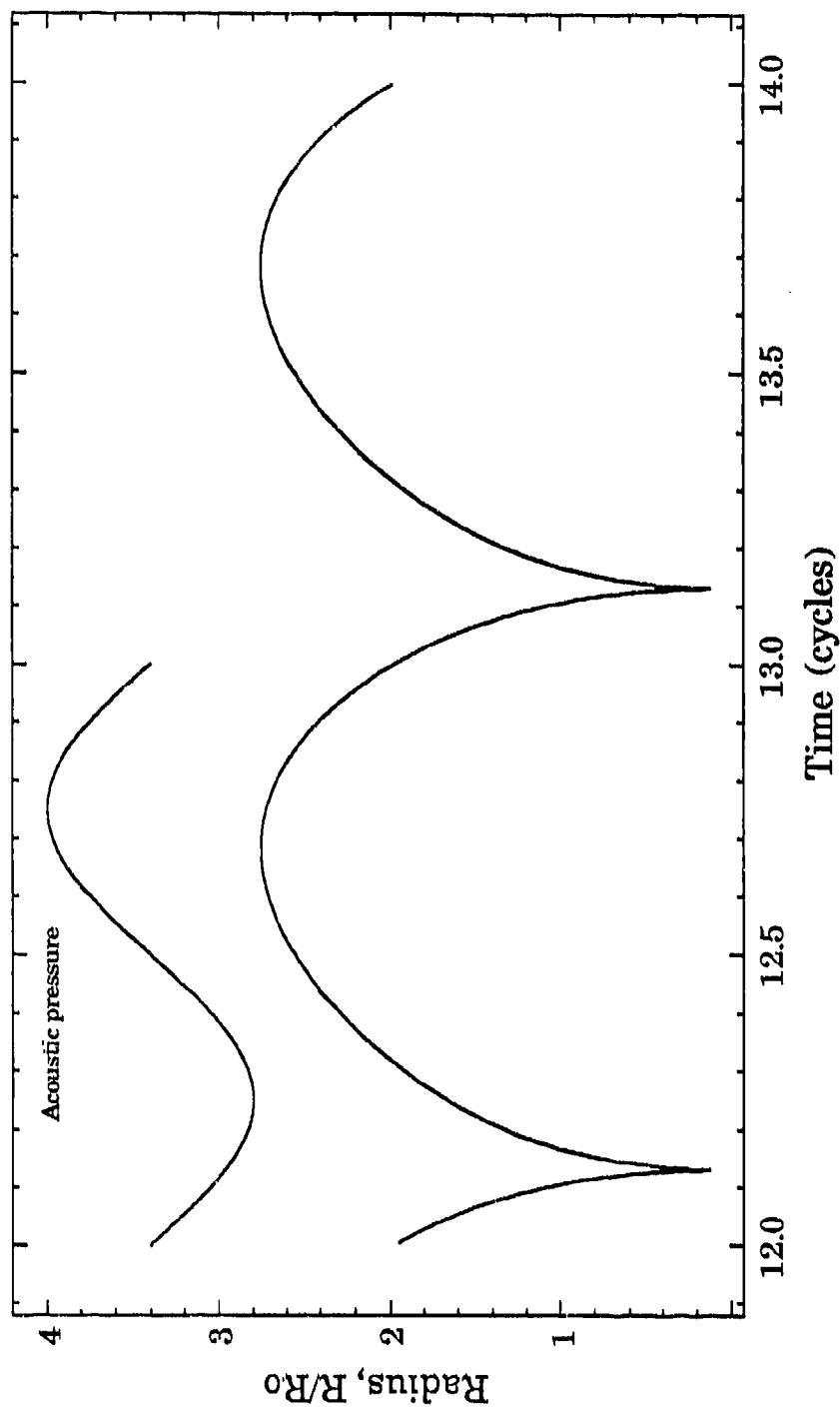


Figure 18. Theoretical radius-time curve calculated using the polytropic formulation for water at $p_A=0.8$ bars, $R_0/R_{res}=0.7$ and $f=21.0$ kHz.

RADIUS-TIME CURVE for WATER

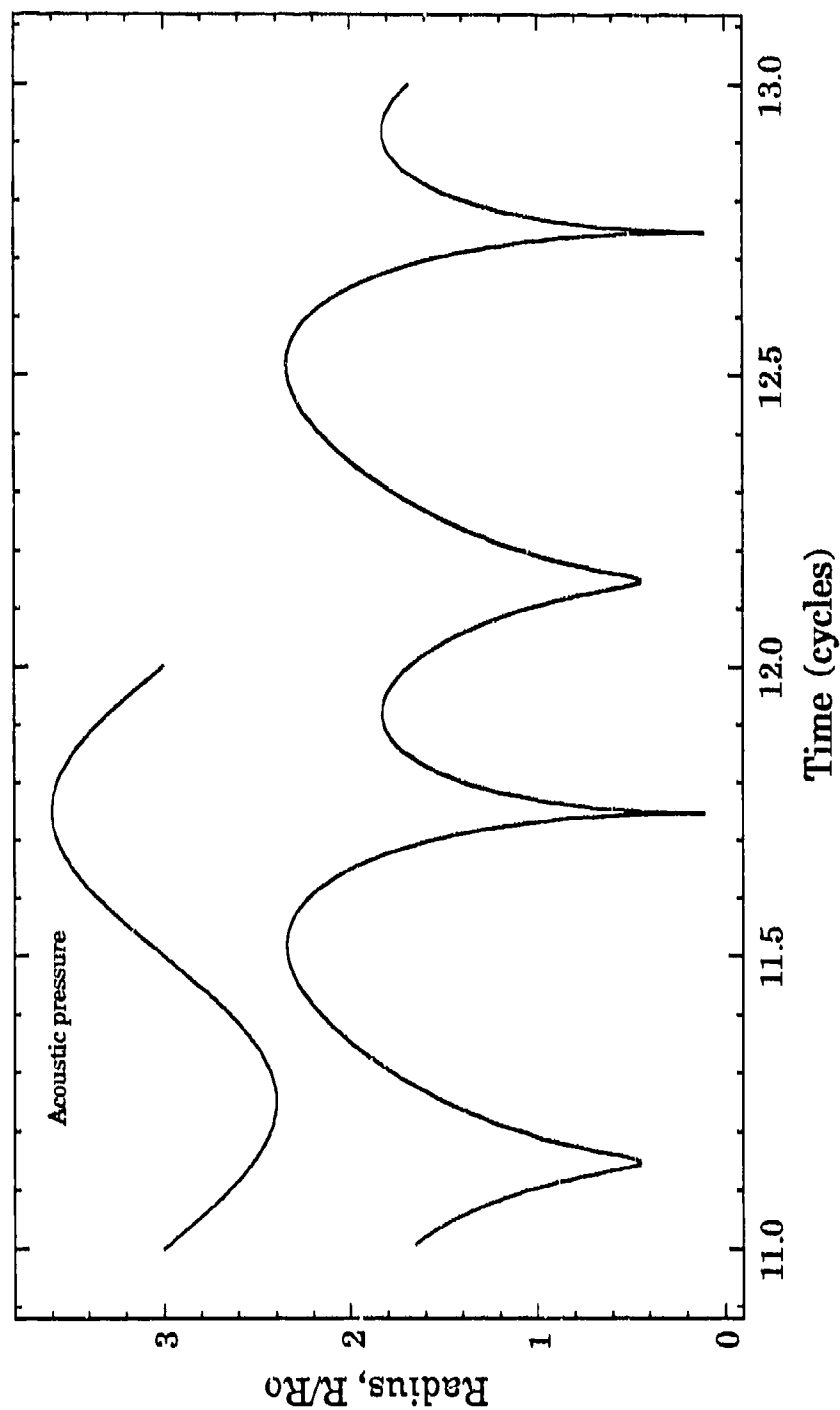


Figure 19. Theoretical radius-time curve calculated using the polytropic formulation for water at $p_4=0.8$ bars, $R_3/R_2=0.39$ and $f=21.0$ kHz.

nonlinear "softening" of the restoring force as the bubble expands. In this case, the shifting causes the left edge of the peaks to steepen and eventually "bend over". At this point, the two solutions exist simultaneously for the same value of the bubble radius, R_o/R_{res} , causing abrupt transitions to occur from one solution to the other for small changes in R_o/R_{res} . Transitions of this type are known as "saddle-node bifurcations" among researchers in the field of nonlinear dynamics.

At pressure amplitudes above 1 bar, the pulsations of small bubbles ($< 40 \mu\text{m}$) develop a characteristic shape. An example of a radius-time curve at large pressure amplitudes is shown in Fig. 20. This particular example is for a $20 \mu\text{m}$ bubble in water at $p_A=1.2$ bar. In general, the motion consists of a relatively slow growth during the first half of the acoustic cycle when the pressure is negative, followed by a rapid collapse and several rebounds. The word "collapse" here refers to the first bubble contraction after R_{max} has been reached, and which is usually very fast and violent. This timing is usually referred to as the phase of the collapse, ϕ_c , and is measured in degrees from the beginning of the negative pressure cycle, where $\phi=0^\circ$. The beginning of the compression cycle corresponds to $\phi_c=180^\circ$. The collapse in Fig. 20, for example, occurs near 220° .

Not surprisingly, the highest temperatures and pressures are generated in the interior of the bubble during this collapse. Fig. 21 is a plot of the temperature inside the bubble for the same conditions as Fig. 20. The large temperature spikes are generated during the violent, nearly adiabatic, collapses. It is during these collapses that sonoluminescence is believed to be generated. Similarly, high pressures are generated in the bubble interior as the gas is rapidly compressed, as

RADIUS-TIME CURVE FOR WATER

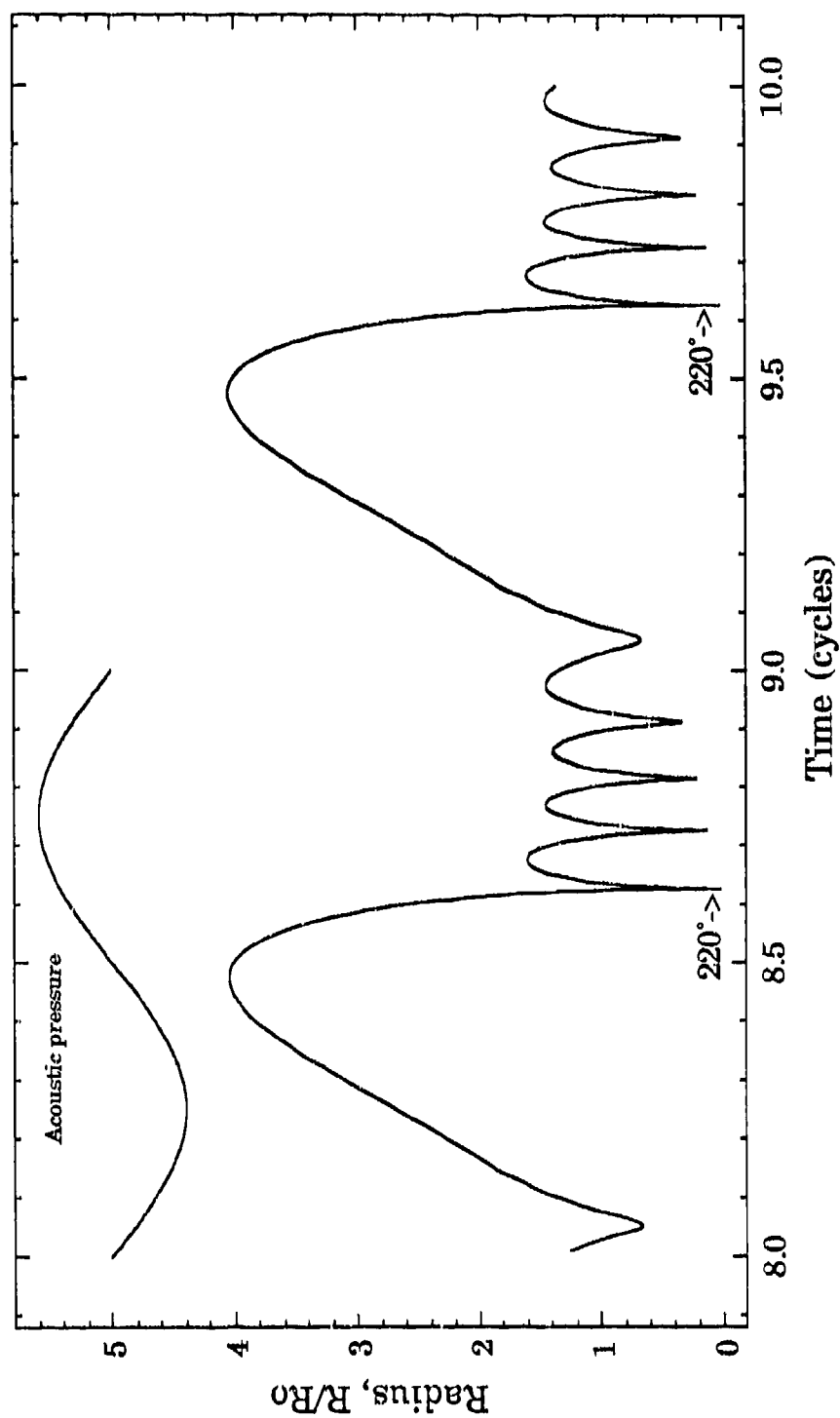


Figure 20. Theoretical radius-time curve calculated using Prosperetti's formulation for water at $p_A=1.2$ bars, $R_0/R_{\infty}=0.14$, $f=21.0$ kHz.

INTERNAL TEMPERATURE for WATER

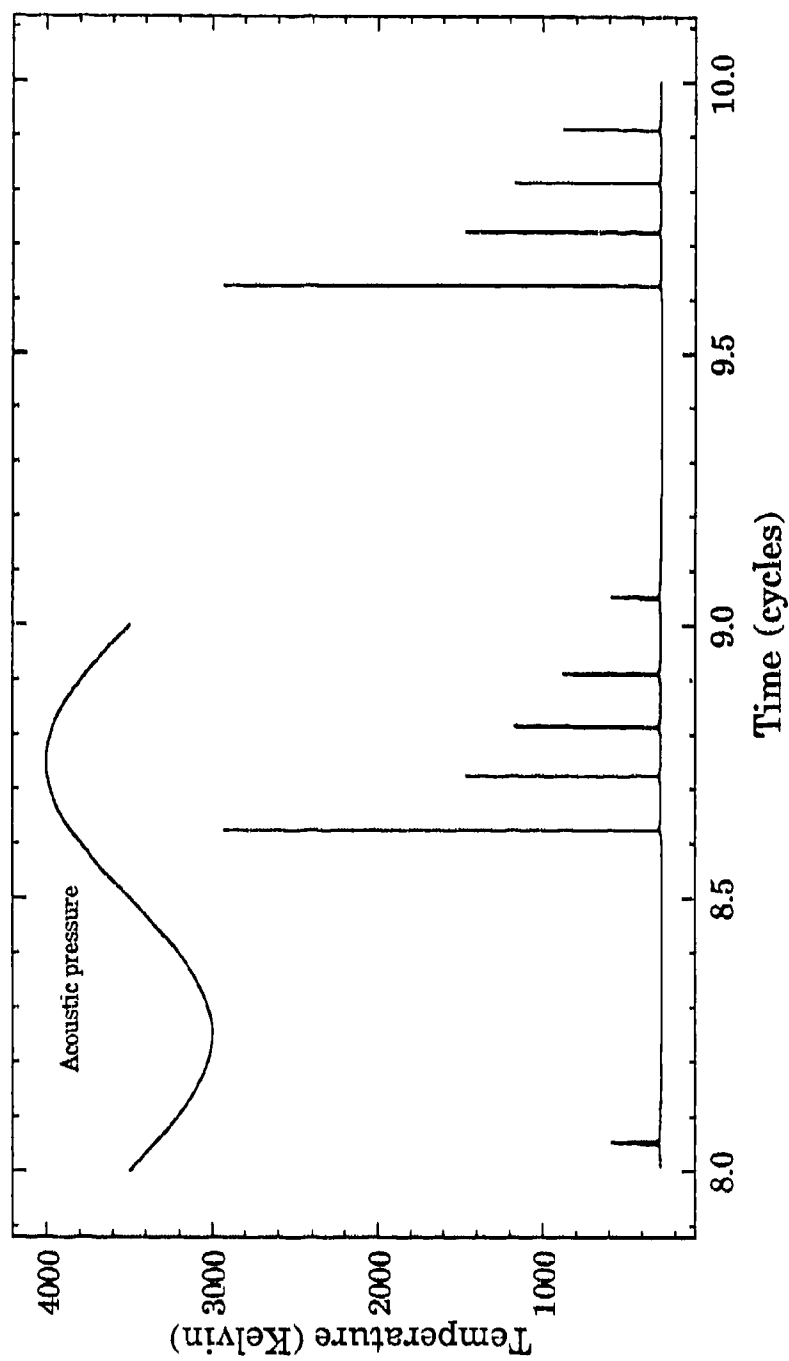


Figure 21. Theoretical internal temperature-time curve calculated using Prosperetti's formulation for the same conditions used in figure 20.

shown in Fig. 22. The data shown in Figs. 21 and 22 are mostly for illustrative purposes, and the values of the maximum temperatures and pressures, T_{max} and P_{max} respectively, are only estimated.

In general, then, three quantities can be used to describe the radial pulsations of bubbles at high pressure amplitudes: the maximum response or pulsation amplitude (R_{max}), the phase of the collapse (ϕ_c) and the number of minima (M) which includes the first minima (i.e., the collapse). Note that, just as for low pressure amplitudes, the number of minima increases as the equilibrium radius decreases.

Up to this point, all quantities have been given a single value for each solution assuming that, after reaching steady state, the solutions have the same period as the driving pressure. This is not always the case, however, especially at high pressure amplitudes where nonlinear effects are more prominent. In this regime and under certain conditions, the motion of the bubble is such that it repeats itself only after a multiple number of acoustic periods. This is usually referred to as subharmonic motion ($n=2,3,\dots$). For example, subharmonic motion of period two ($n=2$), also known as period-two motion, occurs when the period of the radial pulsations is twice the period of one acoustic cycle ($T_R=2T$). In this case, the values of R_{max}^i , ϕ_c^i and M^i where the superscript $i=1,2$, i.e., they alternate between two different values from one acoustic period to the next. Although period 3, 4, ...etc. are possible, only period-two solutions were found numerically for the conditions used in the experiments. Examples of period-two motion can be found in the response curve shown in Fig. 23 calculated for a bubble driven at 1.2 bars in water according to Prosperetti's formulation. This type of motion is indicated by

INTERNAL PRESSURE for WATER

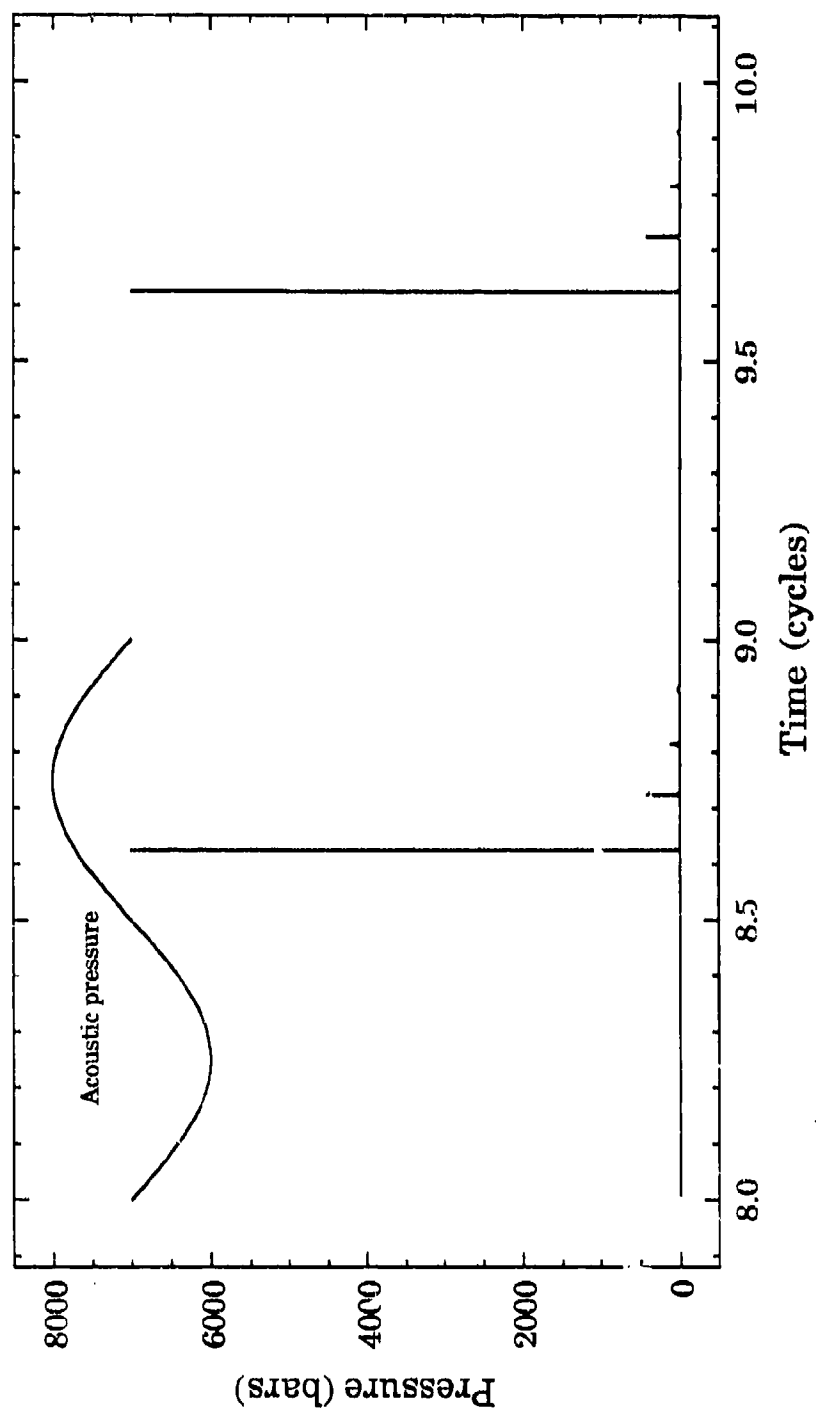


Figure 22. Theoretical internal pressure-time curve calculated using Prosperetti's formulation for the same conditions used in figure 20.

BUBBLE RESPONSE CURVE for WATER

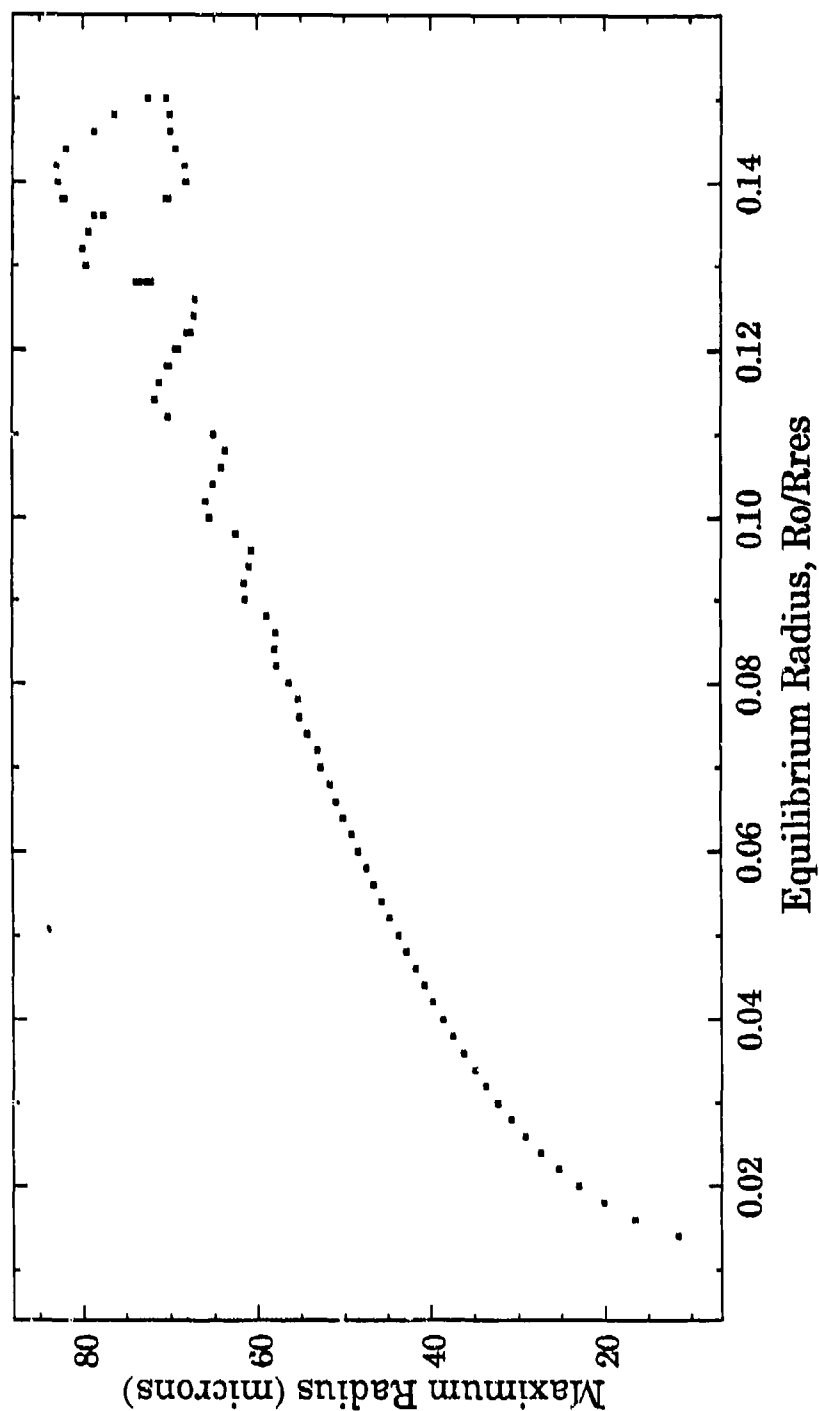


Figure 23. Theoretical bubble response curve calculated using Prosperetti's formulation for water at $p_A=1.2$ bars and $f=21.0$ kHz. $R_{res}=150$ μm .

the double value of the maximum radius for each value of R_o/R_{res} , and is usually referred to as a period-doubling or pitchfork bifurcation. It should be noted that the values of R_{max}^i plotted in Fig. 23 and all subsequent similar plots did not occur during the same phase of the driver, as is usually done in the "Poincaré sections" often used in the nonlinear dynamics literature. Instead, values of R_{max} are calculated over each acoustic period. For the rest of this dissertation, the superscript i will be dropped from the quantities R_{max} , ϕ_c and M , unless confusion is likely to arise. For the parameters of interest in this study, R_{max} was usually found to occur near the same phase, e.g., 200 degrees. The peaks observed in Fig. 23 are due to nonlinear resonances of the radial motion encountered as the equilibrium bubble radius changes. The height of these peaks is usually dependent on the amount of damping included in the model.

Similarly, a period-two bifurcation can be seen in the phase of collapse curves at $R_o/R_{res} \approx 0.14$ (20.3 μm) in Fig. 24. The data in this figure were calculated using the same conditions as in Fig. 23. Not only does the bifurcation occur in the same location, but every change in the curve does as well; i.e., an increase (decrease) in R_{max} results in an increase (decrease) in ϕ_c . This correlation is not surprising since a larger response requires the bubble to spend additional time during the growth and collapse phase. Since a larger pulsation amplitude results in a stronger collapse (other parameters remaining constant), then a greater phase of collapse corresponds to a more violent collapse. Thus, after the period-doubling bifurcation occurs, the uppermost branch corresponds to the larger pulsation amplitude and the stronger collapse. A "stronger" collapse means a smaller collapse ratio (R_{min}/R_o) which generates higher gas densities, as well as higher

PHASE OF COLLAPSE for WATER

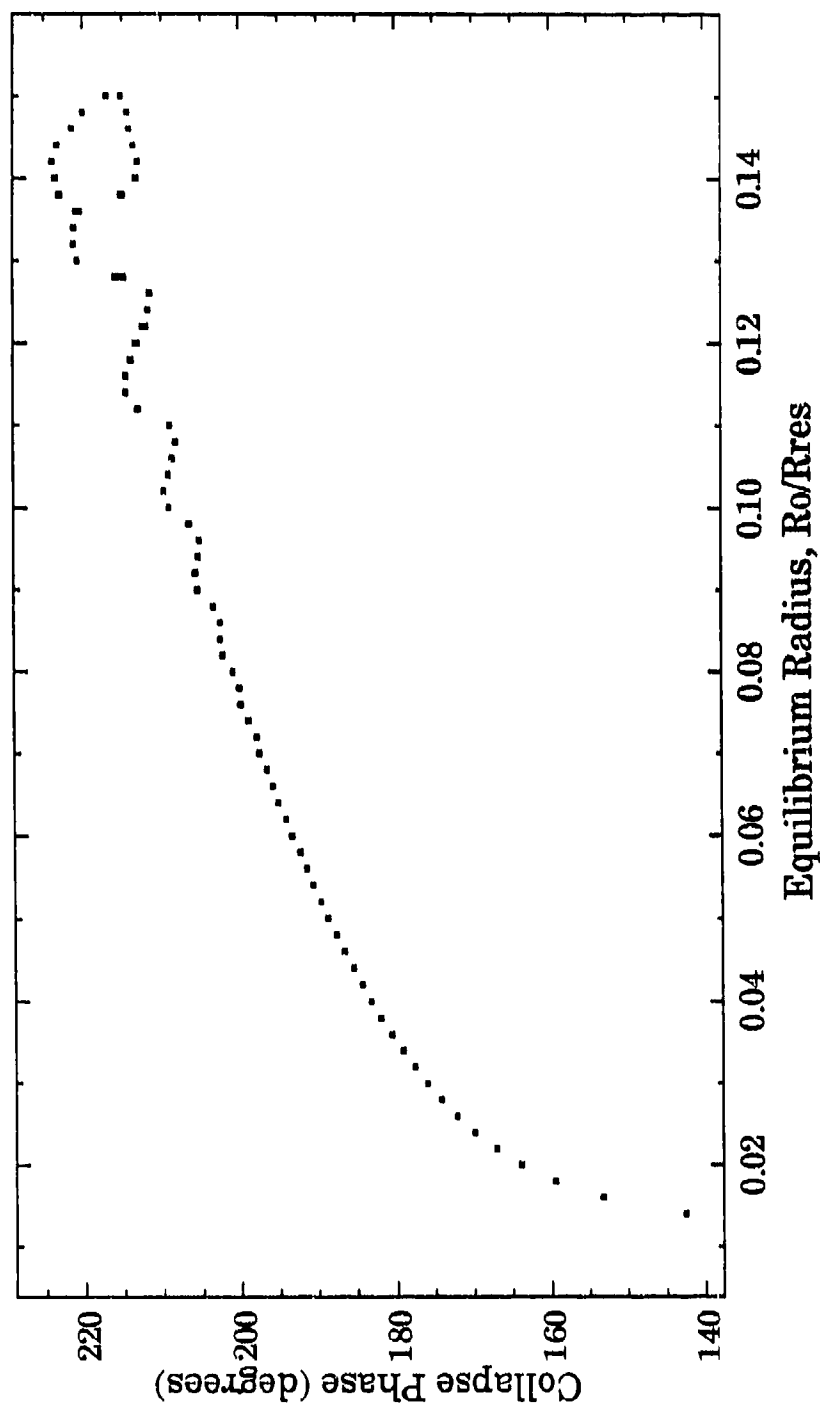


Figure 24. Theoretical phase of bubble collapse calculated using Prosperetti's formulation for the same conditions used in figure 23.

temperatures and pressures. This is illustrated in Figs. 25 and 26 where the maximum internal temperature (T_{max}) and pressure (P_{max}) generated during each period has been plotted, respectively, for the same conditions used in Fig. 23. T_{max} has been averaged over the bubble interior. Again, note that these two quantities are directly correlated to the pulsation amplitude. Also note the high sensitivity of the temperature and pressure to the pulsation amplitude, i.e., a small change in R_{max} results in a fairly large change in T_{max} and P_{max} . The close relationship among the quantities R_{max} , ϕ_c , T_{max} , and P_{max} will be useful in Chapter IV where the experimental results will be discussed.

III. B. 3 Limitations of the Theoretical Formulations.

The range of acoustical parameters being considered in this study has been determined by the measurements made during the experiments. These parameters are the following: driving frequencies between 21 and 25 kHz, pressure amplitudes between 1 and 1.5 bars, and bubble radii between 15 and 25 microns for five different water/glycerine mixtures. For these parameters, the temperatures and pressures generated inside the collapsing bubbles have been measured and calculated in this and other studies (see Chapter I) to be on the order of thousands of degrees Kelvin and thousands of bars. To date, no model of cavitation exists which can treat the gas - or even the adjacent liquid - inside a collapsing bubble adequately for these extreme physical conditions. Each of the models considered in this study makes different approximations when treating the bubble's interior. In order to compare the results of the different formulations,

MAXIMUM TEMPERATURE CURVE FOR WATER

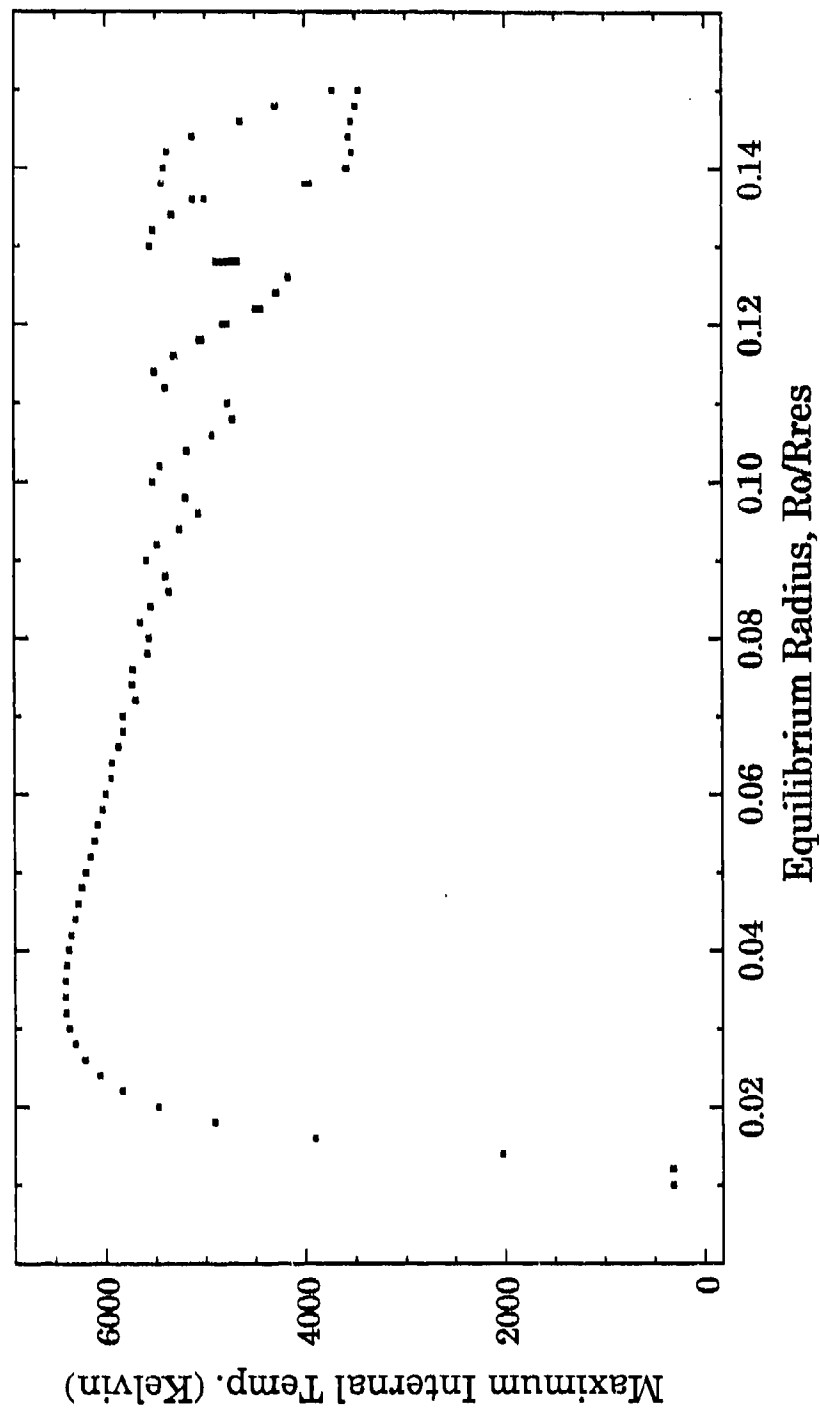


Figure 25. Theoretical internal temperatures calculated using Prosperetti's formulation for the same conditions used in figure 23.

MAXIMUM PRESSURE CURVE for WATER

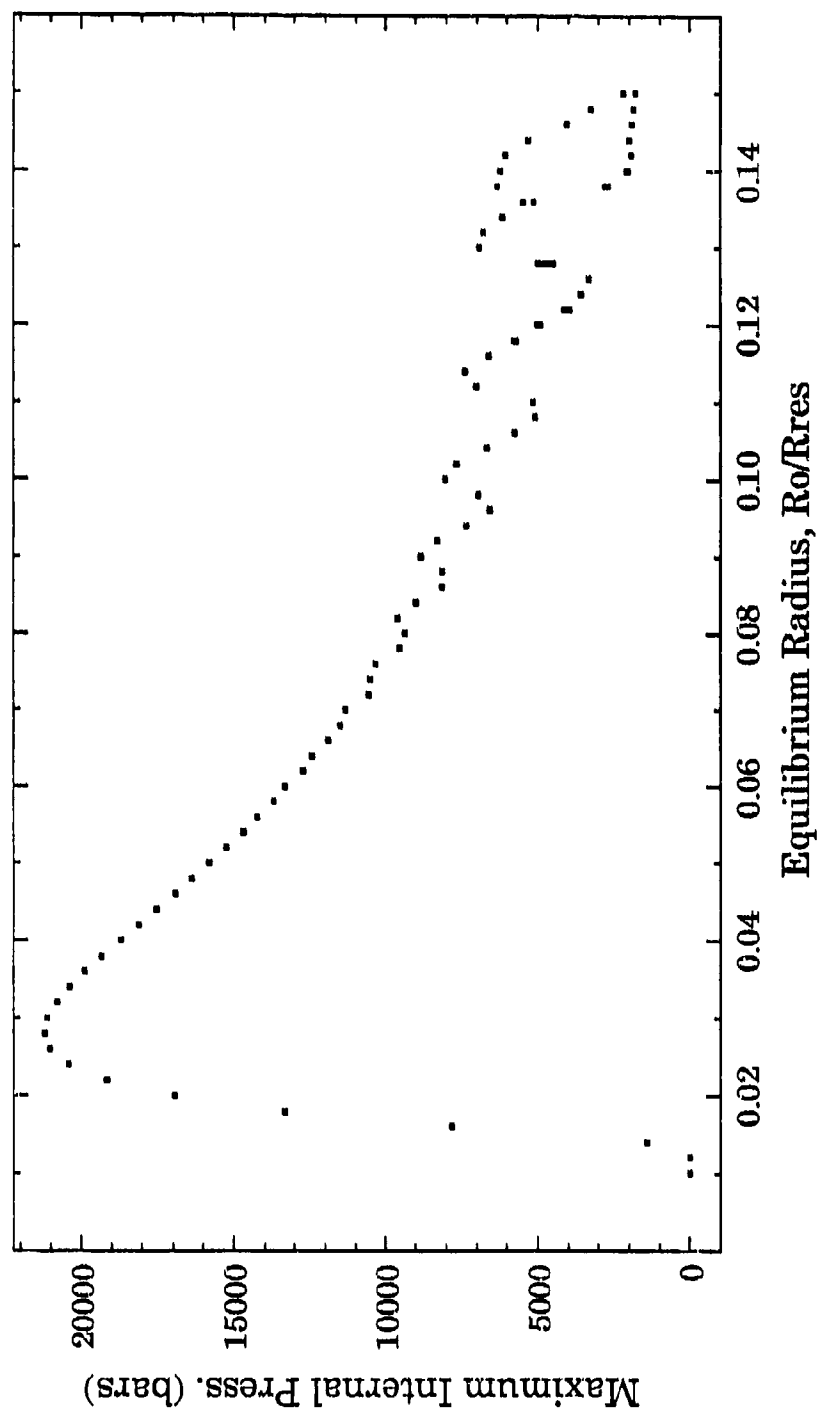


Figure 26. Theoretical internal pressure calculated using Prosperetti's formulation for the same conditions used in figure 23.

the assumptions and limitations of each must be considered. These assumptions and their general validity for the physical conditions encountered during the calculations are discussed in this Section. Although we have no *a priori* certainty of the accuracy of the theoretical results, an evaluation of the validity of the assumptions will be made at the maximum values of temperature and pressure predicted by the more reliable models, for the range of experimental parameters stated above. These values represent the worst-case scenario predicted by the theories and should provide a good test case to their applicability. These values are 10,000 K and 30,000 bars for the gas temperature and pressure, respectively, and 2,000 K and 30,000 bars for the liquid. For the collapse ratio, (R_{min}/R_o) , a value of 0.12 is used, which corresponds roughly to a 500-fold increase in the gas density. A wall velocity of the order of the speed of sound in the gas (340 m/sec measured at STP) is also used.

Five major assumptions were made in deriving the three formulations considered in this study. Four of them are common to all the models. These are: (a) The bubble remains spherical; (b) The bubble contents obey the ideal gas law; (c) The internal pressure remains uniform throughout the bubble; and (d) No evaporation or condensation occurs inside the bubble. The fifth assumption pertains to the thermodynamic behavior of the liquid surrounding the bubble. Let us now consider the first four assumptions.

Although most criteria of surface instabilities (discussed in the next Section) do not predict the bubble motion to remain radially symmetric under the conditions given above, assumption (a) is believed to remain valid based on the

experimental observations, namely the light scattering data. This evidence will be presented in Chapter IV in more detail.

The ideal gas law assumption (assumption (b)) is known experimentally to be valid in the limit as the specific volume v (volume/unit mass) approaches infinity, or, equivalently, as the pressure of the gas approaches zero. The simplest way to test this assumption is by considering van der Waals equation of state,

$$\left(p - \frac{a}{v^2}\right)(v - b) = R_g T, \quad (3.30)$$

where R_g is the universal gas constant. The term a/v^2 is intended to correct for the intermolecular attraction and the constant b to account for the volume occupied by the molecules. At the minimum volume considered in this study, i.e., when $R_{min}/R_o = 0.12$, the term $a/v^2 \leq 0.1$ bars. For the same conditions, the value of b corresponds to a correction to the volume of less than 0.5 per cent. Thus, for all practical purposes, assumption (b) may be considered valid.

Assumption (c) states that the momentum equation (3.13) reduces to $p=p(t)$. The pressure perturbation contributed by each term in the momentum equation has been considered by Prosperetti (1988). He concluded that

$$\frac{\Delta p}{p} = O\left(M_B \frac{R}{c_g t_o}, M_B^2\right) \quad (3.31)$$

where M_B is the Mach number of the bubble wall, c_g is the speed of sound in the gas and t_o is a characteristic time. If t_o is substituted by the theoretical minimum collapse time (~ 10 nsec), R by the equilibrium radius (15 microns), and c_g by its value at the maximum temperature reached inside the bubble, then $R/c_g t_o$ has the

value of ~ 1 . Equation (3.31) then reduces to $\Delta p/p = O(M_B)$. When the temperature dependence of c_g is taken into account, the Mach number for the bubble wall M_B was found to be around 0.2. It thus appears that pressure perturbations may occur inside the bubble in some cases, although the conditions necessary for the formation of shock waves inside the bubble are not likely to be realized.

Assumption (d) states that no condensation or evaporation occurs during the bubble motion. Evaporation would occur during the collapse when the gas temperature is increased by the mechanical work done by the liquid. Some of this energy is transferred to the liquid through regular thermal conduction, causing some liquid molecules to evaporate. As the bubble rebounds and expands rapidly, the temperature is decreased, causing the same molecules to condense, releasing heat into the gas. The result of this process is to transfer energy from one part of the cycle to the other, acting as a form of thermal damping. It should also be noted, however, that collapse times are on the order of tens of nanoseconds which limit the amount of energy deposited into the liquid. Thermal relaxation times of water are on the order on microseconds. According to the models, temperatures as high as 2000 K may be reached in the liquid side of the interface, as stated above. If we assume that this is the case, there is little doubt that assumption (d) is invalid to some extent, although the short time (≤ 20 nsec) during which these temperatures persist will probably limit the amount of vaporization. In order to estimate this amount, the temperature and pressure during the collapse should be compared to the vapor pressure curve for the liquid. This has been done in Fig. 27 by plotting the pressure vs. temperature in the liquid during one acoustic period for a 20 μm bubble driven at 1.45 bars at 23.6 kHz representing the conditions

PRESSURE vs TEMPERATURE for 42% GLYCERINE

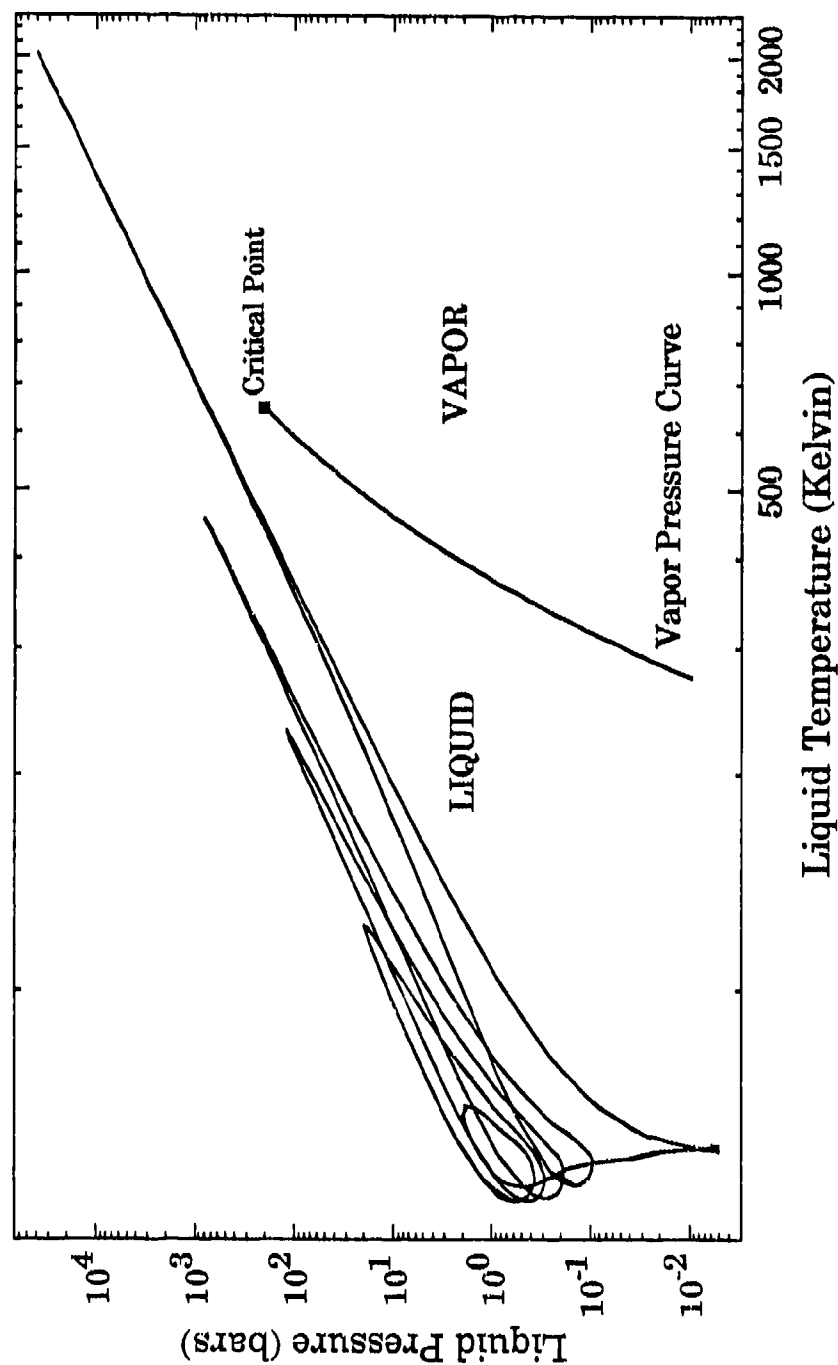


Figure 27. Theoretical liquid pressure vs. liquid temperature at the interface during one acoustic period for GLY42, $R_0 \approx 20 \mu\text{m}$, $p_A = 1.5 \text{ bars}$ and $f = 23.6 \text{ kHz}$. These data were calculated using Flynn's formulation.

stated at the beginning of this Section. The vapor pressure curve for water is also shown, which defines the boiling point of the liquid as follows: if at a given temperature the pressure exerted on the liquid is less than its vapor pressure, then the liquid boils. The vapor pressure curve of water was used in Fig. 27 since the vapor pressure of glycerine is lower. It can be seen from this figure that the boiling point of the liquid is never reached for values below the critical point. At the critical point, the liquid and vapor phase do not separate, i.e., there is no real difference between the two phases. In this case, the latent heat of vaporization is zero and no thermal damping due to vaporization exists. Nevertheless, the thermodynamic properties of the bubble would be very different from those assumed at equilibrium, and the model becomes invalid under these conditions. Thus, of the four assumptions considered, (d) is the most likely to be violated.

The fifth major assumption made in the formulations pertains to the thermodynamics in the bubble's interior. This assumption is reflected in the expression for the internal pressure, p_g . The approximations made in each formulation in order to obtain this expression will be discussed next.

First, let us consider the least sophisticated of the models, the polytropic approximation model. This model is mostly limited by the small-amplitude linear approximation made in calculating the polytropic exponent. In addition, this approximation makes the integral over a cycle of $p \cdot dv$ identically zero, resulting in no net loss of energy associated with the heating and cooling of the gas (Prosperetti, 1988), i.e., no thermal damping. This type of damping is known to be the main energy dissipation mechanism for the parameters under consideration. Furthermore, the polytropic exponent is nearly equal to 1, i.e., the bubble motion is

isothermal, for these same parameters. This results in the bubbles reaching extremely small radii during the collapse and, therefore, unreasonably high pressures and low temperatures. The values of the internal temperature and pressure obtained with this model were thus considered unrealistic and are not discussed any further in this study.

In Prosperetti's model, a spherically symmetric, time dependent temperature field is obtained in order to evaluate the expression for the internal pressure. The temperature at the bubble wall is assumed to remain undisturbed, i.e. equal to the ambient temperature. This assumption has been shown to be valid at low pressure amplitudes by Prosperetti (1988). By equating the heat fluxes across the interface, he obtained the following expression:

$$\frac{T_c - T_\infty}{T_c - T_s} = \left(\frac{K_g C_{pg} \rho_g}{K_l C_{pl} \rho_l} \right)^{\frac{1}{2}}, \quad (3.32)$$

where T_c and T_s are the center and surface temperatures respectively, and the subscripts g and l indicate values in the gas and liquid respectively. The right-hand side of (3.32) has typical values of 10^{-3} , which indicates that the change of the surface temperature is negligible compared to the gas temperature. During violent collapses, however, values of K_g , C_{pg} and ρ_g can actually approach values comparable to those in the liquid, and the right-hand side of (3.32) becomes as large as $1/3$. In fact, results obtained with Flynn's formulation have shown that the temperature on the liquid side of the interface can reach values $1/3$ times the temperature in the cavity. By assuming that the temperature of the liquid at the interface remains undisturbed, the thermal gradient at the interface becomes

larger, increasing the amount of heat diffusion into the liquid. Thus, it is expected that the results of this model would be overdamped for the parameters under consideration.

In Flynn's model, the energy equation in the liquid is included in the derivation of the expressions for the internal pressure and temperature. In order to reduce the amount of computer time, however, Flynn was forced to make further approximations. Although Flynn's formulations appears more complicated, it was found that they both required about the same amount of computer time to obtain the solutions for the parameters used in this study.

In Chapter IV, theoretical results of these three models will be presented and compared with each other. The only known comparison of theoretical results of bubble pulsations using different models is that by Lastman *et al.* (1980) who considered five different radial equations. They assumed adiabatic motion and found "similar quantitative behavior, even under intense cavitation conditions", although they only compared pulsation amplitude and phase of collapse. As shown above, however, the internal temperature and pressure during the collapse are very sensitive to R_{max} and ϕ_c . Thus, it is expected that the major difference among the theoretical results of the formulations considered in this study will be in the internal temperature and pressure.

III. C. Surface Instabilities

In order to understand the long term behavior of bubbles (over thousands of acoustic periods) in cavitation fields, the different mechanisms controlling the size

and shape of the bubbles must be considered first. The two principal mechanisms are gas diffusion across the gas-liquid interface and surface instabilities. Both of these processes can cause the bubble to either grow or shrink depending on the physical conditions. Surface tension, by creating a concentration discontinuity across the interface, forces gas out of the bubble. On the other hand, this diffusion can be "rectified" by the action of the sound field, and the bubble can be made to grow. Likewise, surface waves can aid in the growth or dissolution process through the generation of acoustic streaming near the bubble (Gould, 1975). Surface waves also have been observed to cause the ejection of microbubbles, serving as an efficient mechanism of bubble-size reduction (Neppiras *et al.*, 1969). Thus, the time evolution of acoustically driven bubbles is controlled by many factors and the fate of each bubble is determined by, among other things, its equilibrium size and the driving pressure amplitude. In this Section, some theoretical background of surface instabilities will be presented as well as a recent instability threshold curve calculated and measured by Horsburgh (1990). The phenomenon of rectified diffusion will be discussed in the following Section.

When a large bubble is driven at high enough amplitudes, it has been observed to become unstable, usually breaking up into a cloud of smaller bubbles. Smaller bubbles, however, are able to retain their spherical shape longer due to the stronger surface tension effects. These instabilities are caused by the large accelerations experienced during the collapse of the bubble and near the point of minimum radius where the motion is rapidly stopped and reversed. An order of magnitude calculation indicates that a liquid-gas interface becomes unstable

when the inward acceleration of a bubble wall exceeds a critical value $4\sigma/\rho R^3$ (Hsieh *et al.*, 1960).

When bubbles become spherically unstable in a levitation cell, they can be seen to move about in an erratic manner, apparently due to the nonlinear coupling between the sound field and the surface oscillations. The visual observation of this "dancing" motion was used by Eller and Crum (1970) to measure the pressure threshold for instabilities for a range of bubble radii. Except for the less common occurrences of stable surface oscillations, instabilities usually become visually obvious to the observer, especially if the driving pressure is relatively large. This surface oscillation threshold has been measured and calculated in the past by several people (Plesset, 1954; Hsieh, 1974; Prosperetti, 1978) and more recently by Horsburgh (1990).

The calculation of the threshold for surface waves made by Horsburgh (1990) for R_0 in the range 10-60 microns is shown in Fig. 28. These calculations were made for air bubbles in water. Combinations of R_0 and p_A above this curve result in the excitation of surface waves, while those below do not. The oscillations of this curve are due to the harmonic resonances of the radial motion. At these resonances, lower pressure amplitudes are required to excite surface waves, due to the larger bubble response. The curve in Fig. 28 will be used to demonstrate the existence of previously unknown islands of stability in the region above this threshold curve. For completeness, a brief description of the equations used to calculate this threshold is included here. The reader is referred to Horsburgh (1990) for more details. The model is briefly described as follows:

THRESHOLD CURVE for SURFACE WAVES

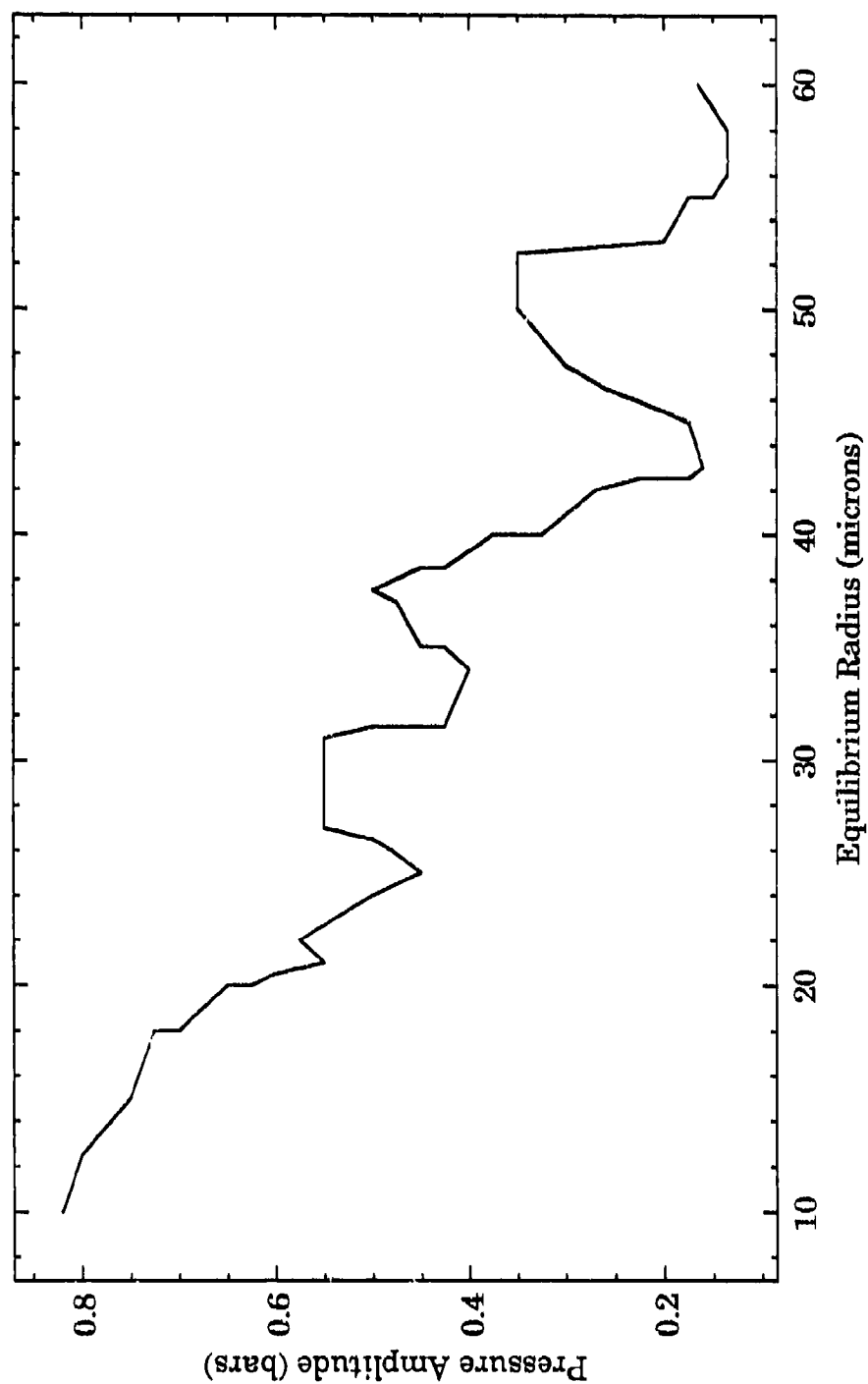


Figure 28. Pressure amplitude threshold curve for the excitation of surface waves calculated by Horsburgh (1990) at $f=22.2$ kHz for air bubbles in water.

Let the bubble boundary be perturbed from a spherical surface of radius R to a surface with radius vector of magnitude r_s . Then one may write

$$r_s = R + \sum_n a_n Y_n, \quad (3.33)$$

where Y_n is a spherical harmonic of degree n , and the a_n 's are functions of time to be determined. The growth or decay of $a_n(t)$ from a small initial value determines whether the spherical shape is stable or unstable. Assuming that

$$a_n(t) \ll R(t), \quad (3.34)$$

and keeping only terms of 1st order in a_n in a linearized perturbation procedure, Plesset (1954) found that the a_n 's are independent of each other and that they satisfy the following differential equation:

$$\ddot{a}_n + \frac{3}{R} \dot{R} \dot{a}_n - A a_n = 0. \quad (3.35)$$

Assuming that the density of the liquid is much greater than that of air, A is given by

$$A = \frac{(n-1)}{R} \ddot{R} - (n-1)(n+1)(n+2) \frac{\sigma}{\rho_l R^3}. \quad (3.36)$$

These equations were derived using an incompressible and inviscid liquid assumption and will thus be integrated along with the corresponding radial motion equation, namely Rayleigh-Plesset's:

$$R \ddot{R} + \frac{3}{2} \dot{R}^2 = \frac{1}{\rho_l} \left(p_s(R, t) - p_A(t) - \frac{2\sigma}{R} - \frac{4\mu\dot{R}}{R} \right) \quad (3.37)$$

where all the variables are defined as in Section B of this chapter and usually, a polytropic approximation is assumed. The threshold, p_t^{SW} , is defined as the value of p_A below which the coefficients a_n decrease and above which they increase in time.

III. D. Rectified Diffusion

Rectified diffusion is a nonlinear phenomenon in which a gas bubble in a liquid can be made to grow by the action of the sound field. This phenomenon is a second order effect in the radial pulsations (proportional to ΔR^2) and constitutes an important mechanism for the instability of a bubble in an acoustic levitation system. Although its effects usually are noticeable only over hundreds of thousands of periods, eventually it causes the bubble to exceed resonance size and to be ejected from the sound field. Before this occurs, however, the bubble will often develop surface instabilities which usually result in bubble breakup. In this way, rectified diffusion is an indirect cause of bubble instabilities.

In this study, we are concerned with the validity of the available rectified diffusion formulations at high amplitudes. As expected, most of the existing formulae for calculating the growth rate of bubbles have been obtained after making several approximations, the most notable one being that a negligible amount of gas diffuses into the bubble during one acoustic period. As pointed out

by Eller and Flynn (1965), this is not always the case for large amplitude pulsations. However, because of the complexity of the mathematical problem and the time constraints, the formulation developed by Eller and Flynn (1965) in which the above approximation is made will be used here. The model can be applied to any periodic radius-time curve and in this respect it is rather general. Using an integration routine written by Church (1988), the rectified diffusion threshold shown in Fig. 29 was calculated. The threshold p_i^{RD} was calculated for 70% air-saturated water at 21 kHz for R_0 in the range 5-60 microns. For a given R_0 , bubbles driven at a value of p_A above this curve will grow while those driven below will shrink in time. Similar to the surface wave thresholds, the curve in Fig. 29 exhibits variations in the threshold p_i^{RD} due to the harmonic resonances of the bubble motion. Generally, at the resonances, a lower value of p_A is needed to make the bubble grow due to the larger response.

The following is a brief outline of Eller and Flynn's formulation for rectified diffusion. As stated before, the main approximation is to neglect any diffusion of gas into the bubble during a single acoustic period. The problem to be solved is thus determining the gas concentration field $c(r,t)$ in the liquid (not the bubble) from which the rate of change of the number of moles of gas in the bubble will be obtained from

$$\frac{dn}{dt} = -4\pi DR^2 \left. \frac{\partial c}{\partial r} \right|_{r=R} , \quad (3.38)$$

where D is the gas diffusion constant and r is the distance from the center of the bubble. The diffusion equation to be used is Fick's law of mass transfer,

THRESHOLD CURVE for RECTIFIED DIFFUSION

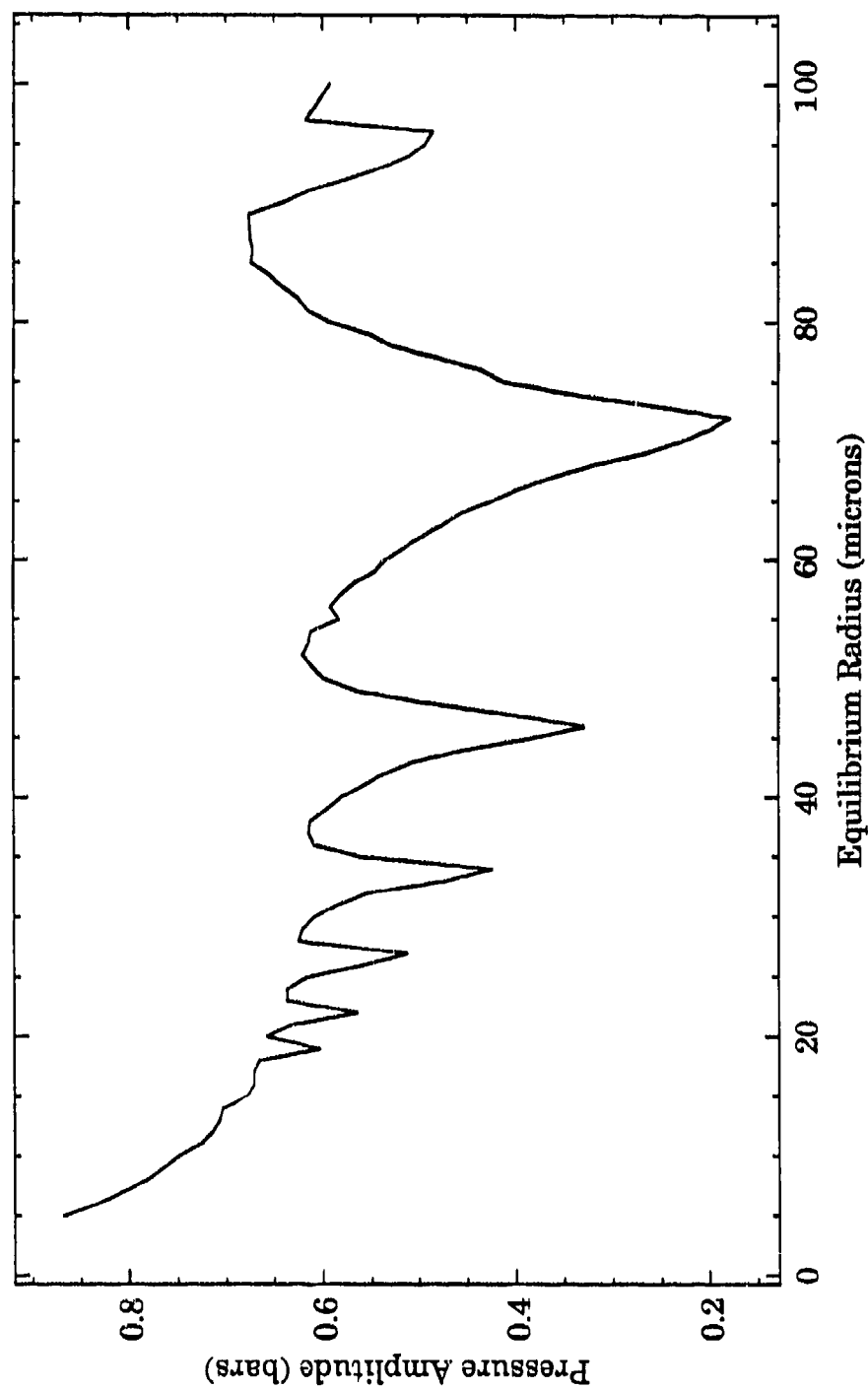


Figure 29. Pressure amplitude threshold curve for bubble growth by rectified diffusion calculated by Church (1990) at $f=21.0$ kHz in 70% air-saturated water.

$$\frac{dc}{dt} = \frac{\partial c}{\partial t} + \vec{u} \cdot \vec{\nabla} c = D \nabla^2 c, \quad (3.39)$$

where \vec{u} is the velocity of the liquid at r . The boundary conditions are given by

$$c(r, 0) = c_i, \quad r > R \quad (3.40)$$

$$\lim_{r \rightarrow \infty} c(r, t) = c_i, \quad (3.41)$$

$$c(R, t) = c_s, \quad t > 0, \quad (3.42)$$

where c_i is the initial, uniform concentration of gas and also the concentration of gas at infinity, and c_s is the concentration of gas in the liquid at the bubble wall. c_s is given by Henry's law, which states that the concentration of gas dissolved in a liquid is directly proportional to the partial pressure of the gas outside the solution. Hence, $c_s = k^{-1} p_g$ where k is Henry's constant and is generally a function of temperature. Introducing a "high" frequency limit in which the rapidly oscillating terms of the gas concentration field are ignored, Eller and Flynn arrived at the following expression for the time-averaged rate of change of the number of moles of gas in a bubble,

$$\frac{dn}{dt} = 4\pi R_o D \left[A + R_o \left(\frac{B}{\pi D t} \right)^{1/2} \right] c_{so} \left(\frac{c_i}{c_{so}} - \frac{A}{B} \right), \quad (3.43)$$

where c_{so} is the value of c_s when $R = R_o$ and A and B are given by

$$A = \frac{1}{T} \int_0^T \frac{R}{R_0} dt \quad \text{and} \quad B = \frac{1}{T} \int_0^T \left(\frac{R}{R_0} \right)^4 dt, \quad (3.44)$$

respectively, t is the time and T is one period of the bubble pulsation. Defining the threshold pressure as the pressure of the acoustic field at which the average diffusion is zero, we have

$$\frac{c_l}{c_0} = \left[1 + \frac{2\sigma}{R_0 p_A} \right] \frac{A}{B}. \quad (3.45)$$

Thus, A and B are calculated for a given R_0 and p_A such that the above equality is satisfied to within a certain criterion. When this criterion is met, the value of p_A is, by definition, the rectified diffusion threshold, p_t^{RD} .

Chapter IV

Results and Discussion

IV. A. Introduction

The first experiment performed in this study was designed to determine the range of active bubble radii in a cavitation field at pressure amplitudes above 1 bar, that is, above the pressure threshold for light emission (sonoluminescence, SL). This determination was made by measuring the phase of SL relative to the sound field and comparing it to the phase of bubble collapse predicted by the different theories of radial bubble pulsations. Because the SL flashes are very short, and assuming that they are emitted at the time of the collapse, one can then measure the phase of SL to determine the phase of bubble collapse. Fig. 30 illustrates these observations by plotting the light flashes as detected by the PMT (top trace) simultaneously with the acoustic pressure (bottom trace) as a function of time. These data were taken at $f=21$ kHz, $p_A=1.5$ bars in water. According to the theories, the phase of bubble collapse varies over a wide range of values depending on the bubble size and pressure amplitude, as can be seen in Fig. 24, p. 93. It is thus possible to estimate the bubble sizes that are active during cavitation by measuring the phase of SL emission, assuming the theories are correct and that SL is emitted during the collapse of the bubble. Furthermore, if enough information is available about the bubble radii and the pressure amplitude, the applicability of the models can be tested.

SONOLUMINESCENCE vs SOUND FIELD

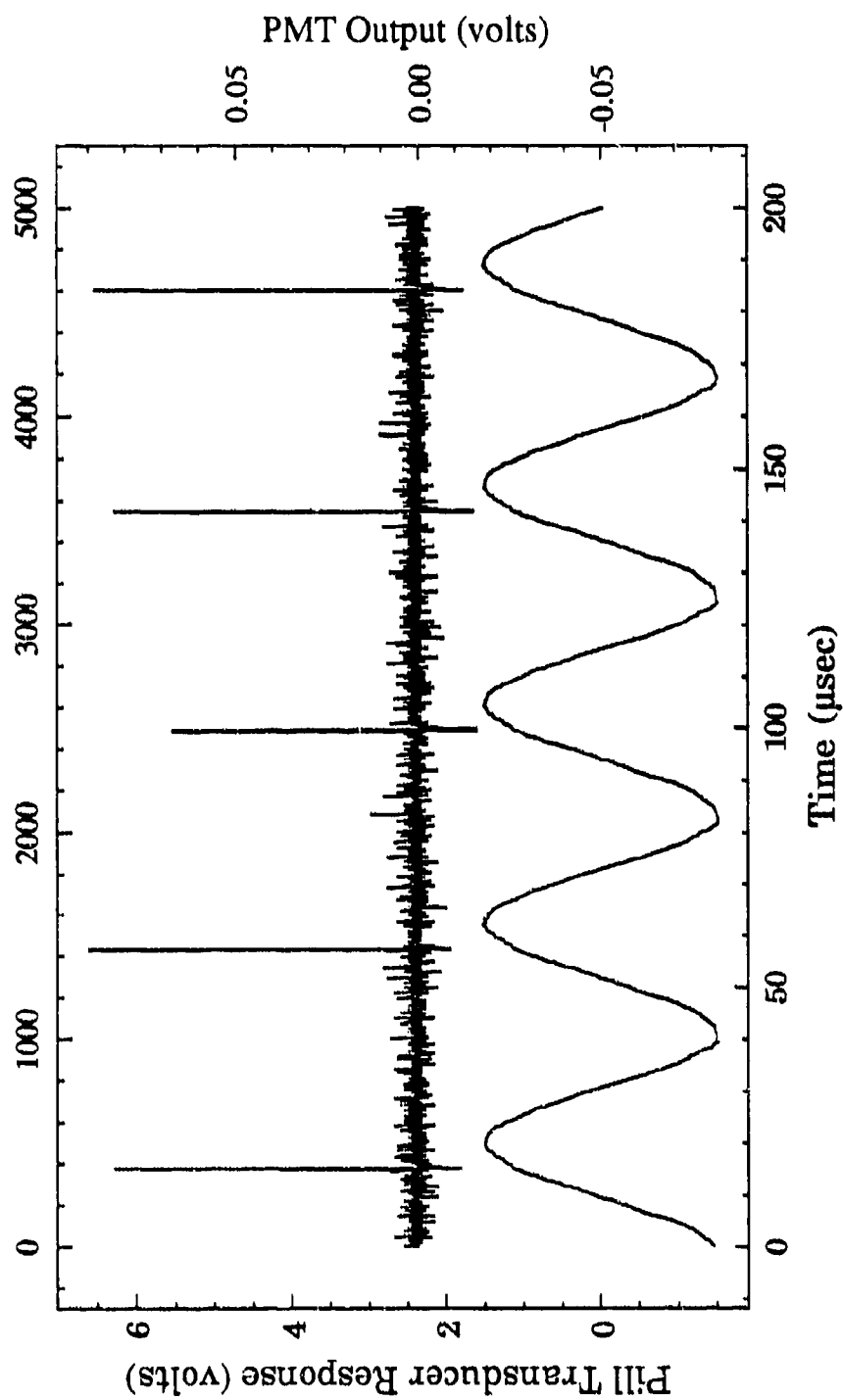


Figure 30. Simultaneous oscilloscope traces of sonoluminescence (top) and acoustic pressure (bottom) for water at $f=21.0$ kHz ($T=47.6$ μm).

This initial experiment was performed in a cavitation field generated in a levitation cell at around 1.5 bars of pressure amplitude. Fig. 31 illustrates the type of cavitation generated for this experiment. This cavitation consists of streamers of bubbles nucleated near the cell wall or the liquid surface and driven towards the pressure antinode by radiation pressure forces also known as Bjerknes forces (Crum, 1975). The phase of SL emission was measured to be about 200 degrees in air-saturated water with a standard deviation as large as ± 15 degrees. These large fluctuations are not due to experimental error. Instead, the large scatter in the data is probably caused by the influence that the cavitation bubbles had on the acoustic pressure field in the levitation cell. More specifically, the sound scattered by the bubbles may be large enough to affect neighboring bubbles, causing the pressure field experienced by each bubble to fluctuate significantly from one acoustic period to the next. Furthermore, the presence of bubbles in the cell is known to change its resonance frequency, causing the cell to "detune" and the pressure amplitude to change. Since the phase of collapse depends on the pressure amplitude, these fluctuations result in a large standard deviation of the data, making the determination of the bubble sizes very imprecise. In addition, the bubbles in the cavitation field could not be assumed to pulsate with radial symmetry, and the effect of asymmetric motion on the phase of the collapse was difficult to determine. The cause of the asymmetric bubble motion will be discussed later. Thus, although the data obtained allowed an estimate of the range of initial bubble sizes based on the theories by assuming a constant pressure amplitude, more data were needed before any comparison between the theories

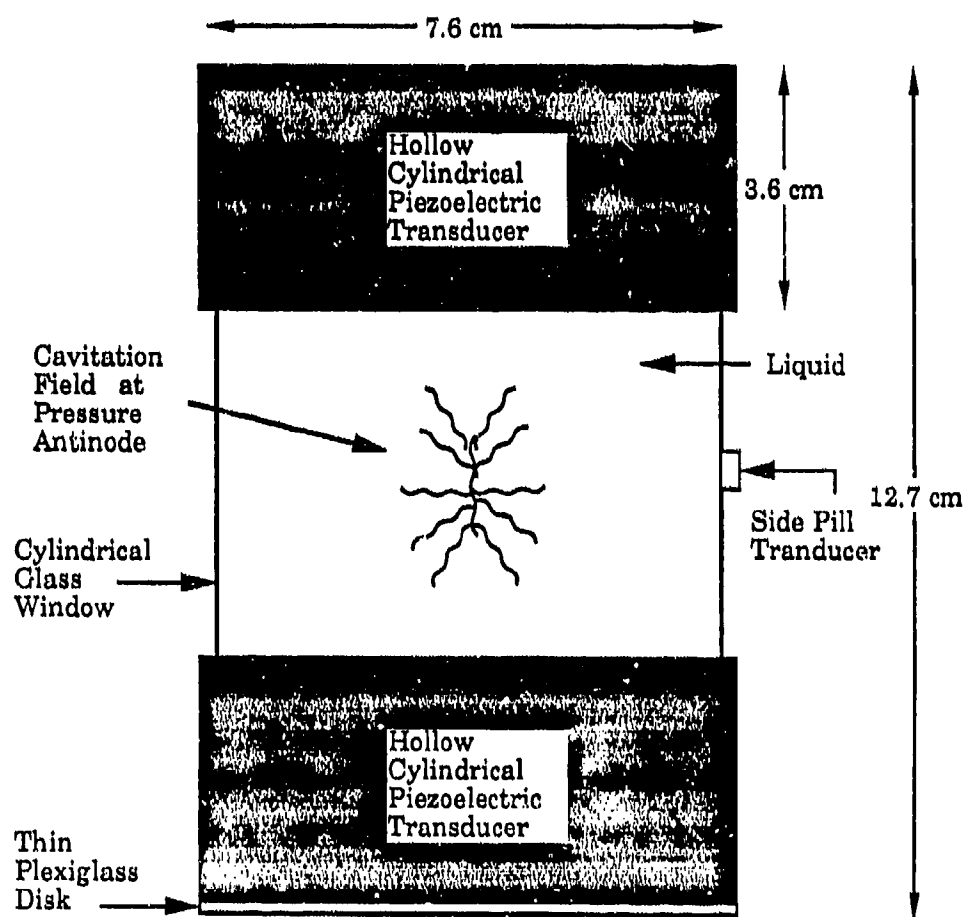


Figure 31. Depiction of cavitation streamers in the cylindrical levitation cell

could be made. Thus, a better experiment for studying cavitation was needed. Fortunately, a solution for overcoming these difficulties was soon found.

During some of the initial experiments it was noted that the scatter in the measurements of the phase of SL was occasionally reduced to less than ± 1 degree, i.e., down to the noise level, making the phase practically constant in time. After many trials the conditions necessary to reproduce this phenomenon were found. It was learned that as the pressure was increased the degassing action of the sound field was reducing the number of bubbles, causing the cavitation streamers to become very thin until only a single bubble remained. The remaining bubble was approximately 20 microns in radius and positioned near the antinode. At this point, it was remarkably stable, remained fairly constant in size and was later determined to be pulsating in a purely radial mode. Furthermore, with the room lights dimmed, a greenish luminous spot the size of a pinhead could be seen with the unaided eye, near the bubble's position in the liquid. The luminous spot was then located at the bubble's geometric center by observing it through a microscope. This light emission was sonoluminescence generated during the collapse of the bubble at its minimum radius. Although this type of luminescence had been observed before by several researchers (Saksena *et al.*, 1970, etc.), very sensitive instruments were usually required and it had never been observed from a single bubble.

The stabilization of a single, radially pulsating bubble was achieved in slightly degassed water-glycerine mixtures with glycerine concentrations below 60%. A description of the visual observations of the stabilization process as the acoustic pressure was increased can be given as follows: After injecting a gas bubble with a

small syringe at about $p_A=0.6$ bars, the bubble exhibited dancing motion indicative of surface waves and asymmetric collapses (Lauterborn, 1982). As the pressure amplitude was increased, the dancing motion became more vigorous, causing the bubble to fragment. A bubble cluster was then formed as the residual bubbles moved around the parent bubble. In glycerine mixtures with concentrations greater than 60%, the radial stability became very difficult, if not impossible, to achieve. The bubble system looked more like a cloud and very often developed into what has been termed a "shuttlecock". When observed through a microscope, the shuttlecock appeared to be a cloud of microbubbles surrounding a larger bubble of approximately 50 μm in radius. Through the interaction with the sound field, this cloud developed a definite pattern of motion from one side of the bubble to the other. In contrast with single bubbles, the position of the shuttlecock was not on the levitation cell's axis but a small distance away from it (0.5-1.0 cm). Microbubbles appeared to be ejected from the side of the cloud directly away from the antinode and were immediately attracted towards the cloud by Bjerknes forces (Crum, 1975). As the microbubbles reached the opposite end of the bubble cloud from which they had been ejected, they were pulled in, possibly by interbubble forces directed towards the center of the cloud. Thus, a rotational pattern was established. For lack of a better analogy, the three dimensional pattern formed by the bubbles has been likened to that formed by the earth's magnetic field lines. The shuttlecock was observed to emit a low rate of SL flashes.

If the amount of glycerine were less than 60%, however, the bubble cluster was observed to become smaller and denser as the pressure amplitude was increased. Just before the stability threshold, the cloud could be seen to collapse

upon itself until, at a rather well-defined value of the pressure, a single radially pulsating bubble emerged. As soon as this transition occurred, the count rate of SL increased to nearly one flash per cycle. Instead of the usual distorted shape when streamers were present, the output of the side pill transducer was now very clean and symmetric. When observed through the microscope, the blurry but unmistakable outline of the radial pulsation could be discerned. When the sound field was turned off, the bubble could be seen to rise towards the surface. The pulsation amplitude was estimated to be between 4 and 5 times the equilibrium radius.

An interesting observation already mentioned was the well defined pressure threshold, p_t^{ST} , at which stability was reached, in addition to a hysteresis effect. After reaching stability, the pressure could be decreased below the threshold p_t^{ST} and stability was maintained. In general, stable bubbles could be driven at values of the acoustic pressure 0.1 bar below the stability threshold. If driven above a certain pressure, the bubble disappeared possibly due to dynamic instabilities. For convenience, we will call these the lower, p_t^{ST} , and upper, p_{ut}^{ST} , stability thresholds respectively. These thresholds are illustrated in Fig. 32. In water, for example, p_t^{ST} was measured to be around 1.2 bars, p_{lt}^{ST} at around 1.1 bars and p_{ut}^{ST} at around 1.3 bars. The range of pressures at which bubbles were stable was $1.1 \leq p_A \leq 1.5$ bars depending on the liquid mixture. For water, it was $1.1 \leq p_A \leq 1.3$ bars whereas for GLY 42 it was $1.3 \leq p_A \leq 1.5$ bars. Thus, higher concentrations of glycerine required slightly higher pressures in order to achieve radial stability. It was also found that these ranges could be enlarged (towards the lower pressures) by decreasing the dissolved gas content of the liquid. As the amount of dissolved

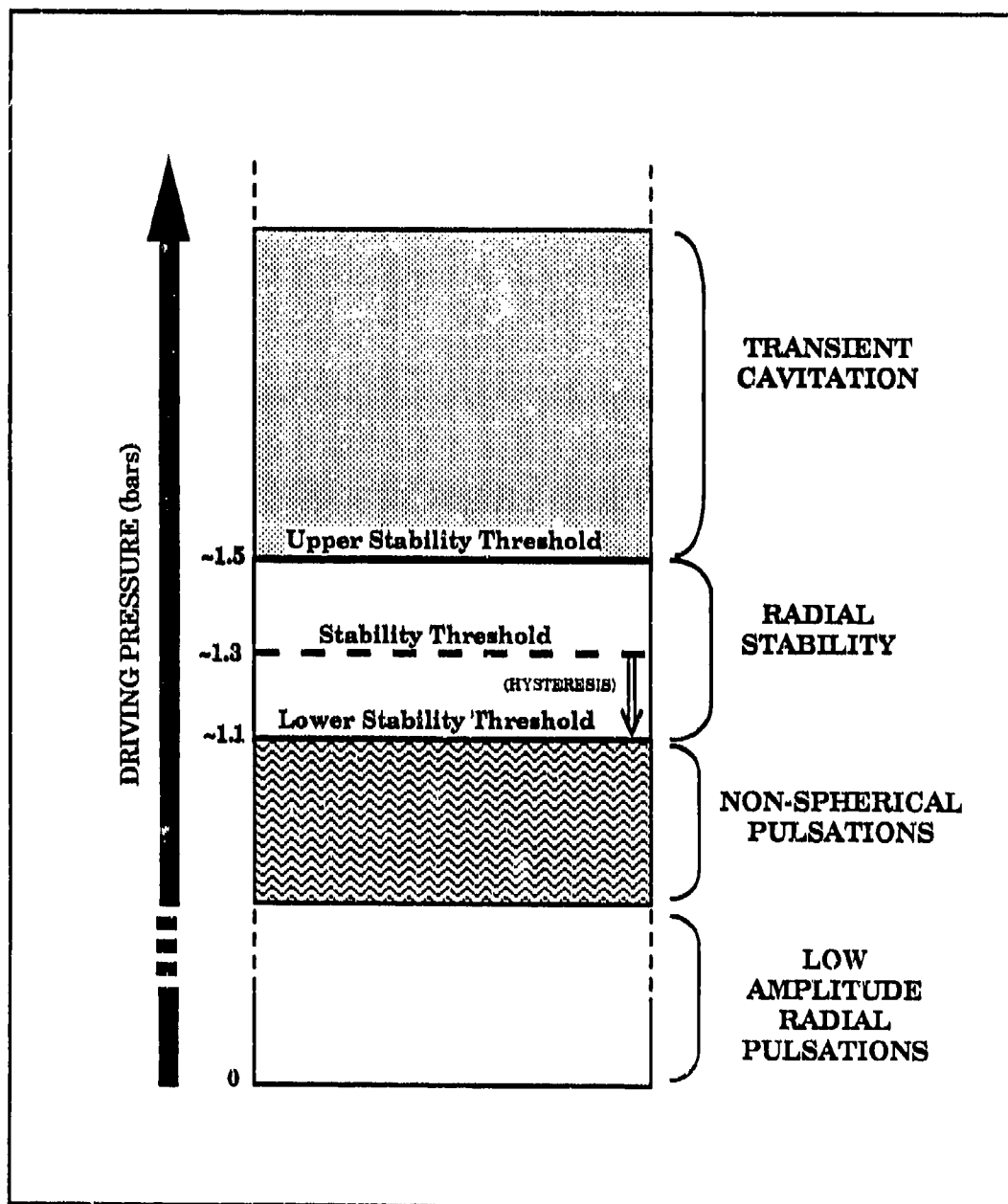


Figure 32. Diagram of the observed radial stability thresholds for 15-20 μm bubbles in water/glycerine mixtures in an acoustic levitation system at $f=21-25$ kHz.

gas increased, regions of instability within the stability pressure range began to appear. The upper pressure threshold, p_{ut}^{ST} , at which the bubble disappeared, remained constant, however. It became clear then that rectified diffusion played an important role in the stability process.

The observation of an upper pressure amplitude threshold, p_{ut}^{ST} , above which pulsating bubbles cannot exist, seems to confirm the existence of a transient cavitation threshold as defined by Flynn (1964, 1975b). According to Flynn (1975b), the motion of bubbles pulsating with an expansion ratio (R_{max}/R_o) above a certain value become inertia controlled. When that happens, the collapse of the bubbles tends to be rather violent, often resulting in the destruction of the bubbles during the collapse. The bubbles studies here ($\sim 20 \mu m$) fall under the "large" category ($> 5 \mu m$) which, according to Flynn's model of cavitation bubbles, should exhibit thermally-related effects (e.g. sonoluminescence) before reaching the transient cavitation (dynamical) threshold. For $20 \mu m$ bubbles, Flynn predicted a dynamical threshold of $R_{max}/R_o \approx 2.2$. These predictions appear to be confirmed by the observations made here, since SL has been observed from stably pulsating bubbles. After reaching a value of the expansion ratio $R_{max}/R_o \approx 4$, the bubbles become unstable, i.e., disintegrate. Although the observed values of the dynamical threshold differ somewhat from those predicted by Flynn, it should be noted that the threshold values defined in his model "most likely act as lower limits to experimental thresholds", as pointed out by Flynn (1975b).

Despite the lack of understanding about the particular mechanisms involved, the discovery of a single bubble pulsating at large amplitudes has many important consequences. Among these is the ability to acquire new, previously unavailable

and more accurate data about the motion of bubbles in cavitation fields. These data include (i) an experimental radius-time curve of the bubble, which allowed us to measure the phase of the collapse, (ii) the phase of sonoluminescence emission, and (iii) the pulsation amplitude which can be used to test the applicability of the bubble models. In addition, the simultaneity of SL and the collapse of the bubble may be verified. We will present the results of the single bubble experiments first, along with the theoretical results. After this, the results of the measurements of the phase of SL in multibubble cavitation fields will be discussed.

IV. B. Light Scattering Experiments

1. Comparison between Theories and Experiment: Prosperetti's Theory

a. Radius-time Curve of a Single Bubble

Figure 33 shows a plot of the bubble radius *vs* time (R-t) at $p_A=1.2$ bars in GLY21 as measured by the photodetector. This figure is a single trace obtained from the LeCroy oscilloscope. The y-values have been converted from intensity to radius using the transfer function obtained during the calibration procedure (Section II.D.2.a). The uncertainty has been calculated to be about $\pm 5 \mu\text{m}$. This figure is a typical example of an R-t curve obtained from a single bubble pulsating at large amplitudes with a period equal to that of the driving pressure. R-t curves for a range of pressures between 1.1 and 1.5 bars were obtained for all the liquid mixtures. The pressure amplitude was determined with an accuracy of about ± 0.1 bars, although changes of $\Delta p_A = \pm 0.01$ bars were possible with the apparatus used in

EXPERIMENTAL RADIUS vs TIME for GLY21

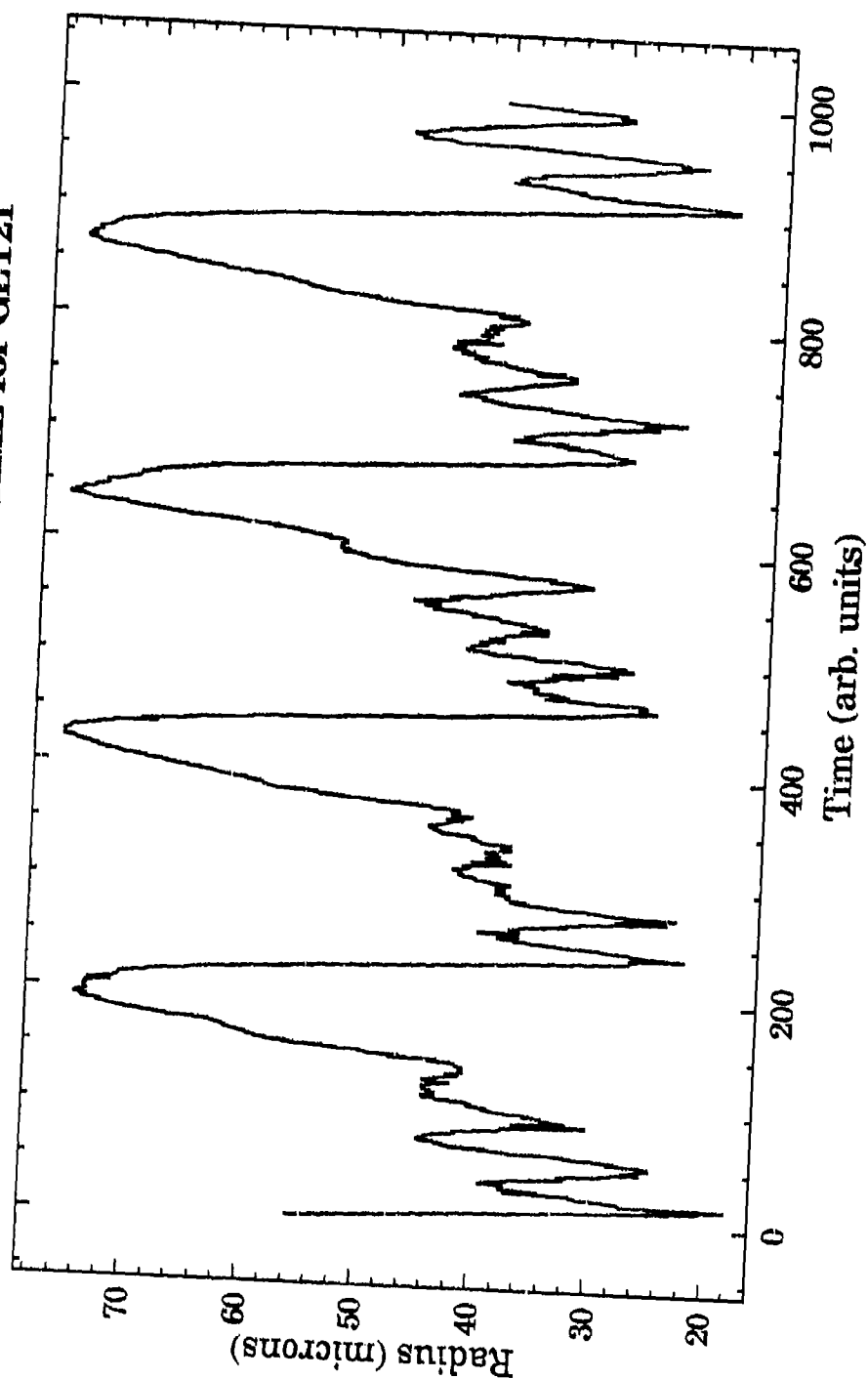


Figure 33. Experimental radius-time curve obtained with the light-scattering apparatus in 21 % glycerine at $p_A=1.22$ bars and $f=22.3$ kHz.

this experiment. All of the radius-time plots obtained at these high driving pressure amplitudes are characterized by a relatively slow expansion ($\sim 15\text{-}20\ \mu\text{sec}$), followed by a rapid collapse ($\sim 5\text{-}10\ \mu\text{sec}$) after which several rebounds occur before the next cycle starts. The minima of these radius-time curves are bounded by the background noise level of the detection system, which in this case was around 20 microns. The occasional glitches in the data causing the bubble radius to drop below 20 microns were due to electrical random noise and therefore have no significance. Curves similar to Fig. 33 were also obtained for the other mixtures and representative curves can be found in Appendix A, Figs. A6-A9. The number of radial minima during one cycle was usually 4 or 5, although 3 minima occurred occasionally. The differences in the traces taken in different liquids were mainly in the amplitude of the pulsations and the phase of the first radial minimum.

For comparison, a theoretical R-t curve using the same experimental conditions as those of Fig. 33 with $R_0 = 20\ \mu\text{m}$ is shown in Fig. 34. The reasons for choosing this value of R_0 will be explained below. The overall shape of the two figures is obviously very similar, including the magnitude of the bubble response and the rebounds after the collapse. One discrepancy, however, is the number of minima and the apparent increase in the amplitude of the rebounds in the experimental R-t curve (Fig. 33), as opposed to the decrease predicted by the theory (Fig. 34). Some of these small discrepancies will be discussed in the next Sections. Nevertheless, the resemblance is obvious. Periodic pulsations such as those seen in Fig. 33 were observed continuously for thousands of acoustic periods. These R-t curves and the observation of the spherical outline of the bubble pulsations

THEORETICAL RADIUS vs TIME for GLY21

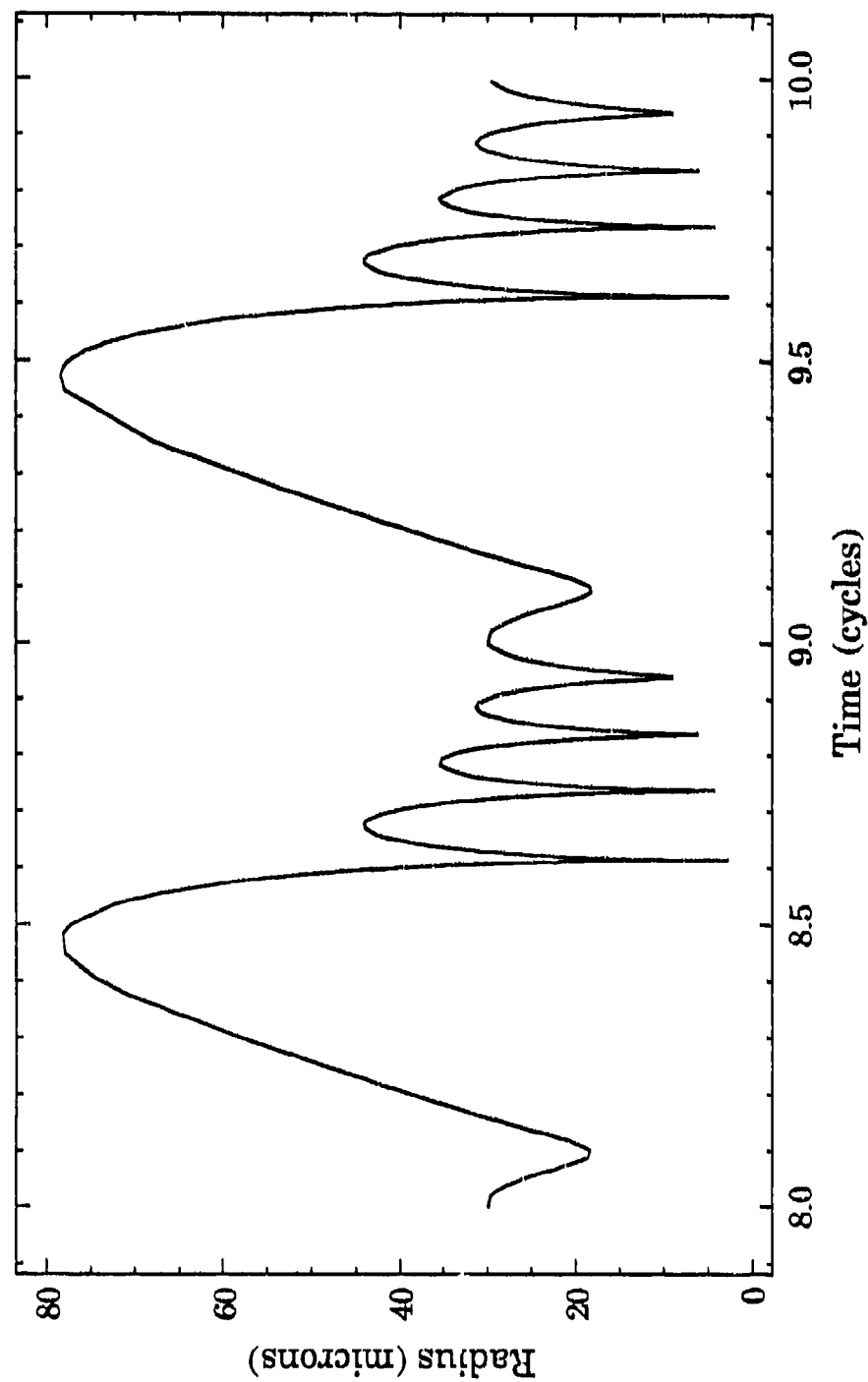


Figure 34. Theoretical calculation of the steady state solution of the bubble radius for the experimental conditions described in Fig. 33 and $R_0=20$ mm using Prosperetti's formulation.

through the microscope when bubbles were levitated in the rectangular cell constitute the most convincing evidence of the periodicity, stability and spherical symmetry of the bubble pulsations.

Several parameters of nonlinear bubble pulsations have been measured using the R - t curves of single bubbles pulsating at large amplitudes ($R_{max}/R_0 > 3$). In the next Sections, some of these measurements will be presented and compared to the theoretical values predicted by the different formulations. However, since it was not possible to determine the equilibrium bubble size accurately, calculations were made for $R_0=15$, 20 and 25 microns. Although the mechanism by which the bubbles are stabilized is still not well understood, the bubbles did appear to remain constant in size for the same acoustical parameters (pressure amplitude, gas concentration, etc.). However, not all of these parameters were controlled during the experiments and, for this reason, it cannot be assumed that the data were taken with the same bubble radius. One of the objectives of this study, then, is to determine which value or values of R_0 give the best agreement between a particular theory and experiment for the three independently measured parameters: pulsation amplitude R_{max} , phase of the bubble collapse ϕ_c , and the number of radial minima M . If agreement is found for the same value of R_0 for all three parameters, it can then be said, with reasonable certainty, that the theory and experiment agree for those values of R_0 . If different values are found, it can then be said that the theory and experiment disagree. Since the theories used for comparison with the experimental results have been shown to exceed their limits of applicability, perfect agreement is not expected. Thus, a second objective of this

study is to estimate the range of parameters over which these theories are applicable.

Comparison between the measurements and Prosperetti's model will be made in the next three sections. Comparison with the other models will be made in Section B.1.e with the intent of determining the most accurate theory, although this has proven to be a difficult task due to the large experimental error. It will be shown that the difference in the predictions of the three theories using the same conditions is smaller than the error bars of the experimental data. Instead, the consistency of the results of each particular theory has been used as a test of applicability. In Section B.2, the theoretical values of the internal temperatures, pressures and relative densities predicted by Prosperetti's and Flynn's formulations will be compared. These values will be shown to differ by as much as 100% in some cases. The theoretical temperature calculated at the experimentally determined threshold for SL will be discussed and compared with previous measurements. In Section B.3, results for sonoluminescence emitted from a single bubble will be presented. Also, the experimental radius-time curve will be plotted simultaneously with the SL flashes in order to demonstrate the simultaneity of the bubble collapse and the light emission.

IV. B. 1. b. Pulsation Amplitude

For each of the R-t curves obtained in the previous Section, the pulsation amplitude R_{max} was measured and plotted versus p_A as shown in Figs. 35-39. In the same figures, values of the theoretical predictions made by Prosperetti's model

PULSATION AMPLITUDE FOR WATER

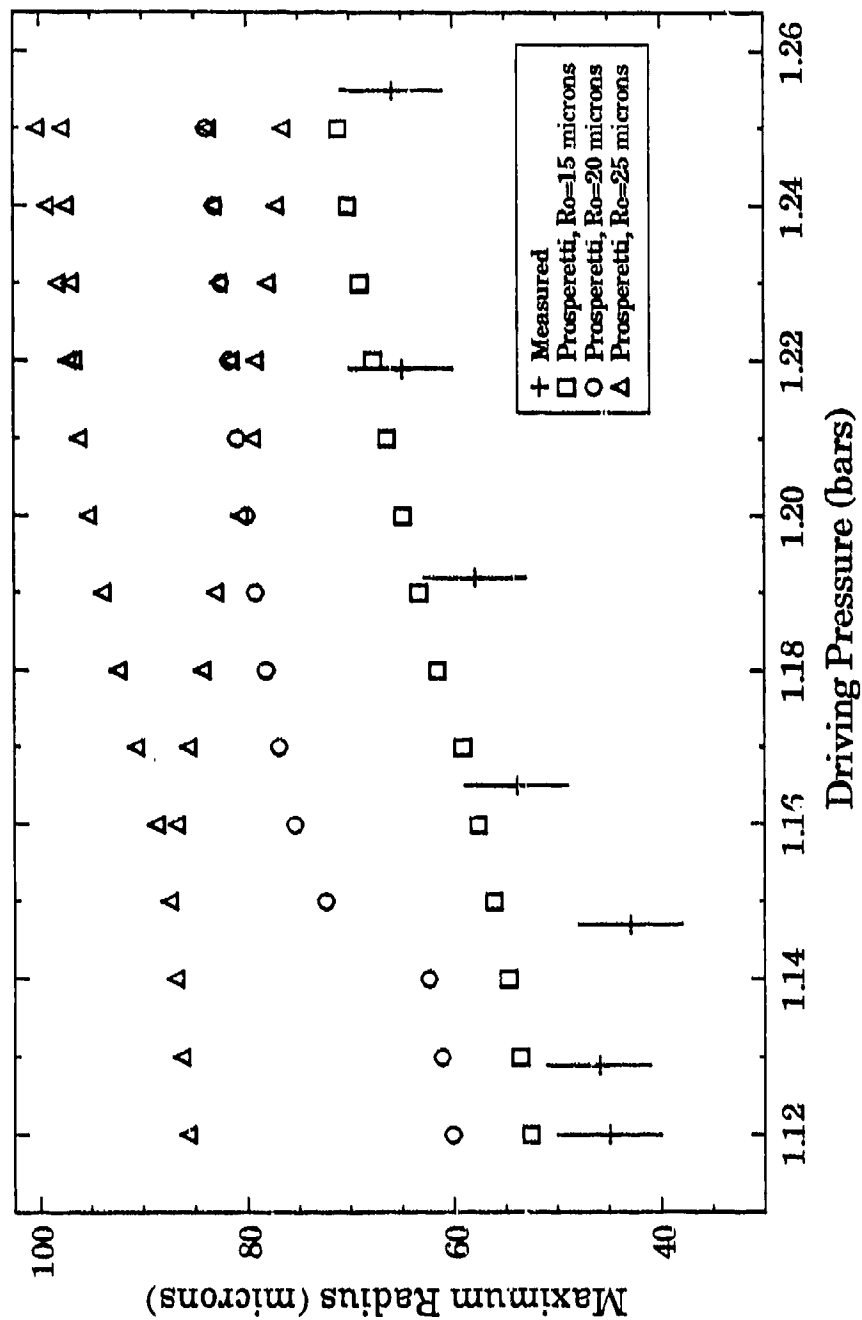


Figure 35. Measured and theoretical pulsation amplitude (R_{max}) vs acoustic pressure amplitude in water using Prosperetti's formulations at $f=21.0$ kHz.

PULSATION AMPLITUDE for 21% GLYCERINE

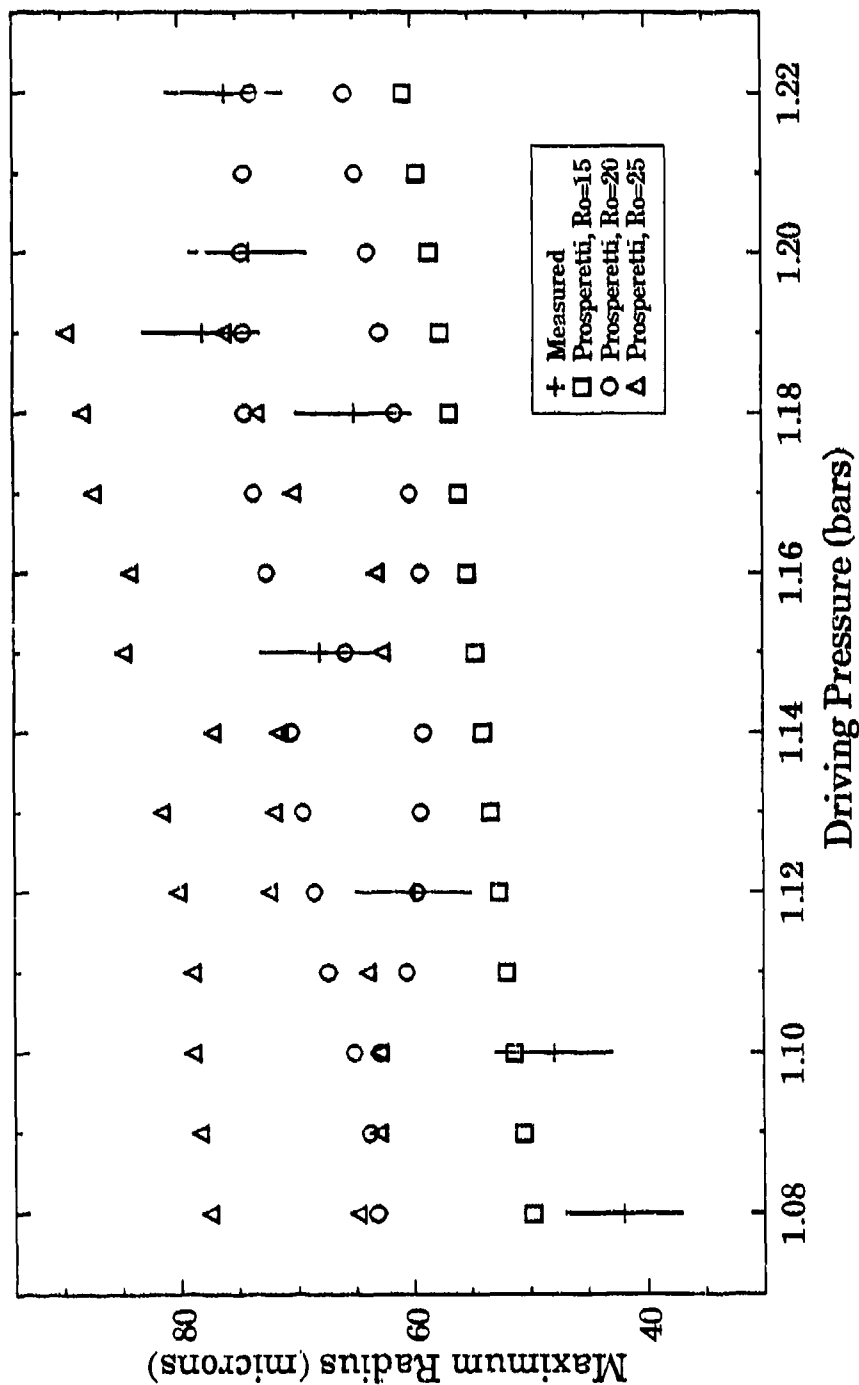


Figure 36. Measured and theoretical pulsation amplitude (R_{max}) vs acoustic pressure amplitude in GLY21 using Prosperetti's formulations at $f=22.3$ kHz.

PULSATION AMPLITUDE for 35% GLYCERINE

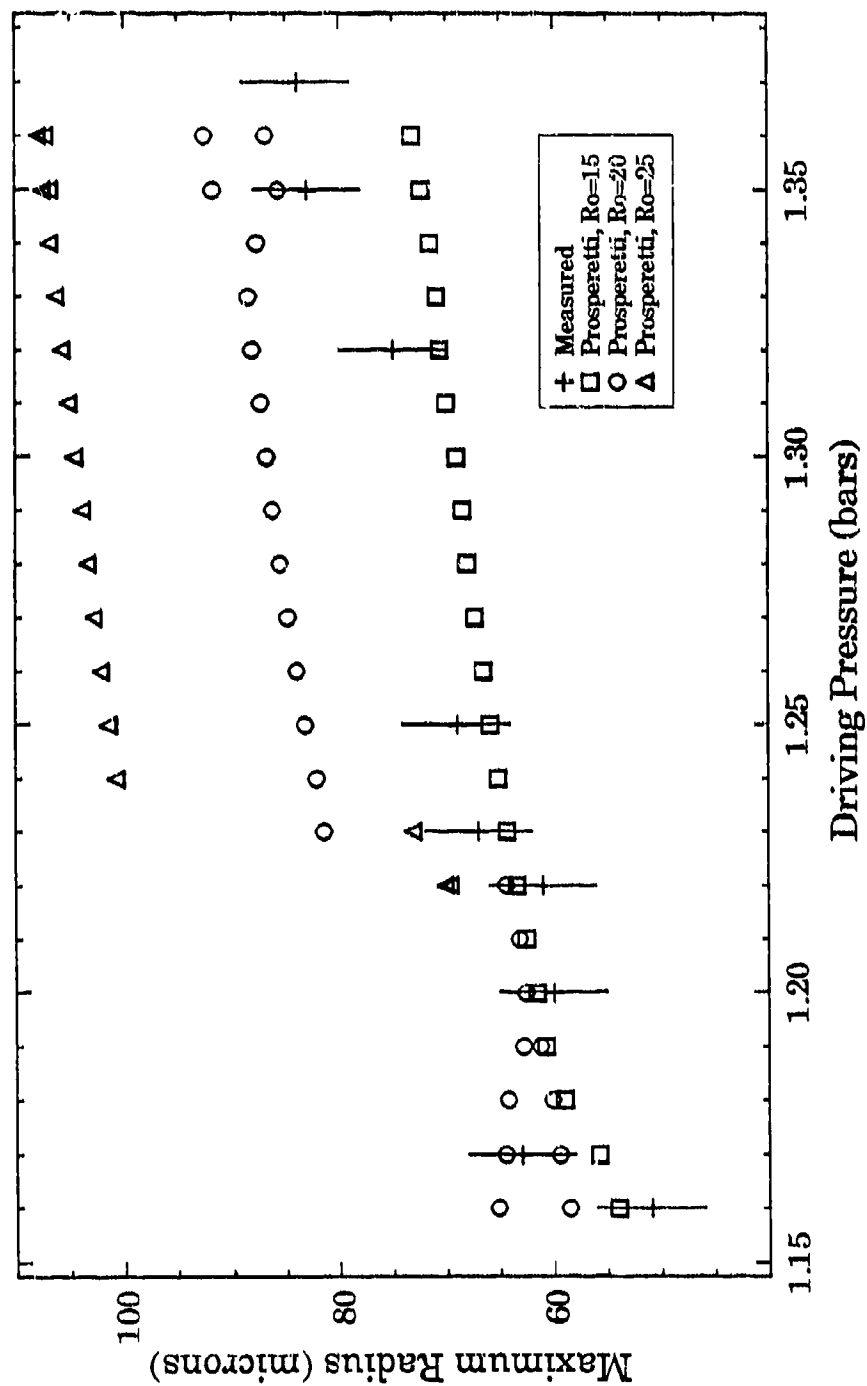


Figure 37. Measured and theoretical pulsation amplitude (R_{max}) vs acoustic pressure amplitude in GLY35 using Prosperetti's formulations at $f=23.0$ kHz.

PULSATION AMPLITUDE for 42% GLYCERINE

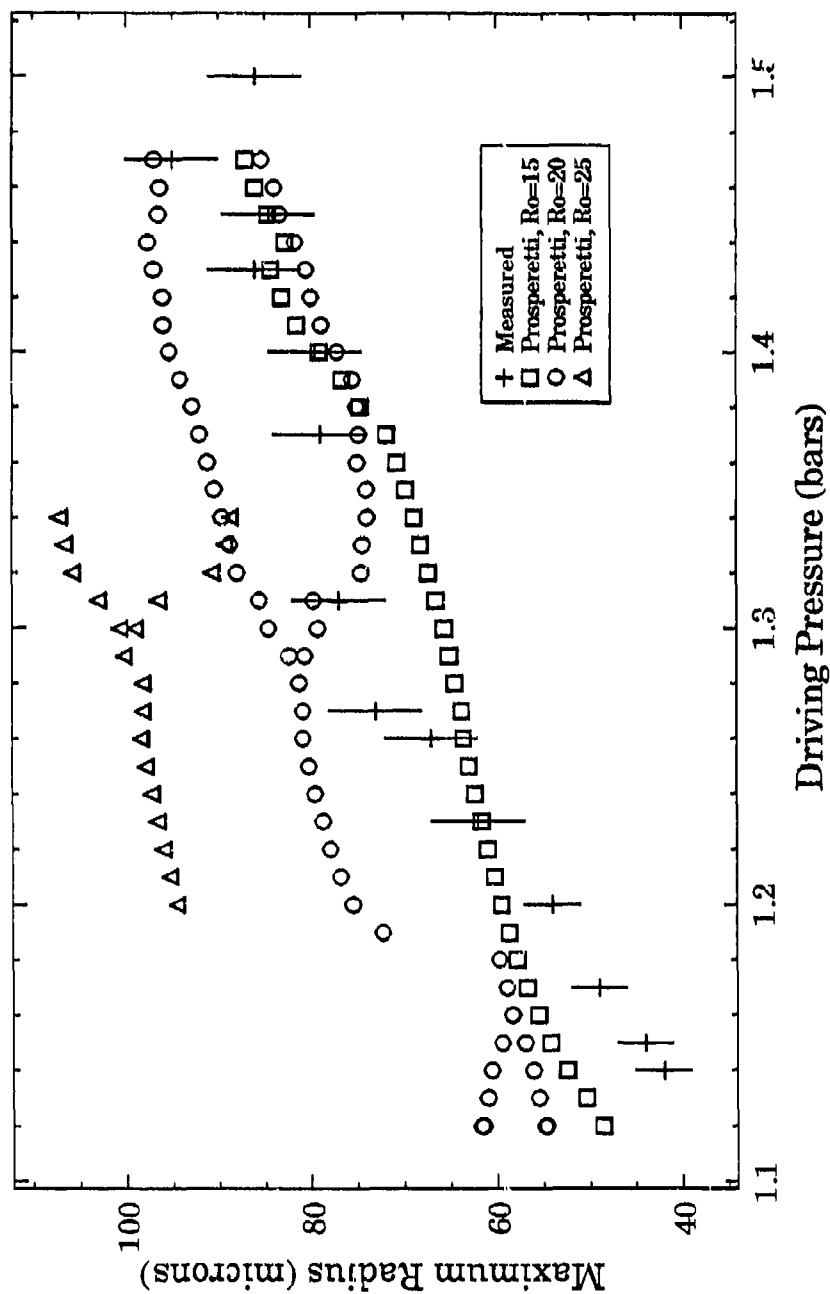


Figure 38. Measured and theoretical pulsation amplitude (R_{max}) vs acoustic pressure amplitude in GLY42 using Prosperetti's formulations at $f=23.6$ kHz.

PULSATION AMPLITUDE for 60% GLYCERINE

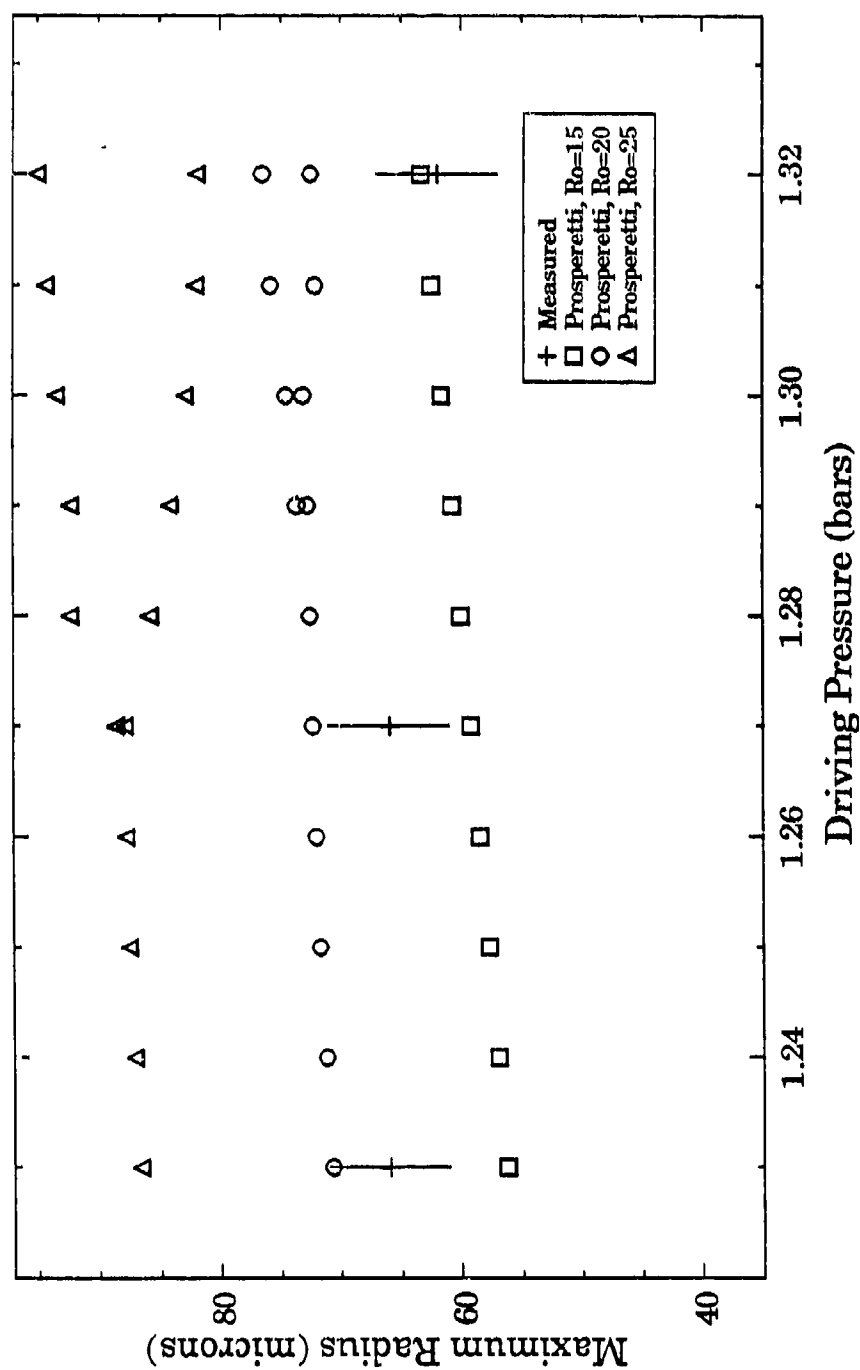


Figure 39. Measured and theoretical pulsation amplitude (R_{max}) vs acoustic pressure amplitude in GLY60 using Prosperetti's formulations at $f=24.8$ kHz.

for the same experimental conditions have been plotted for $R_0=15, 20$ and 25 microns, as indicated in the legend. Each measured data point in Figs. 35-39 was taken from stored oscilloscope traces each consisting of several acoustic periods for each value of p_A . Most of the time only one trace was stored for each value of p_A due to the large amount of time and storage space that each trace required. The error bars placed on these data represent the combined experimental uncertainty of ± 5 microns, as explained in Section II.E.1. Because of the difficulty in stabilizing bubbles in GLY60, only a few data points were obtained. Some of the theoretical curves exhibit abrupt changes caused by resonances of the radial motion excited at different values of p_A . Bifurcations into period-2 and period-4 solutions also occur, especially for the 20 and $25 \mu\text{m}$ bubbles. These resonances and bifurcations have been discussed in Section III.B.2 and illustrated in Figs. 23 and 24 where the variables were plotted as a function of R_0 instead of p_A . When p_A is varied, resonances occur due to the shifting of the peaks toward smaller radii. Although values were calculated in increments of $p_A=0.01$ bars for each value of R_0 , not all of the data were displayed. These gaps in the theoretical curves indicate that no steady state solutions were found in a reasonable (20 acoustic periods) amount of time.

In general, comparison of the pulsation amplitude data indicates better agreement with the $15 \mu\text{m}$ bubble, although this is not true in every case. The experimental data for GLY21, for example, agrees partially with the theoretical results of the $20 \mu\text{m}$ bubble. It should be noted here that it was probable that the bubble radius changed as the pressure amplitude was increased. In fact, closer agreement was found in GLY21 with the theoretical results using the $15 \mu\text{m}$

bubble at the lower pressures but with the 20 μm bubble at the higher pressures. The experimental data for GLY42 could even be interpreted as a decrease in the bubble radius below 15 μm at the lowest values of p_A . This increase in radius with pressure amplitude may be effected through the phenomenon of rectified diffusion which, in general, results in larger bubble growth rates as p_A is increased, as stated in Section III.D.

Theoretically, the resonances and bifurcations occur in different places of the bubble response curve, the exact location being very sensitive to the exact set of parameters, even for the same values of p_A and R_o . It was thus not expected to find agreement between theory and experiment in the regions where quick transitions occurred. It is interesting to note that although subharmonic motion was predicted quite often in the range of parameters considered, it was never observed in the laboratory.

In summary, the pulsation amplitude data shown in Fig. 35 (water), Fig. 37 (GLY35) and Fig. 39 (GLY60) imply that $R_o \approx 15 \mu\text{m}$ and remains approximately constant for the range of p_A . Fig. 36 (GLY21) and Fig. 38 (GLY42), however, imply that R_o increases with p_A . In GLY21, R_o increases from 15 μm to 20 μm , whereas in GLY42 it increases from less than 15 μm to about 15 μm . It should be noted that in the last two sets of data (GLY42 and GLY60), the values of p_A reached slightly lower values than the other sets, which may explain the lower values for R_o . Period-2 motion was predicted for the 20 μm bubble in GLY21, GLY35 and GLY60 for some values of p_A . Period-4 motion was predicted only for water (Fig. 35) for 25 μm .

IV. B. 1. c. Phase of Collapse

From the same R-t curves considered in the previous Section, the phase of collapse ϕ_c was measured using the procedure described in Section II.D.2.b. They have been plotted in Figs. 40-44 along with the theoretical predictions of Prosperetti's formulation for 15, 20 and 25 μm bubbles. The estimated total error of the calibration procedure was ± 5 degrees and it is indicated by the error bars. These measurements involved a different calibration procedure and the data obtained are therefore considered independent from the pulsation amplitude data.

The results of the phase of collapse measurements were very similar to the pulsation amplitude measurements in the previous Section. In summary, these results can be interpreted as follows: In Fig. 42 (GLY35) and Fig. 44 (GLY60), $R_o \sim 20 \mu\text{m}$ and remains approximately constant. In Fig. 40 (water), R_o appears to increase from $10 \leq R_o \leq 15 \mu\text{m}$ to $15 \leq R_o \leq 20 \mu\text{m}$ as p_A increases, whereas in Fig. 41 (GLY21) and Fig. 43 (GLY42), $R_o \sim 15 \mu\text{m}$ at low p_A and $R_o \sim 20 \mu\text{m}$ at high p_A . The largest disagreement between these results and the results of the previous Section was found for GLY35 and GLY42. The collapse phase data for water predicted larger radii than the pulsation amplitude data shown in the previous Section, although the discrepancy was small enough to be within the experimental error. The reason for this discrepancy is not clear. The fact that more data were taken for GLY42 and over a larger pressure amplitude range than the other liquids may be part of the reason. It should also be pointed out that some of the data for GLY42 were taken over a two week interval.

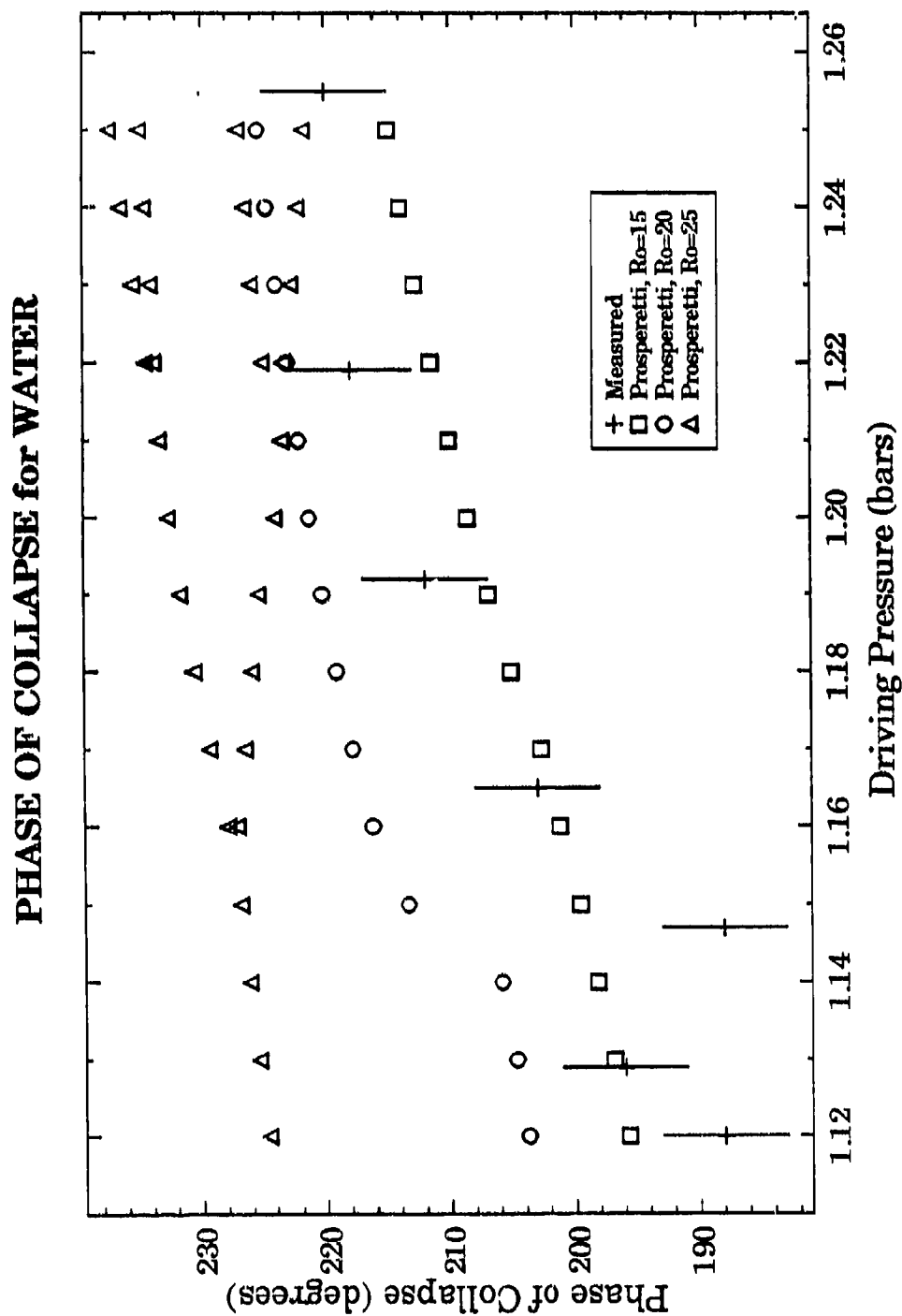


Figure 40. Measured and theoretical phase of bubble collapse (ϕ) vs acoustic pressure amplitude in water using Prosperetti's formulation at $f=21.0$ kHz.

PHASE OF COLLAPSE for 21% GLYCERINE

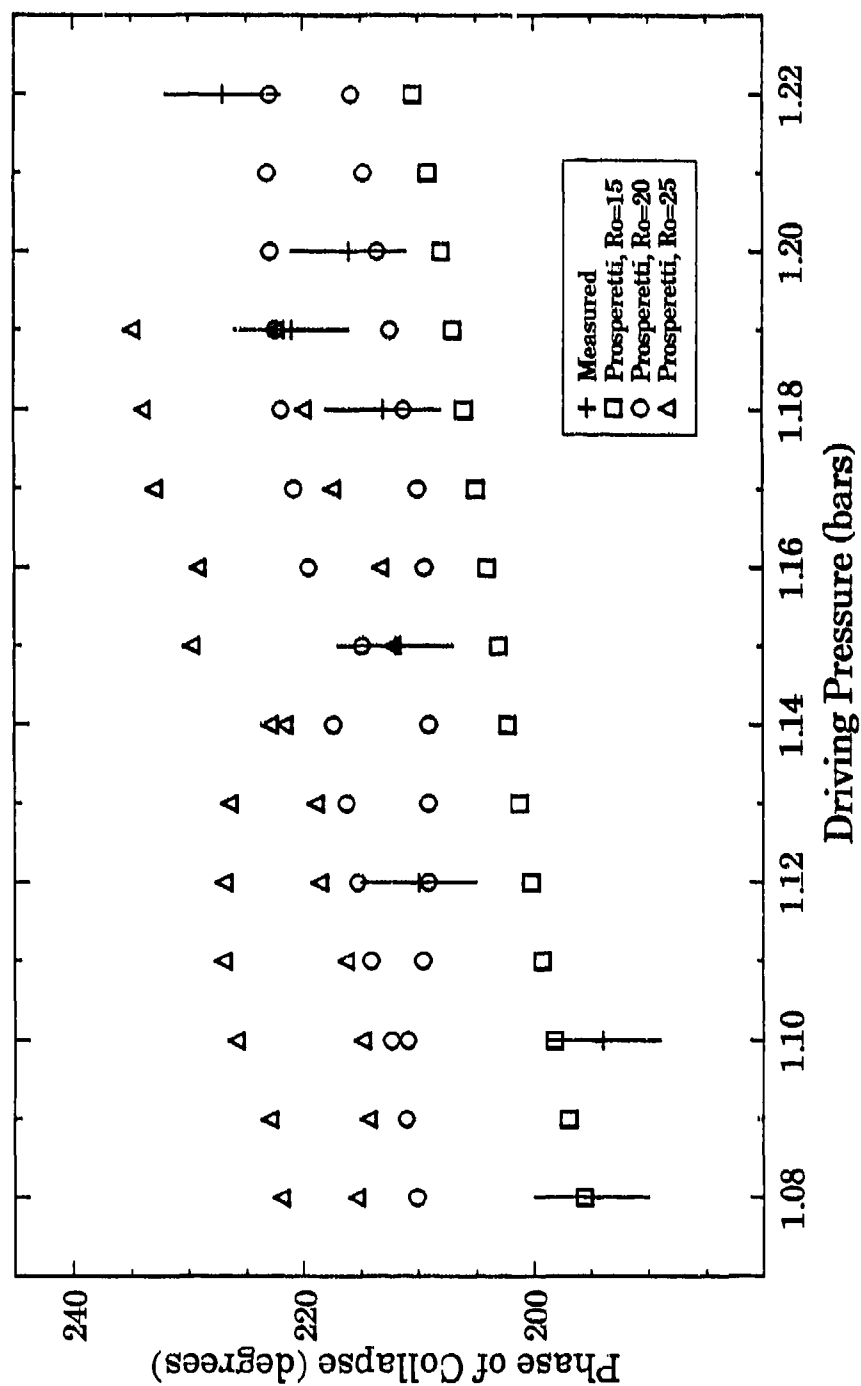


Figure 41. Measured and theoretical phase of bubble collapse (ϕ_c) vs acoustic pressure amplitude in GLY21 using Prosperetti's formulation at $f=22.3$ kHz.

PHASE OF COLLAPSE for 35% GLYCERINE

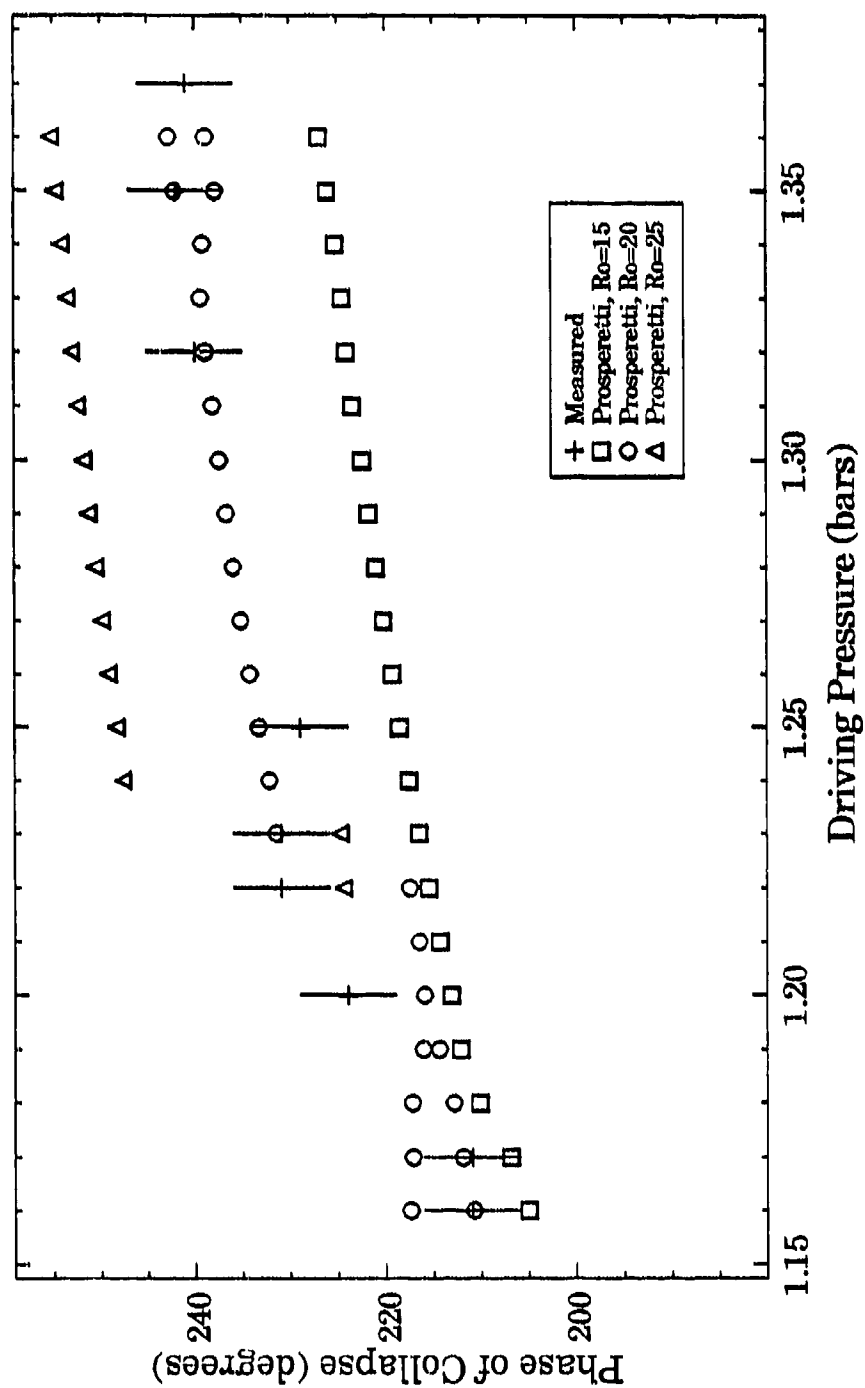


Figure 42. Measured and theoretical phase of bubble collapse (Φ_c) vs acoustic pressure amplitude in GLY35 using Prosperetti's formulation at $f=23.0$ kHz.

PHASE OF COLLAPSE for 42% GLYCERINE

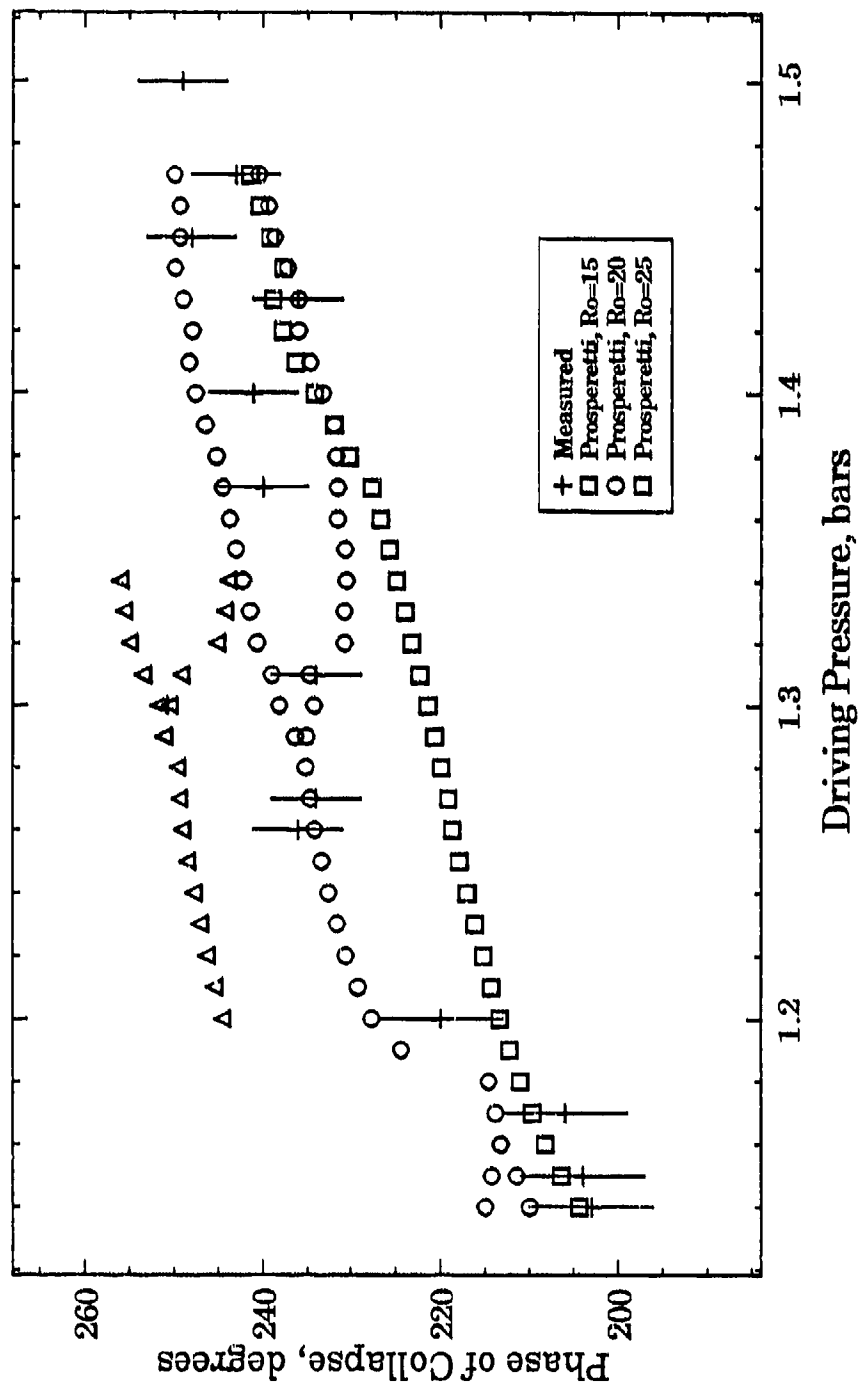


Figure 43. Measured and theoretical phase of bubble collapse (Φ_c) vs acoustic pressure amplitude in GLY42 using Prosperetti's formulation at $f=23.6$ kHz.

PHASE OF COLLAPSE for 60% GLYCERINE

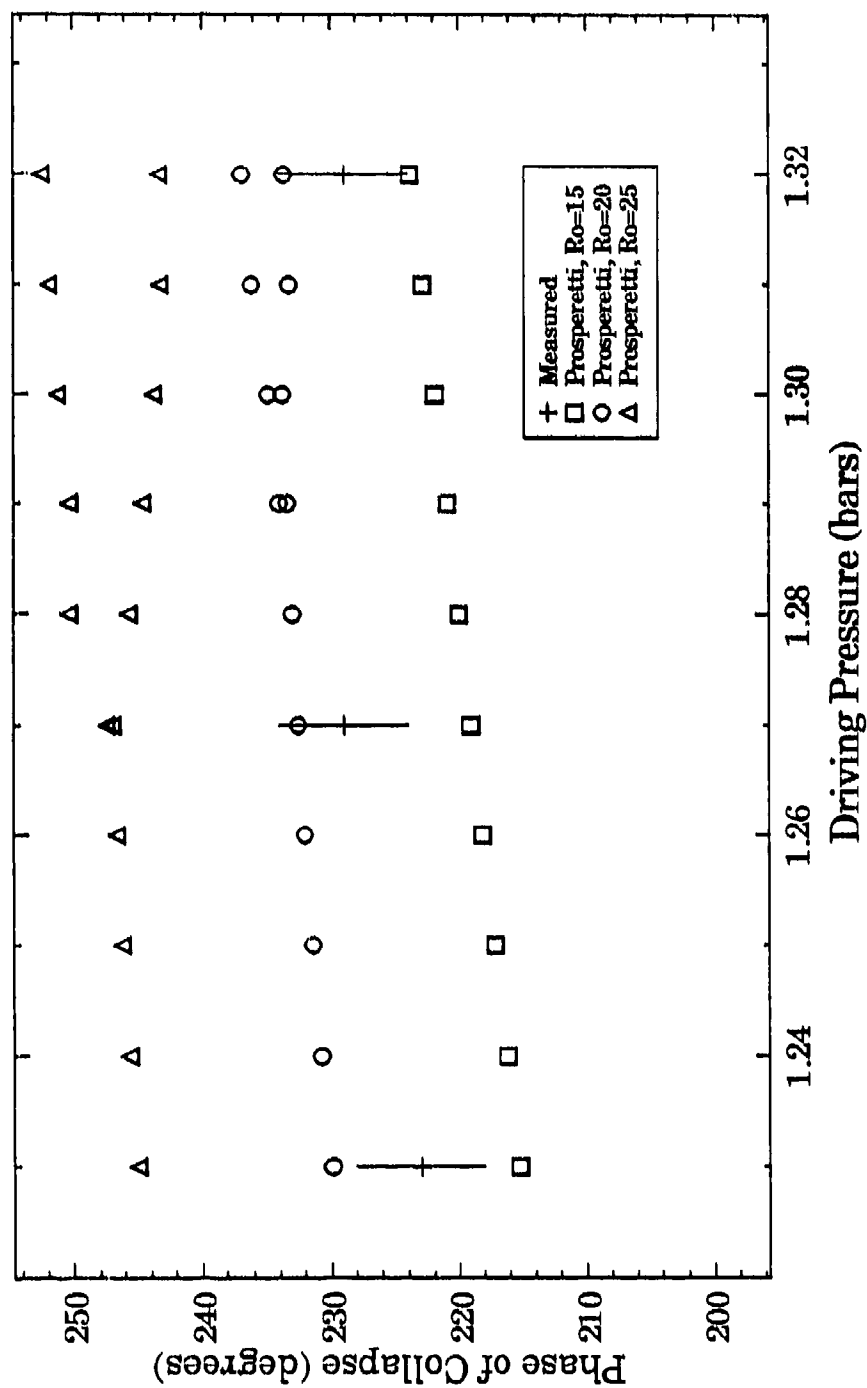


Figure 44. Measured and theoretical phase of bubble collapse (ϕ_b) vs acoustic pressure amplitude in GLY60 using Prosperetti's formulation at $f=24.8$ kHz.

IV. B. 1. d. Number of Radial Minima

A third experimental determination that can be used to test the theory is the number of radial minima observed during one acoustic period. This parameter is mainly dependent on the bubble size, although some dependence on the pressure amplitude was found from the calculations, as pointed out in Section III.B.2. Figs. 45-49 show the number of minima measured in each liquid mixture and those predicted by Prosperetti's model for 15, 20 and 25 microns. Non-integer values of the measured number of minima indicate that two different values were observed in the same radius-time curve. In that case, the mean of the two values was plotted. The error bars indicate the estimated error in the measurement. This error was mostly due to random noise in the R-t curves, which sometimes resembled the real radial (intensity) minima and interfered with the counting process. Double values in the theoretical data indicate that a different number of minima occurred per period in the steady state solution, usually due to subharmonic motion i.e., $m > 1$ (see Chapter III). Note that subharmonic motion observed in the figures showing the pulsation amplitude and collapse phase was not always reflected in the figures showing number of minima. This is because only an integer number of minima can occur in one acoustic period, unlike the pulsation amplitude and collapse phase, which can change in a continuous fashion.

The number of minima observed were, in general, fewer than the number expected from the theoretical predictions based on the pulsation amplitude and collapse phase measurements. This means that the bubble radii predicted based

NUMBER of MINIMA for WATER

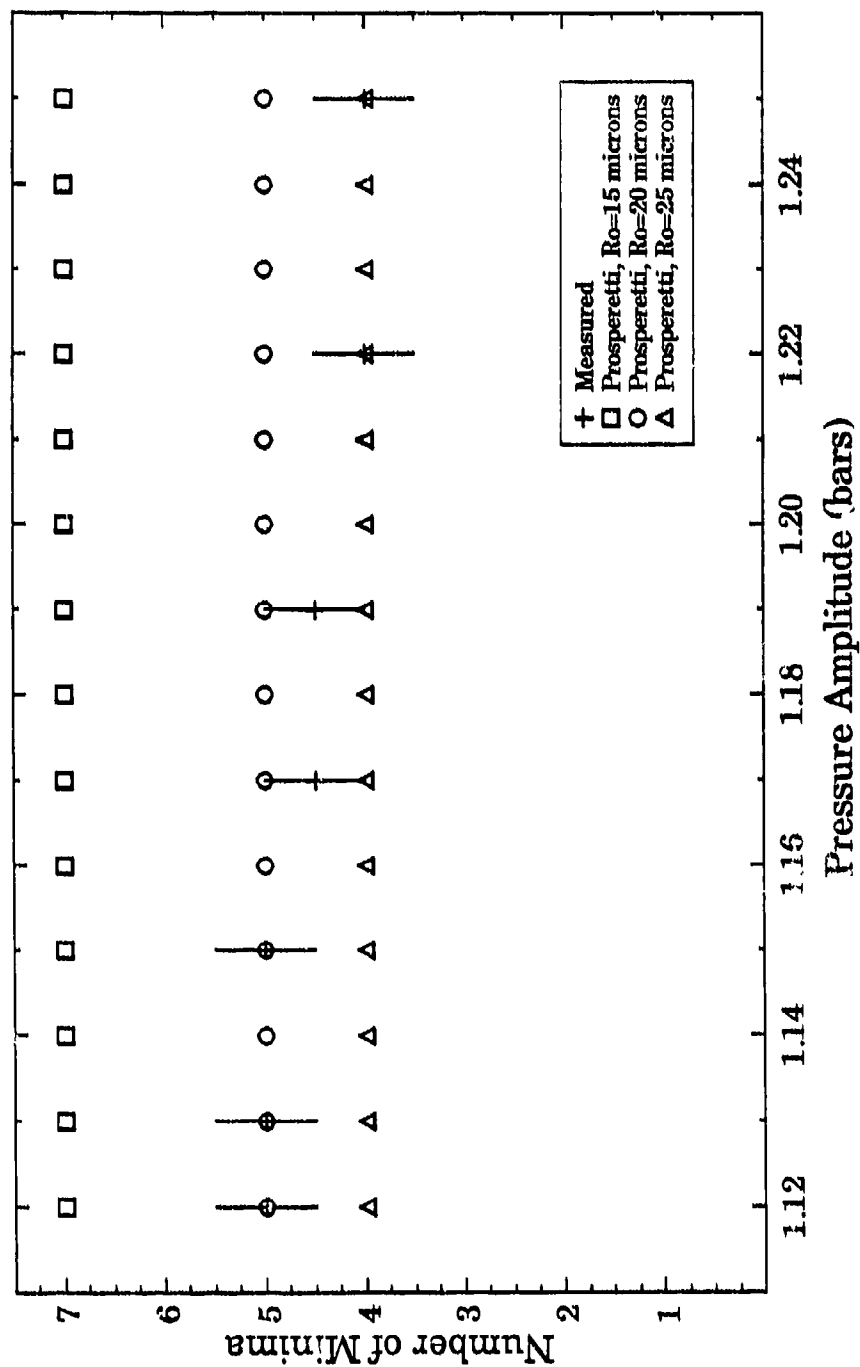


Figure 45. Measured and theoretical number of minima (M) vs acoustic pressure amplitude in water using Prosperetti's formulation at $f=21.0$ kHz.

NUMBER of MINIMA for 21% GLYCERINE

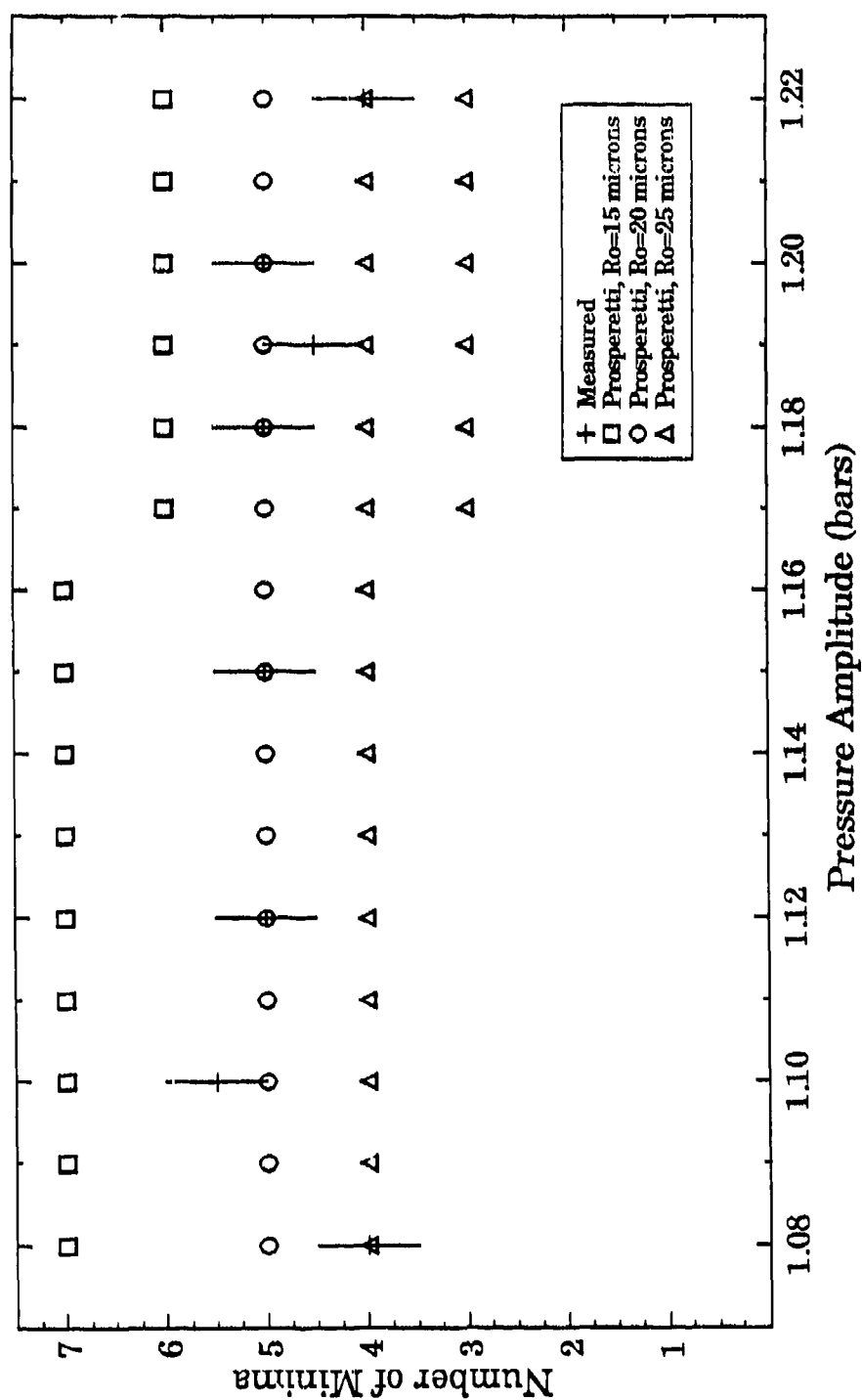


Figure 46. Measured and theoretical number of minima (M) vs acoustic pressure amplitude in GLY21 using Prosperetti's formulation at $f=22.3$ kHz.

NUMBER of MINIMA for 35% GLYCERINE

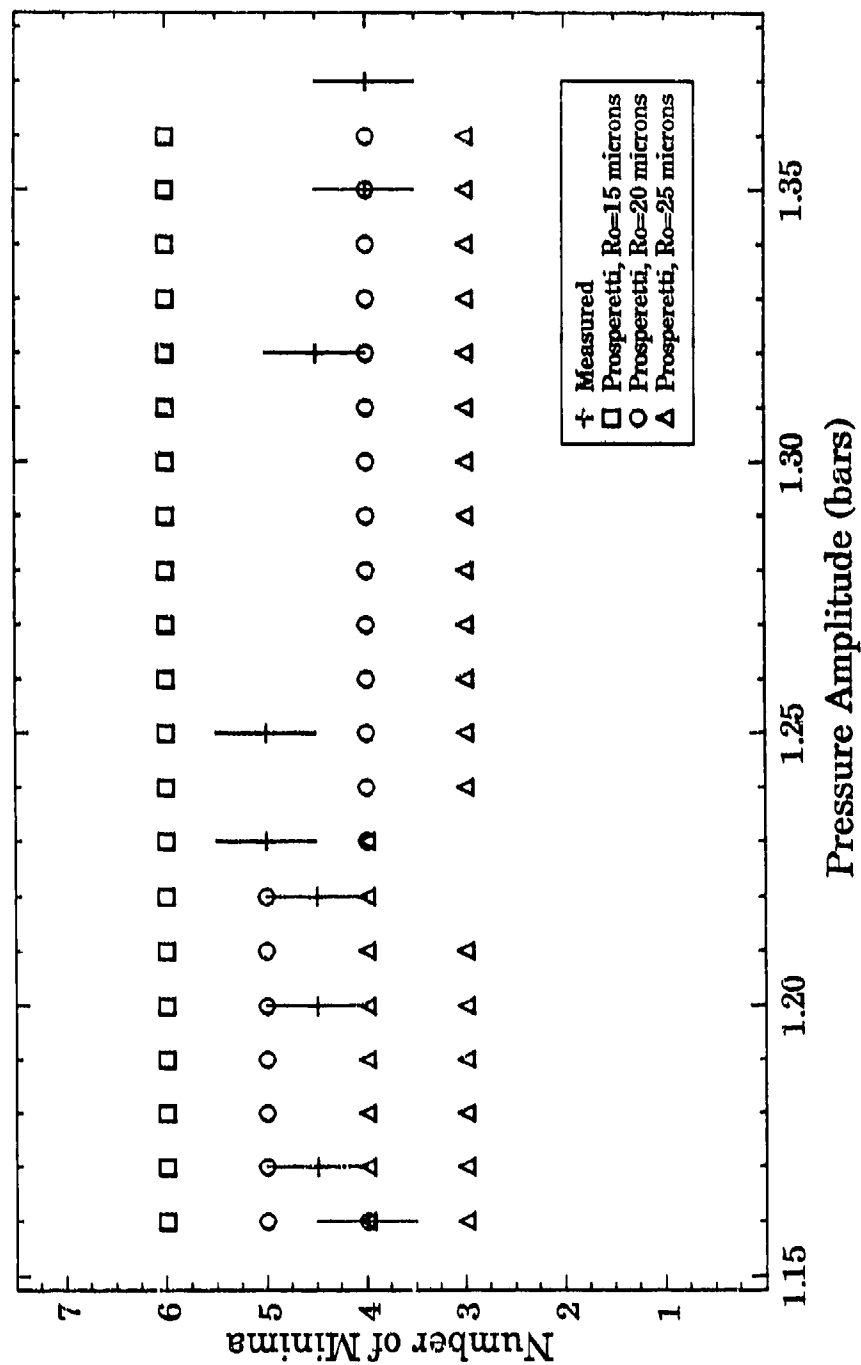


Figure 47. Measured and theoretical number of minima (M) vs acoustic pressure amplitude in GLY35 using Prosperetti's formulation at $f=23.0$ kHz.

NUMBER of MINIMA for 42% GLYCERINE

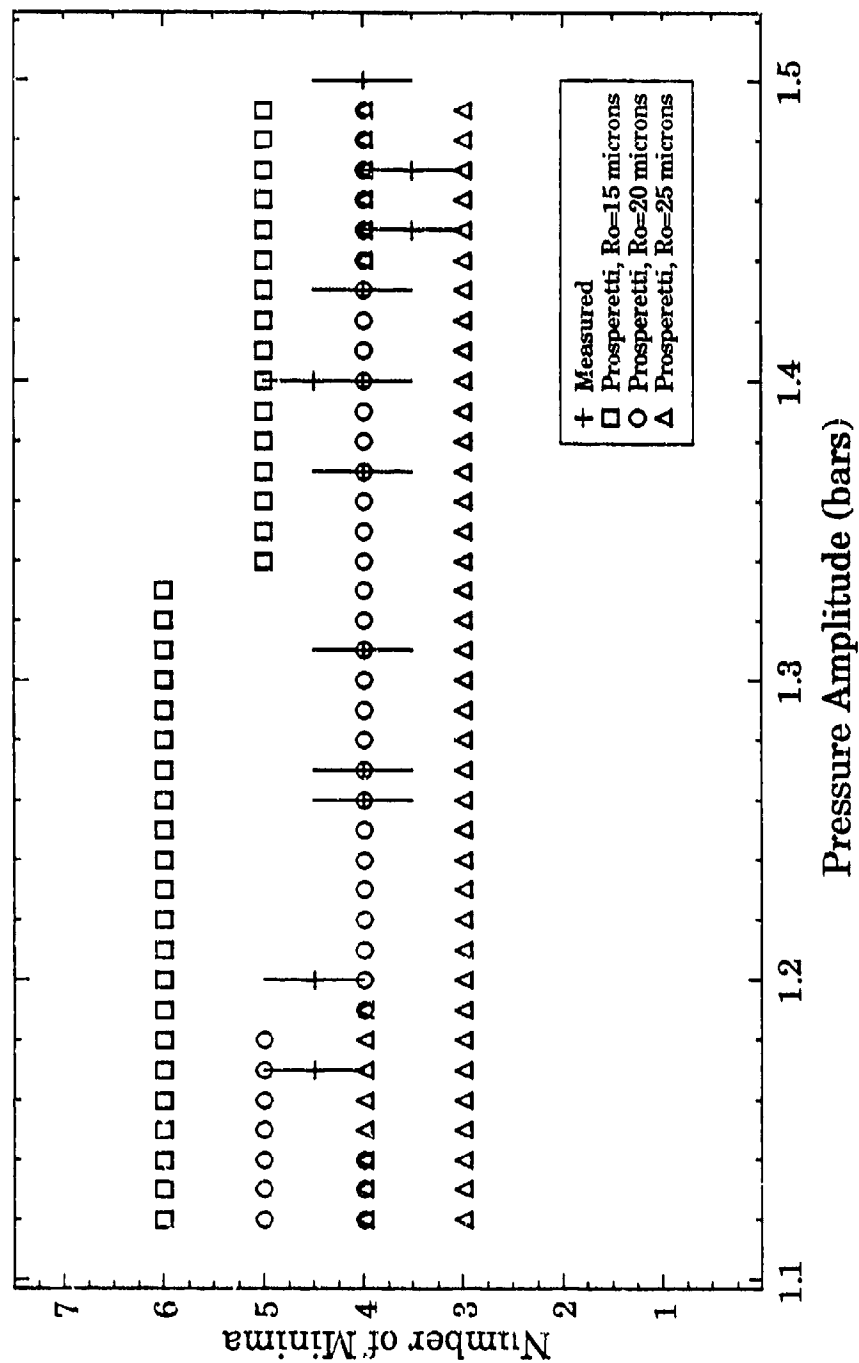


Figure 48. Measured and theoretical number of minima (M) vs acoustic pressure amplitude in GLY42 using Prosperetti's formulation at $f=23.6$ kHz.

NUMBER of MINIMA for 60% GLYCERINE

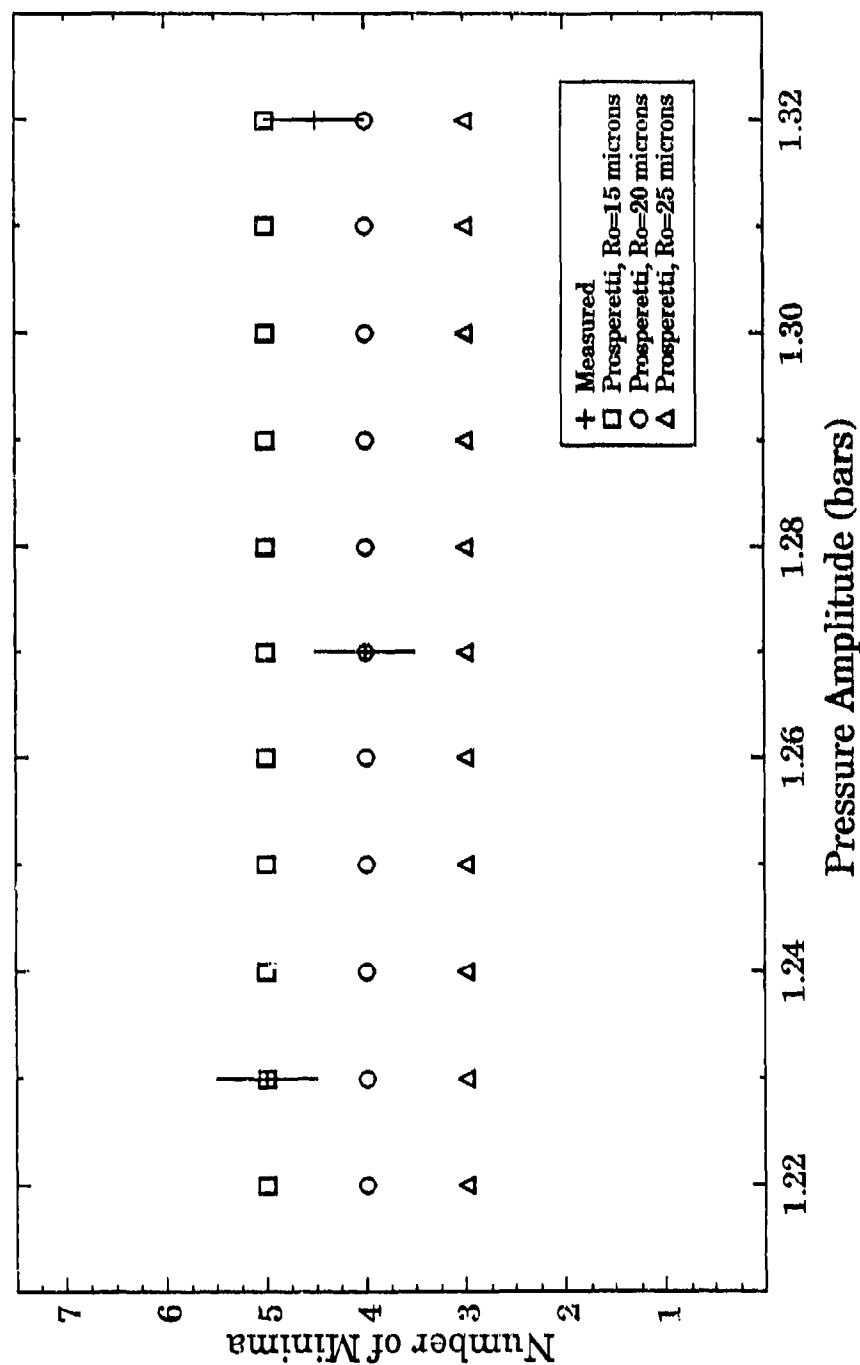


Figure 49. Measured and theoretical number of minima (M) vs acoustic pressure amplitude in GLY60 using Prosperetti's formulation at $f=24.8$ kHz.

on the number of minima were larger since, as shown previously, larger bubbles pulsate with fewer minima. For instance, Figs. 45 (water) and 46 (GLY21) predict $R_o \approx 20 \mu\text{m}$ at low values of p_A and $R_o \approx 25 \mu\text{m}$ at the higher values of p_A . Figs. 47 (GLY35) and 48 (GLY42) predict $R_o \approx 20 \mu\text{m}$ remaining constant for the range of p_A considered. The results of Fig. 49 (GLY60) are very imprecise due to the few data points taken. It is not clear why the number of minima observed was fewer than predicted by the theories. The explanation may be linked to another anomalous observation in the rebounds of the radius-time curves. As can be seen in Fig. 33, the bubble rebounds appear to increase in time within each period instead of decreasing in the normal decaying fashion, as shown in Fig. 34 where the theoretical R-t curve has been plotted. The experimental R-t curves seem to indicate much larger amplitudes for the rebounds. Larger amplitudes would indeed result in fewer rebounds because each rebound would require more time. In this respect, the observed fewer number of minima is consistent with the large rebound amplitudes observed in the scattered-light data. However, no explanation has been found for this increase in the amplitude of the bubble rebounds.

Additional evidence on the size of the bubbles can be obtained by considering the periodicity of the solutions. For example, notice that period-two solutions were predicted by the theory quite often for the $20 \mu\text{m}$ bubble, except for the case of water. For the $25 \mu\text{m}$ bubble few stable, period-1 solutions were obtained. However, all of the solutions for $R_o = 15 \mu\text{m}$ were stable and with the same period as that of the driving pressure. In this respect, the fact that only bubble pulsations with the same period as that of the sound field were observed in the laboratory suggests that the bubble radius was less than $20 \mu\text{m}$.

The conclusions drawn in the last three Sections have been summarized in Table 4 below.

Table 4. Summary of predictions of R_0 obtained from Prosperetti's formulation.

Theoretical Range of R_0 for Single Bubble Pulsations

	From R_{max}	From ϕ_c	From M
water	10-15 μm	13-18 μm	20-25 μm (>)*
GLY21	15-20 μm (>)	15-20 μm (>)	20-25 μm (>)
GLY35	15 μm	20 μm	20 μm
GLY42	10-15 μm (>)	15-20 μm (>)	20 μm
GLY60	18 μm	20 μm	15-20 μm

* (>) indicates that the value of R_0 increased as p_A increased.

In summary, the data presented in the last three Sections may be interpreted to indicate that the equilibrium radii of stabilized bubbles driven at pressure amplitudes between 1.1 and 1.5 bars in different water/glycerine mixtures were between 15 and 20 μm . It also is inferred from some of the data that the equilibrium bubble radii increased as the driving pressure was increased. The predicted values of R_0 based on the measurements of R_{max} and ϕ_c are consistent for 2 of the 5 data sets. Inconsistencies were found in the predictions for water, GLY35 and GLY42, indicating a disagreement between theory and experiment. The discrepancy in the water data is within the experimental error, however. The measured number of minima indicated that the equilibrium bubble radii were larger - between 20 and 25 μm - in apparent contradiction to the previous results.

A possible explanation for this disagreement was given in terms of the larger than expected amplitude of the bubble rebounds evidenced by the scattered-light data. The moderate agreement found means that Prosperetti's theory, although fairly applicable, is not a complete description of a cavitation bubble pulsating at these amplitudes. The predictions of the theory should not, therefore, be considered quantitatively correct but only accurate to within a factor of 2 for the parameters under consideration.

IV. B. 1 e. Comparison with the Polytropic Theory and Flynn's Theory

The pulsation amplitude, collapse phase, and number of minima calculated using the polytropic theory and Flynn's theory for water and GLY42 have been plotted in Figs. 50-55. For comparison, the experimental and Prosperetti's results have been plotted simultaneously.

Let us first consider the results from Flynn's model. For clarity, only values of $R_o = 15$ and $20 \mu\text{m}$ have been plotted using the solid symbols as indicated in the legend. However, extrapolated values will be estimated for Flynn's and the polytropic model data when necessary. The pulsation amplitude data shown in Fig. 50 (water) indicate that $R_o \geq 15 \mu\text{m}$, increasing as p_A increases. Furthermore, based on previous results, R_o is most likely $\leq 25 \mu\text{m}$. The data shown in Fig. 51 (GLY42) indicate that $R_o \leq 15 \mu\text{m}$, with R_o increasing to $15 \mu\text{m}$ as p_A was increased. The phase of collapse data shown in Fig. 52 (water), however, suggest that $10 \leq R_o \leq 20 \mu\text{m}$ with R_o also increasing as p_A increases. The data in Fig. 53 (GLY42) indicate that $15 \leq R_o \leq 20 \mu\text{m}$ increasing with p_A . The number of minima

PULSATION AMPLITUDE for WATER

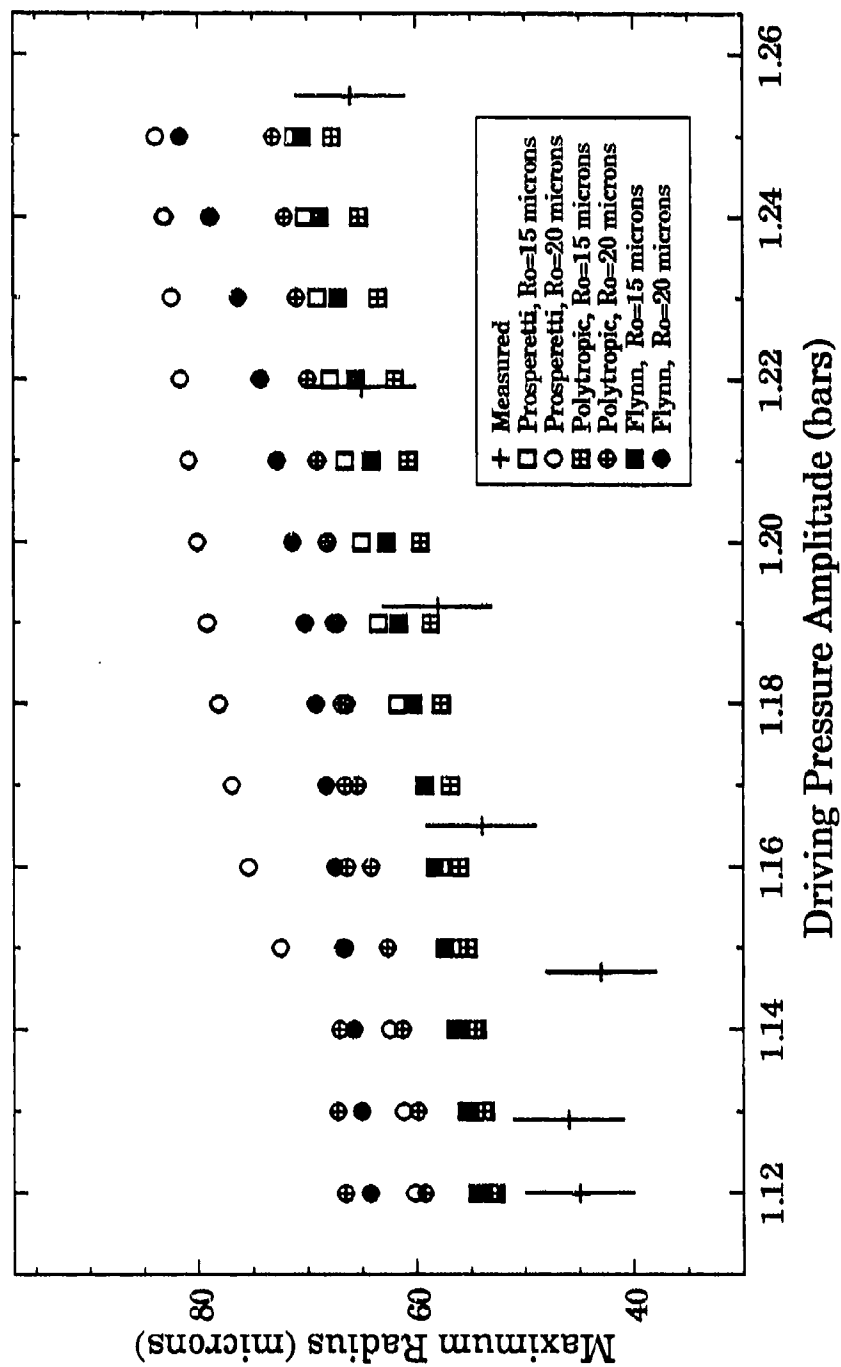


Figure 50. Measured and theoretical pulsation amplitude (R_{max}) vs acoustic pressure amplitude in water using all three formulations at $f=21.0$ kHz.

PULSATION AMPLITUDE for 42% GLYCERINE

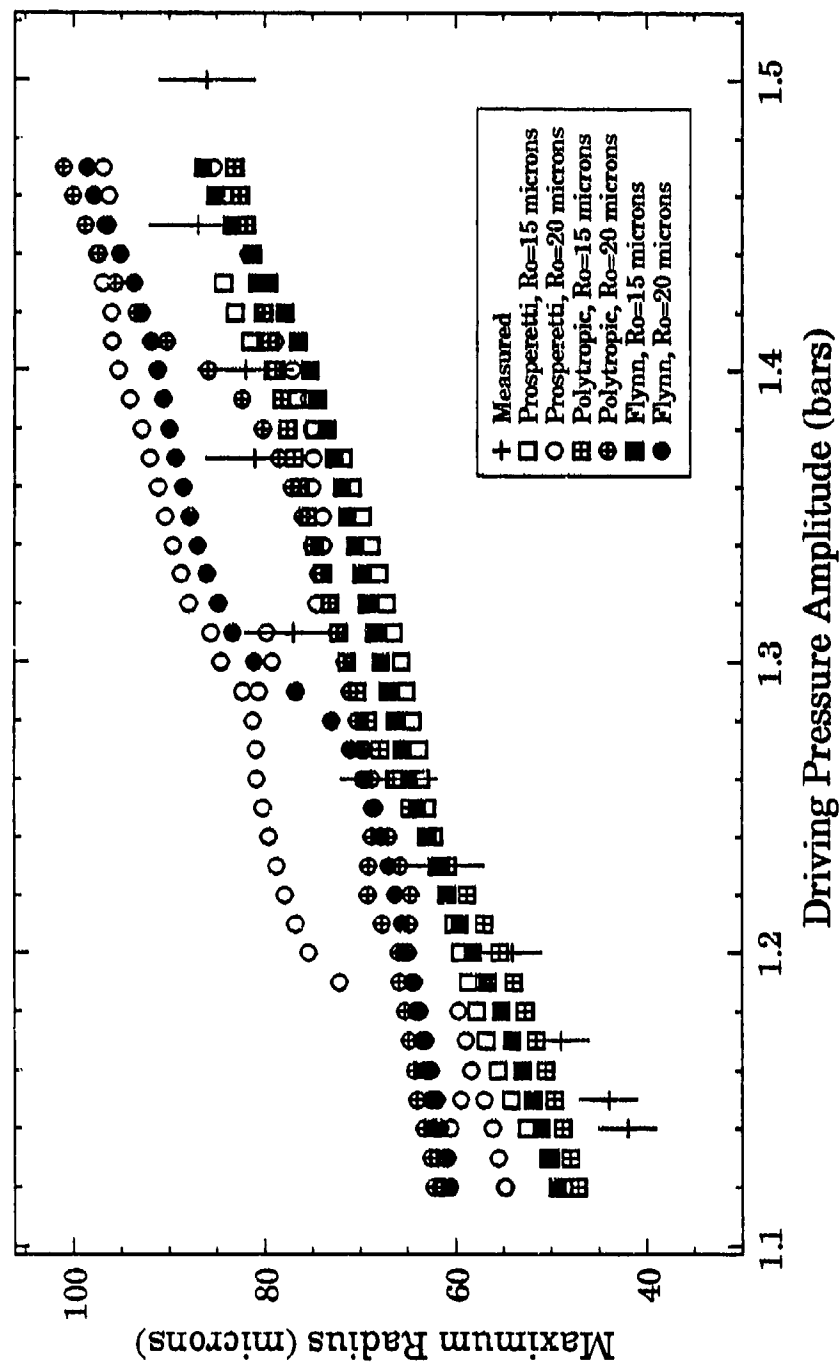


Figure 51. Measured and theoretical pulsation amplitude (R_{max}) vs acoustic pressure amplitude in GLY42 using all three formulations at $f=23.6$ kHz.

PHASE OF COLLAPSE for WATER

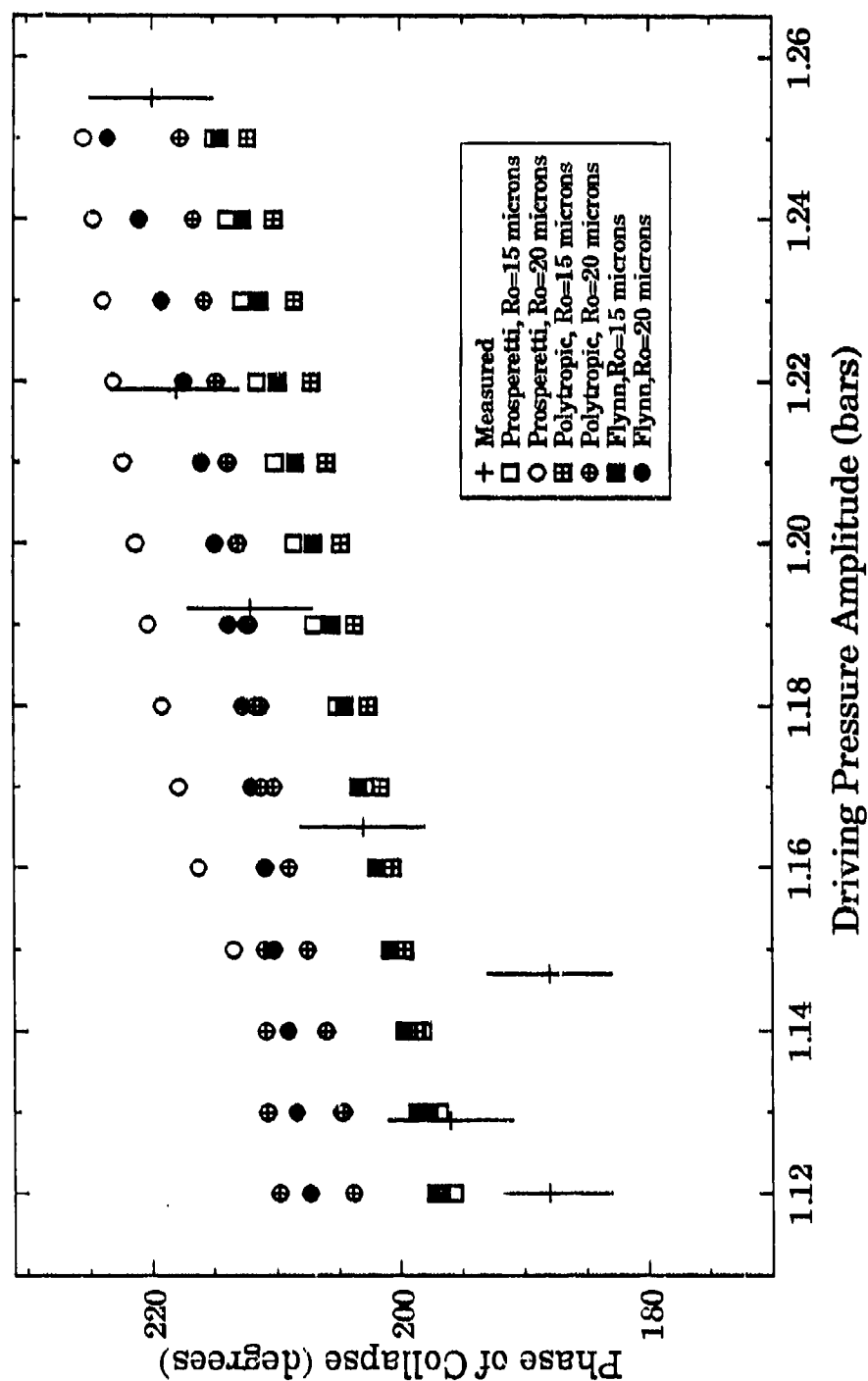


Figure 52. Measured and theoretical phase of bubble collapse (ϕ) vs acoustic pressure amplitude in water using all three formulations at $f=21.0$ kHz.

PHASE OF COLLAPSE for 42% GLYCERINE

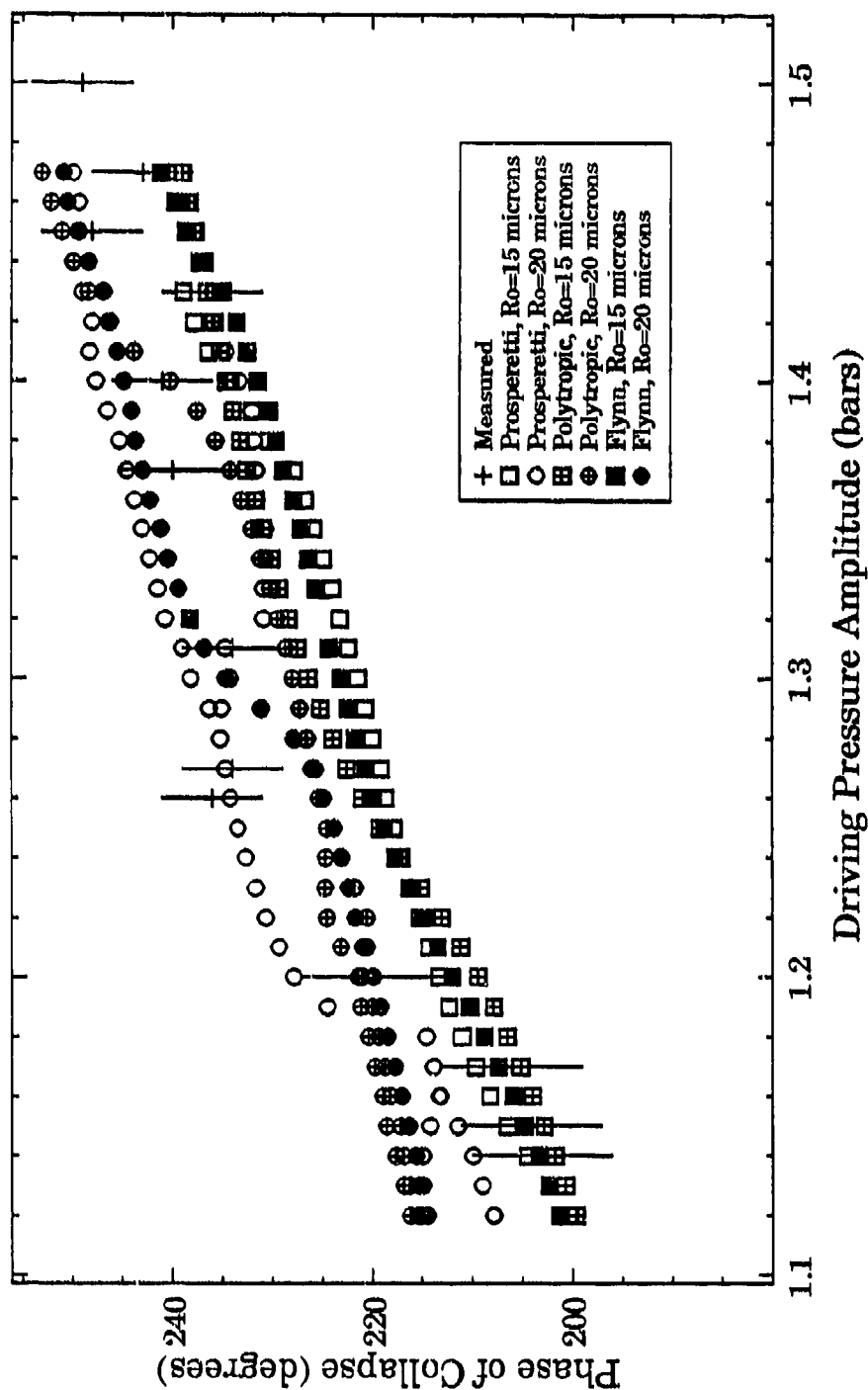


Figure 53. Measured and theoretical phase of bubble collapse (ϕ_c) vs acoustic pressure amplitude in GLY42 using all three formulation at $f=23.6$ kHz.

NUMBER of MINIMA for WATER

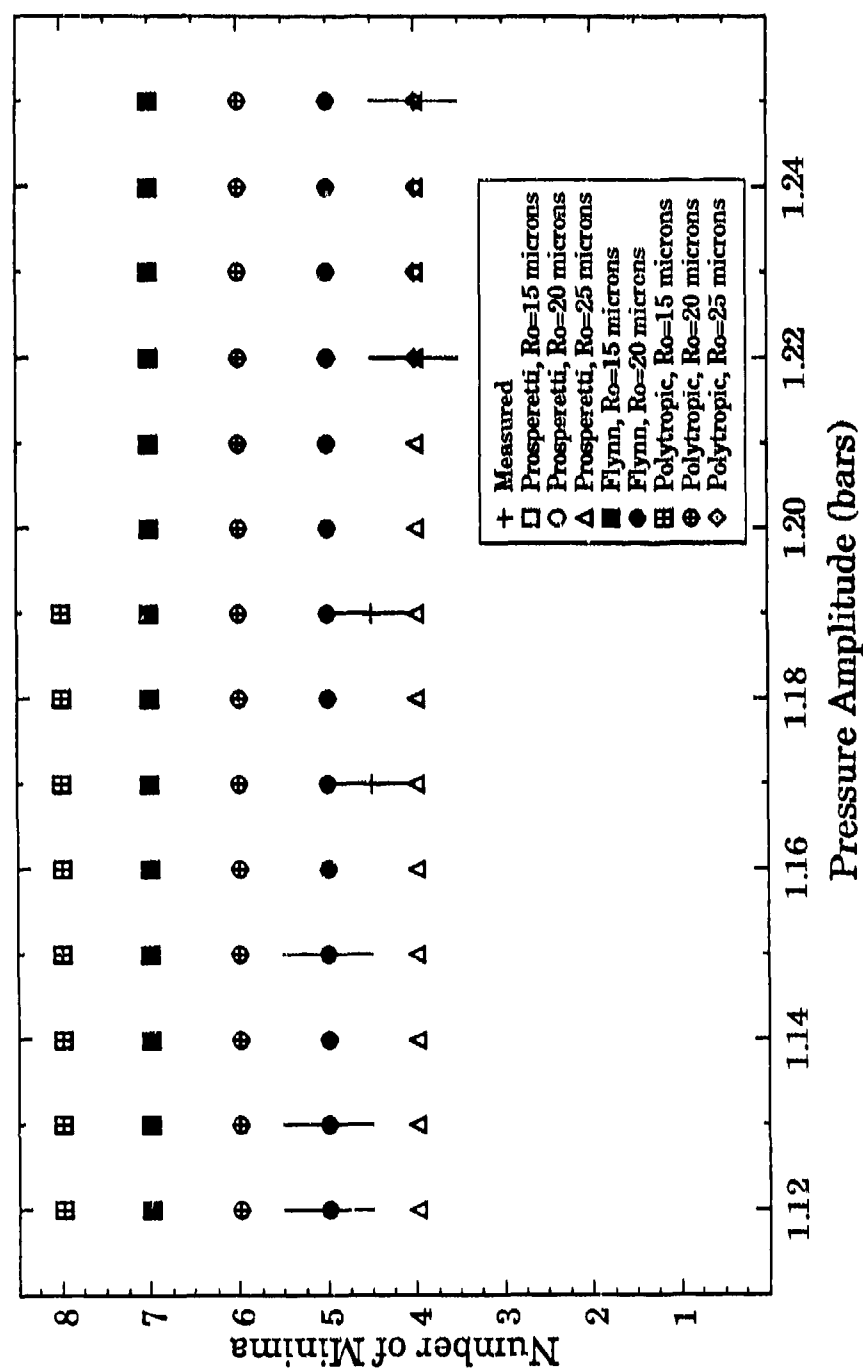


Figure 54. Measured and theoretical number of minima (M) vs acoustic pressure amplitude in water using all three formulation at $f=21.0$ kHz.

NUMBER OF MINIMA for 42% GLYCERINE

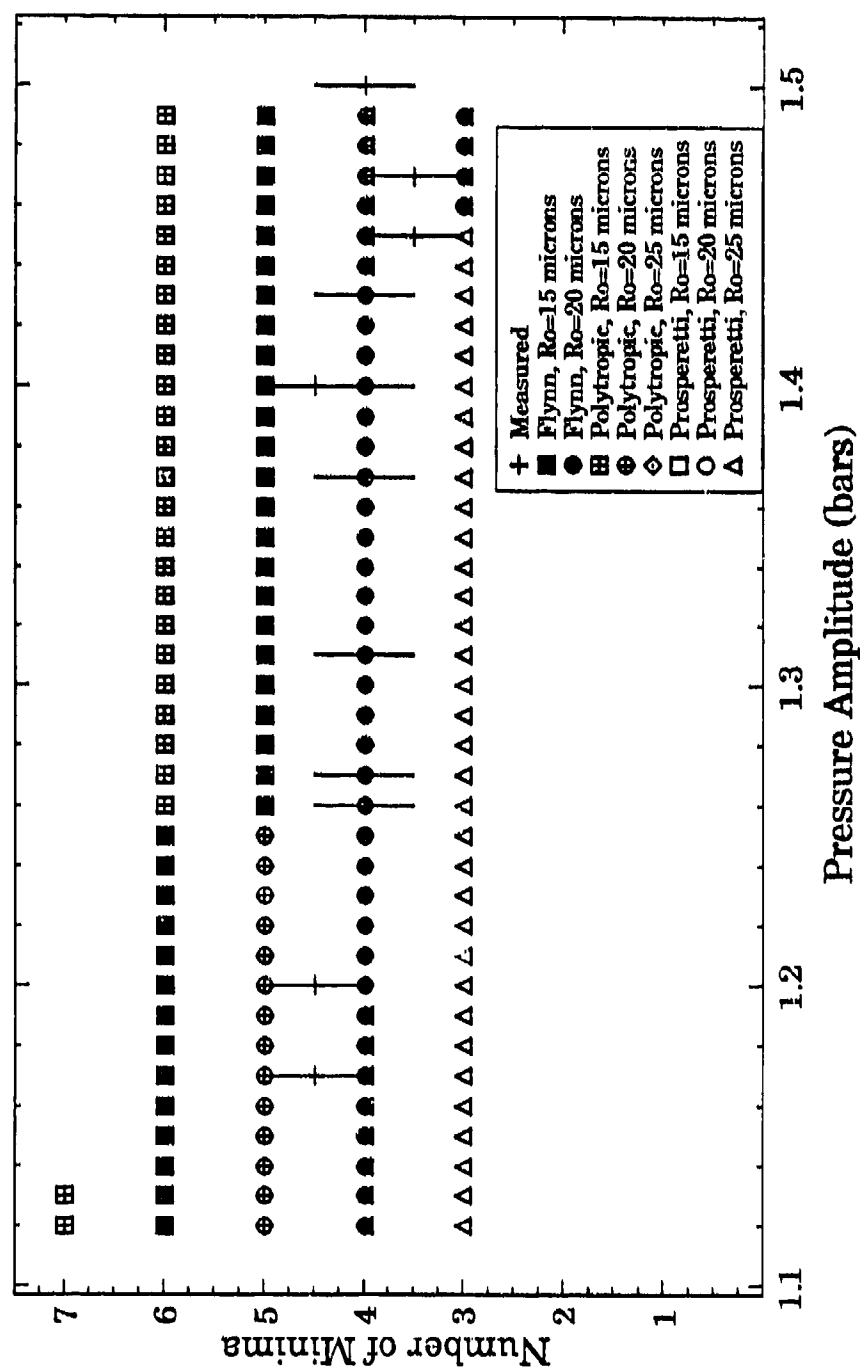


Figure 55. Measured and theoretical number of minima (M) vs acoustic pressure amplitude in GLY42 using all three formulations at $f=23.6$ kHz.

data shown in Fig. 54 (water) imply that $20 \leq R_o \leq 25 \mu\text{m}$ increasing with p_A and those in Fig. 55 (GLY42) indicate that $R_o \sim 20 \mu\text{m}$ also increasing slightly with p_A . Note that, in general, the conclusions agree fairly well with Prosperetti's in the previous Section. The results of Flynn's data have been summarized in Table 5 below.

Table 5. Summary of predictions of R_o obtained from Flynn's formulation.

Theoretical Range of R_o for Single Bubble Pulsations

	From R_{max}	From ϕ_c	From M
water	10-15 μm (>)*	10-20 μm (>)	20-25 μm (>)
GLY42	10-15 μm (>)	15-20 μm (>)	20 μm (>)

* (>) indicates that the value of R_o increased as p_A increased.

Let us now consider the results from the polytropic model plotted in the same Figures using the crossed symbols as indicated in the legend. The pulsation amplitude data shown in Fig. 50 (water) indicate that $10 \leq R_o \leq 20 \mu\text{m}$, increasing as p_A increases. The data shown in Fig. 51 (GLY42) indicate that $R_o \leq 15 \mu\text{m}$, with R_o increasing to $15 \mu\text{m}$ or more as p_A increases. The phase of collapse data shown in Fig. 52 (water), however, suggest that $10 \leq R_o \leq 20 \mu\text{m}$ with R_o also increasing as p_A increases. The data in Fig. 53 (GLY42) indicate that $15 \leq R_o \leq 20 \mu\text{m}$ increasing with p_A . The number of minima data shown in Fig. 54 (water) imply that $22 \leq R_o \leq 25 \mu\text{m}$ increasing with p_A . Note that some of the data points are hidden behind the solid symbols used to represent Flynn's results. For example, the number of minima for $R_o=15$ is equal to 7 for the higher values of p_A and for $R_o=25$ is equal to 5

for the lower values of p_A . Confusion can be avoided if one knows that the number of minima usually decreased by one unit (at the most) as p_A increased. The data in Fig. 55 (GLY42) indicate that $R_o \approx 20 \mu\text{m}$ also increases slightly with p_A . In general, these values of R_o agree fairly well with those based on Prosperetti's predictions shown in the previous sections, and even better with those based on Flynn's predictions. The results of the polytropic model data have been summarized in Table 6 below.

Table 6. Summary of predictions of R_o obtained from the polytropic formulation.

Theoretical Range of R_o for Single Bubble Pulsations

	R_{max}	ϕ_c	M
water	15-20 μm (>)*	10-20 μm (>)	22-25 μm (>)
GLY42	10-15 μm (>)	15-20 μm (>)	20 μm (>)

* (>) indicates that the value of R_o increased as p_A increased.

From Tables 4, 5, and 6 it can be seen that the values of R_o predicted by the three formulations based on the same measured parameter (R_{max} , ϕ_c or M) are very similar - between 15 and 25 microns. Also, self-consistency was found for Prosperetti's theory in 2 out of 5 liquid mixtures (GLY21 and GLY60), where the values of R_o based on the measurements of R_{max} were the same as those based on the measurements of ϕ_c , as shown in Table 4. This was not the case for water, GLY35 and GLY42, however. Since theoretical data for Flynn's and the polytropic theories were calculated for water and GLY42 only (due to time constraints), the lack of consistency in those two theories is not surprising. However, by looking at

the results of Prosperetti's theory and the fact that all theories gave similar results, we can conclude that although disagreement was found in some cases, disagreement is not expected to occur in every case. In summary, two conclusions can be made: 1) The measurements do not constitute a good test to discriminate between the theories, since the experimental error is larger than the difference between the values predicted by the theories using the same conditions; 2) the values of R_0 predicted by each particular theory based on the experimental R_{max} and ϕ_c are not consistent, indicating that the models are not completely applicable for the range of parameters considered here.

Based on the theoretical results, some general comments will be made on the characteristics of each model in the second half of this Section. As seen in Fig. 50 (water) and 51 (GLY42), Prosperetti's model predicted, in general, larger values of the pulsation amplitude than the other two theories. As expected, the phase of collapse is also larger, as seen in Figs. 52 (water) and 53 (GLY42). On the other hand, the values predicted by the polytropic theory were the lowest of the three theories. These results may be explained in terms of the thermodynamics in the interior of the bubble.

For the case of the polytropic formulation, the small bubble sizes used in the calculations resulted in a value of the polytropic exponent nearly equal to 1. This means the motion is essentially isothermal. Isothermal motion produces no rise in the internal temperature, allowing the radius to reach much smaller values, and generating very high internal pressures and densities. In addition, isothermal motion usually resulted in lower pulsation amplitudes for the range of parameters considered in this study. On the other hand, adiabatic collapses

produce higher internal temperatures, lower pressures and larger pulsation amplitudes than isothermal collapses. Thus, the lower pulsation amplitudes predicted by the polytropic theory can be attributed to the isothermal motion of the bubbles.

The theoretical values of the pulsation amplitude using Flynn's formulation are also consistently lower than those predicted by Prosperetti's, although somewhat larger than those predicted by the polytropic's, as can be seen in Figs. 50 and 51. These results are the opposite of those expected if the same argument given above were applied. As stated in Chapter III, the rise in temperature at the bubble wall predicted by Flynn's model would theoretically result in a decrease of the heat flux away from the bubble and, consequently, a more adiabatic motion. The theoretical results shown in Figs. 50 and 51, however, indicate just the opposite. Thus, an alternative explanation had to be found. Besides the expression for the internal pressure, the only other significant difference between Flynn's and Prosperetti's formulation is the extra compressibility term in the radial equation (see Chapter III). Calculations made using Prosperetti's formulations with the extra term found in Flynn's radial equation resulted in slightly smaller pulsation amplitudes but much larger radial minima. The larger radial minima are naturally expected to affect significantly the internal temperature and pressure during the bubble's collapse. It should be noted that only period-1 solutions were predicted by Flynn's model, in contrast to Prosperetti's which predicted period-2 and period-4 solutions.

In summary, Prosperetti's model was found to give the largest pulsation amplitude and collapse phase, whereas the polytropic model was found to give the

smallest. This was explained by the essentially isothermal behavior predicted by the polytropic formulation. In addition, the extra compressibility term found in Flynn's model was found to affect the bubble motion especially during the collapse, resulting in slightly smaller pulsation amplitude and collapse phase. The values of R_o predicted by Flynn's theory and polytropic theory are essentially the same as those predicted by Prosperetti's.

IV. B. 2. Theoretical Values of Temperature, Pressure and Relative Density

The calculated maximum internal temperature (T_{max}) and pressure (P_{max}) reached during the collapse predicted by Prosperetti's and Flynn's theories for the set of parameters used during the experiment have been plotted in Figs. 56-59. In Prosperetti's calculations, the temperatures have been averaged over the bubble's interior in order to compare them with the temperatures predicted by Flynn's theory. The internal pressure is assumed uniform in both cases. Because of the isothermal bubble motion of the polytropic formulation, the predicted pressures were unreasonably high and the temperatures unreasonably low. We have, therefore, not included them in this analysis.

The maximum internal temperatures, pressures and relative densities have been summarized in Table 7, 8 and 9 below. The relative densities, which have been normalized with respect to equilibrium conditions, were calculated from $\rho_{max}=(R_o/R_{min})^3$. Note that for water, $1.12 \leq p_A \leq 1.25$ whereas for GLY42, $1.12 \leq p_A \leq 1.47$ so that higher values are expected for GLY42.

THEORETICAL TEMPERATURES FOR WATER

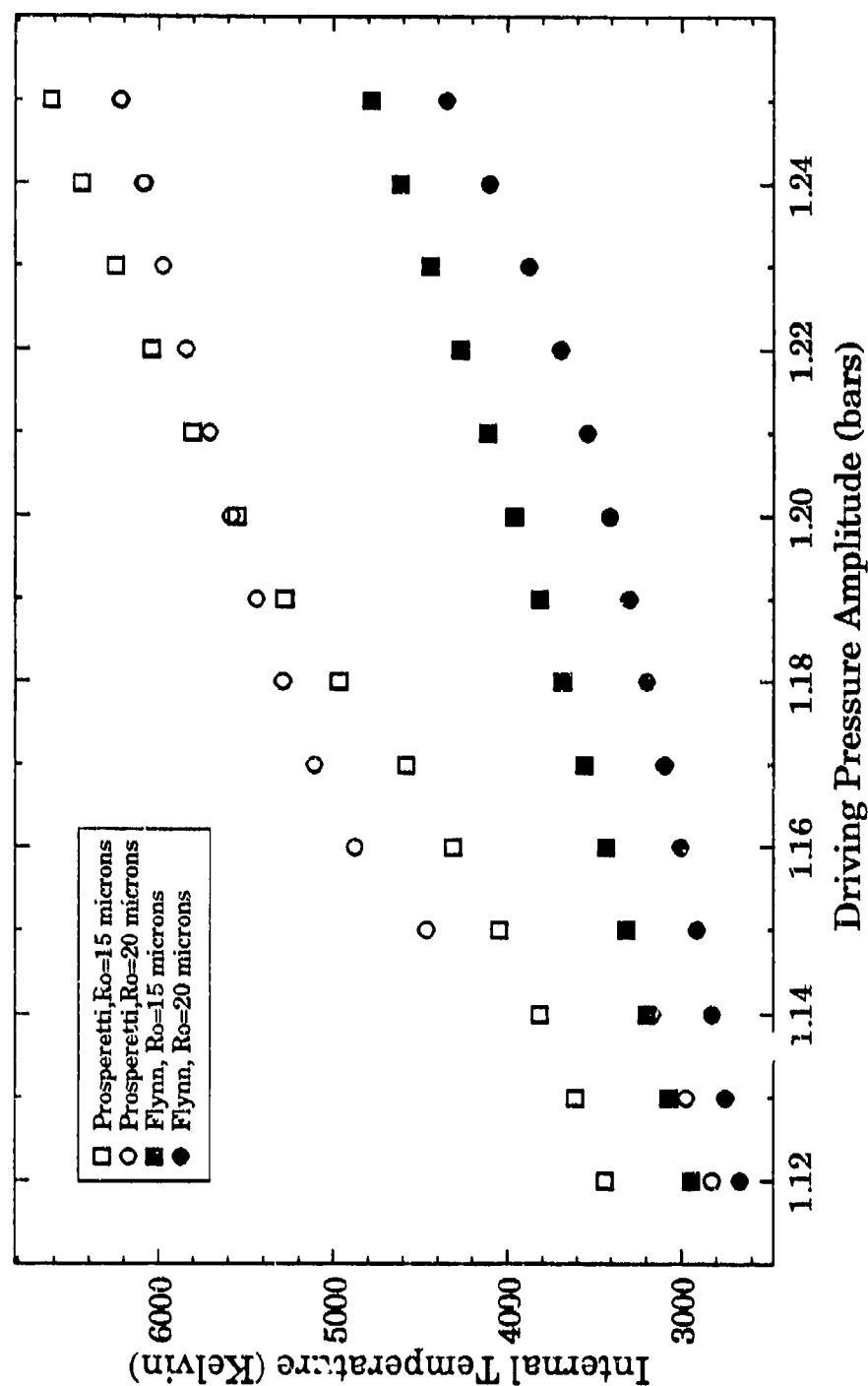


Figure 56. Theoretical maximum gas temperature reached during the bubble collapse in water for $R_0=15$ and 20 microns at $f=21.0$ kHz.

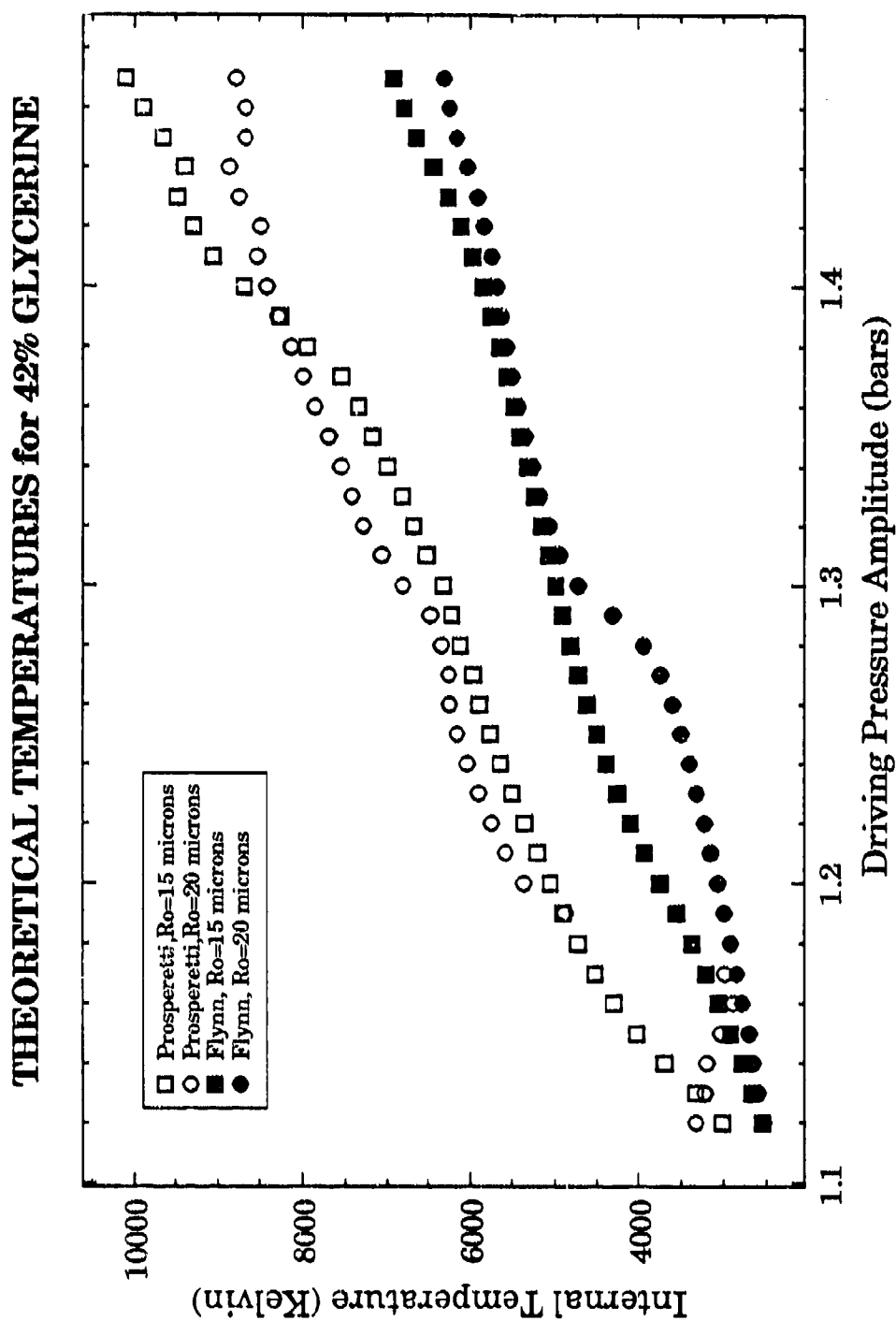


Figure 57. Theoretical maximum gas temperature reached during the bubble collapse in GLY42 for $R_o=15$ and 20 microns at $f=23.6$ kHz.

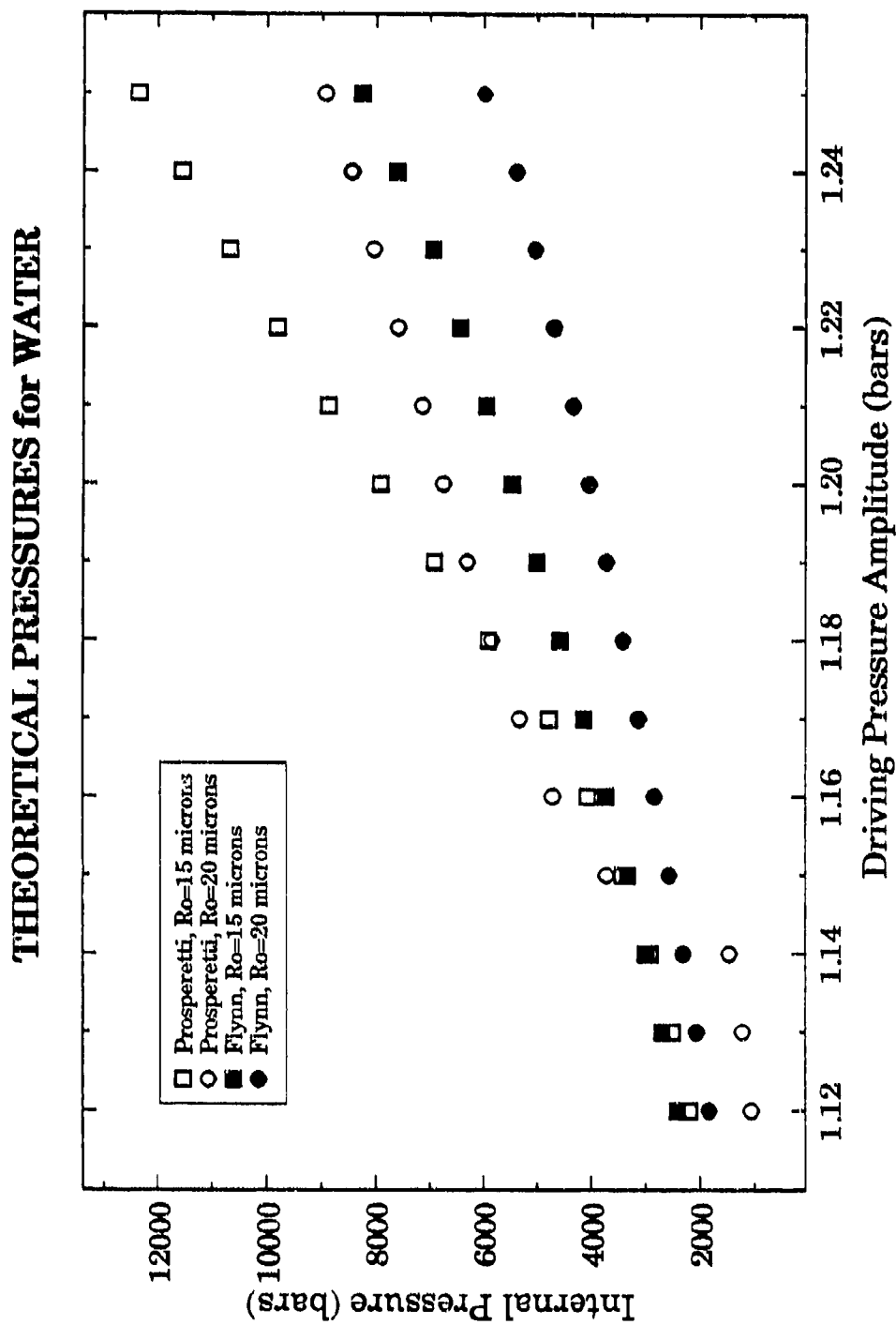


Figure 58. Theoretical maximum gas pressure reached during the bubble collapse in water for $R_0=15$ and 20 microns at $f=21.6$ kHz.

THEORETICAL PRESSURES for 42% GLYCERINE

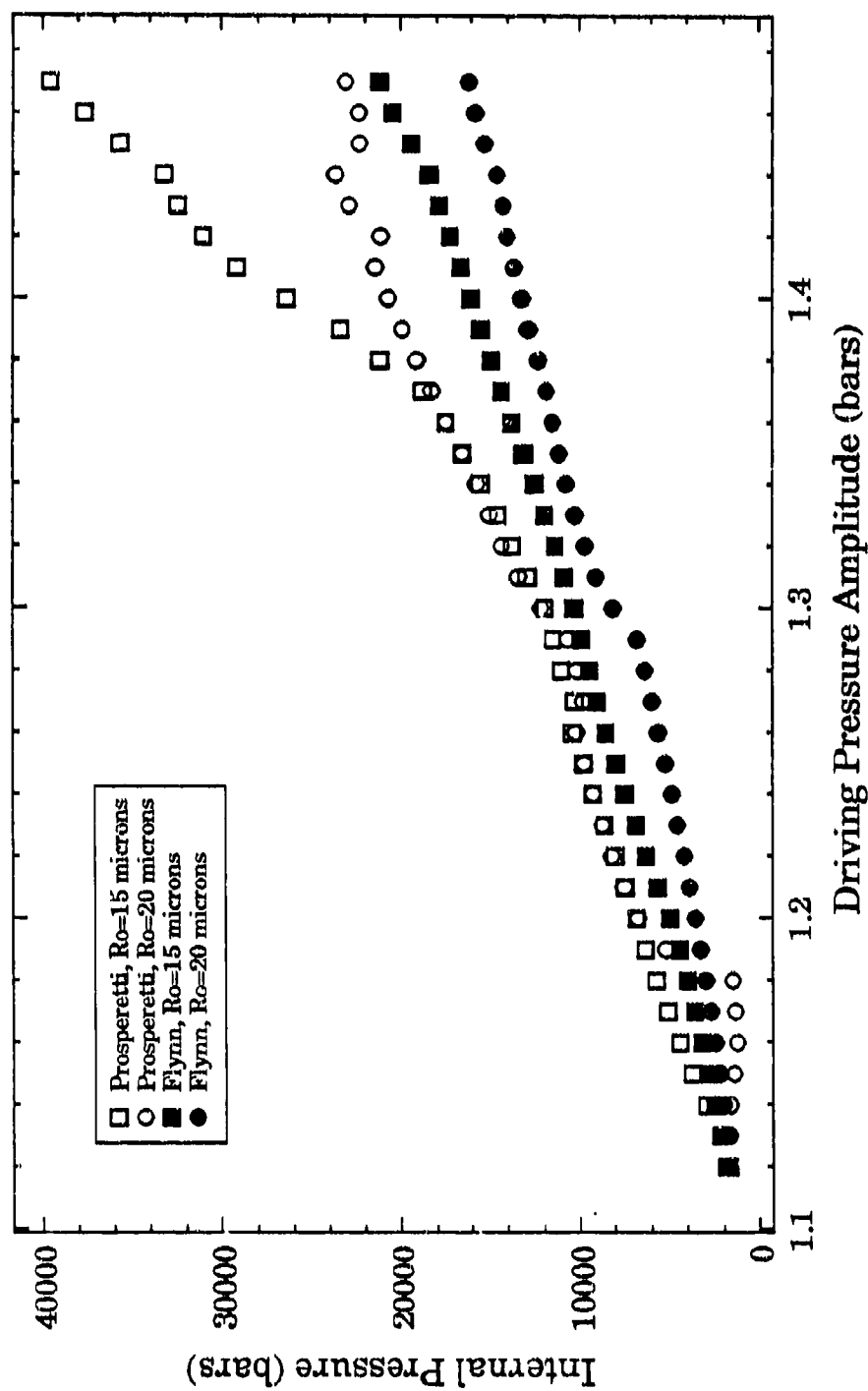


Figure 59. Theoretical maximum gas pressure reached during the bubble collapse in GLY42 for $R_0=15$ and 20 microns at $f=23.6$ kHz.

Table 7. Summary of maximum theoretical temperatures inside 20-25 μm bubbles for the range of p_A used during the experiments.

Theoretical Range of T_{max} for Single Bubble Pulsations (Kelvin)

	p_A (bars)	Prosperetti	Flynn	Prosperetti (Flynn)
water	(1.12-1.25)	2,500-7,000	2,500-5,000	2,500-6,000
GLY42	(1.12-1.47)	3,000-10,000	2,500-7,000	3,000-8,000

Table 8. Summary of maximum theoretical pressures inside 20-25 μm bubbles for the range of p_A used during the experiments.

Theoretical Range of P_{max} for Single Bubble Pulsations (bars)

	p_A (bars)	Prosperetti	Flynn	Prosperetti (Flynn)
water	(1.12-1.25)	1,000-12,000	2,000-7,000	2,000-8,000
GLY42	(1.12-1.47)	2,000-40,000	2,000-22,000	2,000-20,000

Table 9. Summary of maximum theoretical relative densities inside 20-25 μm bubbles for the range of p_A used during the experiments.

Theoretical Range of ρ_{max} for Single Bubble Pulsations

	p_A (bars)	Prosperetti	Flynn	Prosperetti (Flynn)
water	(1.12-1.25)	150-500	200-400	100-400
GLY42	(1.12-1.47)	200-1300	150-700	200-700

The third column of each Table contains the maximum internal temperatures (T_{max}), pressures (P_{max}), and relative densities (ρ_{max}) predicted by Prosperetti's

theory, and those predicted by Flynn's theory are shown in the fourth column. Note that, in every case, the temperatures and pressures predicted by Prosperetti's theory are higher than those predicted by Flynn's for the same bubble size, even for the cases where the pulsation amplitude predicted by Prosperetti's was less. The fifth column of each Table contains the same quantities calculated using Prosperetti's formulation with Flynn's radial equation (instead of Keller's). These values will be referred to as Prosperetti (Flynn)'s. The difference in the predictions shown in columns four and five is entirely due to the way in which the internal pressure is obtained by each formulation, i.e., the thermodynamics in the bubble's interior. Notice how the values of T_{max} , P_{max} and ρ_{max} predicted by Prosperetti's theory are lower when Flynn's radial equation is used instead of Keller's, suggesting that the additional compressibility term plays a significant role during the collapse. The values of T_{max} and P_{max} predicted by Prosperetti (Flynn), however, are still higher than those predicted by Flynn's theory by about 10-20%. The values of ρ_{max} are about the same in both cases. These results indicate that Prosperetti's theory does not allow as much heat to diffuse out into the liquid resulting in higher temperatures and pressures than Flynn's theory for the range of parameters considered here.

As stated earlier in Chapter I, the phenomenon of sonoluminescence is primarily of thermal origin, i. e., caused by high temperatures rather than high pressures or densities. The determination of the minimum temperature required for light emission is, therefore, important in understanding the mechanisms involved. Since the acoustic pressure threshold for light emission was measured in this study to be around 1.1 bars, this indicates that, according to the theories,

the minimum temperature necessary to generate SL is between 2,000 and 3,000 K, corresponding to relative densities about 100-200. In the second half of this Section, previously measured temperatures and relative densities in the interior of cavitation bubbles during SL emission will be compared with the theoretical values. These previous experiments have been described in Chapter I. Since in this study sonoluminescence has been observed to be generated only by bubbles between 15-25 μm , it will be assumed that, during all the previous experiments (at insonation frequencies around 20 kHz), only bubbles in this size range were responsible for the light emission. It should be pointed out that this observation does not agree with others made in the past by various researchers which indicate, based on the phase of the light flashes, that SL was also emitted by much larger bubbles, e.g. 220 μm (Jarman *et al.*, 1970). However, strong evidence has been gathered in this study which indicates that only small bubbles collapsing radially are capable of producing high enough temperatures to generate sonoluminescence.

Relative densities of about 60 were measured by Taylor *et al.* (1970) and about 40 by Sehgal *et al.* (1979) (see Table 3 in Chapter I) during spectral studies of sonoluminescence. These values are smaller than the minimum (100-200) predicted by the theories at the measured threshold for light emission. Assuming that SL was produced by bubbles in the size range measured in this study (15-25 μm), tests performed using Prosperetti's theory indicate that a relative density of 60 would not generate temperatures higher than 2000 K, just enough to produce light emission by most estimates (Saksena *et al.* 1970). The 10,000 K temperature reported by Taylor *et al.* was obtained from spectral measurements assuming

blackbody radiation, which is now known to be an incorrect assumption. Even an adiabatic collapse in which the density increased by a factor of 60 would only result in temperatures less than 5,000 K and pressures less than 1000 bars.

The relative density measured by Sehgal *et al.* (1979) of 40 is even lower, which is also rather unexpected, since bubble dynamics theories that include thermal dissipation predict higher densities at higher insonation frequencies. This is because, at the higher frequencies, the motion of the active bubbles is more isothermal (due to their smaller size), requiring a stronger collapse in order to generate temperatures high enough to produce sonoluminescence. The temperature of 2450 K calculated by Sehgal *et al.* using Young's (1976) equation is, therefore, much larger than that expected from Flynn's or Prosperetti's theory for a relative density of 40 and the set of parameters used in Sehgal's experiment. In short, a relative density of 40 is too low to generate the temperatures necessary for light emission.

In a second experiment, Sehgal *et al.* (1980) reports measurements of the temperature of sonoluminescence emission of 1350 and 860 in NO- and NO₂-saturated water at 459 kHz. Again, these temperatures are low by most estimates of the temperatures necessary for light production. Since these experiments required measuring the spectra of SL, it can be assumed that relatively high intensities (much above the threshold for light emission) were used during the experiments to obtain as much light as possible in order to improve the precision and accuracy of the measurements. It is mainly for this reason that the relative densities and temperatures obtained from these experiments are believed to be rather low. It should be pointed out that some authors justify these results by

arguing that bubble breakup must occur early during the collapse, preventing the bubble contents from being compressed as much as would be expected from the theories. This, however, is not supported by the spark-induced cavitation experiment performed by Golubnichii *et al.* (1979), or the observations made during the present study. Golubnichii *et al.* measured collapse ratios $R_m/R_{min}=30$, indicating that the cavity remained spherical during most of the collapse. Note that, in this case, collapse ratios are measured relative to the maximum radius R_m and should not, therefore, be compared directly with those measured relative to an equilibrium radius, as is customarily done in acoustic cavitation. Since the cavities generated by electric sparks are mostly composed of vapor, an equilibrium radius does not exist under normal conditions. Golubnichii *et al.* also calculated a temperature of 9,000 K and a pressure of 19,000 bars assuming an adiabatic collapse and a perfect gas inside the cavity.

The most recent and precise measurement of temperatures inside cavitation bubbles is that by Suslick *et al.* (1986b), using a comparative rate thermometry technique in aqueous solutions at 20 kHz. They measured a temperature of 5200 ± 650 K at acoustic intensities of 24 W/cm^2 , which corresponds to about 8 bars assuming plane waves. This temperature falls in the middle of the range of the theoretical temperatures calculated in this study, corresponding to $p_A \approx 1.3$ bars, much lower than the estimated 8 bars used in Suslick's experiment. It is, however, more than sufficient to generate sonoluminescence based on the evidence collected in this study.

As stated earlier, most experiments in which the temperature of collapsing cavities was measured probably required high intensity sound fields which

generated many cavities at once. In addition, transient cavitation was most likely the prevalent type of cavitation, implying that light emitting cavities did not last for more than a couple of acoustic periods. In the stable cavitation observed in this study, it has been determined that an increase in the acoustic pressure amplitude results in higher temperatures, as evidenced by the increase in the light emitted from the bubble. In a cavitation field where many bubbles are present, it is not obvious whether an increase in light emission is due to an increase in the amount of light emitted by each bubble, or an increase in the number of bubbles emitting light. Since the light emitted by each bubble should be proportional to the temperatures reached in its interior, it should be interesting to measure the dependence of the internal temperature on the acoustic intensity in experiments such as Suslick's. Furthermore, the internal temperatures measured in Suslick's experiments, which were performed at much higher pressure amplitudes, (~ 8 bars as opposed to ≤ 1.5 bars used in this study), indicate that present theories of bubble pulsations overestimate the internal temperature and possibly the internal pressure too. This overestimation may be explained by the failure of the assumptions made in the models. Specifically, the possible dissociation of the gas molecules due to the high temperatures attained would increase the number density and, therefore, the internal (gas) pressure, arresting the bubble collapse sooner. When temperatures of 5,000 K or higher are reached, it is also very likely that the energy of the collapse begins to go into other chemical processes, instead of increasing the temperature of the gas. Some of these processes include dissociation of the gas molecules and ionization. Thus, as the strength of the collapse increases i.e., larger values of p_A , the internal

temperature is expected to reach a maximum saturation value. In addition, The models underestimate the effects of energy dissipation due to the compressibility of the liquid. A highly compressible liquid results in the formation of shock waves which may carry a significant portion of the collapse energy away from the bubble.

IV. B. 3. Phase of Sonoluminescence *vs* Bubble Motion

In order demonstrate the simultaneity of SL and the minimum radius of an acoustically driven bubble, simultaneous traces of the radius of the bubble and the light emission have been obtained. Fig. 60 is a plot of the experimental results clearly showing that SL is produced during the collapse of the bubble. These data were obtained with the light scattering apparatus and the PMT. We were unable to obtain an appropriate filter for the PMT which would allow the simultaneous operation of both the laser and the PMT. Thus, an intermediate phase reference had to be used in order to properly correlate the light scattered with the PMT output. This common reference was the side pill transducer whose voltage output was proportional to the acoustic pressure in the cell. In this way, a trace of the light intensity scattered and the pill voltage output were obtained simultaneously, transferred to the computer and stored on disk. Immediately after, traces of the PMT output (with the laser light turned off) and the pill output were also stored on disk. A graphics program was then used to determine the correlation by plotting the two traces simultaneously as shown in Fig. 60. Since the two sets of data were taken within a few seconds of each other, it was ensured that all the experimental conditions remained identical. The uncertainty in this experiment was estimated

SONOLUMINESCENCE vs BUBBLE COLLAPSE

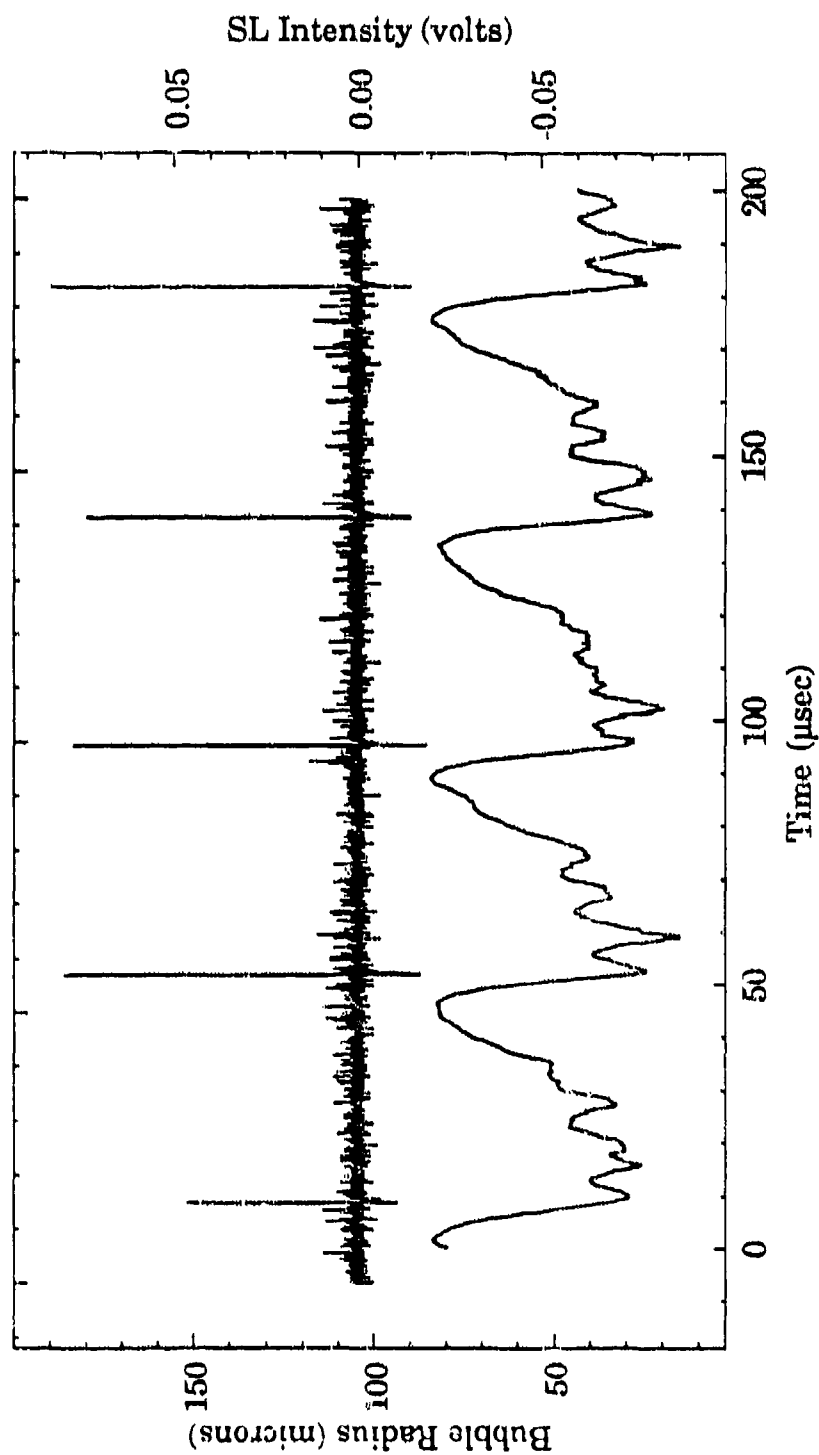


Figure 60. Simultaneous plots of the bubble radius (bottom) and sonoluminescence (top) in GLY21 at $p_A=1.2$ bars and $f=22.3$ kHz.

to be ± 5 degrees and it is mostly due to the time delay introduced by the photodetector built-in electronics.

The objective of this experiment was to verify the coincidence of SL with the minimum bubble volume. The results obtained were interpreted as an indication that SL and the phase of the bubble collapse occurred simultaneously. In the next Section, this result will be used to study the phase of the motion of cavitation bubbles by measuring the phase of SL emission.

IV. C. Time to Amplitude Converter System: Sonoluminescence *vs* Sound Field

1. Single Bubble Cavitation Field

After the simultaneity of the light emission and the collapse of the bubble was established, the phase of the SL emission was used to study the behavior and the time evolution of cavitation bubbles as they interacted with the sound field and with each other. This was done by measuring the phase of the light emitted by the bubbles in order to obtain the phase of the bubble collapse. In view of the already established coincidence of the light emission and the bubble collapse, these two terms will be used interchangeably. In order to interpret the observations made in multibubble cavitation fields, the results for a single bubble will be examined in this Section. These data were obtained by enclosing the levitation cell system in the light tight box and measuring the phase of SL emission as described in Section E of Chapter II.

Figure 61 shows the phase of SL at approximately 1.1 bars in water, plotted as a function of time in units of acoustic periods which also corresponded to the

SONOLUMINESCENCE from a SINGLE BUBBLE

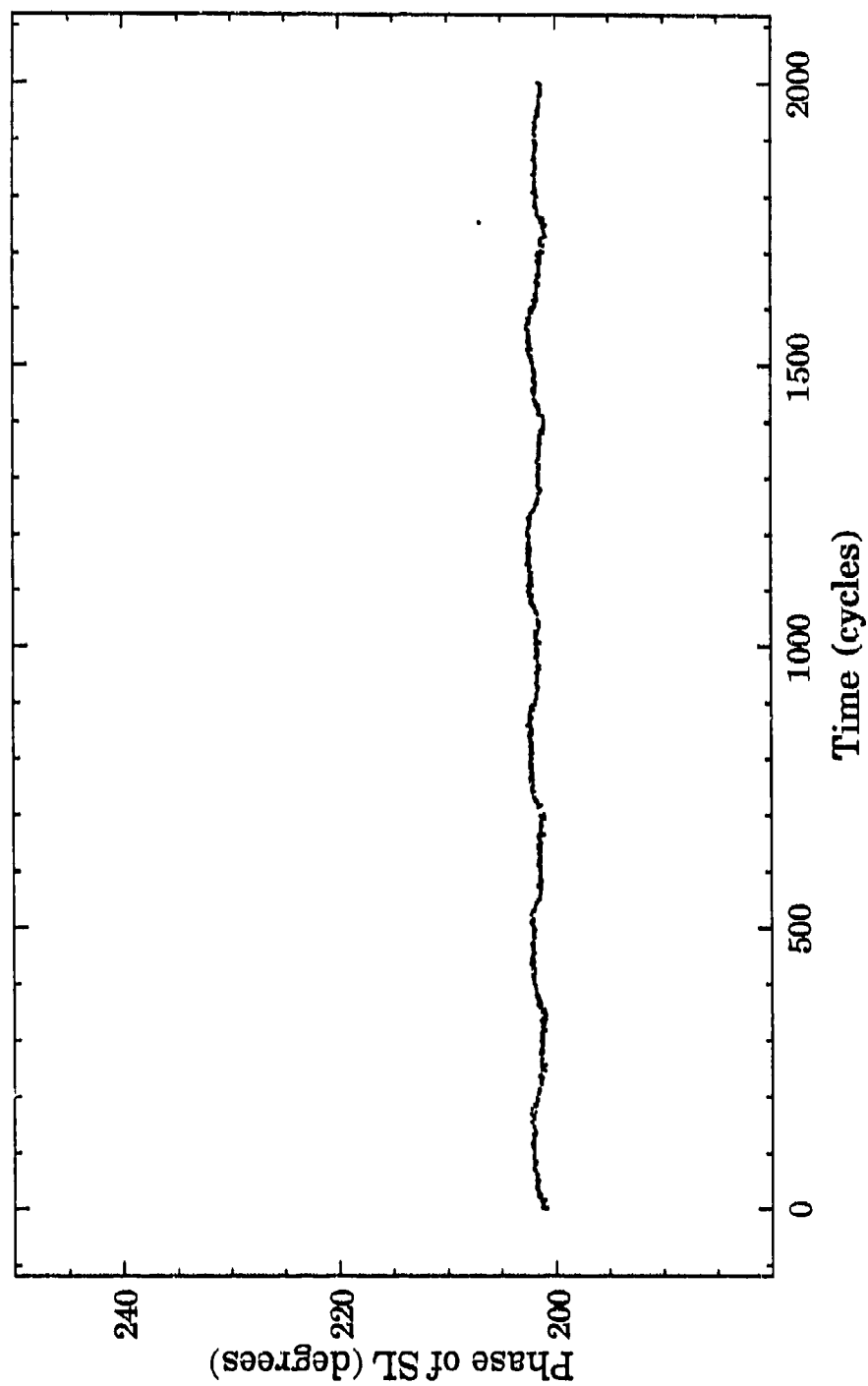


Figure 61. Phase of sonoluminescence emitted by a single bubble as a function of time. It was measured in water at $p_A=1.1$ bars and $f=21.0$ kHz by the time-to-amplitude converter (TAC) system.

sampling period. In this data set, a total 2,000 data points were taken corresponding to approximately 0.1 sec. The small oscillations on these data are due to 60 Hz line noise which could not be easily filtered. Typical 60 Hz noise levels were ± 1 degree which were far less than the actual fluctuations of the data. This is an example of the phase of the light emission for a single bubble pulsating radially. In order to determine if a single bubble were present, the output of the side pill transducer was monitored. This output would become noticeably irregular and noisy when streamers were present. For a single bubble, however, the signal was symmetrical except for a small notch, probably due to the shock wave produced by the bubble collapse. In this case (Fig. 61), the value of the phase was 201 degrees. A range of values was measured between 190 and 220 degrees for pressure amplitudes between 1.0 and 1.4 bars in water.

Occasionally, the levitated bubble was visually observed to become unstable for a fraction of a second, after which stability was restored. This transition was usually accompanied by a vertical shift in the bubble's position. This new position was always higher i.e., away from the antinode. When the light emission during this transition was monitored, it was visually observed that the intensity of each flash was sharply decreased. This occurred simultaneously with a decrease in the phase of the emission. These observations are illustrated in Fig. 62. The phase can be clearly seen to decrease sharply during the transition at 600 cycles. This decrease of the phase may be interpreted as a decrease of the equilibrium bubble radius i.e., a breakup of the bubble due to surface instabilities. This type of breakup usually occurs via the ejection of microbubbles (Nyborg and Hughes, 1967; Neppiras *et al.*, 1969). After reducing its size, the bubble regains its stability due to

SONOLUMINESCENCE from a SINGLE BUBBLE

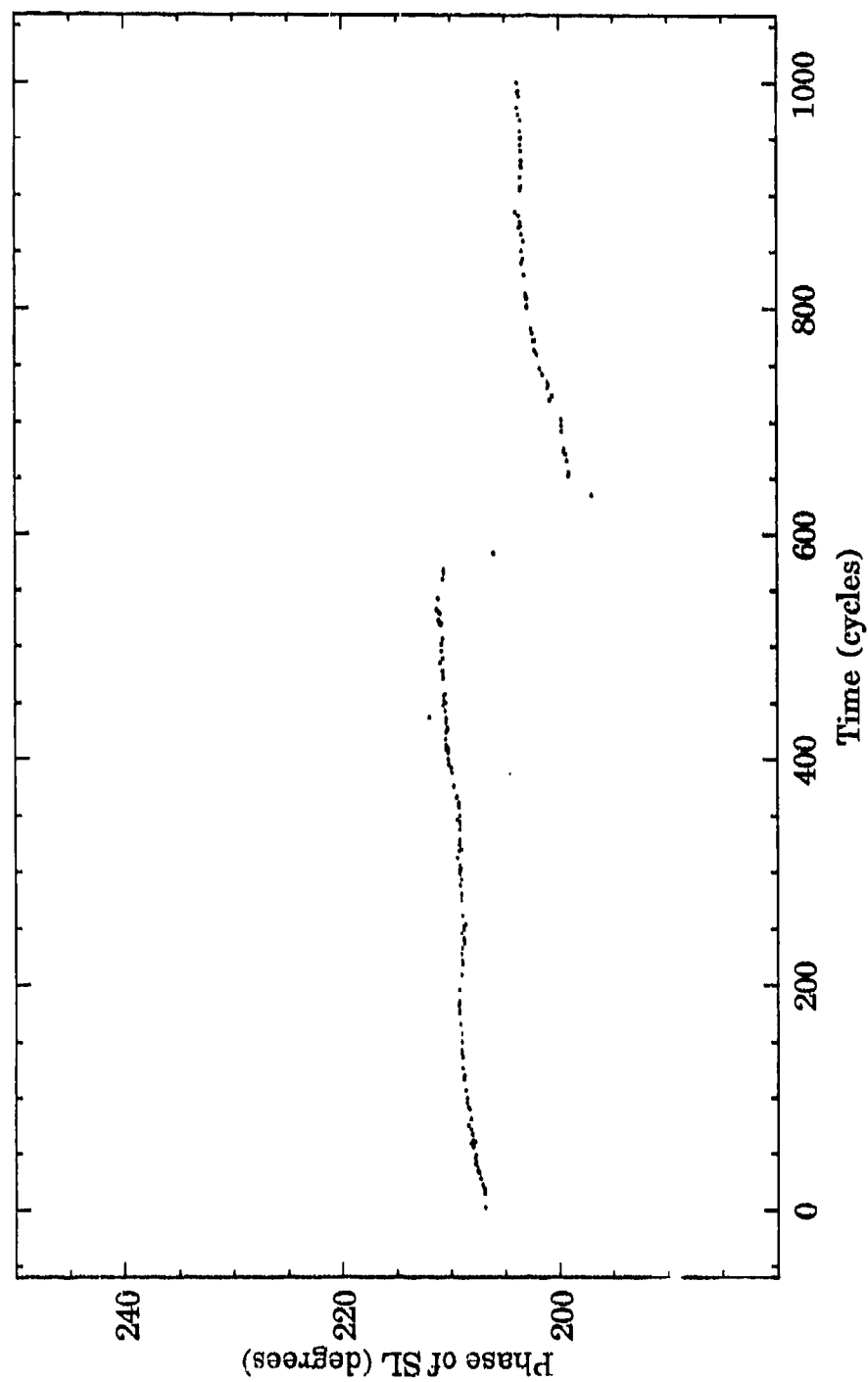


Figure 62. Phase of sonoluminescence emitted by a single bubble as a function of time. It was measured in water at $p_A=1.2$ bars and $f=21.0$ kHz by the time-to-amplitude converter (TAC) system during a transition (see text).

the larger surface pressure ($2\sigma/R_0$). This occasional, and sometimes periodic, breakup can be understood in terms of the bubble response curve as a function of equilibrium radius (Fig. 23). As the bubble grows, resonances are encountered and the bubble response increases rapidly. If the surface instability threshold happens to be below one of these peaks, breakup will occur and the bubble size is quickly reduced. This cycle may repeat depending on p_A and the new value of R_0 , among other parameters. In addition, by plotting the pulsation amplitude, R_{max} , and the phase of the collapse as a function of R_0 , a direct correlation between these two quantities can be established, as shown in Fig. 23 and Fig. 24. Note that when R_{max} increases (decreases) the phase also increases (decreases). Note that a change in the radius R_0 as small as 1 micron can result in the phase of collapse changing by as much as 20 degrees, depending on the bubble size. Thus, it does not require a large change in radius to effect a large change in the phase.

It appears that, before the bubble regains stability, its response amplitude and size must be decreased. This is not surprising, since instabilities in the gas-liquid interface are triggered by large accelerations, as shown in Chapter III. Thus, this observation can be explained as follows: After developing instabilities, the bubble sheds microbubbles, reducing its size and its response amplitude. Both of these increase the stability of the bubble and the pulsations become spherically symmetric again. This behavior is commonly seen in single bubbles at the higher pressure amplitudes (~1.3-1.4 bars).

In some cases, instabilities occurred repeatedly with a period of a few seconds. At the higher end of the pressure range for stability, transitions often occurred

consecutively as shown in Fig. 63. In this case, it may be postulated that the pressure amplitude was so high that surface waves were easily excited, and the bubble was unable to regain its stability. If the residual bubbles were large enough or close enough to the initiating bubble, coalescence may occur before they can dissolve. This may explain the bubble growth implied by the rapid increase in the phase of collapse shown in Fig. 63. Sometimes the bubble disappears unexpectedly, as was the case in this particular data set in which the bubble suddenly stops emitting light around cycle 1250. This bubble disappearance can also be observed with the unaided eye or through the microscope. A similar type of bubble annihilation was reported by Nyborg and Hughes (1967) during observation of cavitation on the surface of a vibrating bar driven at 20 kHz. Using high speed photography, they reported bubbles which disappeared in less than 6 acoustic periods. An explanation similar to the above was given by Nyborg *et al.* (1967) for this phenomenon.

In summary, we can propose that bubbles grow and breakup in a periodic fashion during radial pulsations. A breakup is usually reflected by a decrease in the bubble response and the phase of the collapse. Bubble growth can occur by coalescence or rectified diffusion and can be detected by an increase of the response and the phase of the bubble collapse.

IV. C. 2. Multibubble Cavitation Fields

In this Section, the observations made from a cavitation zone composed of streamers such as those illustrated in Figure 31 will be discussed. High speed

SONOLUMINESCENCE from a SINGLE BUBBLE

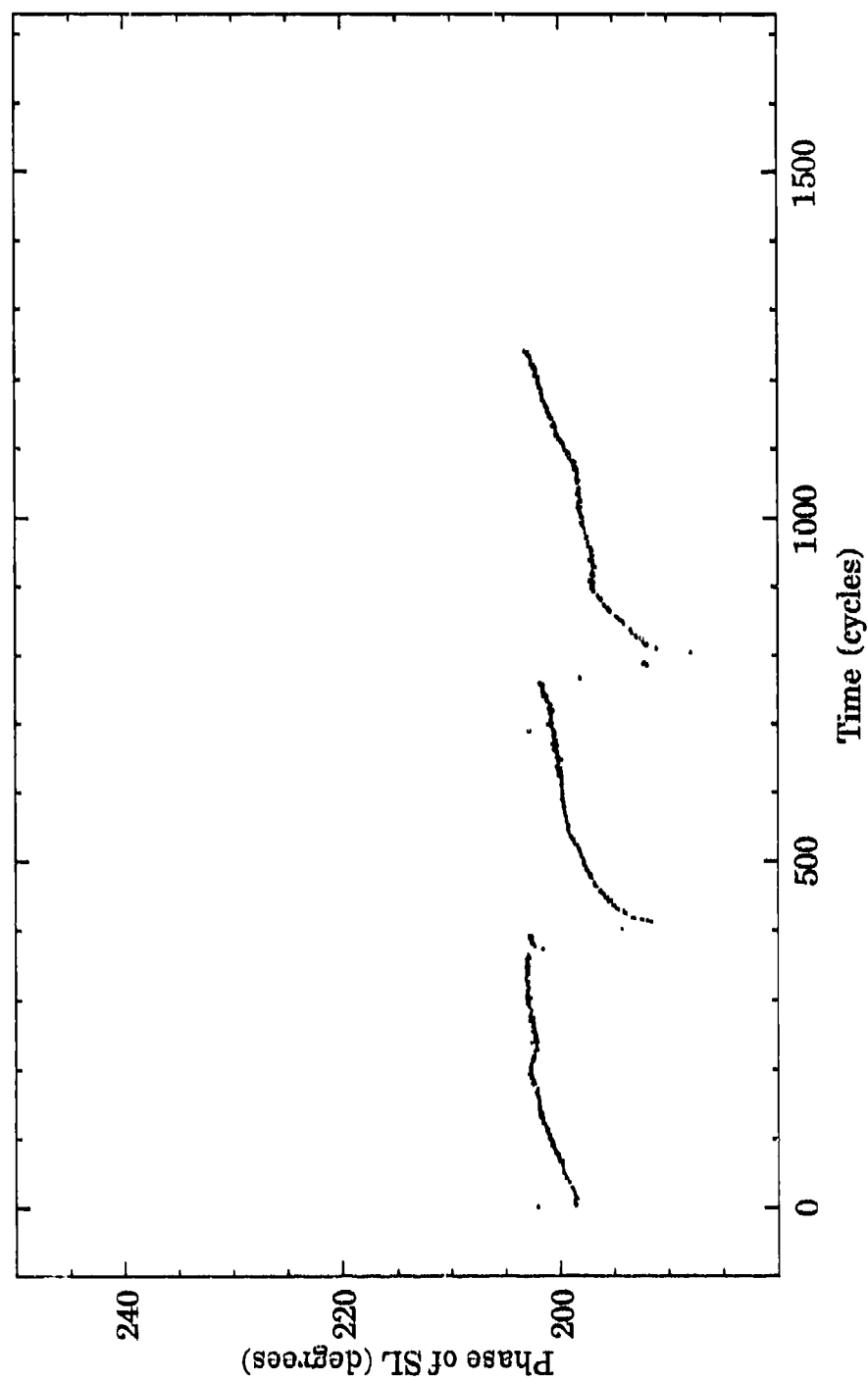


Figure 63. Phase of sonoluminescence emitted by a single bubble as a function of time. It was measured in water at $p_A=1.3$ bars and $f=21.0$ kHz by the time-to-amplitude converter (TAC) system during bubble breakup and disappearance.

photographs taken during the experiments revealed that these streamers consisted of fast-moving bubbles which were rapidly coalescing and breaking up. An example of the measurement of the phase of collapse in water at around 1.3 bars is shown in Fig. 64. In this data set, the phase of collapse appears to change irregularly between 185 and 215 degrees. Most of the measurements made of the collapse phase in multibubble cavitation fields were in this range. This range coincided with the collapse phase measured for single bubbles which were determined to be between 15 and 20 μm in radius. It thus appears that in a cavitation field at 20 kHz, bubbles that emit SL are in the range $15 \leq R_0 \leq 20 \mu\text{m}$. SL is produced by high temperatures and pressures in the interior of the bubbles, and these high temperatures and pressures are responsible for most cavitation-related effects. It may then be said that bubbles in the range $15 \leq R_0 \leq 20 \mu\text{m}$ are the only active bubbles in cavitation fields at 20 kHz. This range of bubble sizes may be even smaller since some of the scatter in the measured values of the phase may be due to fluctuations of the driving pressure. Furthermore, the fact that the range of values for the phase of collapse of single bubbles and cavitation field bubbles coincide may be an indication that only bubbles pulsating radially emit SL. Evidence for this hypothesis is also found in the fact that when a single bubble goes into surface oscillations, the SL output decreases by an order of magnitude. It was not uncommon to observe a single bubble pulsating radially and emitting SL flashes every cycle for as many as 1000 consecutive cycles. However, when surface waves were excited, as evidenced by dancing motion, the average number of SL flashes was about one in ten cycles. This seems to imply that a spherical collapse

SONOLUMINESCENCE from MANY BUBBLES

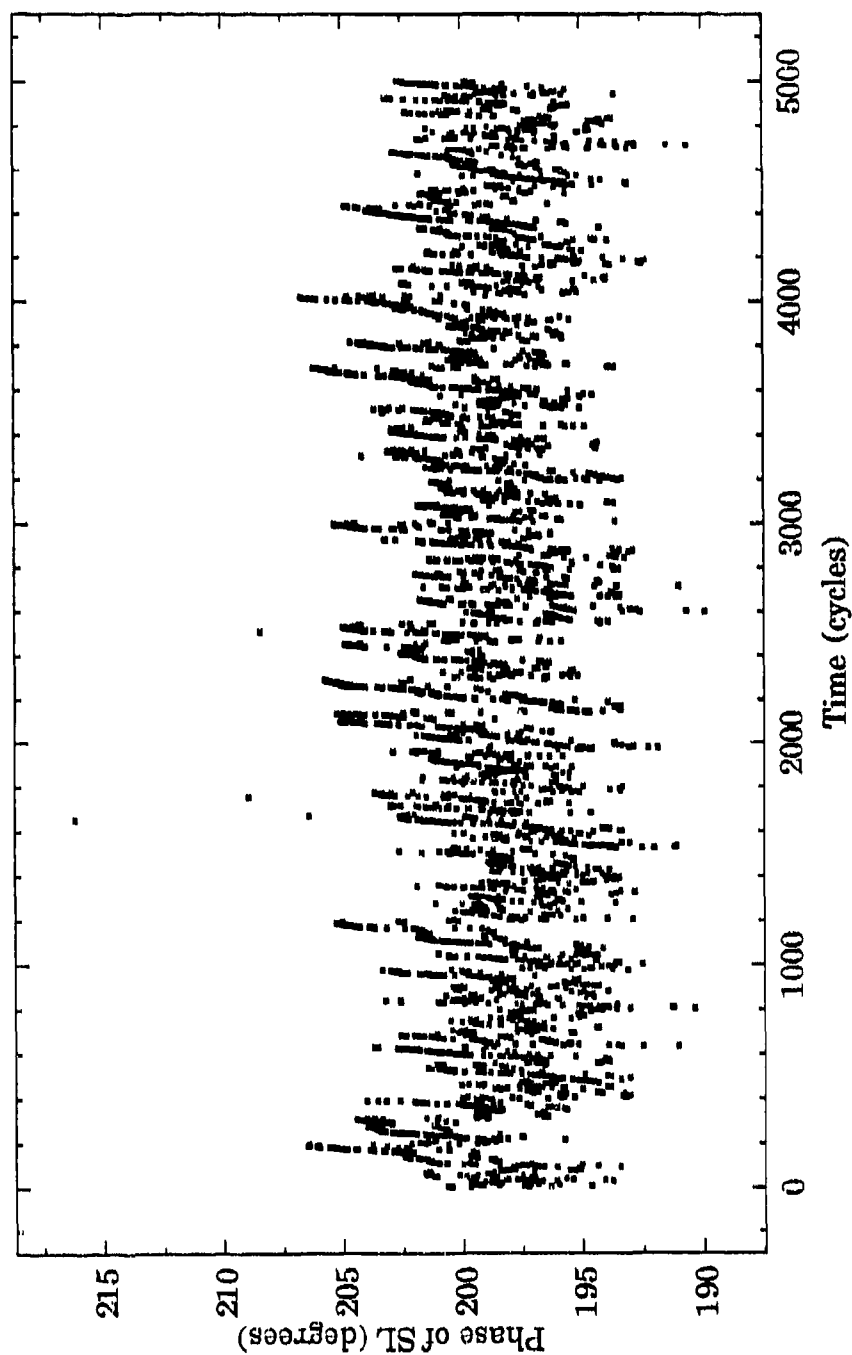


Figure 64. Phase of sonoluminescence emitted by a multibubble cavitation field as a function of time. It was measured in water at $p_A=1.3$ bars and $f=21.0$ kHz by the time-to-amplitude converter (TAC) system.

is necessary to generate sufficiently high temperatures and pressures in the interior of the bubble.

In addition, the data displayed in Fig. 65 reveal the same type of cyclic behavior observed in a single bubble as described in the previous Section. This behavior was observed often in a multibubble cavitation field, although it was not always repeatable. It was usually observed at the higher pressure amplitudes (1.3-1.5 bars). Nevertheless, these data show that the same cyclic behavior observed in a single bubble also occurs in a multibubble cavitation field. Similarly, this behavior can be attributed to the breakup of bubbles by surface instabilities followed by coalescence or rectified diffusion.

In summary, we have observed cyclic behavior in both single and multibubble cavitation fields. This behavior has been observed before by other investigators and can be caused by resonances of the bubble motion encountered as the bubble grows. These resonances trigger surface instabilities which in turn result in a reduction of the bubble size due to breakup. As the bubbles regrow by rectified diffusion or coalescence, the process repeats itself. In addition, the coincidence of the phase of collapse for both single and multibubble cavitation suggests that spherical collapses are required to generate the high temperatures and pressures responsible for most cavitation-related effects.

SONOLUMINESCENCE from MANY BUBBLES

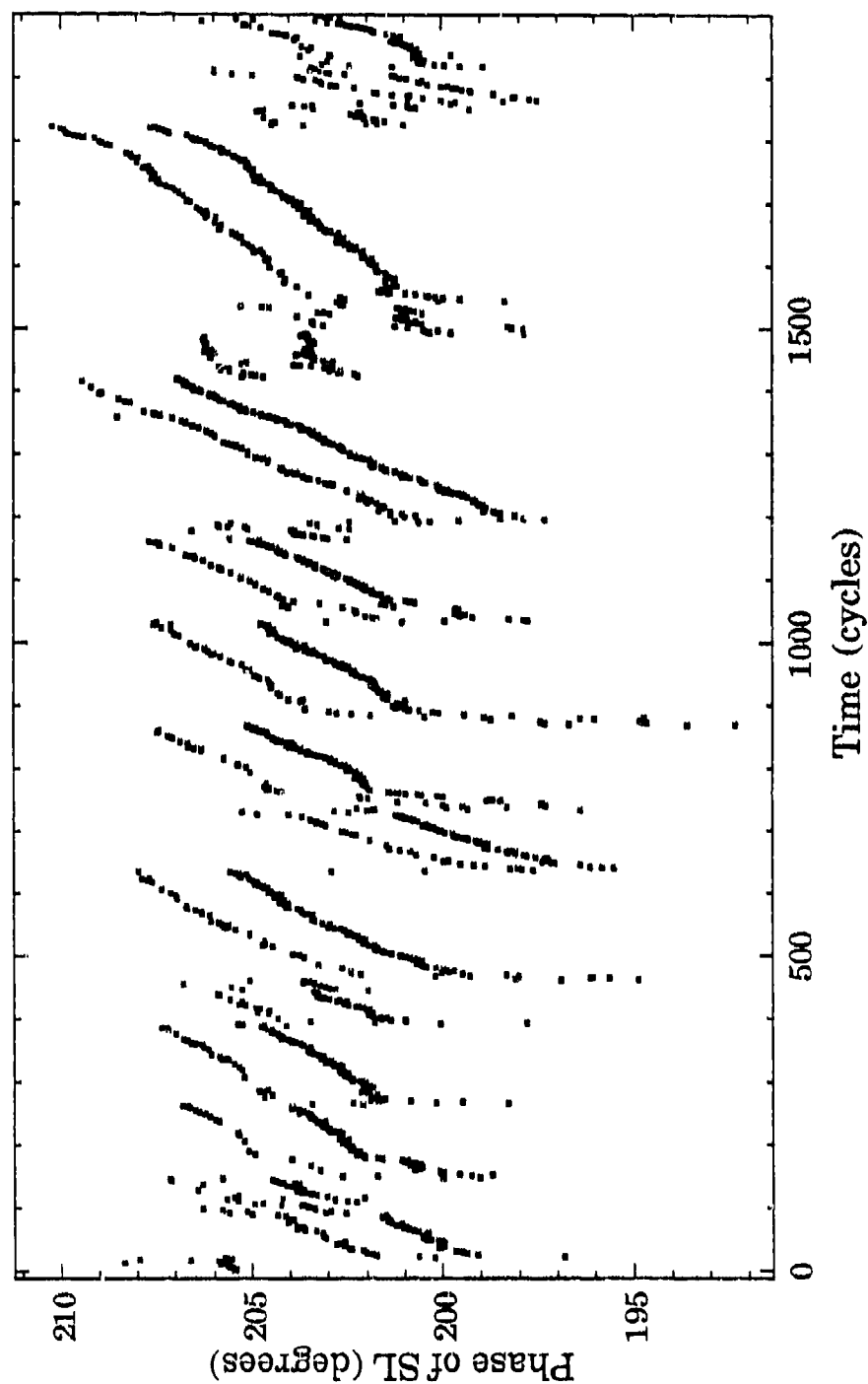


Figure 65. Phase of sonoluminescence emitted by a multibubble cavitation field as a function of time. It was measured in water at $p_A=1.3$ bars and $f=21.0$ kHz by the time-to-amplitude converter (TAC) system.

Chapter V

Summary, Conclusions and Topics for Future Study

V. A. Summary of the Dissertation

The purpose of this dissertation was to increase the understanding of the dynamics of bubbles in cavitation fields. In trying to reach this goal, the following accomplishments have been made:

1. Experimental radius-time curves for single bubbles pulsating radially at large amplitudes have been obtained. These bubbles were obtained in water/glycerine mixtures at pressure amplitudes between 1.1 and 1.5 bars at 20 kHz. These bubbles were observed to exhibit sonoluminescence. The pulsation amplitude, the phase of the collapse and the number of minima have been measured for a range of pressure amplitudes and bubble sizes.

2. After verifying the simultaneity of the light emission and the bubble collapse, the phase of the light emission was observed for thousands of acoustic periods in order to monitor the long-term behavior of bubbles in the cavitation field.

3. The applicability of three theoretical formulations of bubble dynamics has been evaluated in a range of acoustic pressure amplitudes near the threshold for sonoluminescence. These theories have been used to evaluate the internal temperatures and pressures reached during the bubble collapse at the experimentally determined threshold for light emission.

V.B. Conclusions

The following conclusions were made from the experimental evidence and the numerical calculations:

1. Sonoluminescence from stable cavitation at 20 kHz is emitted by bubbles in the size range 15-20 microns. These bubble are small enough so that, although pulsating at large amplitudes, they retain the spherical symmetry necessary to attain the high temperatures required for light emission. Discrepancies were found between the experimental and theoretical values of the pulsation amplitude, phase of collapse and the number of rebounds, however. The number of rebounds was observed to be lower and the amplitude of each rebound larger in amplitude than expected from the theories. It was concluded that the physical conditions attained during the collapse were outside the limits of the theories.

2. From the observations of the phase of light emission, it was concluded that violently pulsating bubbles often undergo fragmentation and coalescence in a periodic fashion. This process has a period on the order of 500 acoustic periods, and varies depending on the acoustic pressure amplitude and other parameters.

3. From the theoretical calculations made for the parameters measured at the threshold for light emission, it was concluded that internal temperatures in the range 2,000-3,000K were necessary to produce sonoluminescence. This finding supports the Chemiluminescent model as the mechanism for light production. Previous measurements of internal temperatures at $p_A \sim 8$ bars indicate that present models of bubble pulsations overestimate the internal temperature and pressure. Internal temperatures are expected to reach an asymptote as more of

the collapse energy is deposited into other chemical processes such as dissociation and ionization.

4. A previously undiscovered stable region exists in the pressure-radius parameter space above both surface instability and rectified diffusion thresholds for radially pulsating bubbles. The mechanisms through which this stability is attained are not yet understood. Nevertheless, the observations made of bubble stability indicate the existence of a transient cavitation threshold, which had been observed and predicted previously in other systems. Above this threshold, rapid bubble collapse promotes surface instabilities which cause the bubble to disintegrate.

V. C. Topics for Future Study

The following are some of the improvements that can be made to the experiments performed in this study as well as suggestions for further investigations.

1. The equilibrium radius of single pulsating bubbles must be determined accurately in order to confirm the applicability of the models. Thus, a technique must be developed to measure bubble radii in the range 15-25 microns. This technique must be precise (to within 5-10%) and take not more than a couple of seconds in order to minimize the amount of diffusion in or out of the bubble.

2. Several techniques exist, including the measurement of SL spectra, that can be used to measure the internal temperatures and pressures during the collapse of the bubble. One of the difficulties encountered in performing these

measurements previously, is the inhomogeneity of the cavitation field which contains an undetermined range of bubble sizes. The use of a single pulsating bubble to generate sonoluminescence should improve the precision of these measurements.

3. The low signal-to-noise ratio obtained with the laser scattering technique for small bubble radii presented a major obstacle to the study of the bubble motion during the final stages of collapse. Techniques using high speed photography and holography offering high spatial and temporal resolution may provide important data on the radial stability of pulsating bubbles.

4. The mechanism or mechanisms through which the radial stability of the bubble is achieved certainly deserve further study. This mechanism may prove to be important in understanding the motion of bubbles in moderate to high intensity cavitation fields.

References

- A. A. Atchley. "The nucleation of cavitation in aqueous media". Dissertation, U. of Mississippi (1984).
- V. G. Benkovskii, P. I. Golubnichii and S. I. Maslennikov. Sov. Phys. Acoust. **20**, 14(1974).
- F. G. Blake. "The onset of cavitation in liquids". Tech. Memo. No. 12, Harvard Acoustics Research Laboratory, (1949).
- A. A. Buzukov and V. S. Teslenko. Soviet Phys. J.E.T.P. Lett. **14**, 189
- L. A. Chambers. Phys. Rev. **49**, 881 (1936).
- C. C. Church. "Prediction of rectified diffusion during nonlinear bubble pulsations at biomedical frequencies". J. Acous. Soc. Am. **83**, 2210-2217 (1988).
- C. C. Church. Private communication (1990a); Private communication (1990b); Private communication (1990c).
- K. W. Commander. "A theoretical investigation of acoustic cavitation". Dissertation, U. of Mississippi (1985).
- L. A. Crum. "The acoustic radiation pressure on a liquid droplet in a stationary sound field". Tech. Report, U.S. Naval Academy (1970).

L. A. Crum. "Bjerknes forces on bubbles in a stationary sound field". J. Acous. Soc. Am. **57**, 1363 (1975).

L. A. Crum and A. Prosperetti. "Erratum and comments on 'Nonlinear oscillations of gas bubbles in liquids: An interpretation of some experimental results' [J. Acous. Soc. Am. **73**, 121 (1983)]". J. Acous. Soc. Am. **75**, 1910 (1984).

M. Degrois and P. Baldo. Ultrasonics **12**, 25 (1974).

A. Eller and G. H. Flynn. "Rectified diffusion during nonlinear pulsations of cavitation bubbles". J. Acous. Soc. Am. **37**, 493 (1965).

A. I. Eller and L. A. Crum. "Instability of the motion of a pulsating bubble in a sound field". J. Acous. Soc. Am. **47**, 762 (1970).

R. D. Finch. "Sonoluminescence". Ultrasonics, **1**, 87 (1963).

H. G. Flynn. "Physical Acoustics". W. P. Mason ed. vol. 1, part B (Academic Press, New York, 1964).

H. G. Flynn. "Cavitation dynamics. I. A Mathematical formulation". J. Acous. Soc. Am. **57**, 1379 (1975a).

H. G. Flynn. "Cavitation dynamics. II. Free pulsations and models for cavitation bubbles". J. Acous. Soc. Am. **58**, 1160 (1975b).

J. Frenkel. Acta Phys.-chim. U.R.S.S. **12**, 317 (1940) (in Russian): as referenced by Verral *et al.* (1988).

H. Frenzel and H. Schultes. Z. Phys. Chem. **27B**, 421 (1935): as referenced by Verral *et al.* (1988).

F. R. Gilmore. "The collapse and growth of a spherical bubble in a viscous compressible liquid". Caltech Hydrodynamics Laboratory report No. 26-4 (1952).

G. Gimenez. "The simultaneous study of light emission and shock waves produced by cavitation bubbles". J. Acoust. Soc. of Am. **71**, 839-846 (1982).

P. I. Golubnichii, V. D. Goncharov and Kh. V. Protopopov. "Sonoluminescence in liquids: Influence of dissolved gases, departures from thermodynamic theory". Sov. Phys. Acoust. **15**, 464 (1970).

P. I. Golubnichii, V. M. Gromenko and A. D. Filonenko Soviet Phys. tech. Phys. Lett. **5**, 233 (1979).

R. K. Gould. "Simple method for calibrating small omnidirectional hydrophone". J. Acous. Soc. Am. **43**, 1185 (1968).

R. K. Gould. "Rectified diffusion is the presence of, and absence of, acoustic streaming". J. Acous. Soc. Am. **56**, 1740 (1975).

V. Griffing. J. Chem. Phys. **18**, 997 (1950).

V. Griffing. J. Chem. Phys. **20**, 939 (1952).

P. Gunther, E. Heim, A. Schmitt and W. Zeil. Z. Naturf. **12A**, 521 (1957a).

P. Gunther, W. Zeil, U. Grisar and E. Heim, Zeit. fur Elektrokem. **61**, 188 (1957b): as referenced by Walton *et al.* (1984).

G. M. Hansen. " Mie scattering as a technique for the sizing of air bubbles". Dissertation, U. of Mississippi (1984).

E. N. Harvey. J. Am. Chem. Soc. **61**, 2392 (1939).

R. Hickling. "Effects of thermal conduction in sonoluminescence". J. Acous. Soc. Am. **35**, 967 (1963).

R. G. Holt. "Experimental observations of the nonlinear response of single bubbles to an applied acoustic field". Dissertation, U. of Mississippi (1988).

S. D. Horsburgh. "Radial instabilities of a pulsating air bubble in water". Dissertation, U. of Mississippi (1990).

D. Y. Hsieh. "Theory of rectified diffusion of mass into gas bubbles". J. Acous. Soc. Am. **33**, 206-215 (1960).

D. Y. Hsieh. "On the thresholds for surface waves and subharmonics of an oscillating bubble". J. Acous. Soc. Am. **56**, 392 (1974).

IMSL. Mathematical software library. (IMSL, Houston, 1987).

P. Jarman. Proc. Phys. Soc. **B 72**, 628 (1959).

P. Jarman. "Sonoluminescence: A discussion". J. Acoust. Soc. of Am. **32**, 1459 (1960).

P. Jarman and K. J. Taylor. "The timing of the main and secondary flashes of sonoluminescence from acoustically cavitated water". Acustica **23**, 243 (1970).

V. Kamath and A. Prosperetti. "Numerical integration methods in gas-bubble dynamics". J. Acous. Soc. Am. **85**, 1538 (1989).

J. B. Keller and M. Miksis. "Bubble oscillations of large amplitude". J. Acous. Soc. Am. **68**, 628 (1980).

M. Kerker. The scattering of light and other electromagnetic radiation. Chapters 3-5. (Academic Press., New York, 1969).

J. G. Kirkwood and H. A. Bethe. "The pressure wave produced by an underwater explosion". OSRD Report No. 558 (1942).

H. Kuttruff. Acustica **12**, 230 (Akustische Beihefte) (1962); as referenced by Walton *et al.* (1984).

G. J. Lastman and R. A. Wentzell. "Comparison of five models of spherical bubble response in an inviscid compressible liquid". J. Acous. Soc. Am. **69**, 638-642 (1980).

W. Lauterborn. "Numerical investigation of nonlinear oscillations of gas bubbles in liquids". J. Acous. Soc. Am., **59**, 283-293 (1976).

W. Lauterborn and W. Hentschel. "Cavitation bubble dynamics studied by high speed photography and holography: part two". *Ultrasonics* **26**, 59 (1986).

W. Lauterborn. "Cavitation dynamics - new tools for an intricate problem". *Applied Scientific Research* **38**, 165-178 (1982).

V. L. Levshin and S. N. Rzhetsky. *Doklady Akad. Nauk SSR*, **16**, 407 (1937); as referenced by Verral *et al.* (1988).

R. Q. Macleay and L. V. Holroyd. "Space-time analysis of the sonoluminescence emitted by cavitated water". *J. Appl. Phys.* **32**, 449-453 (1961).

M. A. Margulis. "Investigation of electrical phenomena connected with cavitation. II. On the theory of appearances of sonoluminescence and sonochemical reactions". *Russ. J. Phys. Chem.* **58**, 1450 (1984).

N. Marinenco. J. J. Trillat, *C. R. Acad. Sci.* **196**, 858 (1933); as referenced by Walton *et al.* (1984).

E. Meyer and H. Kuttruff. *Z. angew. Phys.* **11**, 325 (1959); as referenced by Walton *et al.* (1984).

K. Negishi. *Acustica* **10**, 124 (1960); as referenced by Walton *et al.* (1984).

K. Negishi. *J. Phys. Soc. Japan* **16**, 1450 (1961); as referenced by Walton *et al.* (1984).

E. Neppiras and E. E. Fill. "A cyclic cavitation process". J. Acous. Soc. Am. **46**, 1264 (1969).

E. Neppiras. "Acoustic cavitation: review". Phys. Lett. Rev. **61**, 159 (1980).

B. E. Noltingk and E. A. Neppiras. "Cavitation produced by ultrasonics". Proc. phys. Soc. B **63**, 674 (1950).

W. Nyborg and D. E. Hughes. "Bubble annihilation in cavitation streamers". J. Acous. Soc. Am. **42**, 891 (1967).

M. S. Plesset. "On the stability of fluid flows with spherical symmetry". J. Applied Physics **25**, 96 (1954).

M. S. Plesset. "The dynamics of cavitation bubbles". J. Applied Mech. **16**, 277 (1949).

H. Poritsky. Proc. 1st U.S. National Congress in Applied Mechanics (A.S.M.E.) 813 (1952).

A. Prosperetti. "Nonlinear oscillations of gas bubbles in liquids: steady-state solutions". J. Acous. Soc. Am. **56**, 878 (1974).

A. Prosperetti, L. A. Crum and K. W. Commander. "Nonlinear bubble dynamics". J. Acous. Soc. Am. **83**, 502 (1986).

A. Prosperetti. "Acoustic cavitation series part two - Bubble phenomena in sound fields: part one". Ultrasonics **22**, 69 (1984).

A. Prosperetti and G. Seminara. "Linear stability of a growing or collapsing bubble in a slightly viscous liquid". *Physics of Fluids* **21**, 1465 (1978).

A. Prosperetti. Private communications (1990)

Lord Rayleigh. "On the pressure developed in a liquid during the collapse of a spherical cavity". *Phil. Mag.* **34**, 94 (1917).

T. K. Saksena and W. L. Nyborg. "Sonoluminescence from stable cavitation". *J. Chem. Phys.* **53**, 1722 (1970).

L. D. Rozenberg. High Intensity Ultrasonic fields. (Plenum Press, New York, 1971).

C. Sehgal, R. P. Steer, R. G. Sutherland, and R. E. Verral. "Sonoluminescence of argon saturated alkali metal salt solutions as a probe of acoustic cavitation". *J. Chem. Phys.* **70**, 2242-2248 (1979).

C. Sehgal, R. P. Steer, R. G. Sutherland, and R. E. Verral. "Sonoluminescence of NO- and NO₂-saturated water as a probe of acoustic cavitation". *J. Phys. Chem.* **84**, 396-401 (1980).

C. M. Sehgal and R. E. Verral. "A review of the electrical hypothesis of sonoluminescence". *Ultrasonics* **20**, 37-39 (1982).

K. S. Suslick and D. A. Hammerton. "The site of sonochemical reactions". *IEEE Trans. Ultrason. Ferroelectr. Freq. Control* **UFFG-33**, 143-147 (1986a).

K. S. Suslick, D. A. Hammerton and R. E. Cline. "The sonochemical hot spot". *Am. Chem. Soc.* **108**, 5641,5642 (1986b).

K. S. Suslick. "Sonochemistry". *Science* **247**, 1439 (1990).

K. J. Taylor and P. D. Jarman. "The spectra of sonoluminescence". *Aust. J. Phys.* **23**, 319 (1970).

R. E. Verral and C. Sehgal. "Sonoluminescence". Sonochemistry: Its chemical, physical and biological effects. K. S. Suslick ed. (VCH Publishers, New York 1988).

W. U. Wagner. *Zeit. fur angew. Phys.* **10**, 445 (1958); as referenced by Finch (1983).

A. J. Walton and G. T. Reynolds. "Sonoluminescence". *Advances in Physics* **33**, 595 (1984)

W. A. Weyl and E. C. Marboe. *Research* **2**, 19 (1949); as referenced by Verral *et al.* (1988).

G. W. Willard. "Ultrasonically induced cavitation in water: a step-by-step process". *J. Acous. Soc. Am.*, **25**, 669 (1953)

W. J. Wiscombe. "Improved Mie scattering algorithms". *Applied Optics*, **19**,1505 (1980).

F. R. Young. "Sonoluminescence from water containing dissolved gases". *J. Acous. Soc. Am.* **60**, 100 (1976)

Appendix A

ADDITIONAL FIGURES

EXPERIMENTAL MIE SCATTERING FOR WATER

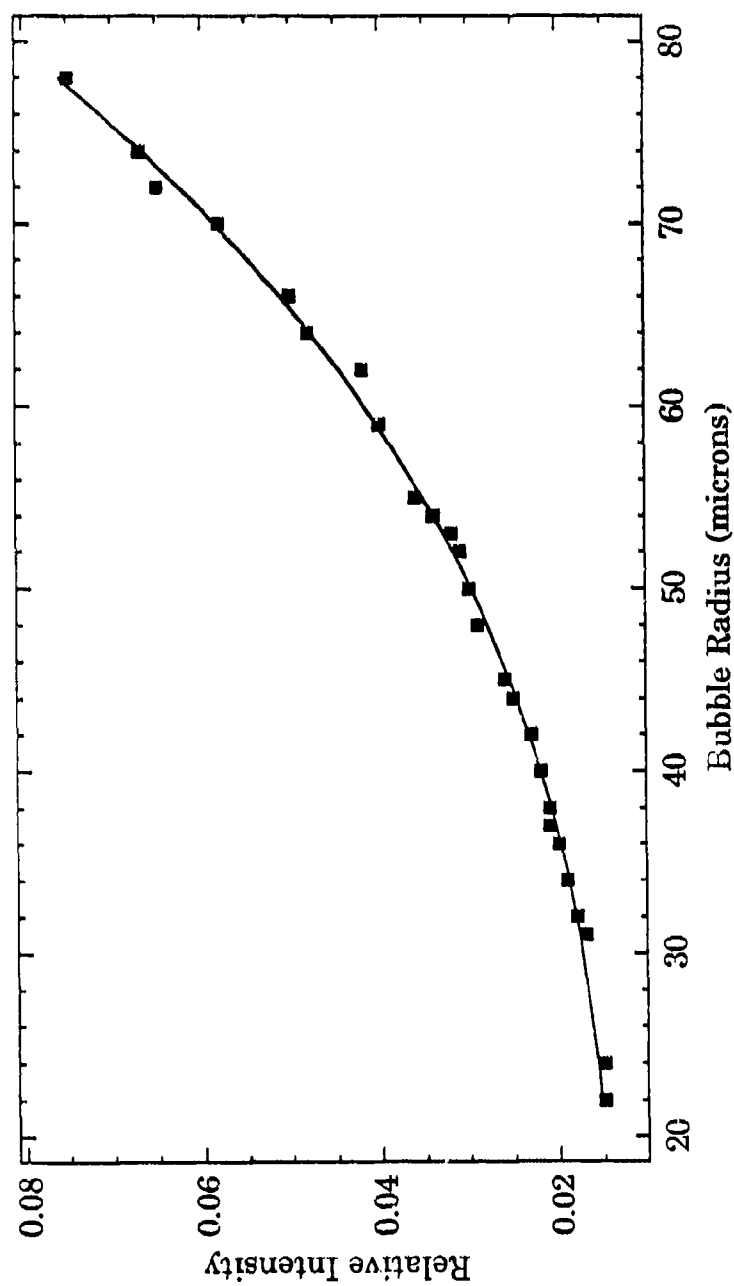


Figure A2. Measured scattered light intensity vs equilibrium bubble radius for water at $f=21.0$ kHz. The solid line corresponds to a 2nd degree polynomial fit.

EXPERIMENTAL MIE SCATTERING FOR 21% GLYCERINE

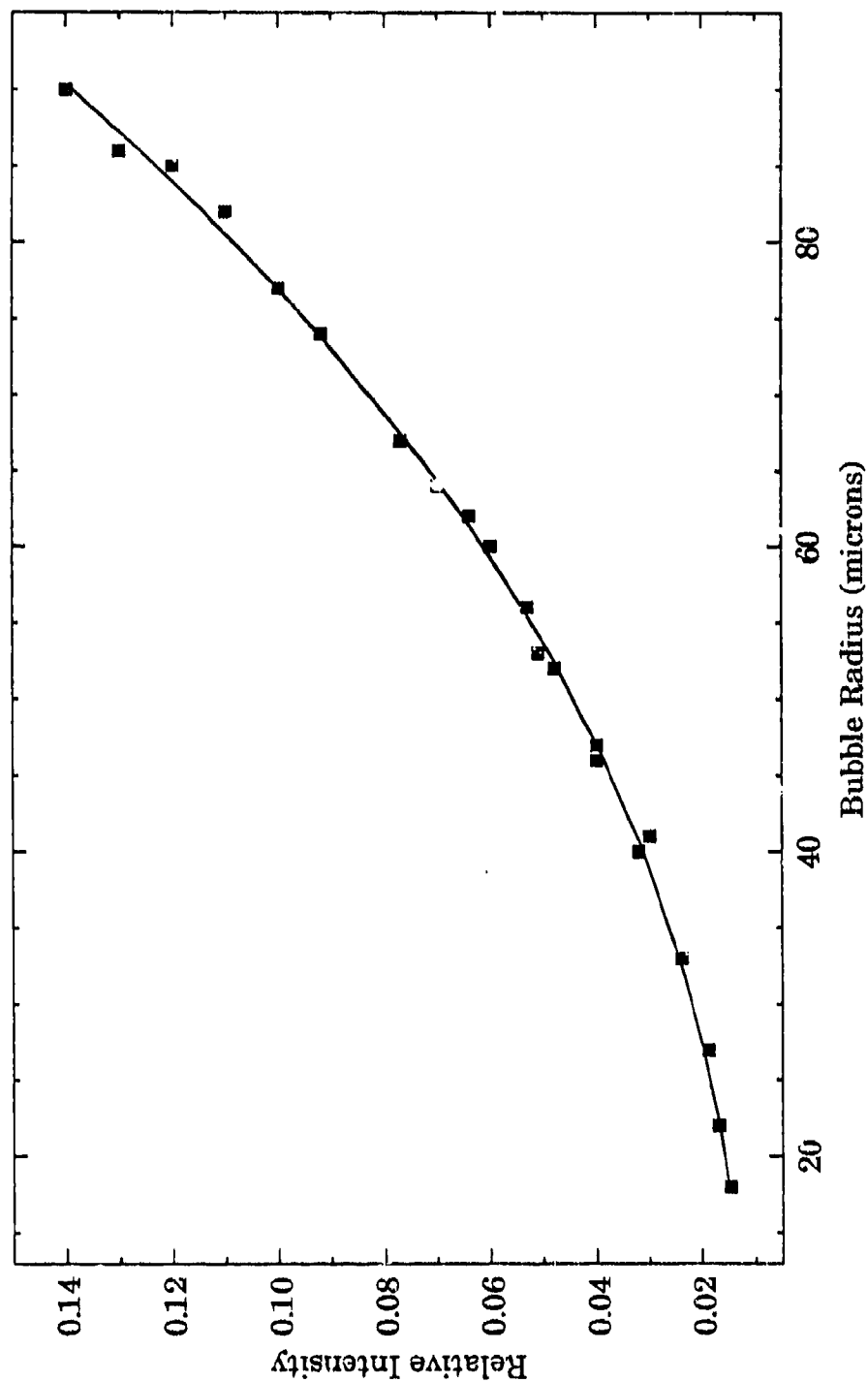


Figure A3. Measured scattered light intensity vs equilibrium bubble radius for GLY21 at $f=22.3$ kHz. The solid line corresponds to a 2nd degree polynomial fit.

EXPERIMENTAL MIE SCATTERING FOR 35% GLYCERINE

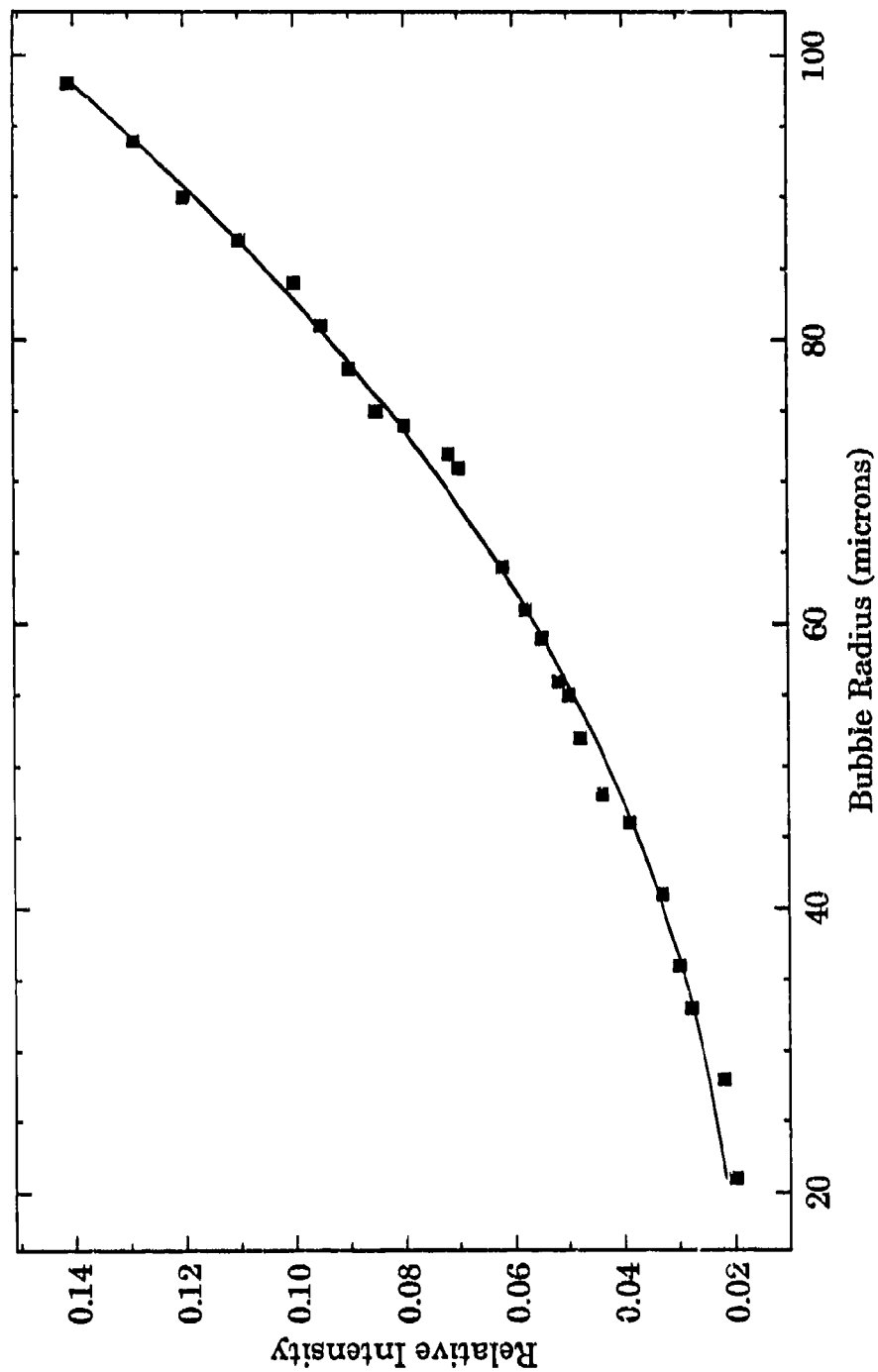


Figure A4. Measured scattered light intensity vs equilibrium bubble radius for GLY35 at $f=23.0$ kHz. The solid line corresponds to a 2nd degree polynomial fit.

EXPERIMENTAL MIE SCATTERING FOR 60% GLYCERINE

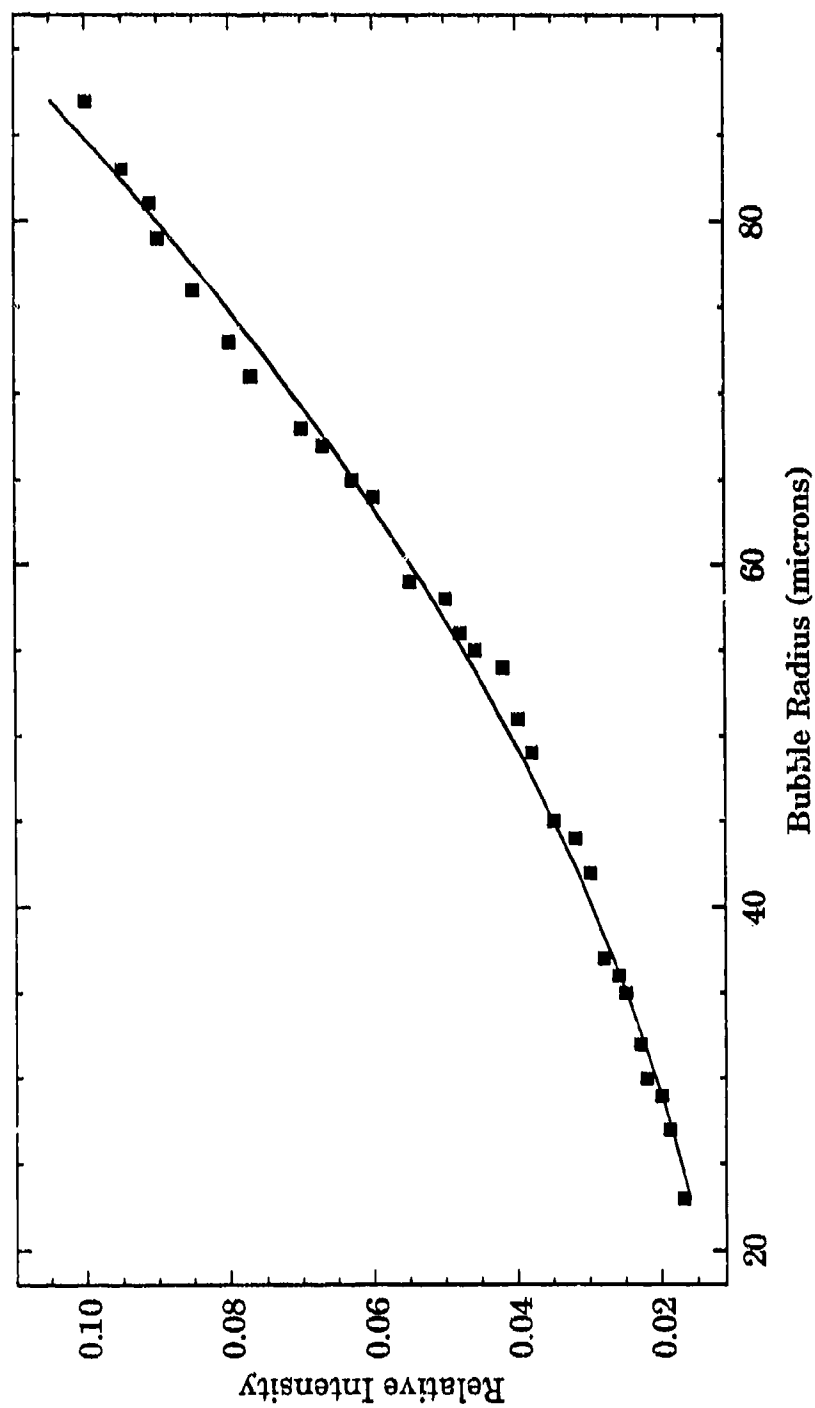


Figure A5. Measured scattered light intensity vs equilibrium bubble radius for GLY60 at $f=24.8$ kHz. The solid line corresponds to a 2nd degree polynomial fit.

EXPERIMENTAL RADIUS vs TIME for WATER

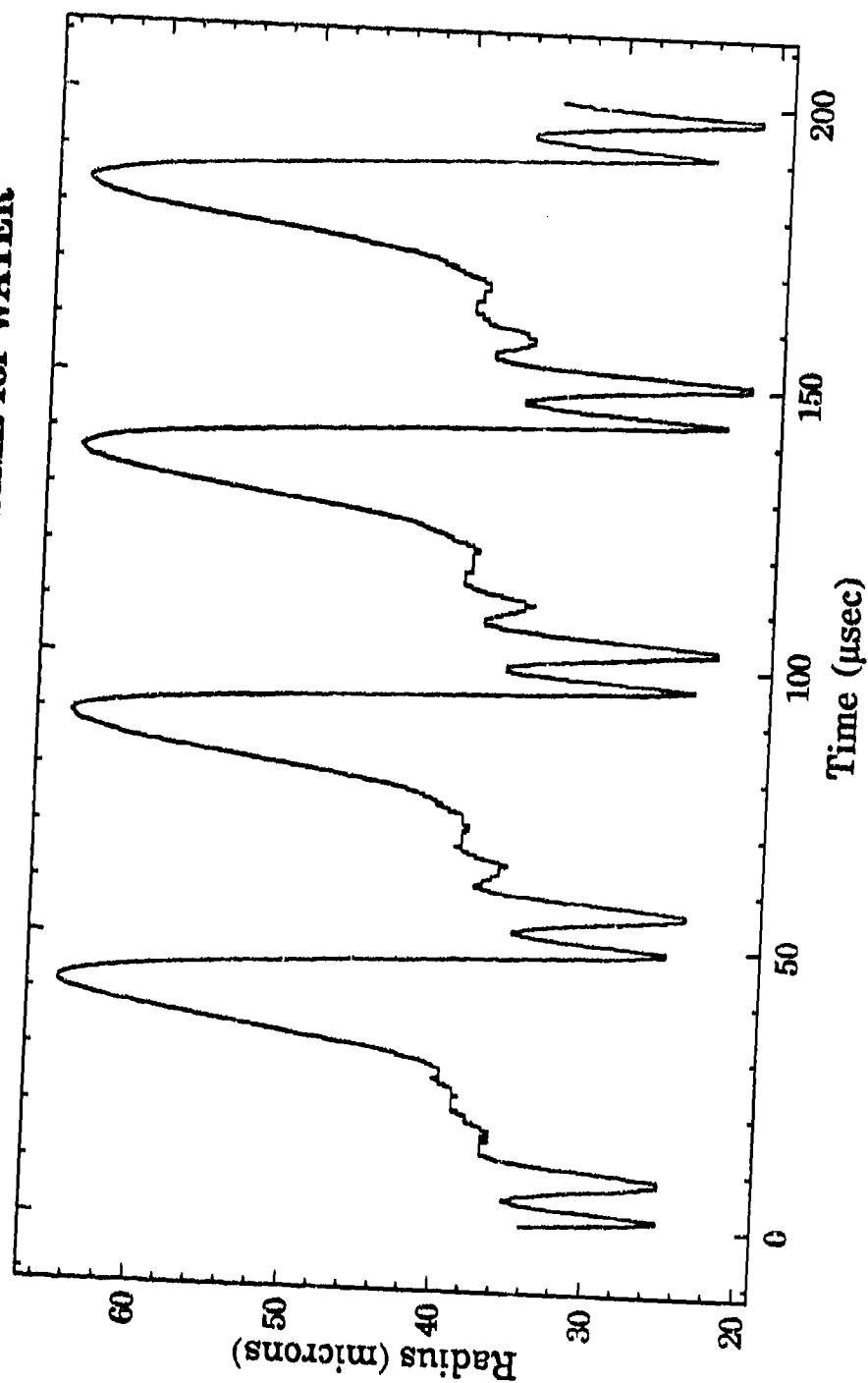


Figure A6. Experimental radius-time curve obtained with the light-scattering apparatus in water at $f=21.0$ kHz.

EXPERIMENTAL RADIUS vs TIME for GLY35

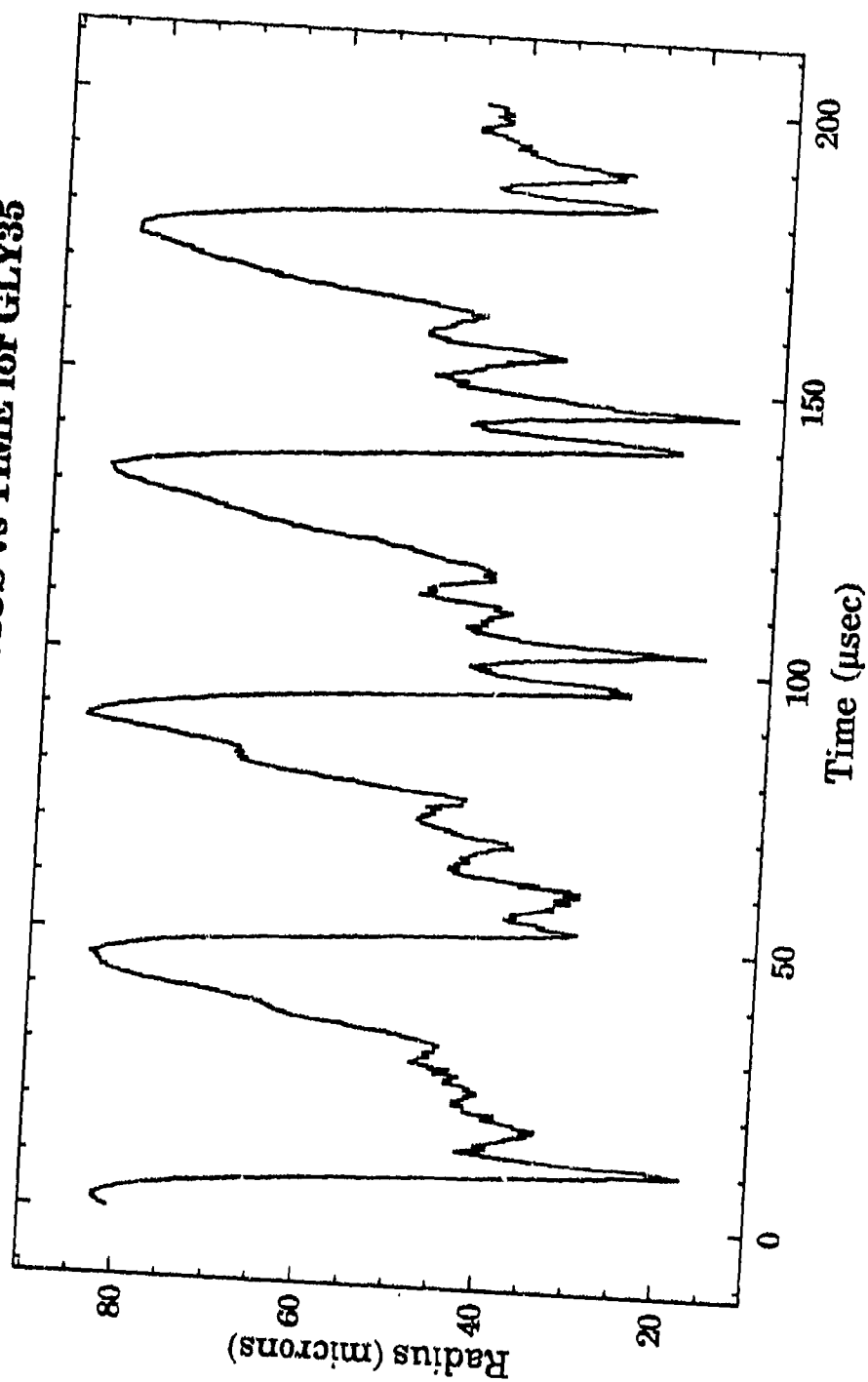


Figure A7. Experimental radius-time curve obtained with the light-scattering apparatus in GLY35 at $f=23.0$ kHz.

EXPERIMENTAL RADIUS vs TIME for GLY42

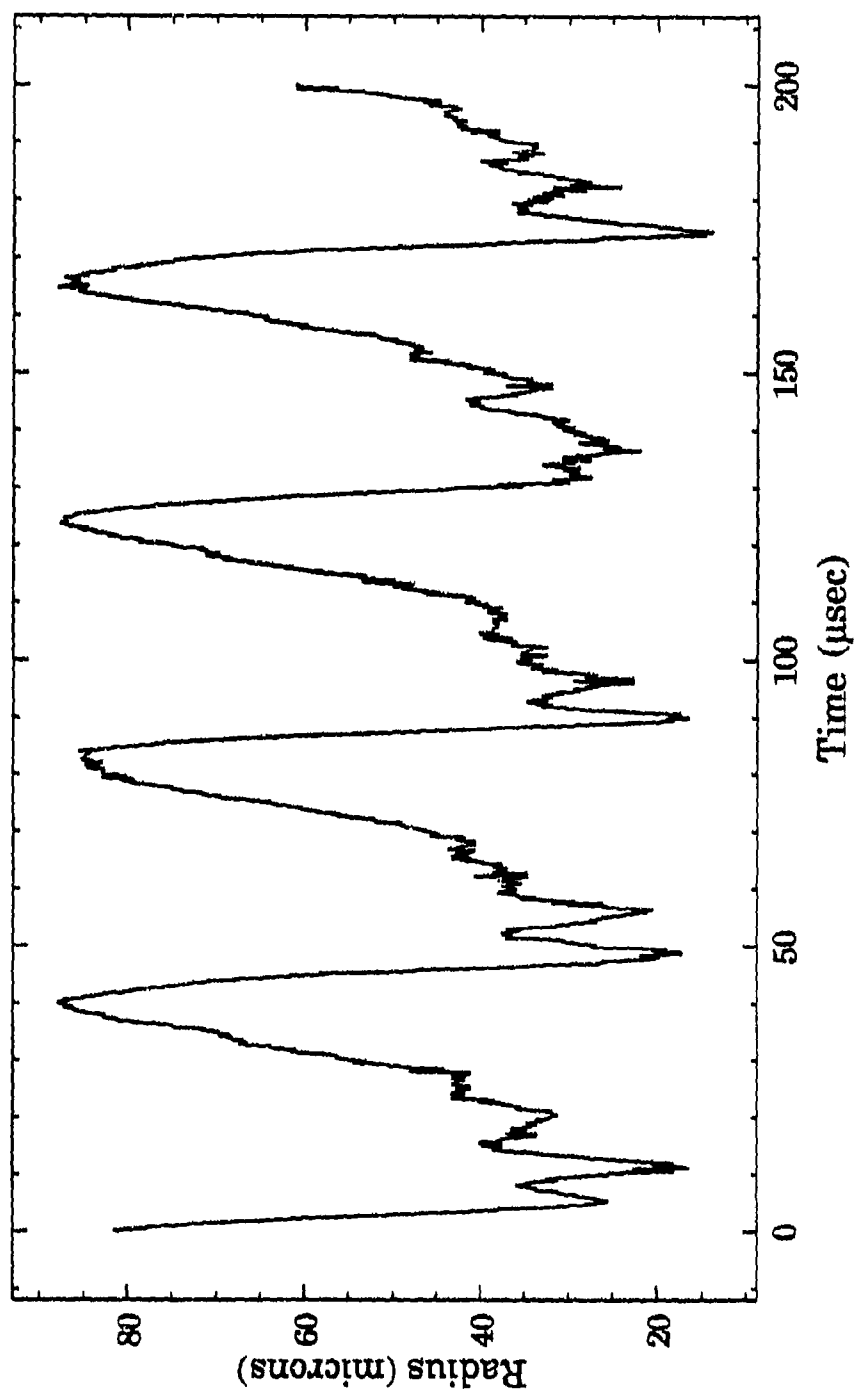


Figure A8. Experimental radius-time curve obtained with the light-scattering apparatus in GLY42 at $f \approx 23.6$ kHz.

EXPERIMENTAL RADIUS vs TIME for GLY60

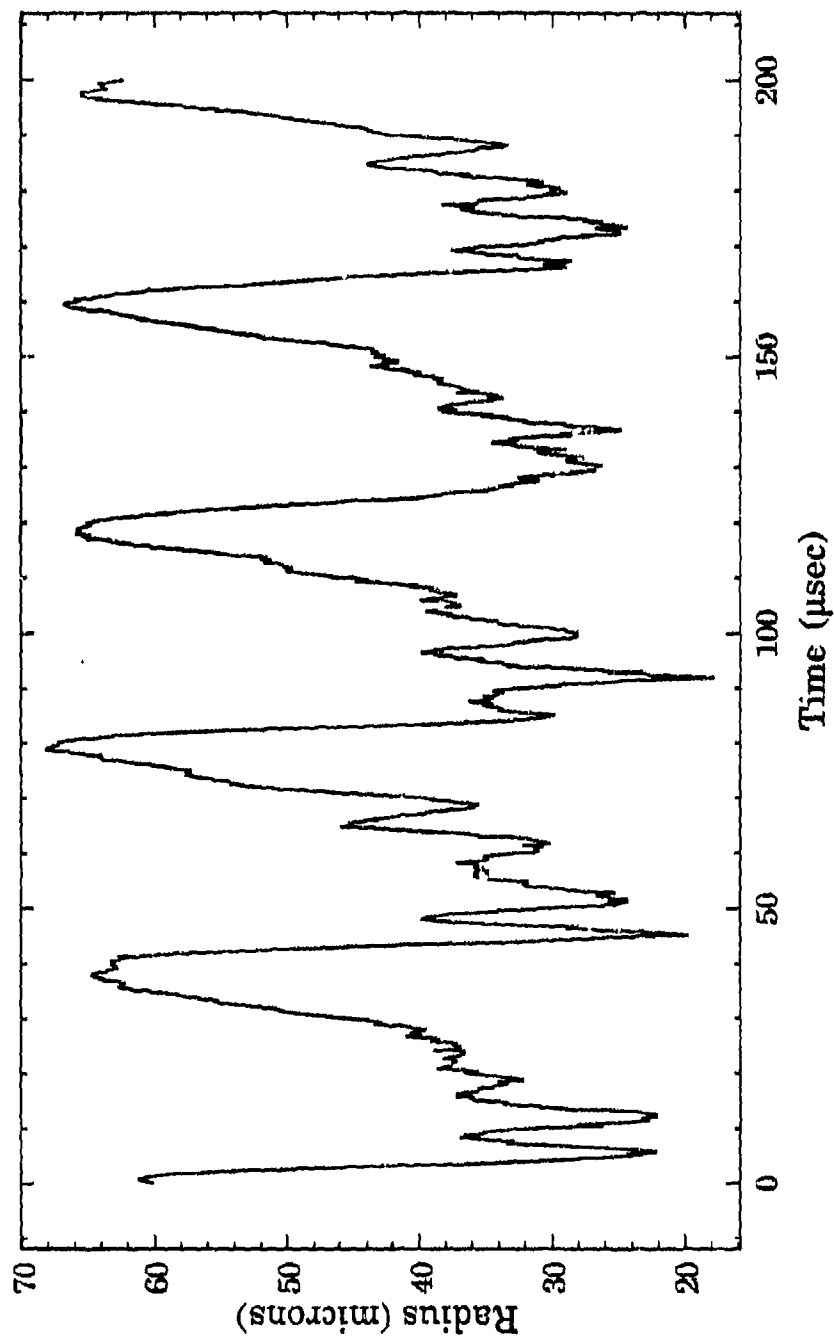


Figure A9. Experimental radius-time curve obtained with the light-scattering apparatus in GLY60 at $f=24.8$ kHz.

Biographical Sketch of the Author

Dario Felipe Gaitan was born in Medellin, Colombia on June 2, 1961, the son of Dario Gaitan and Luz Gaviria de Gaitan. He attended high school in Medellin at Colegio de San José, graduating in November, 1978. He received a B.S. in physics from the University of Southwestern Louisiana in May, 1984.

Felipe is a member of Sigma Pi Sigma, The American Physical Society, and the Acoustical Society of America. He enjoys volleyball, racquetball, scuba diving, hiking, and travelling. He plans to pursue a career in research and teaching and is currently looking for a post-doctoral position.

His permanent address is Crra. 43E No. 8-20, Medellin, Colombia, South America.

DISTRIBUTION LIST FOR
NCPA LC.02.90
TECHNICAL REPORT UNDER CONTRACT N00014-90-J-4021

COPY NO.

1	Chief of Naval Research Office of Naval Research Department of the Navy Attn. Marshall Orr
2	Director Naval Research Laboratory Washington, D.C. 20375 Attn: Library
3	Commander David Taylor Naval Ship Research and Development Center Target Physics Branch Bethesda, MD 20084 Attn: S. Schreppler (Code 1965)
4	Superintendent Naval Postgraduate School Department of Physics Monterey, CA 93940 Attn: Anthony Atchley
5-9	Commanding Officer and Director Defense Technical Information Center Bldg. 5, Cameron Station 5010 Duke Street Alexandria, VA 22314
10-20	Dr. I. A. Crum Associate Director for Basic Research National Center for Physical Acoustics University of Mississippi University, MS 38677
21-30	D. Felipe Gaitan National Center for Physical Acoustics University of Mississippi University, MS 38677

- 31 Joseph Townsend
Business Manager
National Center for Physical Acoustics
University of Mississippi
University, MS 38677
- 32 J. E. Matthews
NOARL Numerical Modeling Division
NSTL, MS 39529-5004
- 33 Phil Marston
Department of Physics
Washington State University
Pullman, WA 99164
- 34 Bob Gould
Department of Physics
Middlebury College
Middlebury, VT 05753
- 35 Andrea Prosperetti
Mechanical Engineering Department
The Johns Hopkins University
Baltimore, MD 21218
- 36 Seth Putterman
Physics Department
University of California
405 Hilgard Avenue
Los Angeles, CA 90024
- 37 Wesley Nyborg
Physics Department
University of Vermont
Burlington, VT 05405
- 38 A. J. Walton
Cambridge University Physics Department
Cavendish Laboratory
Madingley Road
Cambridge CB3 0HE
United Kingdom
- 39 Robert C. Dean, Jr.
Dean Technology, Inc.
P.O. Box A-56
Hanover, NH 03755

- 40 Kenneth Suslick
School of Chemical Sciences
University of Illinois
Urbana, IL 61801
- 41 Robert D. Finch
Mechanical Engineering Department
University of Houston
Houston, TX 77204-4792
- 42 Hugh G. Flynn
Center for Biomedical Ultrasound
University of Rochester
Rochester, NY 14627
- 43 Robert Hickling
National Center for Physical Acoustics
University of Mississippi
University, MS 38677
- 44 C. Sehgal
Department of Physiology and Biophysics
Mayo Foundation
Rochester, MN 55905
- 45 R. E. Verral
Department of Chemistry
University of Saskatchewan
Saskatoon, Saskatchewan S7N 0W0
Canada
- 46 Steve Daniels
Physical Science Laboratory
Oxford University
South Parks Road
Oxford OX1 3QZ
United Kingdom
- 47 Steve Garrett
Naval Postgraduate School
Physics Department
Monterey, CA 93943